UNIVERSITY OF SOUTHAMPTON

FACULTY OF PHYSICAL SCIENCES AND ENGINEERING
Optoelectronics Research Centre

All-optical Signal Processing in Novel Highly Nonlinear Fibres and Waveguides

by

Mohamed A. Ettabib

Thesis for the degree of Doctor of Philosophy

May 2014

UNIVERSITY OF SOUTHAMPTON

ABSTRACT

FACULTY OF PHYSICAL SCIENCES AND ENGINEERING
Optoelectronics Research Centre

Doctor of Philosophy

ALL-OPTICAL SIGNAL PROCESSING IN NOVEL HIGHLY NONLINEAR FIBRES AND WAVEGUIDES

by Mohamed A. Ettabib

All-optical signal processing has recently become an attractive research field, a result of nonlinear optical systems making major advances in terms of cost, compactness, energy consumption, integrability and reliability. This technology has impacted several areas ranging from telecommunications and biomolecular sensing to military and quantum communications, and spanning a vast range of frequencies from the near to mid-infrared. This PhD research project was aimed at investigating the features and feasibility of two state-of-the-art all-optical signal processing technologies: highly nonlinear soft glass fibres and silicon-based waveguides.

Of the various soft glasses available, lead silicate and tellurite are considered within this thesis. The optical properties of a highly nonlinear lead silicate W-type fibre are studied and the design process of such fibres is explained in detail. A number of telecommunications-based all-optical processing applications are also demonstrated in this fibre technology. Phase sensitive amplification is demonstrated in the W-type fibre and the process is used to regenerate the phase of 40 Gbit/s differential phase shift keying (DPSK) signals.

The optical characteristics of a highly nonlinear tellurite fibre are also studied both at 1.55 and 2 μm. Efficient four wave mixing (FMW)-based wavelength conversion of 1.55 μm signals is demonstrated in the fibre and a detailed numerical study into the potential of the fibre in realizing phase-matched mid-infrared (MIR) to near-infrared (NIR) spectral translation is conducted.

The second all-optical signal processing platform investigated in this project is silicon germanium (SiGe) waveguides. A detailed account of the linear and nonlinear optical properties of this newly emerging silicon-based technology is reported for the first time and the potential of this platform is highlighted by demonstrating wavelength conversion of 40 Gbaud DPSK and QPSK signals. Broadband spectral translation is also demonstrated in the SiGe waveguides with record FWM bandwidths.

Contents

List of Figures

List of Tables

Declaration of Authorship

I, Mohamed A. Ettabib , declare that the thesis entitled *All-optical Signal Processing in Novel Highly Nonlinear Fibres and Waveguides* and the work presented in the thesis are both my own, and have been generated by me as the result of my own original research. I confirm that:

- this work was done wholly or mainly while in candidature for a research degree at this University;
- where any part of this thesis has previously been submitted for a degree or any other qualification at this University or any other institution, this has been clearly stated;
- where I have consulted the published work of others, this is always clearly attributed;
- where I have quoted from the work of others, the source is always given. With the exception of such quotations, this thesis is entirely my own work;
- I have acknowledged all main sources of help;
- where the thesis is based on work done by myself jointly with others, I have made clear exactly what was done by others and what I have contributed myself;
- parts of this work have been published as: *See List of Publications*

Signed:..

Date:..

Acknowledgements

My time at the ORC has been a wonderful adventure, an experience that has left me with many unforgettable memories. This journey would not have been completed without the help and encouragement of a number of people whom I would like to humbly thank here.

First of all I would like to show my deepest gratitude to my supervisor, Prof. Periklis Petropoulos, for giving me this PhD studentship and supervising me throughout its time. His support and encouragement have been invaluable. Since my first days at the ORC, he guided me through my first steps in the lab and provided the necessary supervision whenever I needed it. During my low points he was always understanding, patient and encouraging. I feel fortunate and honoured to have worked under his supervision and to have been part of his research team. Periklis, Thank you!

I would also like to sincerely thank Dr. Kamal Hammani for his invaluable support during the second half of my PhD project. I benefited immensely from his technical knowledge, and his ability to excel in new fields has been a true inspiration to me. He is a wonderful colleague to work with and I can safely say that getting to know and befriend him have been some of the highlights of my time at the ORC.

I would also like to say thank you to all the people at the ORC I have worked with in the last few years. A special thank you goes to Dr. Francesca Parmigiani for all her help with the equipment in the lab and her invaluable support and advice throughout. I would also like to thank Dr. Xian Feng for fabricating the soft glass fibres I used for my experiments, Dr. Radan Slavík for his help with the phase regeneration experiment, Prof. Neil Broderick and Dr. Tim Lee for helping me with the numerical modelling, and Dr. Mohammad Belal for his help on the tellurite fibre work. I would also like to thank Dr. Adonis Bogris and Dr. Alexandros Kapsalis for their help with the CLARITY project. Our collaboration has been a very rewarding experience that I wish to be repeated again in the future. Special thanks also go to Prof. David Richardson, whose busy schedule has not prevented him from always showing interest in my work and providing insightful advice and assistance on how to progress my research.

I would also like to show my appreciation to all of my friends and colleagues who have helped make my time at the ORC enjoyable. In particular, I would like to thank Liam Jones, Victor Rancano, Xin Yang and David Wu both for their technical help and for the fun times we shared together in the lab. I would also like single out Tareg Aldeeb and Mohamed Esayah for being such good friends and for helping me through the tough times.

I feel truly indebted to my wonderful family, whom I would not have been able to complete this journey without their continuous support. I would like to dedicate this thesis to my parents, Abdulhamid and Amal, who have showed me the utmost affection and encouragement and always believed in me. I would also like to express my love and gratitude to my sisters Dunia, Ansam, Mawada and Tagrid and brother Ahmed, for always caring and feeling proud of what I do.

Nomenclature

ASE	Amplified Spontaneous Emission
BER	Bit Error Ratio
CW	Continuous-Wave
DFG	Difference Frequency Generation
DPSK	Differential Phase Shift Keying
DS	Dispersion Slope
DSF	Dispersion Shifted Fibre
EDFA	Erbium-Doped Fibre Amplifier
EOM	Electro-optic Modulator
EVM	Error Vector Magnitude
FLIM	Florescence Lifetime Imaging Microscopy
FOPA	Fibre Optic Parametric Amplifier
FWM	Four Wave Mixing
GVD	Group Velocity Parameter
HP EDFA	High Power EDFA
HNLF	Highly Nonlinear Fibre
IR	Infra-Red
MIR	Mid Infra-Red
MOF	Microstructured Optical Fibres
NA	Numerical Aperture
NIR	Near Infra-Red
NLSE	Non-Linear Schrödinger Equation
NRZ	Non Return-to-Zero
OCT	Optical Coherence Tomography
OMA	Optical Modulation Analyser
OOK	On-Off Keying
OPO	Optical Parametric Oscillator
OSA	Optical Spectrum Analyser
OSNR	Optical Signal to Noise Ratio
PC	Polarisation Controller
PF	Parametric Fluorescence
PI	Phase Insensitive

PIA	Phase Insensitive Amplifier
PI-FOPA	Phase Insensitive Fibre Optic Parametric Amplifier
PPLN	Periodically Poled Lithium Niobate
PRBS	Pseudo Random Bit Sequence
PS	Phase Sensitive
PSA	Phase Sensitive Amplification or Phase Sensitive
PSDR	Phase Sensitive Dynamic Range
PS-FOPA	Phase Sensitive Fibre Optic Parametric Amplifier
PSK	Phase Shift Keying
QPSK	Quaternary Phase Shift Keying
SBS	Stimulated Brillouin Scattering
SHG	Second Harmonic Generation
SFG	Sum Frequency Generation
SMF	Single Mode Fibre
SPM	Self Phase Modulation
SRS	Stimulated Raman Scattering
SSFM	Split Step Fourier Method
TDFA	Thulium-Doped Fibre Amplifier
TPA	Two Photon Absorption
WDM	Wavelength Division Multiplexing
XPM	Cross Phase Modulation
ZDW	Zero Dispersion Wavelength

Chapter 1

Introduction

1.1 Research Area and Motivation

The field of nonlinear optics has seen a tremendous growth since the first observation of a nonlinear optical phenomenon in 1961, when a crystalline quartz was used to generate the second harmonic of a ruby laser [1]. Nonlinear optics concerns the intensity-dependent interaction of light with matter occurring inside a dielectric medium. All dielectric media exhibit a nonlinear response when subject to an intense electromagnetic field. The interaction between electromagnetic waves in this instance results in exchanging energy and momentum, and the superposition principle no longer holds [2]. This interaction, depending on the type of the dielectric medium, can result in a range of interesting optical phenomena. For instance, non-centrosymmetric inorganic crystals such as potassium dihydrogen phosphate (KDP) and lithium niobate (LNB) exhibit strong second order nonlinearities. The interaction of light waves in such materials can result in the generation of optical fields at new frequencies, including sum- or difference-frequency generation or optical harmonics of the incident beam [3]. On the other hand, non-crystalline optically isotropic media such as most glasses exhibit strong third order nonlinearities. The intensity dependence of the refractive index of those materials gives rise to such effects as self-phase modulation (SPM), cross-phase modulation (XPM)) and the mixing of several waves and the generation of new frequencies through four-wave mixing (FWM) [4].

All of these second and third order nonlinear effects can be exploited to implement a range of useful all-optical processing functions such as wavelength conversion, parametric amplification, phase conjugation and nonlinear spectral broadening, with potential applications covering a vast spectral span extending from the near to mid infrared.

For instance, the presence of mature laser and amplification technology in the 1-1.5 μm wavelength region has resulted in numerous demonstrations of all-optical processing applications in this wavelength band. The development of high power ytterbium (Yb) fibre lasers operating around 1 μm, has enabled the realisation of broadband supercontinuum sources [5] suitable for a range of useful applications such as such optical coherence tomography (OCT), microsurgery, frequency metrology, and fluorescence lifetime imaging microscopy (FLIM)[6, 7, 8, 9].

Similarly, the invention of erbium doped fibre amplifiers (EDFAs) which have an amplification window that coincides with the minimum transmission loss window of silica has led to an unprecedented growth in the field of optical fibre communications. In fact, the increasing demand in traffic capacity driven by ever expanding broadband applications such as ultra-high definition television, high quality real-time video conferencing and remote diagnosis and surgery is now threatening to create what is known in the community as the capacity crunch [10]. This has sparked efforts to enhance transmission efficiency and to reduce networking operating costs. For instance, modulation formats deploying the phase of the signal have begun to replace the previous industry standard of intensity-modulated on-off keyed (OOK) signals, in order to either achieve a better receiver sensitivity as in the case of differential phase shift keying (DPSK), or increase the spectral efficiency as in the case of quaternary-phase shift keying (QPSK). This recent deployment of more complex modulation formats and higher transmission data rates has highlighted the need for alternative data handling technologies to electronic processing systems where even specialist electronic components and radio frequency techniques are becoming either impractically sophisticated or prohibitively expensive [11]. All-optical processing devices and systems have thus been proposed as alternatives due to the advantages of the optical approaches in terms of speed, power and cost over their electronic counterparts. For instance, FWM-based wavelength conversion is becoming increasingly attractive for applications in dense high speed wavelength division multiplexed (WDM) networks, where transparency to the bit rate and the modulation format are critical requirements [12]. Furthermore, the removal of the overhead incurred from optical to electronic to optical conversions promises to cut network costs and reduce its complexity.

A recent alternative research line has emerged investigating the extension of the usable fibre bandwidth by implementing communication systems at wavelengths which have not been previously considered. In this respect, the progress on the realisation of both thulium-doped fibre amplifiers (TDFA) which possess a broad gain region around 2 μm, and hollow-core photonic band-gap fibres which offer the potential for low transmission losses at the same wavelength window, are promising indications that the realisation of 2 μm fibre communication systems is viable [13]. This has thus driven research efforts towards developing materials and devices suitable for optical signal processing applications not only at the conventional telecommunication window of 1.55 μm but also the emerging transmission window of 2 μm.

Furthermore, all-optical signal processing functions have also found use in applications beyond 2 μm. The mid-IR 2-5 μm region is one of the two atmospheric transmission regions where the Earth's atmosphere is relatively transparent. Light sources operating at this wavelength region have a multitude of important security and industrial applications, such as infrared counter-measures, covert communication systems and explosives detection [14]. Extensive research has thus been ongoing to develop moderate to high brightness wide-bandwidth laser sources operating at this wavelength region. Laser sources based on nonlinear effects in fibres such as supercontinuum sources [15] and fibre optical parametric oscillators [16] have been demonstrated and proven to be a reliable and economical way to achieve light emission in the mid-IR. The mid-IR spectral region is also important because the molecular fingerprints of most organic and inorganic compounds occupy this band. This opens the prospect of several important applications in spectroscopy or in chemical and biomolecular sensing. However, mid-IR photo-detection technology is the least developed area in Mid-IR photonics, as photo-detectors at these wavelengths suffer from a slow response and poor sensitivity. To overcome this problem, all-optical wavelength conversion into near-infrared (NIR) through either sum frequency generation (SFG) [17] or FWM [18] has been suggested as a promising alternative.

This vast array of all-optical signal processing applications has driven the research community to design and develop the necessary nonlinear devices capable of realising efficient nonlinear effects over a broad operating range. The bulk of this research effort has been dedicated towards the development of state-of-the-art highly nonlinear fibres as well as nonlinear photonic waveguides.

In general, highly nonlinear optical fibres represent an attractive platform for realising efficient all-optical signal processing functions. Their long interaction lengths and high power handling capability enable high effective nonlinearities and facilitate the realisation of a wide range of all-optical processing devices. Of the various fibre technologies currently available, silica-based fibres represent the most mature and well-developed technology. They offer very low losses at the near-IR window and can be engineered routinely to exhibit near-zero dispersion at telecoms wavelengths. However, silica is not a particularly strong nonlinear medium, since it possesses a relatively low nonlinear refractive index n_2 ($\sim$2.6x10^{-20} m^2/W) [19]. Consequently, high launch pump powers and/or long fibre lengths of a few hundred metres are often required to achieve sufficiently high effective nonlinearity for efficient nonlinear effects. These requirements often impose performance limitations in terms of the parametric gain bandwidth, device latency and stability. Moreover, silica shows poor transparency beyond 2 μm wavelengths, due to the strong vibrational absorption of the OH molecule at 2.7 μm and the presence of multi-phonon absorption of Si-O network beyond 3 μm [20].

Recently, soft glass fibres have emerged as an alternative technological competitor to silica-based fibres. Most soft glasses possess superior nonlinear characteristics compared to silica glasses. For instance, the increase by in excess of twentyfold in nonlinear index in the case of a soft glass such as lead silicate in comparison to silica, leads to realising the same effective nonlinearity in a much shorter length of the soft glass fibre and/or with less required pump power [21, 22]. Furthermore, the use of microstructured optical fibre (MOF) technology provides a further enhancement to the nonlinearity and allows control over the dispersion profile [23]. This leads to the realisation of highly-nonlinear low-latency dispersion-engineered optical devices. Furthermore, soft glasses such as tellurite, fluoride and chalcogenide, possess good optical transparency in the wavelength range of 0.5-5 μm, 0.4-6 μm and 1-16 μm respectively and thus represent an attractive fibre platform for both near and mid-IR signal processing applications [20, 24].

These advantages of novel highly nonlinear soft glass fibres are considered of great potential in realising efficient nonlinear applications, and thus significant research efforts are being devoted to further improve the fabrication techniques, enhance some parameters such as fibre losses and overcome current technological challenges such as those associated with fibre splicing.

Meanwhile, the attraction of realising ultra-fast low power highly nonlinear integrated devices has recently made highly nonlinear photonic chips a hot research topic and an alternative technological competitor to highly nonlinear fibres [25, 26]. For instance, chalcogenide glass photonic chips made from heavy elements such as sulfur (S), selenium (Se) and tellurium (Te) possess a large third order nonlinearity of over two orders of magnitude greater than silica [27]. Furthermore, chalcogenide's relatively low nonlinear losses and weak free carrier effects which can inhibit the speed of the nonlinear response, makes it an excellent platform for ultra-fast all-optical signal processing [28, 29].

Silicon (Si) photonics has also been a hot research topic in recent years. The high index of silicon can be exploited through silicon-on-insulator (SOI) technology to realise devices that benefit both from the high nonlinear refractive index of the material ($n_2 = 4.5\text{x}10^{-18}\ m^2/W$) and the tight confinement of optical beams in the small-dimension, high-refractive-index-contrast waveguides. Silicon is also an excellent candidate for mid-IR applications thanks to its transparency up to 8 μm and to the reduced two photon and free-carrier absorptions beyond 2 μm. Although such promising attributes are possible thanks to the good optical properties of silicon waveguides, a mix of silicon with other elements, and in particular germanium (Ge), can strongly enhance the nonlinear response. Silicon germanium (SiGe) alloys have thus been identified as promising candidates for all-optical processing applications in the nearwave and midwave infrared [30].

1.2 Main Objectives and Results

The aim of this project has been to investigate the features and feasibility of two all-optical signal processing technologies: highly nonlinear soft glass fibres and silicon-based waveguides.

The study into soft glass fibres has focused on two soft glass families: lead-silicate and tellurite. The study on lead-silicate fibres was a continuation from previous work conducted within the Optical Communications group of the Optoelectronics Research Centre (ORC) and was part of the last stage of a European project entitled "PHase sensitive Amplifier Systems and Optical Regenerator and their applicationS" (PHASORS). This work resulted in the design and fabrication of the fibres and the characterisation of some of their properties at 1.55 μm as well as demonstrations of some nonlinear effects reported by A. Camerlingo in [22, 31, 32]. The work reported in this thesis follows on by continuing the characterisation work of optical properties of lead-silicate fibres at 1.55 μm and demonstrating a number of novel all-optical signal processing applications in the fibre, such as phase sensitive amplification and phase regeneration.

The rest of work reported in this thesis closely follows the objectives of a European project entitled "Compact uLtrAefficient midinfRared photonIc sysTems based on low noise quantum cascade laser sources, wide band frequencY converters and nearinfrared photodetectors" (CLARITY). Among the aims of the project (with relevance to this thesis) is to design and implement wide band, highly efficient mid-infrared to near-infrared converters relying on third order nonlinear effects in waveguides based on group IV materials and soft glass fibres (Figure 1.1). SiGe Waveguides and tellurite glass fibres have been identified as suitable candidates to fulfill this aim. Therefore, this thesis reports the characterisation work conducted in these technologies along with demonstrations of some nonlinear effects and all-optical signal processing applications.

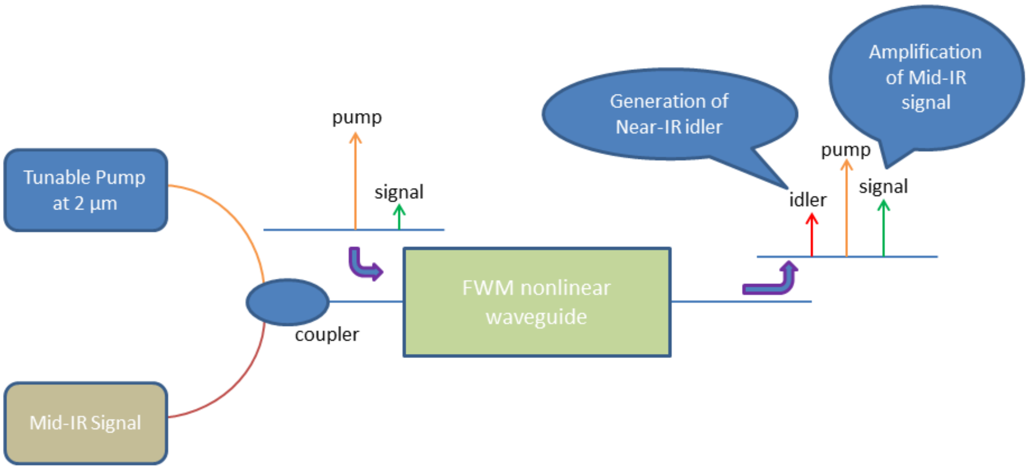

Figure 1.1: Conceptual scheme of a FWM-based wideband converter on which the CLARITY project is based. Using a tunable pump around 2.2 μm, the entire 3-5 μm Mid-IR band can be translated to 1.4-1.7 μm (courtesy of Dr. Adonis Bogris).

The optical characteristics of highly nonlinear tellurite fibres are studied at both 1.55 and 2 μm along with wavelength conversion demonstrations at both of these wavelengths. The potential of using tellurite-based fibre technology in Mid- to Near-IR conversion is also highlighted.

The study into SiGe waveguides highlights the novelty of this material as a nonlinear platform and the potential for its use in a wide range of nonlinear applications. The optical characteristics of the waveguides at telecoms wavelength are discussed in detail. Furthermore, wavelength conversion experiments of telecoms signals in SiGe waveguides are demonstrated. Finally, a comprehensive numerical and experimental study into broadband FWM-based wavelength conversion at 2 μm is conducted.

The main results achieved by the end of those studies are outlined below:

- A demonstration of phase-sensitive amplification in a highly nonlinear and low-dispersion lead-silicate W-type fibre. A phase-sensitive gain variation of 6 dB was observed in a 1.56-m sample of the fibre for a total input pump power of 27.7 dBm. Those results were orally presented in ECOC 2011 [33] and published in Optics Express [34].
- A demonstration of phase regeneration of a 40-Gb/s DPSK signal in a 1.7-m long highly nonlinear lead silicate W-type fibre using a degenerate two-pump phase-sensitive amplifier. Results showed an improvement in the error vector magnitude (EVM) and a reduction by almost a factor of 2 in the phase noise of the signal after regeneration for various noise levels at the input. This work was presented in NP 2012 [35] and published in Optics Express [36].
- A characterisation study of a highly nonlinear tellurite glass fibre at both 1.55 and 2 μm wavelengths. The loss and nonlinearity of the tellurite fibre at 1.55 and 2 μm wavelength regions were measured and found to be 0.58 dB/m and 75 /W/km at 1.55 μm and 2.8 dB/m and 45 /W/km at 2 μm respectively. Wavelength conversion is also demonstrated at both wavelength regions. Those results were orally presented in OFC 2014 [37].
- A systematic experimental study of the linear and nonlinear optical properties of SiGe waveguides, conducted on samples of varying cross-sectional dimensions and Ge concentrations. The evolution of the various optical properties for waveguide widths in the range 0.3 to 2 μm and Ge concentrations varying between 10 and 30 % is considered. The comparative performance of the waveguides, when they are considered for nonlinear applications at telecommunications wavelengths is also discussed. The results of this study were presented in OFC 2013 [38] and published in Optics Express [39].
- A demonstration of four wave mixing (FWM) based wavelength conversion of 40 Gbaud DPSK and QPSK signals in a 2.5 cm long silicon germanium waveguide. For a 290 mW pump power, bit error ratio (BER) measurements showed approximately a 2-dB power penalty in both cases of DPSK (measured at a BER of 10^{-9}) and QPSK (at a BER of 10^{-3}) signals that were examined. This work was presented in OFC 2013 [40] and published in Optics Express [41].

- A demonstration of broadband FWM-based wavelength conversion in a SiGe waveguide. A Mid-IR signal at 2.65 μm was converted to 1.77 μm using a 2.12 μm pump. This work is currently being prepared for submission to Optics Express.

1.3 Contribution to Research

The work carried out during this PhD project has had a number of contributions to the field of nonlinear optics research. Below is a brief account of the novelty of this work and its significance to science.

- The lead silicate work represents the first demonstration of a dispersion-engineered meter-scale high SBS threshold highly nonlinear fibre to be used in a PSA configuration. It is also the first record of using such a fibre in a PSA-based phase regenerator. The work highlighted the importance of the W-type design in achieving both a low and flattened dispersion profile across the C-band and a large nonlinear coefficient. It also represents the first experimental study contrasting the performance of two competing highly nonlinear soft glass fibre technologies in the context of PSAs. Furthermore, the work has also highlighted the major technical challenges associated with this fibre technology, such as fibre splicing, and suggested ways to overcome them.
- The tellurite work represents the first characterisation study of a new generation of highly nonlinear tellurite glass fibres with reduced transmission losses across the 1-5 μm wavelength region, suitable for all-optical signal processing applications at the MIR. The work also represents the first study on the prospect of using tellurite fibres in achieving broadband MIR to NIR nonlinear frequency translation.
- The work on silicon germanium waveguides represents the first detailed study of the optical characteristics of the SiGe alloy at the NIR. It is also the first demonstration of an all-optical signal processing application at those wavelengths, namely the wavelength conversion of high data rate telecoms signals. This is the first account to highlight the potential of using SiGe waveguides at such wavelengths for applications beyond detection.
- The work on SiGe waveguides also represents the first demonstration of broadband FWM-based MIR to NIR wavelength conversion with record bandwidths. Furthermore, the experiments conducted at the MIR have also highlighted the importance of the precise definition of the geometry and refractive index profile of SiGe waveguides during the design phase in order to accurately predict and model the dispersive properties of such waveguides. Overall, this work has highlighted the potential of SiGe waveguide as a competing all-optical signal processing platform suitable for applications both at the NIR and MIR.

1.4 Thesis Outline

The thesis is organised as follows.

Chapter 2 provides the theoretical background of the work presented in later chapters. Key effects affecting the optical field propagating inside a third order nonlinear medium are explained. Those include both linear effects such as linear losses and group velocity dispersion (GVD) and nonlinear effects such as nonlinear losses, SPM, XPM, FWM and stimulated light scattering. Furthermore, the Nonlinear Schrödinger Equation (NLSE), which governs pulse propagation inside an optical fibre is derived and the split-step Fourier method (SSFM) is described as a numerical tool to solve the NLSE. Finally, the chapter closes by giving an overview of the state-of-art optical fibres and waveguides technologies and comparing their attributes.

Chapter 3 introduces the work carried out in highly nonlinear lead-silicate fibres. It starts with a discussion of the key properties of lead silicate as a fibre material and then describes the W-type fibre design. An algorithm describing the process of choosing the core size and core-cladding index difference to tailor the dispersive properties of a fibre to suit a particular application is discussed in detail. The characterisation of some of the fibre's optical properties is then presented. Finally the chapter concludes with a demonstration of FWM-based wavelength conversion in the fibre and gives an accompanying numerical analysis highlighting the importance of the fibre's novel dispersion proprieties in achieving a broadband operation.

Chapter 4 discusses the demonstration of phase sensitive amplification (PSA) in the lead silicate fibre. It begins by introducing the principles of PSA and then proceeds to explain the two PSA experiments conducted in the fibre: the parametric fluorescence (PF) experiment and phase sensitive dynamic range (PSDR) measurement. Important conclusions are drawn about the fibre merits and limitations which lay the foundation of subsequent work: phase regeneration of DPSK signals in the lead-silicate fibre. The regeneration experiment is explained in detail and performance of the fibre as a phase squeezing device is discussed by presenting constellation diagrams and EVM and phase error figures of the data signal before and after regeneration.

Chapter 5 discusses the work done on highly nonlinear tellurite fibres. It starts with highlighting the attributes of tellurite glass as a fibre material and then gives an account of the fibre design and fabrication process. This is followed by a characterisation study of the fibre's loss and nonlinearity at 1.55 and 2 μm. Wavelength conversion experiments are demonstrated at both of these wavelength regions and a numerical study is presented to highlight the potential of the fibre in Mid-IR applications.

Chapter 6 gives a detailed account of the study conducted to characterise the linear and nonlinear properties of SiGe waveguides at telecommunication wavelengths. It starts with a discussion of the waveguide design and the fabrication process and then proceeds with presenting the results of the characterisation work. The waveguides' loss, nonlinearity and two-photon absorption (TPA) are characterised for different waveguide sizes and varying germanium concentration and the data is supported by numerical simulations. A figure of merit (FOM) is used to choose the best waveguide size and Ge concentration combination for optimum nonlinear performance.

Chapter 7 describes the all-optical signal processing applications conducted in SiGe waveguides at 1.55 and 2 μm. FWM-based wavelength conversion of 40 Gbaud phase-shift keyed (PSK) signals at 1.55 μm is demonstrated and BER results are presented. Broadband wavelength conversion experiments of 2 μm signals are then discussed in detail. The experimental data collected is then analysed with aid of numerical simulations to help estimate the position of the zero dispersion wavelength (ZDW) of the waveguide.

Chapter 8 presents a summary of the results and addresses the conclusions from all this work. Finally, the thesis closes with Chapter 9 where directions for future work are discussed.

Chapter 2

Background

2.1 Introduction

This chapter discusses the main linear and nonlinear wave propagation effects in optical fibres and waveguides. The chapter starts by explaining the origin of linear effects such as loss and dispersion, and nonlinear phenomena, such as nonlinear refraction and stimulated light scattering. The impact of each phenomenon on pulse propagation is described and close attention is paid to effects of importance to this thesis such as chromatic dispersion, four wave mixing (FWM) and stimulated Brillouin scattering (SBS). Furthermore, the Nonlinear Schrödinger Equation (NLSE) is introduced and its importance in describing the nonlinear and dispersive effects occurring during pulse propagation is highlighted. The chapter also presents a description of a numerical method, based on the split step fourier transform (SSFT), that is used to solve the NLSE. Finally, the chapter concludes by presenting an overview of the various optical fibre and waveguide technologies and contrasting their attributes.

2.2 Wave Propagation Effects in Optical Fibres and Waveguides

All dielectric media exhibit a nonlinear response when subject to an intense electromagnetic field. Physically, this stems from the anharmonic oscillatory motion that the bound electrons of the medium show in response to the radiating electromagnetic field $\vec{E}$. As a result, the induced polarisation $\vec{P}$ of the dielectric dipoles is a nonlinear function of the electric filed [2, 42]:

$$\vec{P} = \epsilon_0(\chi^{(1)}.\vec{E} + \chi^{(2)} : \vec{E}\vec{E} + \chi^{(3)} \vdots \vec{E}\vec{E}\vec{E} + \dots) \tag{2.1}$$

Where, ϵ_0 is the vacuum permittivity and $\chi^{(n)}$ is a tensor of rank n+1 that describes the n-th order dielectric susceptibility. The first order linear susceptibility $\chi^{(1)}$ relates to the attenuation coefficient of the dielectric medium and also describes the wavelength dependence of the refractive index, while the second order susceptibility $\chi^{(2)}$ represents the origin of such nonlinear phenomena as second harmonic generation (SHG), sum frequency generation (SFG) and difference frequency generation (DFG). In glasses such as silica, however, because of the symmetric nature of the silica molecule, the second-order susceptibility is zero, unless it is induced by poling [2]. Therefore, for non-crystalline optically isotropic media such as optical fibres, the second order nonlinear effects are negligible. The third order susceptibility $\chi^{(3)}$, responsible for nonlinear effects such as third harmonic generation (THG), nonlinear refraction and four wave mixing, thus represents the lowest order nonlinearity in optical fibres. Inelastic scattering effects such as stimulated Raman scattering (SRS) and stimulated Brillouin scattering (SBS), also stemming from third order nonlinear effects, can also be prominent in optical fibres.

The third-order nonlinear susceptibility is characterised by an ultra-fast response time. This stems from the fact that when a material is subject to a strong electric field radiation, the carriers are promoted to higher energy states between the valance and the conduction bands, often referred to as "virtual states". The transition times of these excited carriers from the virtual states back to the valance band is an extremely fast process, often measured in the order of femtosecond. This is an important attribute that makes $\chi^{(3)}$-based nonlinear effects suitable for high speed signal processing applications. A brief description of some of the linear and the $\chi^{(3)}$-originated nonlinear effects mentioned here is given below.

2.2.1 Linear Effects

2.2.1.1 Linear Loss

An optical field with an initial power P_0, propagating through an optical fibre of length L, would have a transmitted power P_T given by:

$$P_T = P_0 \exp\left(-\alpha L\right) \tag{2.2}$$

Where α is called the attenuation parameter and is measured in m^{-1}. The loss of optical fibres is usually expressed in decibels per metre (dB/m) or decibels per kilometre (dB/km). This decibel-based coefficient can be linked to its linear counterpart through the following relation:

$$\alpha_{dB} = -\frac{10}{L}\log\frac{P_T}{P_0} = 4.343\alpha_{Lin} \tag{2.3}$$

The main mechanisms causing linear loss vary among different optical media. For silica, for instance, the intrinsic material absorption and the Rayleigh scattering are the main contributing factors to loss. Rayleigh scattering is a fundamental loss mechanism and is caused by small scale density fluctuations frozen into the fused material during manufacture causing the travelling light through the medium to scatter through all directions. The Rayleigh scattering loss is more significant at shorter wavelengths as it varies as λ^4 according to the relation:

$$\alpha_R = C_R/\lambda^4 \tag{2.4}$$

where α_R is the Rayleigh scattering loss coefficient, C_R (dB/(km-μm^4)) is a material dependent constant and λ is the wavelength of light [2].

2.2.1.2 Chromatic Dispersion

Chromatic dispersion is an effect that originates from the dependence of the refractive index of a dielectric medium on the frequency of light. A time varying electromagnetic field propagating in the z direction can be mathematically expressed as:

$$\vec{E}\left(z,t\right) = \frac{1}{2}[E\left(z,t\right) exp[-i\left(\beta z - \omega t\right)] + c.c], \tag{2.5}$$

Where $\vec{E}\left(z,t\right)$ represents the envelope of the waveform, β the propagation constant, ω the carrier angular frequency and $c.c$ is the complex conjugate. Equation 2.5 follows what is referred to as the slowly varying envelope approximation (SVEA). This approximation assumes that the forward-travelling envelope of the wave changes much slower than the period or the wavelength of the wave [2].

For spectrally broad signals, the frequency dependence of the propagation constant β can be mathematically described as a Taylor series expansion about a reference angular frequency ω_0 [2]:

$$\beta\left(\omega\right) = \beta_0 + \left(\omega - \omega_0\right)\beta_1 + \frac{1}{2}\left(\omega - \omega_0\right)^2\beta_2 + \frac{1}{6}\left(\omega - \omega_0\right)^3\beta_3 + \frac{1}{24}\left(\omega - \omega_0\right)^4\beta_4 + \cdots \tag{2.6}$$

β_i is the i-th order derivative of the propagation constant β with respect to the angular frequency ω, i.e.

$$\beta_i = \left(\frac{d^i\beta}{d\omega^i}\right)_{\omega=\omega_0} \qquad (i = 1, 2, \ldots) \tag{2.7}$$

The lowest order term β_0, represents a common phase shift. The first order term, β_1, is inversely proportional to the group velocity v_g, which is the speed at which the envelope of the waveform travels along the fibre:

$$v_g = \frac{d\omega}{d\beta} = \frac{1}{\beta_1} \tag{2.8}$$

The second order term β_2 is often referred to as the group velocity dispersion (GVD) coefficient. It describes the dependence of the group velocity of light on the frequency. For optical fibres and waveguides, a more common parameter, often referred to as the dispersion parameter D, is used, and it relates to β_2 via:

$$D = -\frac{2\pi c}{\lambda^2}\beta_2 \tag{2.9}$$

Another fibre parameter of significance is the zero dispersion wavelength (ZDW). The ZDW refers to the wavelength at which the GVD coefficient β_2 vanishes. The position of the ZDW varies from one glass material to another. For instance, the ZDW for silica occurs at 1.27 μm, while glasses with higher refractive indices such as tellurite and chalcogenide have their material ZDW at longer wavelengths.

Fibre dispersion is an important parameter for nonlinear interactions since it impacts the phase matching between the propagating signals and thus the efficiency of the nonlinear process (refer to Section 2.2.2.2 for further details). During the design stage of optical fibres and waveguides it is thus important to tailor the GVD parameter at the wavelength of interest. Depending on the application, this could involve shifting the position of the ZDW to the targeted wavelength of operation. For instance, for telecoms applications, the ZDW is usually shifted to 1550 nm. This is often realised through changing the core material properties by introducing dopants and/or by engineering the fibre to have the correct amount of waveguide dispersion such that the ZDW is shifted to the desired wavelength (the detailed process of engineering a fibre/waveguide dispersion is presented in Chapter 3 Section 3.2). Conventionally, a fibre or a waveguide is said to exhibit normal dispersion when $\beta_2 > 0$ ($D < 0$) and anomalous dispersion when $\beta_2 < 0$ ($D > 0$).

The third order dispersion term (β_3) describes the rate of change of β_2 with respect to wavelength. By taking the derivative of Equation 2.9, describing the dispersion, with respect to λ, it is possible to create a term called the dispersion slope (DS) that explains how the dispersion changes with wavelength. Equation 2.10 below shows the simplified derivative used as a definition for the dispersion slope:

$$DS = \frac{2\pi c}{\lambda^3}[\frac{2\pi c\beta_3}{\lambda} + 2\beta_2] \tag{2.10}$$

Higher order dispersion terms are usually neglected due to their insignificant magnitude in relation to lower order dispersion terms. However, in cases where a fibre or a waveguide exhibits low values of β_2 and β_3, considering higher order dispersion terms becomes crucial.

2.2.2 Nonlinear Effects

Some of the nonlinear effects with relevance to the work described in this thesis are explained below. These effects are spilt into three parts according to the mechanism by which they occur: nonlinear losses, nonlinear refraction and stimulated light scattering.

2.2.2.1 Nonlinear Losses

Two-Photon Absorption

Two-Photon Absorption (TPA) is a process whereby two photons are absorbed by an electron in the valance band, promoting it to the lowest conduction band, as Figure 2.1 illustrates. TPA is a nonlinear process that is proportional to the square of the light intensity I, and thus can only occur at significant rates at high optical intensities [43]:

$$\frac{dI}{dz} = -\alpha I - \beta_{TPA} I^2 \tag{2.11}$$

Where z is the distance from the input, α is the linear loss coefficient and β_{TPA} is the TPA coefficient.

In order for an electron to be excited to a higher energy state, the combined energy of the two incident photons must at least be equal to the bandgab energy E_g [44]:

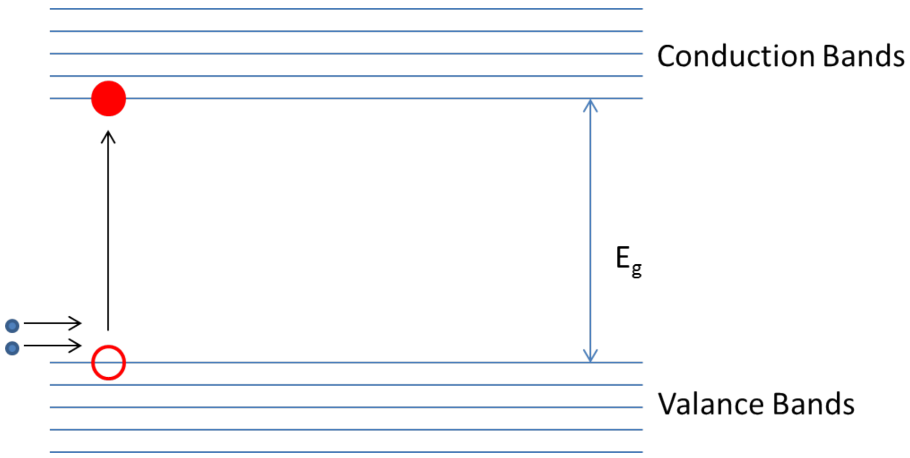

Figure 2.1: Excitation of an electron from the valance band to the conduction band through the absorption of two photons.

$$\frac{2hc}{\lambda} \geq E_g \tag{2.12}$$

Where h is Planck's constant and λ is the wavelength of the incident photons. The condition in Equation 2.12 makes two-photon absorption a material dependent process. For instance, no losses due to TPA take place in silica fibres at 1550 nm, whereas, at the same wavelength, semiconductor materials such as silicon can incur TPA losses due to their lower bandgab energy.

Free Carrier Absorption

As explained above, when two photons are absorbed, an electron is excited to the conduction band and a hole is created in the valance band. These photo-excited carriers are free to move within a band and can absorb a single photon in order to get promoted to a higher energy level within the same band. This process is called Free Carrier Absorption (FCA) [45, 46]. Free carriers not only absorb light but also modify the material refractive index creating what is known as free-carrier dispersion (FCD).

2.2.2.2 Nonlinear Refraction

Nonlinear refraction describes the dependence of the refractive index n of the fibre core, on the intensity of the propagating light beam I [47]:

$$n(\omega, I) = n_0(\omega) + n_2 I \tag{2.13}$$

Where n_0 and n_2 are the linear and nonlinear refractive indices respectively. The nonlinear refractive index n_2 is a material property and is linked to the effective nonlinear coefficient γ via:

$$\gamma = (2\pi n_2)/(\lambda A_{eff}) \tag{2.14}$$

Where λ is the wavelength of operation and A_{eff} is the effective mode area. The effective nonlinear coefficient γ combines the material and waveguide properties and is often used as a measure of the magnitude of nonlinearity in optical fibres. It is interesting to note that for fibre with subwavelenth dimensions, such as nanowires, Equation 2.14 needs to be modified to include the large longitudinal component of the propagating modes present in this case. A$_{eff}$ is replaced in this case by its vectorial equivalent A$^{V}_{eff}$ [48]. In such fibres, the newly calculated γ^V can be 1.3-2 times larger than the γ calculated from Equation 2.14. However, since no fibres studied in this work exhibit wavelength-scale dimensions, Equation 2.14 represents an accurate approximation of the nonlinearity of the reported fibres and is used throughout this thesis.

The frequency dependence of the refractive index in Equation 2.13 is the origin of material dispersion. Conversely, the intensity dependence of n, often termed the Kerr effect, is responsible for such nonlinear effects as self phase modulation (SPM), cross phase modulation (XPM) and four-wave mixing (FWM).

Self-Phase Modulation

Self-phase modulation (SPM) describes the intensity dependent self-induced phase shift that the travelling electromagnetic wave endures as it propagates through the nonlinear medium. SPM leads to pulse spectral broadening, an effect that can be detrimental to the performance of optical systems [4].

The nonlinear phase shift induced by SPM can be expressed as:

$$\phi_{SPM} = \gamma P L_{eff} \tag{2.15}$$

Where P is the optical power of the propagating field, and L_{eff} is the effective fibre length and is related to the physical length L via:

$$L_{eff} = [1 - exp(-\alpha L)]/\alpha \tag{2.16}$$

The interplay of the nonlinear effect of self-phase modulation and the group velocity dispersion can result in the formation of optical solitons, a type of pulses that maintain their temporal and spectral shape during propagation. This often occurs during propagation in the anomalous-dispersion regime of an optical fibre, where dispersive and nonlinear effects can exactly balance out.

Cross Phase Modulation

Cross phase modulation (XPM) takes place when two electromagnetic waves of different frequency or state of polarisation co-propagate inside an optical fibre. Besides the self-induced phase shift that each wave incurs due to SPM, each wave imposes an additional nonlinear phase shift on the other. The corresponding nonlinear XPM-induced phase shift can be expressed as [2]:

$$\phi_{XPM} = r\gamma P L_{eff} \tag{2.17}$$

Where r is the polarisation dependant coefficient which is 2 for linearly co-polarised optical fields and 2/3 for orthogonally polarised optical fields. XPM has been exploited in many different applications such as all-optical switching [49] and re-timing applications [50].

Four-Wave Mixing

Four wave mixing (FWM) occurs when light of two or more different frequencies are launched into an optical fibre. It describes the phenomenon in which two photons belonging to the same (degenerate-FWM - Figure 2.2b) or different (non-degenerate FWM - Figure 2.2a) waves (ω_1 and ω_2) are annihilated and two photons at different frequencies (ω_3 and ω_4) are generated, such that the net energy and momentum is conserved [2]:

$$\omega_3 + \omega_4 = \omega_1 + \omega_2 \tag{2.18}$$

$$\phi_3 + \phi_4 = \phi_1 + \phi_2 \tag{2.19}$$

Where ω_n and ϕ_n are the angular frequency and phase of the n-th optical wave respectively. Furthermore, FWM can also take place when a single pump field is launched into an optical fibre creating two new light beams upshifted and downshifted in frequency from the pump. In this case the new frequencies are generated from noise, and Equation 2.18 also holds with $\omega_1 = \omega_2$.

Simultaneous parametric amplification and frequency conversion can be achieved through FWM in an optical fibre by launching a strong pump together with a weak signal (probe)(Figure 2.3). This results in the amplification of the weak signal and the creation of a wave at a new frequency often termed the idler. This configuration is the most commonly used setup in FWM-based applications to realise such devices as fibre optic parametric amplifiers (FOPA) and wavelength converters.

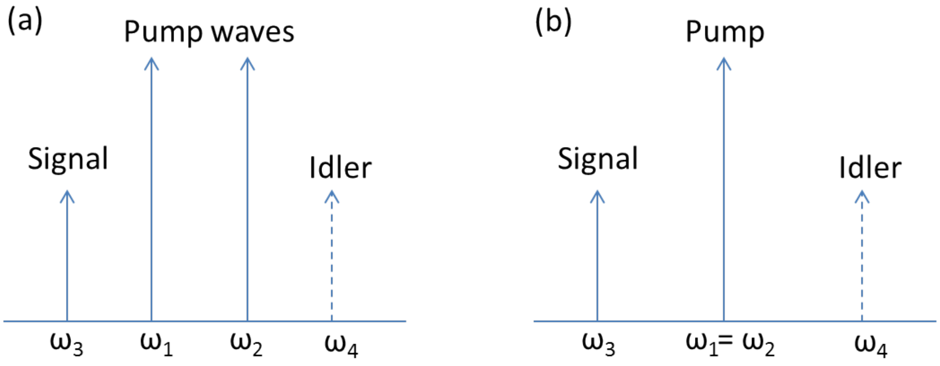

Figure 2.2: A FWM process where (a) two waves are used as pumps (non-degenerate FWM) (b) a single wave is used as pump (degenerate FWM).

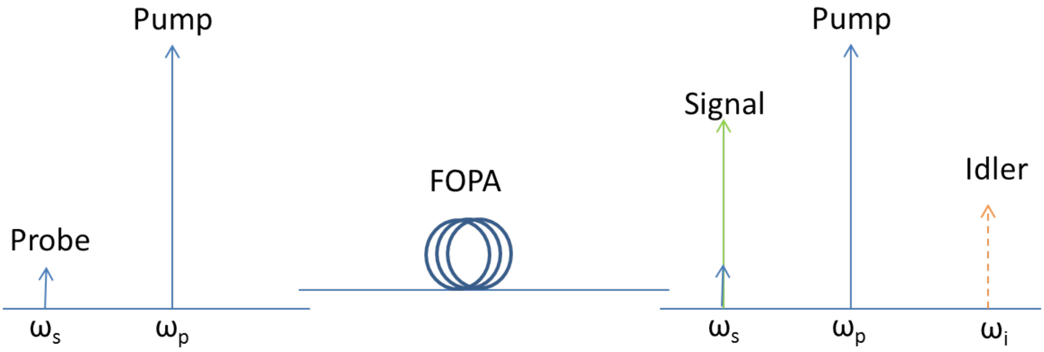

Figure 2.3: The input and output of a degenerate FWM-based fibre optic parametric amplifier (FOPA). The input probe is parametrically amplified by the strong pump and a new idler field is created.

The power flow of the pump, signal and idler within a generic single pump degenerate FWM scheme can be described by the following four coupled differential equations [51, 52]:

$$\frac{dP_p}{dz} = -\alpha P_p - 4\gamma\sqrt{(P_p^2 PsPi)}\sin\theta \tag{2.20}$$

$$\frac{dP_s}{dz} = -\alpha P_s + 2\gamma\sqrt{(P_p^2 PsPi)}\sin\theta \tag{2.21}$$

$$\frac{dP_i}{dz} = -\alpha P_i + 2\gamma\sqrt{(P_p^2 PsPi)}\sin\theta \tag{2.22}$$

$$\frac{d\theta}{dz} = [\Delta\beta]_L + \gamma(2P_p - P_s - P_i + \left[\sqrt{\frac{P_p^2 P_s}{P_i}} + \sqrt{\frac{P_p^2 P_i}{P_s}} - 4\sqrt{P_s P_i}\right]\cos\theta) \tag{2.23}$$

Where P_p, P_s and P_i are the optical powers of the pump, signal and idler respectively and $[\Delta\beta]_L$ is the linear phase mismatch.

Efficient FWM requires that the phase mismatch between the participating fields is minimised. The total phase mismatch κ is approximately equal to the sum of linear- and the nonlinear-phase mismatch:

$$\kappa \simeq \Delta\beta = [\Delta\beta]_L + [\Delta\beta]_{NL} \tag{2.24}$$

Where the linear phase mismatch $[\Delta\beta]_L$ is equal to:

$$[\Delta\beta]_L = \beta_3 + \beta_4 - \beta_1 + \beta_2 \tag{2.25}$$

where β_n is the propagation constant of the n-th optical wave. The second term in Equation 2.24, $[\Delta\beta]_{NL}$, is the nonlinear phase mismatch that takes place during propagation due to the nonlinear phase modulation effects such as self-phase modulation (SPM) and cross phase modulation (XPM) [4].

The nonlinear phase mismatch $[\Delta\beta]_{NL}$, is given by:

$$[\Delta\beta]_{NL} = 2\gamma P \tag{2.26}$$

where γ is the nonlinear coefficient of the fibre and P is the total pump power. Significant FWM process can only take place if the phase mismatch κ is minimised.

The overall relative phase θ in Equations 2.20-2.23 can be described as:

$$\theta(z) = \phi_s(z) + \phi_i(z) - 2\phi_p(z) \tag{2.27}$$

Where $\phi_s(z)$, $\phi_i(z)$ and $\phi_p(z)$ are the phase contributions of the signal, idler and pump after propagating a distance z along the fibre.

The overall relative phase described in Equation 2.27 can also be expressed in terms of the initial phase of the launched optical fields and the phase mismatch term:

$$\theta(z) = \Delta\beta z + \phi_s(0) + \phi_i(0) - 2\phi_p(0) \tag{2.28}$$

$$\theta(z) = \left([\Delta\beta]_L + [\Delta\beta]_{NL}\right) z + \phi_s(0) + \phi_i(0) - 2\phi_p(0) \tag{2.29}$$

Equations 2.20-2.23 also show that in order for FWM to be a phase sensitive process, an idler field must be present together with the pump and the signal at the input of the FOPA. This type of FOPA is called a phase sensitive amplifier (PSA) and the direction of power flow between the participating fields in this case is dependent on the relative phase between them. Further details on the operation of PSAs are given in Chapter 4.

Generally, FWM can be a very efficient process in optical fibres. Indeed, FWM with record parametric gain and bandwidth has been achieved in silica highly nonlinear fibres [53], achieving a FWM bandwidth of 100 nm with a gain of 11.5 ± 2 dB. Furthermore, a host of other ultra-efficient nonlinear processes can also be achieved through FWM. For instance, dispersion compensation in WDM systems can be achieved through FWM

[54]. This application exploits the phase conjugation operation that takes place during the FWM process: the idler generated through FWM possesses a phase that relates the conjugate of the signal. By placing a FWM-based phase conjugator mid-way through an optical link, the conjugated signal (idler) experiences dispersion of an opposite sign during the second half of propagation to that accumulated during the first, and the total dispersion of the link is thus compensated [55]. Other useful nonlinear functions, such as optical multicasting [56] and time division de-multiplexing of high data rate signals [57, 58] have all been demonstrated. Furthermore, parametric amplifiers based on FWM offer an unparalleled flexibility in centering their gain profile about any arbitrary wavelength limited only by the zero dispersion wavelength (ZDW) of the fibre in use.

2.2.2.3 Stimulated Light scattering

Stimulated Brillouin Scattering

In Stimulated Brillouin scattering (SBS), the propagating light beam interacts with the acoustic phonons of the nonlinear medium, setting up an acoustic wave through the process of electrostriction. This results in the creation of an effective Bragg grating due to the modulation of the material's linear refractive index by the generated acoustic wave. The grating thus scatters the incident light wave, creating a new Stokes wave that is only slightly downshifted in frequency, typically by a few GHz. The amount of backscattered light at the Stokes frequency increases rapidly when the Brillouin threshold is reached, resulting in an eventual saturation of the power of the transmitted light beam [59]. SBS is usually considered detrimental in the context of nonlinear optical effects, since it limits the amount of useful pump power that can be launched into the fibre. The critical pump power at which the Brillouin threshold is reached is given by [2]:

$$P_{th} \simeq (21A_{eff})/(g_B L_{eff}) \tag{2.30}$$

Where g_B is the Brillouin gain coefficient.

Fused silica has a Brillouin gain coefficient of 2.5x10^{-11} m/W, while some other non-silica glasses, such as tellurite and chalcogenide, possess a g_B value that is orders of magnitude larger than that of silica [60].

SBS can be a major performance-limiting factor in applications requiring a strong continuous wave (CW) pump. Therefore, depending on application requirements, active steps to increase the SBS threshold may need to be taken. These include using phase modulation to spectrally broaden the signal to exceed the Brillouin bandwidth, applying a temperature/strain gradient during fibre fabrication to increase its SBS threshold and/or core-doping the fibre. All these techniques however, result in added system complexity and/or incur additional losses.

Stimulated Raman Scattering

Stimulated Raman scattering (SRS) is an inelastic scattering processes that differs from SBS in that the propagating light beam interacts with high frequency vibration modes (optical phonons) of the molecules of the medium rather than its acoustic phonons. The interaction results in the annihilation of a photon from the incident pump field pump and the subsequent creation of a photon at a lower frequency (Stokes wave) and an optical phonon conserving the energy and momentum [2]. The frequency downshift of the Stokes wave is very large, typically in the order of few terahertz. Raman effects will be ignored within the context of analytical work in this thesis due to their negligible contribution to the parametric gain at the bandwidths of interest.

2.3 Nonlinear Schrödinger Equation

Numerical and analytical studies are of great importance when studying nonlinear effects in optical fibres. Simulation and verification tools are commonly used before conducting experimental studies to facilitate further understanding of the effects of the various linear and nonlinear phenomena that an electromagnetic wave is subject to when propagating along an optical fibre.

The four Maxwell's equations represent the core from which the nonlinear Schrödinger equation is derived. They are used as the starting point from which a generalised theoretical tool describing electromagnetic wave propagation in optical media under the influence of dispersive and nonlinear effects can be derived:

$$\nabla \times \vec{E} = -\frac{\partial \vec{B}}{\partial t} \tag{2.31}$$

$$\nabla \times \vec{H} = \vec{J} + \frac{\partial \vec{D}}{\partial t} \tag{2.32}$$

$$\nabla . \vec{B} = 0 \tag{2.33}$$

$$\nabla . \vec{D} = \rho_f \tag{2.34}$$

Where $\vec{E}$ and $\vec{H}$ are the electric and magnetic field vectors respectively, and $\vec{D}$ and $\vec{B}$ are the electric and magnetic flux density fields. In a medium such as an optical fibre, the absence of free charges result in the current density vector $\vec{J} = 0$ and the charge density $\rho_f = 0$ [2].

The electric and magnetic flux density fields $\vec{D}$ and $\vec{B}$ can be related to the electric and magnetic field vectors $\vec{E}$ and $\vec{H}$ via:

$$\vec{D} = \epsilon_0 \vec{E} + \vec{P} \tag{2.35}$$

$$\vec{B} = \mu_0 \vec{H} + \vec{M} \tag{2.36}$$

Where ϵ_0 and μ_0 are the vacuum permittivity and the vacuum permeability respectively, and $\vec{P}$ and $\vec{M}$ are the induced electric and magnetic polarisation. For a non-magnetic medium such as an optical fibre, $\vec{M} = 0$ [2].

Maxwell's equations above can be combined to deduce a single equation describing wave propagation in an optical fibre:

$$\nabla^2 \vec{E} = \frac{1}{c^2} \frac{\partial^2 \vec{E}}{\partial t^2} + \mu_0 \frac{\partial^2 \vec{P}}{\partial t^2} \tag{2.37}$$

Where c is the speed of light in vacuum. Equation 2.37 is the so called wave equation.

The induced polarisation density $\vec{P}$, can be split into two parts to account for fibre nonlinearities:

$$\vec{P}(\vec{r}, t) = \vec{P_L}(\vec{r}, t) + \vec{P_{NL}}(\vec{r}, t) \tag{2.38}$$

Where $\vec{P_L}$ and $\vec{P_{NL}}$ represent the linear and nonlinear parts of the induced polarisation density $\vec{P}$ respectively and are defined as follows [2]

$$\vec{P_L}\left(\vec{r}, t\right) = \epsilon_0 \int_{-\infty}^{\infty} \chi^{(1)} \vec{E}\left(\vec{r}, t'\right) exp[-i\omega_0 \left(t - t'\right)] dt', \tag{2.39}$$

$$\vec{P_{NL}}\left(\vec{r}, t\right) \approx \epsilon_0 \epsilon_{NL} \vec{E}\left(\vec{r}, t\right), \tag{2.40}$$

Where $\chi^{(1)}$ is the first order susceptibility, ϵ_0 is the vacuum permittivity and ϵ_{NL} is the nonlinear contribution to the dielectric constant. In Equation 2.40, a number of assumptions to simplify to the solution are made. Among these assumptions is the treatment of the nonlinear $\vec{P_{NL}}$ as a small perturbation of $\vec{P_L}$ due to the weak nature of third order nonlinearities in optical fibres and the assumption that the nonlinear response is instantaneous.

The nonlinear contribution to the dielectric constant ϵ_{NL} is defined as:

$$\epsilon_{NL} = \frac{3}{4}\chi^{(3)}|E\left(\vec{r},t\right)|^2 \tag{2.41}$$

Where the third order susceptibility $\chi^{(3)}$ encompasses all of the nonlinear effects introduced in the previous sections. In general, $\chi^{(3)}$ is a fourth-order tensor with 81 elements. However, the isotropic and Kleinman symmetry principles dictate that only 21 components are non-zero, of which only one is independent from the rest.

In its simplest form, the sole distinct component of the $\chi^{(3)}$ tensor is related to the material nonlinear properties such as the nonlinear refractive index n_2 and the nonlinear loss (two photon absorption) α_2 via:

$$n_2 = \frac{3}{8n}Re\left(\chi^{(3)}\right) \tag{2.42}$$

$$\alpha_2 = \frac{3\omega_0}{4nc}Im\left(\chi^{(3)}\right). \tag{2.43}$$

Where Re and Im refer to the real and imaginary part of $\chi^{(3)}$ respectively, and n and c refer to the material refractive index and the speed of light in vacuum.

Equation 2.37 can be solved by applying a Fourier transform and searching for a solution using the method of separation of variables such that the electric field $E\left(\vec{r},t\right)$ is expressed as:

$$E\left(\vec{r},t\right) = F\left(x,y\right)A\left(z,t\right)exp(i\beta_0 z) \tag{2.44}$$

Where $F\left(x,y\right)$ is transverse mode distribution, $A\left(z,t\right)$ is a slowly varying function of z and β_0 is the propagation constant at the carrier frequency. A mathematical description of the modes supported by an optical fibre has been widely covered in many textbooks [61] and since they do not play a role in the discussion of nonlinear effects, they will not be covered here.

A solution for the pulse envelope $A\left(z,t\right)$ which is subject to the influence of both linear and non-linear effects, can be found by combining Equations 2.37-2.41. The slowly varying field approximation which assumes the slow variation nature of the envelope of the field in comparison with the field's period, is also applied to further simplify the solution. Incorporating all of the assumptions mentioned above, and assuming pulses of width exceeding 5 ps, where the Kerr effect dominates over the Raman effect, one finally arrives at the equation:

$$\frac{\partial A}{\partial z} + \frac{\alpha}{2}A + i\frac{\beta_2}{2}\frac{\partial^2 A}{\partial T^2} - \frac{\beta_3}{6}\frac{\partial^3 A}{\partial T^3} - i\gamma|A|^2 A = 0. \tag{2.45}$$

Where A is slowly varying envelope of the electric field, α is the loss coefficient, $\beta_m = d^m\beta/d\omega^m$ evaluated at $\omega = \omega_0$ and T represent a time frame of reference related to the physical time t through $T = t - z/v_g$, where v_g is the group velocity.

Equation 2.45 is called the Nonlinear Schrödinger Equation and describes the nonlinear and dispersive effects that an optical pulse endures during propagation through an optical fibre. The various terms in the equations account for different physical phenomena:

$\frac{\alpha}{2}A$ accounts for propagation loss

$\frac{i\beta_2}{2}\frac{\partial^2 A}{\partial T^2}$ accounts for second order dispersion

$\frac{\beta_3}{6}\frac{\partial^3 A}{\partial T^3}$ accounts for third order dispersion

$i\gamma|A|^2 A$ accounts for the Kerr effect

Furthermore, Equation 2.45 is a nonlinear partial differential equation very commonly used to study third order nonlinear and dispersive effects in optical fibres and numerous numerical methods have been offered to solve the equation. A brief description follows of one such method adopting the Split-Step Fourier Transform technique.

2.4 Solving the NSE: the Split-Step Fourier Transform Method

The starting point in solving Equation 2.45 numerically is to write it as [2]:

$$\frac{\partial A_p}{\partial z} = (\hat{D} + \hat{N})A \tag{2.46}$$

Where $\hat{D}$ and $\hat{N}$ are operators descripting the linear (attenuation and chromatic dispersion) and nonlinear (Kerr effect) effects respectively. They are defined as follows:

$$\hat{D} = -\frac{\alpha}{2} - \frac{i\beta_2}{2}\frac{\partial^2}{\partial T^2} + \frac{\beta_3}{6}\frac{\partial^3}{\partial T^3} \tag{2.47}$$

$$\hat{N} = i\gamma|A^2| \tag{2.48}$$

By writing the NLSE equation in this manner, and by assuming that the optical field propagates a small distance of h, one can write

$$A(z+h,T) = \exp(h\hat{D} + h\hat{N})A(z,T) \tag{2.49}$$

By fragmenting the propagation distance into sufficiently small sections, one can consider the dispersive and nonlinear effects independently. This commutative property can be expressed mathematically as:

$$A(z+h,T) = \exp(h\hat{D})\exp(h\hat{N})A(z,T) \tag{2.50}$$

Equation 2.50 can now be solved in an iterative manner. First the nonlinear element of the equation can be solved in the time domain by assuming that the dispersive operator $\hat{D} = 0$ and substituting in Equation 2.49:

$$B(z,T) = \exp(h\hat{N})A \tag{2.51}$$

Subsequently, the dispersive element is solved in the frequency domain after applying a Fourier transform:

$$B(z+h,\omega) = \exp(h\hat{D}(i\omega))B(z,\omega) \tag{2.52}$$

Where $\hat{D}(i\omega)$ and $B(z,\omega)$ are the Fourier transforms of their time domain counter parts. An inverse Fourier transform can then be applied to complete the process:

$$\exp(h\hat{D})B(z,T) = F_T^{-1}\exp(h\hat{D}(i\omega))F_T B(z,T) \tag{2.53}$$

This procedure is repeated iteratively in small steps of h until the total distance along which the electromagnetic field is propagating is covered.

A MATLAB model utilising the SSFT method to solve the NLSE was developed for use as a simulation/verification tool for experiments investigating nonlinear and dispersive phenomena in optical fibres in the subsequent chapters.

2.5 Review of Optical Fibre and Waveguide Technologies

There is a wide range of optical fibre technologies that can be used to realise all-optical signal processing applications. The optical properties of these fibre technologies vary in terms of the achievable nonlinearity, the suitability for dispersion engineering and the mechanical attributes. The following is a brief account describing the most common of these technologies in the context on nonlinear optical applications, namely, standard single mode fibres, dispersion shifted fibres, highly nonlinear soft glass fibres, microstructured fibres, fibre tapers and highly nonlinear photonic chips.

2.5.1 Standard Step Index Single Mode Fibres

The standard single mode fibre (SMF) follows a simple step index design. Figure 2.4 depicts the structure of the fibre where a central core of refractive index n_{co} is surrounded by a cladding layer of a slightly lower refractive index n_{cl} ($n_{co} > n_{cl}$). In this case, the guiding mechanism of light inside the fibre core depends on the well-known phenomena of total internal reflection (TIR) [62]. Single mode fibres are designed such that they support a single mode of propagation at a particular wavelength. To achieve this, a relatively small core diameter of a few microns is usually used together with a small value of refractive index difference.

The standard silica-based SMF exhibits extremely low propagation losses of approximately 0.17 dB/km at 1.55 μm. Furthermore, since silica possesses a small value of nonlinear refractive index (n_2 ~2.6x10^{-20} m^2/W), the standard SMF exhibits a weak nonlinear coefficient of the order of 1 /W/km. As a result, the standard silica SMF is often used for long distance fibre communications where low propagation losses and weak nonlinearities are essential requirements.

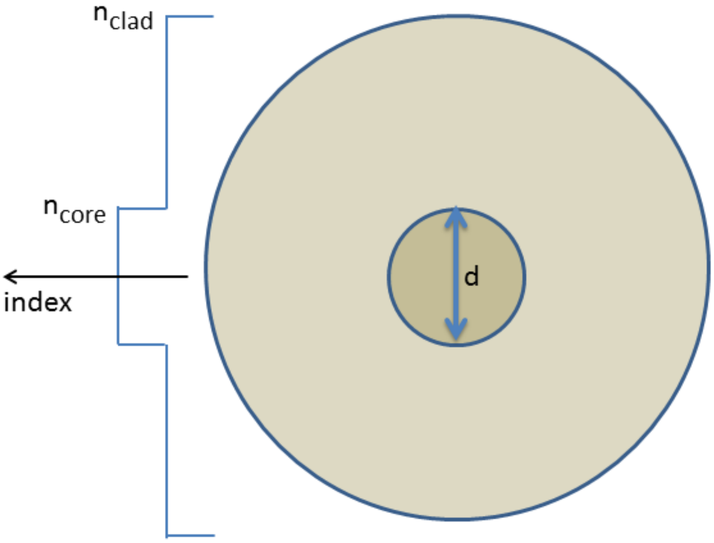

Figure 2.4: Standard step index single mode fibre design

2.5.2 Dispersion Shifted Fibres

The standard SMF exhibits a ZDW at 1.3 μm wavelength. The early telecoms systems operated at this wavelength in order to exploit the absence of dispersive effects which would otherwise result in pulse broadening and compromise the system performance. The advent of erbium doped fibre amplifiers (EDFA) in the 1990s which exhibit a gain profile centred around 1.55 μm has resulted in a new class of fibres, namely dispersion shifted fibres (DSF), which exhibit a ZDW at 1.55 μm and where silica also exhibits minimum transmission loss.

DSFs compensate the high anomalous material dispersion of silica at 1.55 μm by changing the index profile of the fibre through doping the core with small amounts of germania (GeO_2) (about 1%) and/or with adopting a differently shaped refractive index profile such as a graded index profile [2].

The germania-doped core gives rise to a small increase in the value of γ of the fibre to approximately 2 /W/km [63]. However, the absence of dispersive effects in these fibres at 1.55 μm together with their long interaction lengths can give rise to phase-matched four-wave mixing effects which result in signal distortion and deterioration in the performance of multichannel transmission systems, thus limiting the use of these fibres to single channel systems.

To alleviate this problem, DCFs are engineered such that the dispersion is small but not zero at 1.55 μm. Such fibres are often termed near-zero dispersion shifted fibres (NZ-DCF) and are widely used in multichannel transmission systems such as wavelength division multiplexing (WDM) systems, where minimising nonlinear distortions is a necessity. The finite dispersion of these NZ-DCFs at 1.55 μm can be compensated by deploying dispersion compensating fibres (DCF) after the DCFs used for transmission. The dispersion of DCFs is designed such that the ZDW is shifted beyond 1.6 μm resulting in a negative dispersion profile at 1.55 μm which can compensate for the positive dispersion of the transmission fibres [2].

Increasing the percentage of germania in the fibre core to 3 % together with decreasing the size of the fibre core leads to a significant increase in the value of γ [64, 63]. This is because such changes give rise to stronger light confinement in the core and thus a smaller value of effective mode area and an enhanced nonlinearity (Equation 2.14). Typical values of γ can reach 25 /W/km while low propagation loss values of the order of 0.5 dB/km are maintained. This is an important class of DSFs that is often termed highly nonlinear dispersion shifted fibres (HNL-DSF) [63].

HNL-DSFs are one of the most mature and competitive highly nonlinear fibre technologies [65, 66, 67]. They can be easily engineered to exhibit low and flattened dispersion profiles across the C-band and can be spliced to standard SMFs with very low coupling loss. However, the hundreds of meters of fibre length required to achieve high values of effective nonlinearity often result in low values of SBS pump threshold and less compact and stable systems.

2.5.3 Highly Nonlinear Soft Glass Fibres

Equation 2.14 above shows that a high value of the nonlinear coefficient γ can be attained either by using a glass of high nonlinear refractive index n_2 as the fibre core, or by reducing the effective core area guiding the light.

Soft glass such as lead silicate, bismuth oxide, tellurite and chalcogenide possess nonlinear refractive indices which are orders of magnitude greater than that of silica. As such, fibres made of high index glasses achieve a much higher effective nonlinear coefficient than those made of silica of the same effective core area. For instance, a glass such as tellurite possesses a nonlinear refractive index n_2 in excess of 25 times higher than that of silica [68]. As such, soft glass fibres, with unprecedentedly high values of γ can be utilised to relax system power requirements and reduce fibre lengths to only a few metres, thus greatly improving the stability and practicality of devices and systems under use.

Generally, soft glasses suffer from much higher intrinsic material losses than silica at 1.55 μm [69]. Losses in the order of dB/m, as opposed to the 0.17 dB/km achievable through modern silica fibres, are not uncommon in soft glass fibres. A great deal of these losses however can be attributed to impurities and defects associated with the fabrication process. Consequently, further enhancements of the fabrication techniques can be expected to significantly reduce losses to values approaching the material loss. Indeed, a tellurite fibre with a propagation loss of 0.4 dB/m has already been reported [70], while significant progress has been made to achieve a loss value approaching the theoretical minimum of 0.8 dB/m in lead silicate [23]. Furthermore, a number of soft glasses such as tellurite and chalcogenide enjoy enhanced transmission characteristics relative to silica which is highly absorbent beyond 2 μm. As such, such glasses are often termed infrared glasses since their low loss across the MIR makes them suitable for applications beyond the NIR wavelengths [68, 71].

2.5.4 Microstructured Optical Fibres

Microstructured optical fibre (MOF) technology can be used to further improve fibre nonlinearity γ by reducing the effective mode area through core size reduction and/or increasing the fibre NA. Microstructured optical fibres are often divided into two classes: holey fibres and all-solid microstructured fibres (Figure 2.5). They exploit the large index contrast between the core and the cladding to ensure high values of numerical aperture (NA) and therefore tighter mode confinement [23]. Furthermore, suitable design of the wavelength scale features present in the cladding allows control of the dispersion profile of the fibre, and enables novel dispersion characteristics suited for various nonlinear applications. In particular, the geometrical details of holey fibres such as the air-filling fraction and the wavelength-scale alternating high- and low- index coaxial cladding layers present in all solid MOF fibres can be suitably controlled to result in a strong waveguide dispersion which compensates for the material dispersion of the glass, leading to an overall tailored dispersion profile [72].

The combination of high nonlinear index soft glasses and MOF technology, offers a tremendous promise to revolutionise current highly nonlinear optical fibre technologies. For instance, a holey fibre based on a high-index glass such as bismuth oxide can have a nonlinearity coefficient 10^3-10^4 times higher than that of a conventional silica fibre [73]. As such, the orders of magnitude increase of nonlinearity together with the great flexibility in dispersion engineering that MOF technology offers, enable the realisation of highly efficient and broadband nonlinear applications.

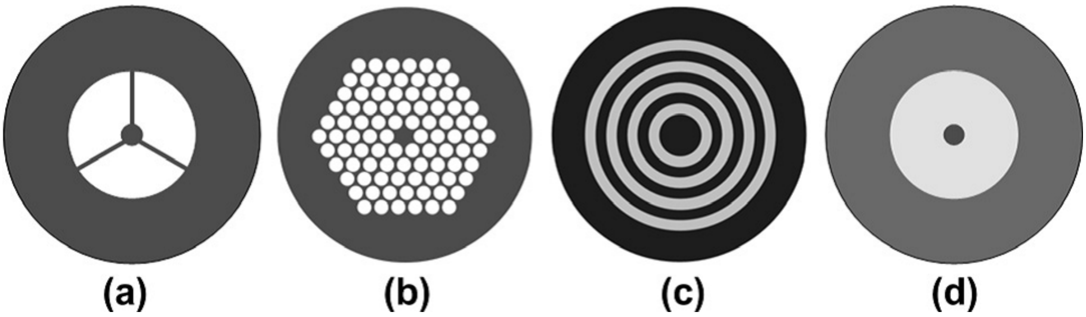

Figure 2.5: Examples of microstructured optical fibres: (a) air-suspended core holey fibre, (b)holey fibre with complex two dimensional microstructured cladding, (c) all-solid one dimensional microstructured fibre and (d) high index contrast W-type fibre (courtesy of Dr. X. Feng)

2.5.5 Tapered Fibres

Tapered fibres are a class of highly nonlinear optical fibres characterised by a small core size and a high refractive index difference. A common way to realize a fibre with such attributes is to start with a length of standard telecommunication fibre with a cladding diameter of 125 μm and heat its middle section beyond the softening point while stretching the fibre from both ends. This process results in the elongation of the middle section of the fibre and a reduction in its diameter, where the cladding diameter can be shrunk from 125 μm down to 1 μm [63, 74]. The few centimetres long fibre taper producible through this procedure can guide light in the shrunk cladding through TIR taking place between the cladding glass and the surrounding air interface. Such high NA small diameter device can confine light very tightly resulting in large values of effective nonlinearity. Furthermore, the nonlinearity can be further increased by using a soft glass of higher nonlinear refractive index n_2 than silica. Such soft glass fibre tapers can result in ultra-high values of nonlinearity and γ values as high as 68000 /W/km have been demonstrated using chalcogenide glass fibre tapers [75].

However, tailoring the dispersion of tapered fibers is a challenging process. The wavelength-scale core size of tapered fibres makes the ZDW very sensitive to any variation in core radius thus limiting the degree of precise control of dispersion available. Furthermore, aggressive tapering where the core size is reduced to an order of optical wavelength to increase the γ values can lead to poor power handling thus greatly limiting the strength of nonlinear effects achievable in these cm-long devices [63].

2.5.6 Highly Nonlinear Photonic Waveguides

While significant progress has been made in advancing highly nonlinear fibre technology by constantly enhancing fabrication techniques to help optimise the loss , dispersion and nonlinearity of the fibres, other technological competitors to HNLFs such as silicon waveguides and chalcogenide glass photonic chips have also gathered increased research attention in recent years. The high index of silicon can be exploited through silicon-on-insulator (SOI) technology to achieve sub-micron confinement of optical beams. In addition, the large third-order nonlinearity that silicon possesses can result in highly efficient nonlinear devices. In fact, the Kerr coefficient of silicon is over two orders of magnitude larger than that of silica and a Raman gain coefficient a thousand times larger is also obtainable near the 1.55 μm wavelengths [76]. Nonlinear coefficients as high as 10^5 /W/km are thus not uncommon in silicon wire waveguides, and γ values of 7x10^6 /W/km have also been reported in optimised silicon slot waveguides. Demonstrations of a number of efficient nonlinear effects and applications such as self-phase modulation, four wave mixing, parametric amplification and silicon Raman lasers have thus been all reported in silicon waveguides at moderate power levels [77, 78].

However, silicon waveguides suffer from losses incurred from the free carriers generated through two photon absorption (TPA), which result in limiting the amount of usable power for nonlinear effects. This is because the TPA's quadratic increase with pump power results in high carrier densities and the incurred losses thus increase significantly with power. A number of schemes to reduce these losses have been suggested, one of which is to increase the length of the device and operate at lower pump power levels. Other techniques which aim to either remove the free carriers through reverse bias or reduce their lifetime by ion implantation have also been proposed [79].

Another technological competitor to HNLFs is chalcogenide glass photonic chips. chalcogenide glasses are composed of heavy elements such as Sulfur (S), Selenium (Se) and Tellurium (Te). These elements contain a number of loosely bound electrons that can easily vibrate around the nucleus, resulting in a strong nonlinear response when an electromagnetic field is applied to the glass. Strong third order nonlinearities over two-three orders of magnitude greater than silica are thus obtainable from chalcogenide glasses [27]. The short device length achievable through chalcogenide glass photonic chips also results in broadband low dispersion, thus reducing the phase mismatch between the propagating waves for broader and more efficient nonlinear processes. Furthermore, the ultra-fast nonlinear response of chalcogenide glasses is unhindered by nonlinear losses as chalcogenides are less prone to losses from free carrier effects commonly associated with silicon waveguides at 1.55 μm wavelengths [28]. In addition, recent years have witnessed significant progress towards reducing losses related to impurity absorption that becomes dispersed in the glass during fabrication [29].

However, chalcogenide-based devices also suffer from a few drawbacks. Fibers and waveguides made from chalcogenide glasses suffer from a lower optical damage threshold than that of silica and other soft glasses. This places a limit on the pump power that can be launched into the device, and thus restricts the use of many chalcogenide-based devices to multimode operation for any applications requiring power delivery [80].

2.6 Conclusion

This chapter provided a theoretical overview of the main topics needed to allow a detailed understanding of the work described in the rest of this thesis.

The chapter starts with explaining the origin of the various linear and nonlinear effects that take place during signal propagation in optical fibres. It then proceeds to discuss each effect and describe its impact. Particular emphasis is laid on effects with major relevance to the work of this thesis such as chromatic dispersion and nonlinear refraction.

The process of phase matching is mathematically described and its importance in achieving efficient parametric processes such as in the case of FWM, is highlighted. Inelastic scattering effects, such as the stimulated Brillouin scattering (SBS), are also described.

The Nonlinear Schrödinger Equation (NLSE), the fundamental equation describing the various linear and nonlinear phenomena during signal propagation in optical fibres, is then introduced and a brief description of a numerical method to solve the NSE, based on the use of the Split Step Fourier Transform (SSFT) method is given.

Finally, the chapter concludes by presenting an overview of the various optical fibre and waveguide technologies. It discusses the attributes and limitations of a number of state-of-art all-optical signal processing platforms, such as dispersion shifted fibres, microstructured fibres and highly nonlinear photonic waveguides.

The work presented in the subsequent chapters focuses on exploiting some of the nonlinear effects presented here in realising all-optical signal processing applications. Chapter

3 reports the design and characterisation of a highly nonlinear lead silicate fibres, and the demonstration of FWM-based wavelength conversion in the fibre at 1550 nm.

Chapter 3

Highly Nonlinear Lead Silicate Fibres

3.1 Introduction

Efficient nonlinear processes generally require a fibre with a high nonlinearity, low loss, broadband low dispersion profile and a high stimulated Brillouin scattering (SBS) threshold [12]. Germanium-doped highly nonlinear fibres (HNLFs) have proven to be an important tool for the observation of these effects, mainly due to their excellent dispersion characteristics and low loss [81, 82, 83]. Their application however, requires the use of long lengths of fibre (typically a few hundreds of meters) which can be limiting in terms of the parametric gain bandwidth, device latency and stability. Moreover, SBS eventually limits the amount of narrow linewidth continuous wave pump power that can be coupled into the fibre unless active steps are taken to broaden either the linewidth of the pump [84] or the SBS gain bandwidth [85] both of which add complexity and ultimately compromise the system performance.

Nonlinear operation in far shorter fibre lengths can be accommodated through the adoption of soft glasses that exhibit both a far higher nonlinear refractive index and a better SBS figure of merit than silica [22, 73, 86]. Figure 3.1 plots the nonlinear refractive index n_2 as a function of the linear refractive index n for various optical glasses, including silica, fluoride, lead silicate, bismuth, tellurite and chalcogenide glasses. It can be seen that soft glasses possess a nonlinear refractive index, which ranges between one order of magnitude higher than silica, such as in the case of Schott SF57 lead silicate glass, to three orders of magnitude higher, such as in the case of chalcogenide-based glass telluride. This indicates that fabricating optical fibres in these soft glasses rather than silica would enhance the nonlinear response of the fibres by at least 1-3 orders of magnitude.

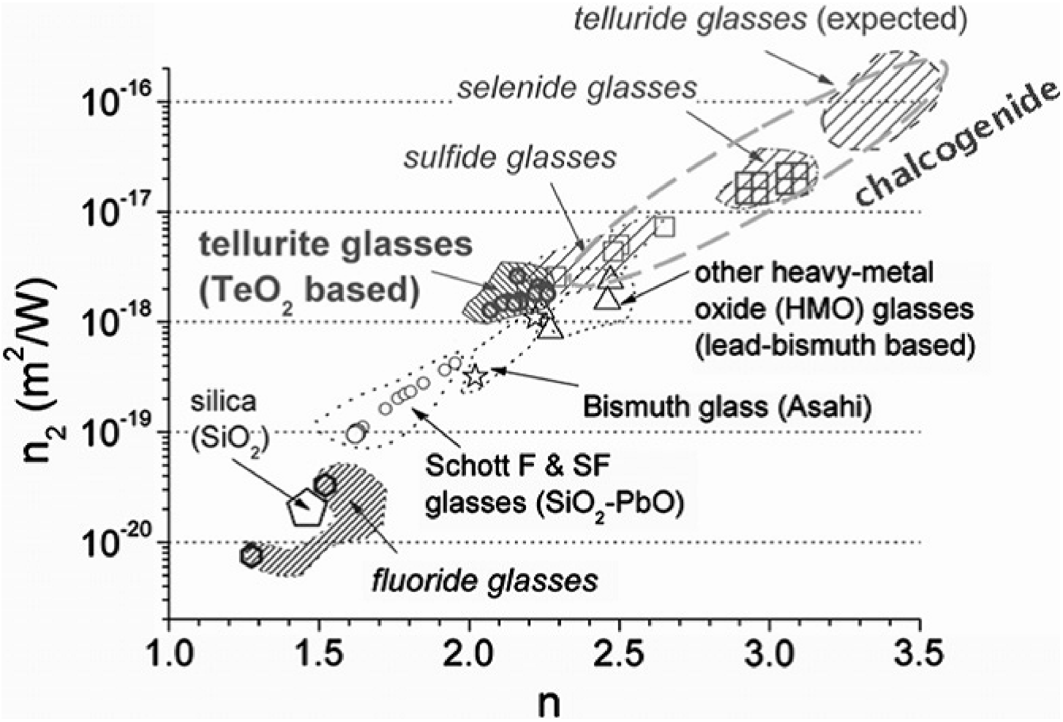

Figure 3.1: The relationship between the linear and nonlinear refractive index for various optical glasses (courtesy of Dr. Xian Feng).

Among the various soft glasses that appear in Figure 3.1, lead silicates are commercially available and possess good chemical and thermal properties for fibre fabrication. For instance, the crystallisation stability and less steep viscosity–temperature characteristic curves of lead silicates as compared to most compound glass alternatives make them a very attractive soft glass platform [87]. Furthermore, the zero dispersion wavelength (ZDW) of lead silicate glasses lies close to 2 μm making dispersion tailoring of lead silicate-based HNLFs to telecommunication wavelengths a relatively easy task. This is in contrast with higher index soft glasses such as chalcogenides, the ZDW of which lies beyond 5 μm (Table 3.1). In such glasses a high numerical aperture (NA) and a small fibre core are necessary to achieve the required ZDW shift to near-IR wavelengths, which often lead to imposing practical limitations in terms of coupling and power handling. Furthermore, such requirements often render simple fibre design structures, such as the step-index design, unsuitable and more complex structures based on microstructured optical fibre (MOF) technology must be adopted.

Due to the advantages discussed above, lead silicate was identified as the glass of choice for implementing a highly nonlinear soft glass fibre suitable for demonstrating efficient nonlinear processes at the telecommunications wavelengths. This chapter reports the design and characterisation of the lead silicate fibres fabricated at the ORC. It follows on from the work carried out by Dr. Angela Camerlingo and colleagues which had started the characterisation of some of the fibre optical properties, such as dispersion and nonlinearity and demonstrated some nonlinear effects in the fibre such as FWM

Glass	λ_0 (μm)	REF
Silica	1.27	[91]
Fluoride	1.5-1.7	[92]
Silicate	2	[23]
Tellurite	2-3	[93]
Chalcogenide	5-7	[94]

Table 3.1: Zero dispersion wavelength (ZDW) of various optical glasses.

[22, 31, 32, 88, 89, 90]. The lead silicate work was part of the final stage of the FP7 EU PHASORS project which aimed to deliver a new class of dispersion engineered highly nonlinear fibres and demonstrate their applicability in PSA-based applications.

The chapter starts by discussing the design of the W-type lead silicate fibre. A numerical model that was developed to predict the chromatic dispersion of the fibre based on its design parameters (core size and the core-cladding refractive index difference) is described. A brief account of the fabrication process is given along with an outline of the outcome of the characterisation work carried out by A. Camerlingo. The results of the new characterisation experiments measuring the fibre's loss and its SBS threshold are also presented. Furthermore, FWM experiments of CW signals in the fibre are reported and the results are contrasted to numerical simulations based on the Split Step Fourier (SSF) method. Numerical simulations are also used to explore the potential of this fibre technology as an efficient nonlinear medium and highlight the advantages of its novel dispersion profile.

The work reported in this chapter represents the stepping stone of this PhD project. It served as an important familiarisation process to soft glass fibre technology as well as to nonlinear optics, both of which constitute central aspects of this project.

3.2 Design of Highly Nonlinear Lead Silicate Fibres

The design of the highly nonlinear lead silicate fibre was chosen to follow the simple well-known step-index design. In addition to a high nonlinearity, an important design goal was to achieve a low and flattened chromatic dispersion profile at 1550 nm. Since, the total chromatic dispersion D of a single mode optical fibre is the sum of the fibre's material dispersion D_m and its waveguide dispersion D_w:

$$D = D_m + D_w \tag{3.1}$$

with careful choice of the core size and the core-cladding refractive indices, the waveguide dispersion can be engineered to precisely compensate for the material dispersion, thus resulting in a flat near-zero dispersion profile at the required wavelength of operation.

Therefore, when designing an optical fibre with specific dispersive properties, one must study the impact of the fibre design parameters, namely the core diameter a and core-cladding refractive index difference Δn, on the waveguide dispersion. Dr. F. Poletti and colleagues have developed a theoretical model which describes the impact of the fibre design parameters on the dispersion [95]. This theoretical model, on which a numerical tool was based on, is described below.

3.2.1 Calculating the Waveguide Dispersion of a Circularly Symmetric Step Index Fibre

The impact of the fibre core diameter a and its core-cladding refractive indices n_{co} and n_{cl} on the waveguide dispersion can be calculated for a step index fibre with a circular radial symmetry. To do so, the exact solution of the characteristic equation describing the mode propagation in optical fibres must be found [96]:

$$\left[\frac{J_1'(U)}{UJ_1(U)}+\frac{K_1'(W)}{WK_1(W)}\right]\left[\frac{J_1'(U)}{UJ_1(U)}+\left(\frac{n_{cl}}{n_{co}}\right)^2\frac{K_1'(W)}{WK_1(W)}\right]=\left(\frac{n_{eff}}{n_{co}}\right)^2\left(\frac{1}{W^2}+\frac{1}{U^2}\right)^2 \tag{3.2}$$

where J_1 and J_1' are the Bessel function of the first kind and its derivative respectively and K_1 and K_1' are the modified Bessel function of the second kind and its derivative respectively. U and W are the transverse wave numbers which can be described via:

$$U=\pi a/\lambda\sqrt{n_{co}^2-n_{eff}^2} \tag{3.3}$$

$$W=\pi a/\lambda\sqrt{n_{eff}^2-n_{cl}^2} \tag{3.4}$$

Furthermore, n_{co} and n_{cl} are the refractive index of the core and the cladding respectively and n_{eff} is the effective index which is related to the propagation constant β through:

$$n_{eff}=\beta/k \tag{3.5}$$

where k is the wavenumber defined as:

$$k=\frac{2\pi}{\lambda} \tag{3.6}$$

For a given step index design parameters, $n_{co}(\lambda)$, $n_{cl}(\lambda)$ and a, Equation 3.2 can be solved (numerically by finding its roots) at different wavelengths yielding a wavelength-dependent effective index $n_{eff}(\lambda)$ relationship. Numerical differentiation of $n_{eff}(\lambda)$ then yields the targeted waveguide dispersion of the fibre:

$$D_w(\lambda) = -\frac{\lambda}{c}\frac{d^2 n_{eff}(\lambda)}{d\lambda^2} \tag{3.7}$$

3.2.2 Calculating the Material Dispersion of a Fibre based on the Sellmeier Equation

To calculate the material dispersion of the fibre, the Sellmeier equation is used [97]. The equation describes the relationship between the refractive index and wavelength for a particular optical glass:

$$n^2(\lambda) = 1 + \frac{B_1\lambda^2}{\lambda^2 - C_1} + \frac{B_2\lambda^2}{\lambda^2 - C_2} + \frac{B_3\lambda^2}{\lambda^2 - C_3} \tag{3.8}$$

Where B_1, B_2, B_3, C_1, C_2 and C_3 are the Sellmeier coefficients of the glass. One can then use the refractive index-wavelength relationship produced by Equation 3.8 in Equation 3.7 to compute the material dispersion:

$$D_m(\lambda) = -\frac{\lambda}{c}\frac{d^2 n(\lambda)}{d\lambda^2} \tag{3.9}$$

Finally, the total chromatic dispersion of the fibre can be calculated using Equation 3.1 above.

3.2.3 Impact of Fibre Design on Dispersion - Demonstration

The equations presented above were solved numerically in MATLAB, producing a numerical tool that predicts the chromatic dispersion given a certain fibre design. For the step index fibre design considered, Schott SF57 glass ($n = 1.80$ at 1550 nm) was chosen as the core material. This is a commercial glass the Sellmeier coefficients of which are readily available (and are reported in Table 3.2 for reference). Based on these values, the material dispersion of the glass was calculated as explained in Section 3.2.2. Figure 3.2 depicts the material dispersion of the Schott SF57 glass, and shows that its ZDW is 1.81 μm.

To demonstrate the effect of the fibre core diameter on the dispersive properties of the fibre, the core-cladding index difference Δn was kept fixed at 0.3 (i.e. $n_{cl} = 1.5$) in the numerical model while the core diameter a was varied. Figure 3.3 depicts the impact

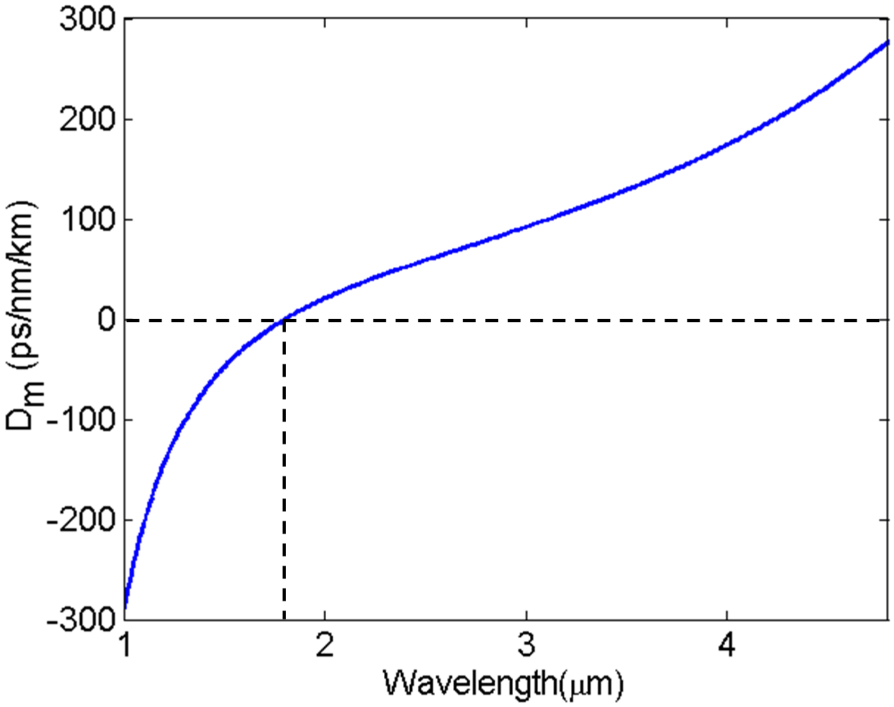

Figure 3.2: The material dispersion of the Schott SF57 glass calculated using the Sellmeier coefficients shown in Table 3.2.

Coefficient	Value
B_1	1.87543831
B_2	0.37375749
B_3	2.30001797
C_1	0.0141749518 μm^2
C_2	0.0640509927 μm^2
C_3	177.389795 μm^2

Table 3.2: Sellmeier coefficients of the Schott SF57 glass [98].

of the diameter a on the effective index (Figure 3.3a), the waveguide dispersion (Figure 3.3b) and the total chromatic dispersion of the fibre (Figure 3.3c).

Figure 3.3a shows that the effective refractive index n_{eff} tends towards the core refractive index value n_{co} at shorter wavelengths ($\lambda \ll a$) and towards the cladding index value n_{cl} at longer wavelengths ($\lambda \gg a$). The net effect of this, is that at those limits (i.e. $\lambda \ll a$ and $\lambda \gg a$), the waveguide dispersion contribution is small, while it exhibits an oscillatory sinusoidal motion in between, going from positive (anomalous) at shorter wavelengths to negative (normal) dispersion at longer wavelengths (Figure 3.3b). It is also worth noting that the value of the fibre diameter can radically change the dispersion slope of the waveguide dispersion at a given wavelength. This effect is also clearly seen in the total chromatic dispersion depicted in Figure 3.3c, where the waveguide dispersion contribution in Figure 3.3b is added to the material dispersion shown as the pink dashed line in Figure 3.3c.

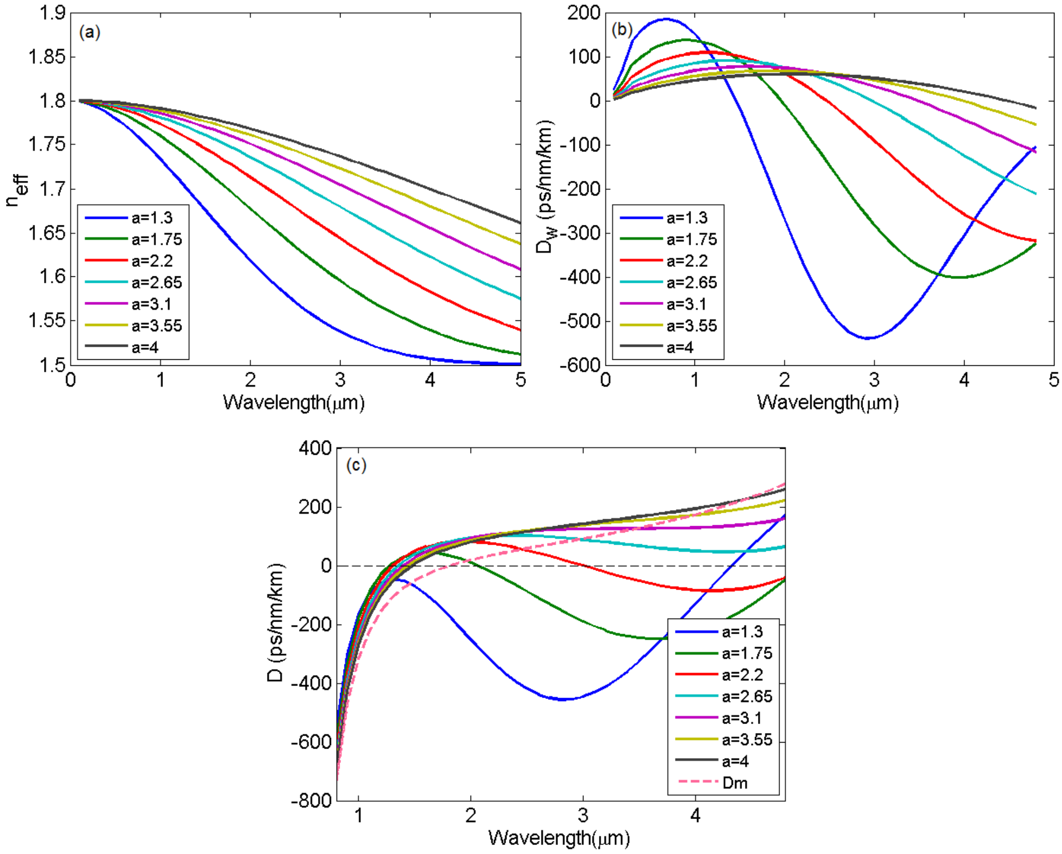

Figure 3.3: The impact of the fibre core diameter on the (a) effective index (b) waveguide dispersion (c) chromatic dispersion. The dashed pink line in (c) represents the material dispersion. The simulations have assumed Δn=0.3.

The impact of the refractive index contrast Δn on the dispersion, for a fixed core diameter of 1.75 μm, was also investigated. Figure 3.4a plots the variation of n_{eff} with wavelength for various values of Δn, where similar conclusions to those drawn from Figure 3.4a are observed. However, the distinction between the effect of changing a and that of changing Δn becomes very clear when contemplating Figure 3.4b. Figure 3.4b shows that the impact of Δn on the waveguide dispersion is to shift the whole dispersion curve towards longer wavelengths for larger values of Δn and vice versa. This is also accompanied with an expansion of the dispersion curves vertically for larger values of Δn and a contraction for smaller values of Δn. Furthermore, these effects can also be seen in Figure 3.4c which illustrates the impact of Δn on the chromatic dispersion. The slope of the dispersion curve remains largely unchanged at a given wavelength while the whole dispersion curve, and thus the position of the ZDW points, move towards longer/shorter wavelengths depending on the value of Δn.

A key conclusion is drawn from Figure 3.3 and Figure 3.4. When designing a fibre of a specific core refractive index n_{co}, and with specific dispersive properties in mind, one starts with an arbitrary value of Δn while the core diameter a is tuned to generate the desired shape (slope) of the dispersion curve. The value of Δn is then adjusted to obtain

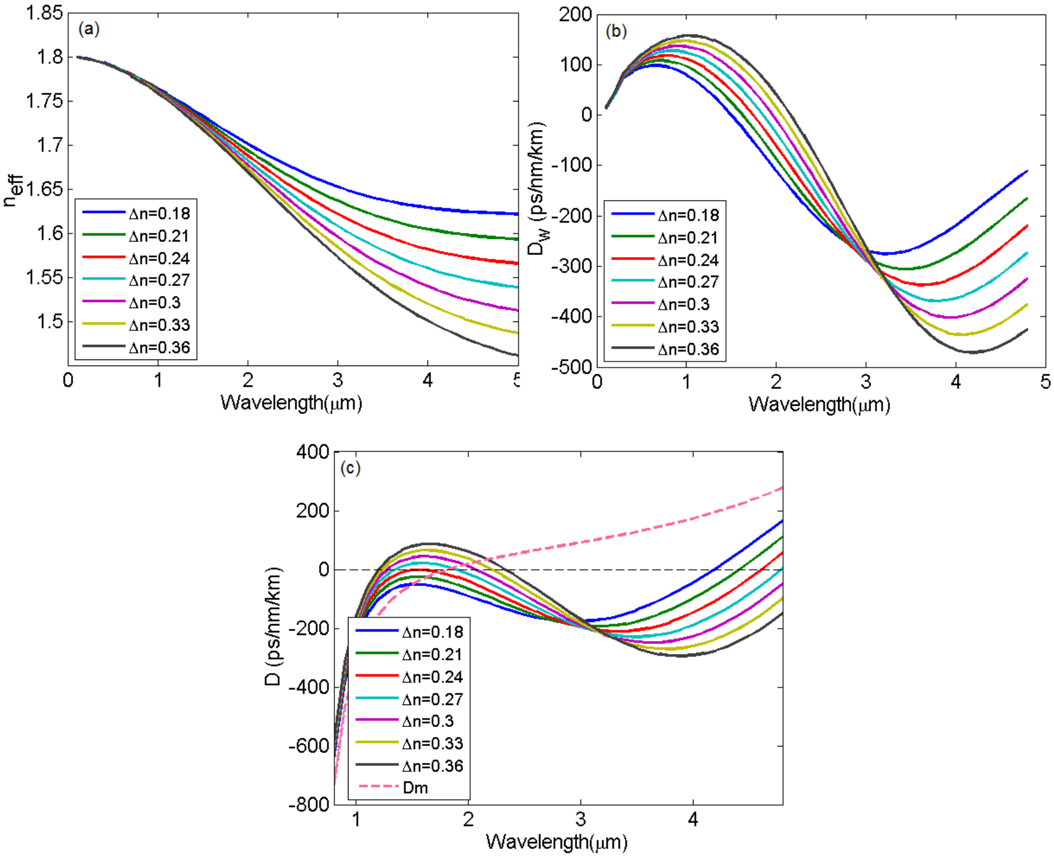

Figure 3.4: The impact of the refractive index difference on the (a) effective index (b) waveguide dispersion (c) chromatic dispersion. The dashed pink line in (c) represents the material dispersion. The simulations have assumed a=1.75 μm.

the exact value of dispersion required at a given wavelength. Finally, while Figures 3.3 and 3.4 demonstrate the influence of specific values of the design parameters on the dispersive properties of the fibre, the conclusions drawn here hold true for any values of a, n_{co} and n_{cl} [95].

3.2.4 Fabrication of Highly Nonlinear Lead Silicate Fibres

The lead silicate fibre was designed for all-optical processing applications at telecommunications wavelengths. As such, a high value of nonlinearity and broadband nonlinear function were highly desired. To achieve the latter goal, a low value of dispersion ($D <$ 10 ps/nm/km) and a very flat dispersion profile (dispersion slope $\sim$ 0 ps/nm^2/km) at 1550 nm were targeted.

Numerical simulations have found that a fibre with a core diameter of 1.66 μm and refractive index contrast of 0.27 would give rise to the desired dispersive properties. Figure 3.5 depicts the dependence of the effective refractive index, waveguide dispersion and chromatic dispersion on wavelength for the stated design. The simulations show that a fibre with the stated values of a and Δn would have a chromatic dispersion of ~4.5 ps/nm/km and a dispersion slope of -0.001 ps/nm^2/km at 1550 nm.

As the Schott SF57 glass (n = 1.80 at 1550 nm) was chosen as the core glass material of the fibre, Schott LLF1 glass (n =1.53) was selected as the cladding medium, achieving the Δn=0.27 value required. In effect the high index contrast that SF57-LLF1 provided two key benefits. Firstly it provided a strong waveguide dispersion when the core diameter was reduced to wavelength-scale dimensions, enabling the compensation for the high intrinsic core material dispersion at 1550 nm. Secondly, it provided strong mode confinement in the core, enabling a small effective area and thus strong nonlinearity.

To guarantee single mode operation, an additional cladding layer of Schott SF6 glass (n = 1.76) with a higher index than the effective index of the LP$_1$1 mode was added as an outer cladding layer to provide a high LP$_1$1 mode confinement loss [23, 22]. This approach is very effective in inducing high losses for higher propagation modes without affecting the dispersive properties of the fibre [99]. Fibres made following this design, are referred to as W-type fibres due to the shape of the refractive index profile.

The lead silicate W-type fibre was fabricated by Dr. X. Feng and colleagues using the rod-in-tube method [90]. The resulting SF57-LLF1-SF6 W-type fibre had a_0 = 1.66 μm and a_1 = 7.4 μm as depicted in the schematic of Figure 3.6. Arc-fusion splicing with an

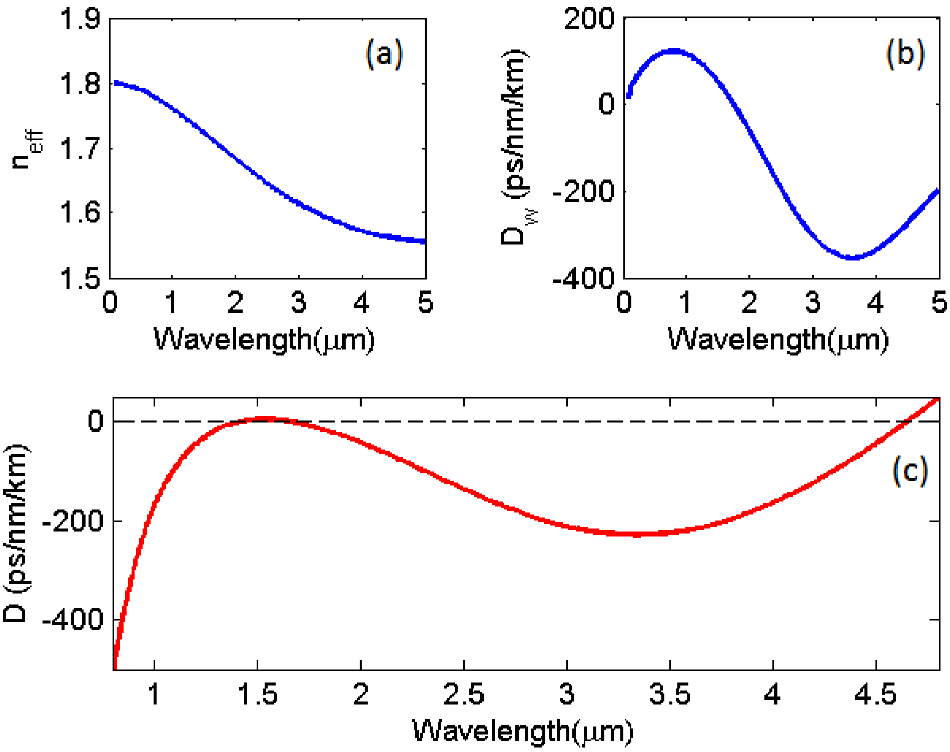

Figure 3.5: The variation of (a) the effective refractive index (b) waveguide dispersion and (c) chromatic dispersion with wavelength for a fibre with a = 1.66 μm and Δn = 0.27.

asymmetric configuration [23, 100] was used to splice the lead-silicate glass HNLF with a commercial high-NA Nufern silica fibre UHNA3 and then with a conventional silica SMF28 fibre. A loss of 5 dB per splice was obtained between the lead silicate fibre and UHNA3, and 0.25 dB between UHNA3 and SMF28.

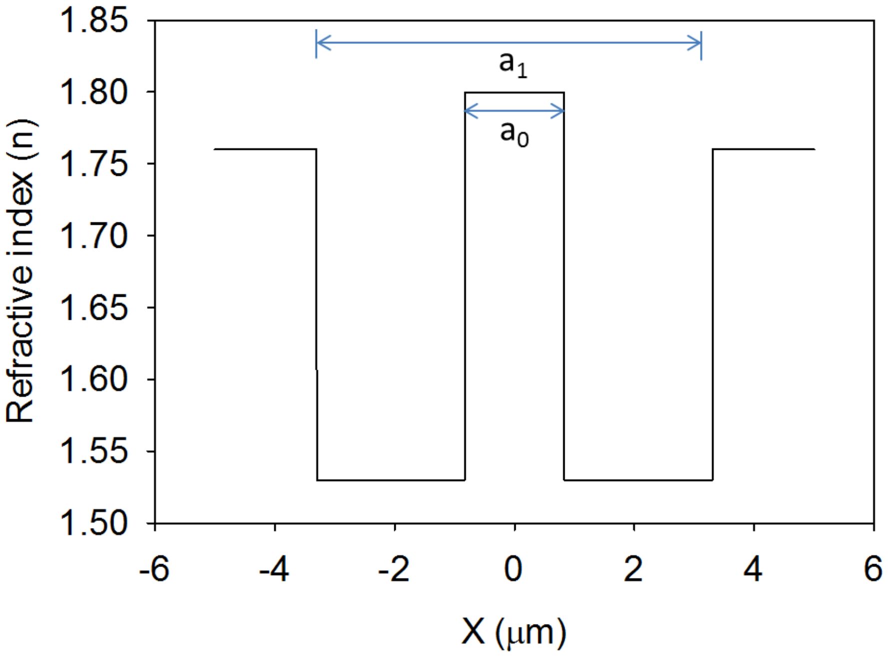

Figure 3.6: Schematic of the W-type index profile of SF57-LLF1-SF6 fibre. a_0 is the fibre core and a_1 the inner diameter of the second cladding.

3.2.5 Characterisation of Highly Nonlinear Lead Silicate Fibres

3.2.5.1 Basic Fibre Characteristics - Dispersion and Nonlinearity Measurements

As mentioned in Section 3.1, the fibre dispersion and nonlinearity were characterised by A. Camerlingo and the measurements were reported in [22].

The fibre dispersion was measured using a supercontinuum source and a Mach–Zehnder interferometric setup shown in Figure 3.7. A beam-splitter was used to divide the light from the supercontinuum source into two paths, where the length of the reference air-path could be varied through adjusting the position of the moving prism (prism #1). A beam-combiner was then used to recombine the light at the end of the two paths and the collected light was coupled into an OSA. The time delay between the test and reference beam could be adjusted by tuning the position of prism #1 such that the optical path length was matched for certain wavelengths. The chromatic dispersive effects of the fibre resulted in different wavelength components of the supercontinuum source travelling at different speeds and hence experiencing different group delays τ_g. This led to the

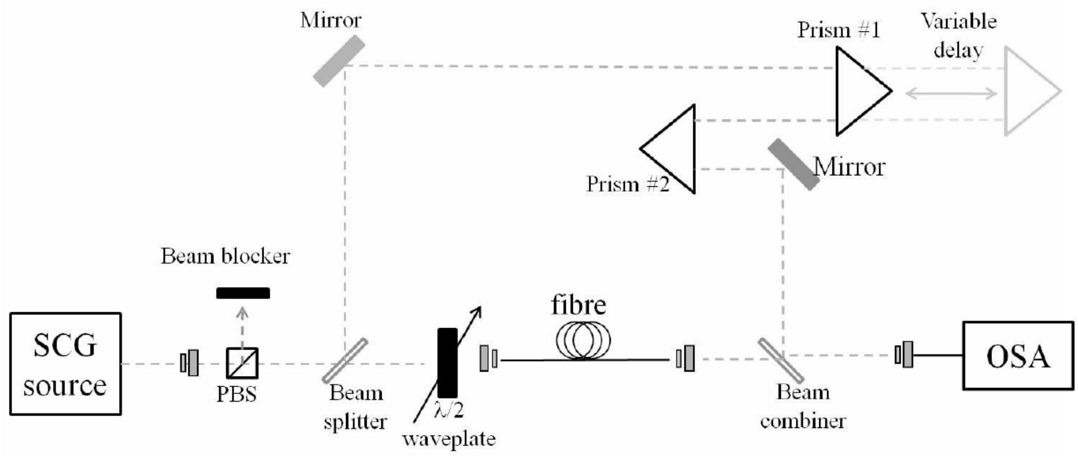

Figure 3.7: The experimental setup used for the measurement of the chromatic dispersion of the lead silicate fibre. SCG source: supercontinuum generation source, PBS: polarization beam-splitter (courtesy of Dr. Angela Camerlingo).

formation of spectral interference patterns (fringes) which could be viewed on the OSA and from which the chromatic dispersion could be calculated [101].

The measurement revealed that the lead silicate W-type fibre exhibited a near-zero dispersion profile at telecommunications wavelengths. The fibre had a dispersion of ~2 ps/nm/km and dispersion slope of -0.009 ps/nm^2/km at 1550 nm (Figure 3.8). The experimental data agree well with the simulations (Section 3.2.4) which predict a dispersion of ~4.5 ps/nm/km and dispersion slope of -0.001 ps/nm^2/km at 1550 nm.

The fibre's effective nonlinear coefficient γ was also measured and found to be 820 /W/km at 1550 nm, while the effective mode area A_{eff} was numerically calculated from

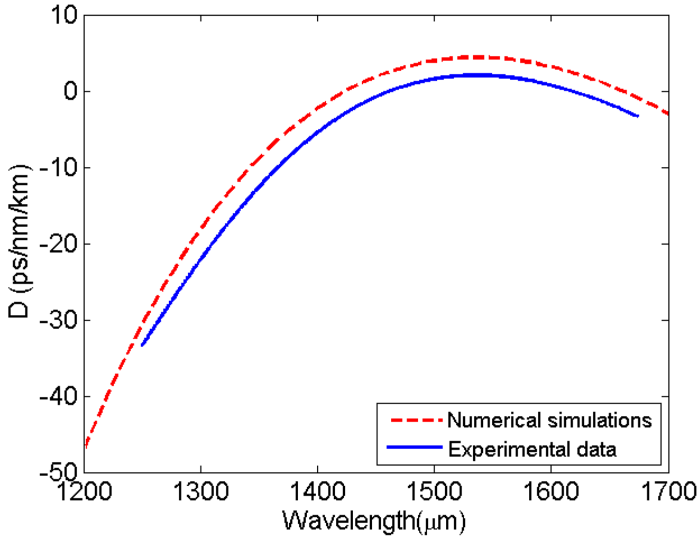

Figure 3.8: Experimental and calculated chromatic dispersion of the lead silicate W-type fibre.

the SEM images of the fiber to be ∼1.9 μm^2[22].

3.2.5.2 Further Characterisation Work - Loss and SBS Measurements

The first experimental task in this project was to continue on the characterisation work of this lead silicate fibre. This involved measurement of the distributed loss of the lead silicate fibre as well as its SBS threshold.

The loss measurement was conducted using the Optical Time-Domain Reflectometry (OTDR) technique. OTDR measurements are usually considered to be less accurate than cut-back measurements, particularly for high loss fibre samples, where detection noise resulting from the weak backreflected signal could cause measurement errors [102, 103]. However, OTDR was the only practical method available in this case, since the lead-silicate sample had already been spliced to SMF pigtails.

To increase the accuracy of the measurement, the loss of the sample was measured from each end and averaged and the process was repeated several times. The OTDR measurements revealed a propagation loss of 2.7 dB/m and a fibre length of 1.56 m as indicated by Figure 3.9.

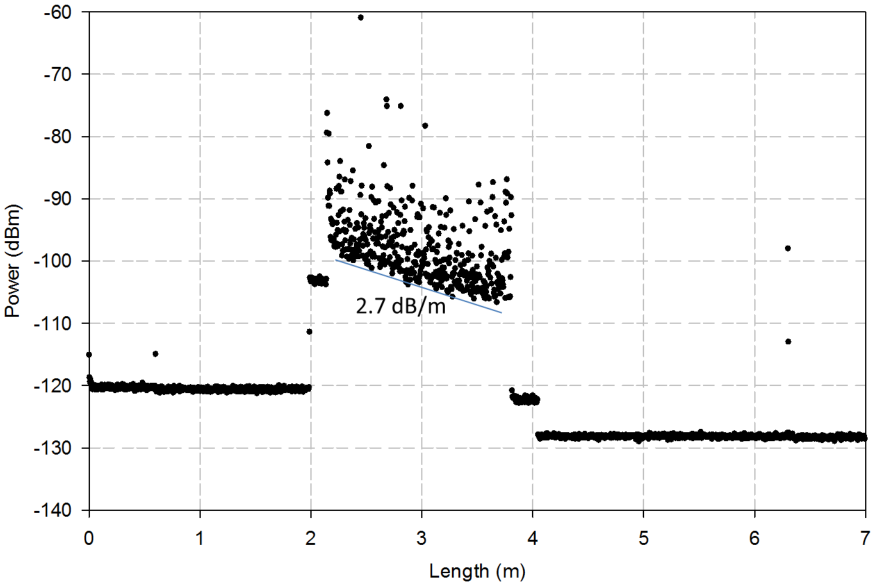

Figure 3.9: OTDR loss measurement of the lead silicate fibre.

An SBS characterisation of the fabricated fibre was also carried out to deduce its Brillouin threshold [104]. Figure 3.10 shows the experimental setup which used a CW pump beam at 1562.65 nm amplified through a 5 W EDFA. The amplified beam was then launched into port 1 of a circulator, whose forward output port was connected to one end of the lead silicate W-type fibre. The backreflected spectra were monitored through port 3 of the circulator using a high resolution OSA. The input power to the fibre (power after splice points) was varied from 20.5 dBm to 30.5 dBm through the high power EDFA.

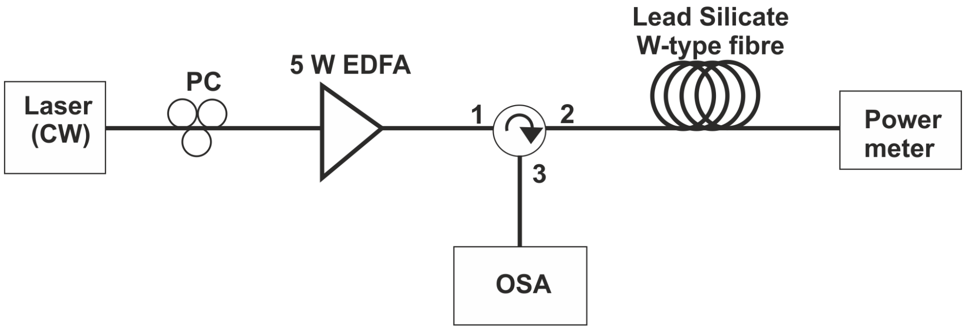

Figure 3.10: The experimental setup used for the SBS characterisation measurement.

The backreflected spectra (Figure 3.11a) show a down-shifted Stokes wave 61 pm (7.61 GHz) away from the pump beam. Analysis of the results (Figure 3.11b) shows that the SBS threshold of this fibre sample is reached at ∼30 dBm of input power.

Recalling from Section 2.2.2.3, Equation 2.30 which was used for calculating the SBS power threshold of a fibre sample, can be re-arranged as follows:

$$g_B \simeq (21A_{eff})/(P_{th}L_{eff}) \tag{3.10}$$

The Brillouin gain coefficient g_B is a more commonly used parameter to describe the SBS characteristics of a particular fibre design. Given that the effective area of this lead silicate W-type fibre is $\sim$1.9 μm^2, its effective length is $\sim$1 m (calculated from Equation 2.16 and based on the loss value of 2.7 dB/m) and SBS threshold power is 1 W, the Brillouin gain coefficient g_B is found to be 4x10^{-11} m/W (this assumes that the laser source used in this characterisation measurement was nearly monochromatic).

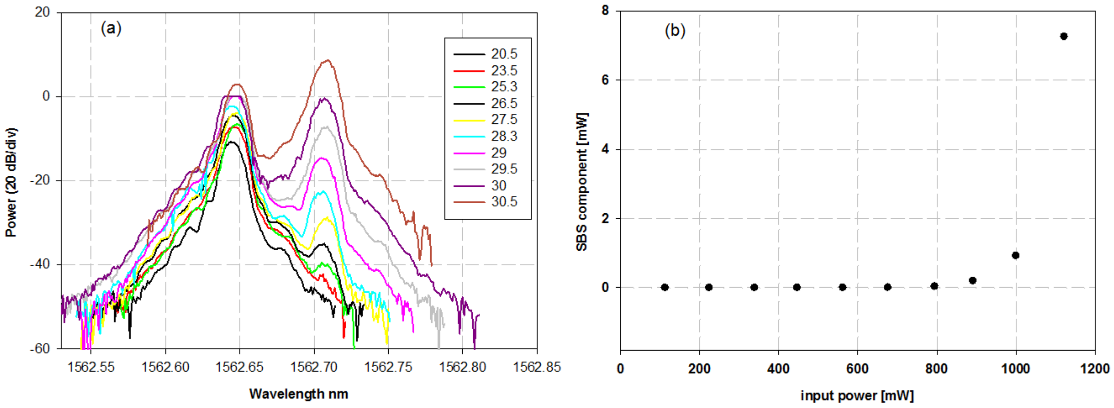

Figure 3.11: (a) Spectral traces of the output signals reflected back from the fibre for power levels ranging from 20.5 to 30.5 dBm into the fibre (b) Measured stokes' power as a function of input power into the fibre.

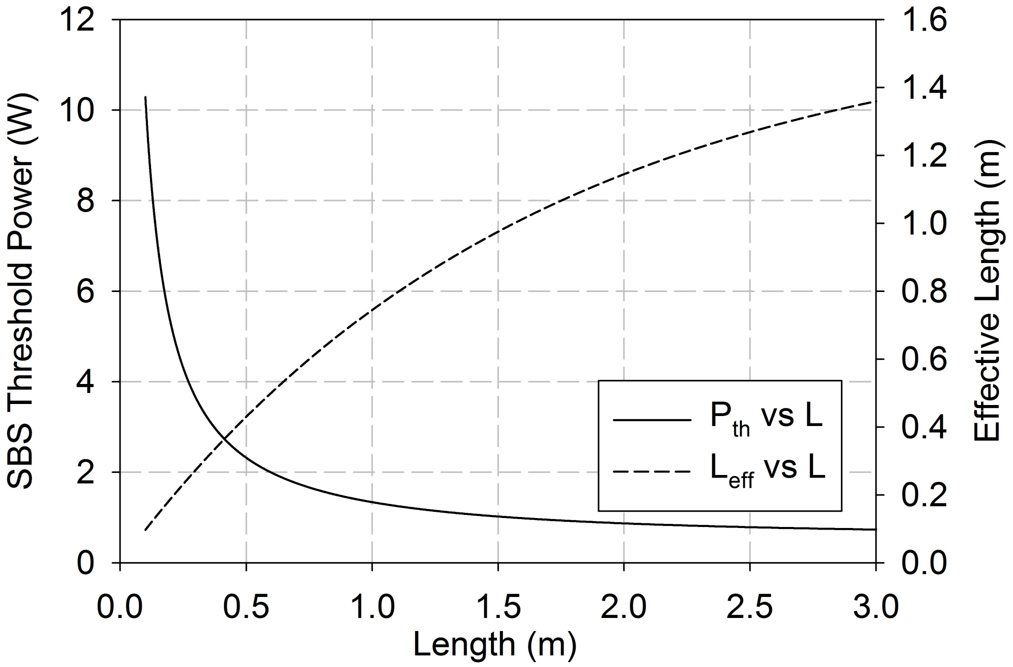

Figure 3.12: The SBS power threshold P_{th} (left) and the effective length L_{eff} (right) as a function of fibre length L for the lead silicate W-type fibre.

Furthermore, the Brillouin gain coefficient g_B, can be used to determine the SBS power threshold P_{th} as a function of the fibre length L [59]. Figure 3.12 depicts the P_{th} vs L relationship for the lead silicate W-type fibre, where it can be seen that increasing the sample length beyond 3 m, would result in approximately the same L_{eff} and thus the same threshold power P_{th}.

3.3 FWM in a Highly Nonlinear Lead Silicate W-type Fibre

The lead silicate W-type fibre was used to demonstrate FWM of CW signals at 1550 nm. Furthermore, the the accuracy of the SSFT-based MATLAB model developed in Chapter 2, Section 2.4 was checked by comparing the experimental data to that predicted from the model.

3.3.1 Experimental Data

The wavelength conversion efficiency and bandwidth of a four-wave mixing-based wavelength converter based on the lead silicate W-type fibre was characterised. The experiment (Figure 3.13) involved a CW laser operating at 1563 nm and used as the pump wave and another wavelength-tuneable CW laser used as the signal wave. The pump power was boosted through a 2W EDFA, before being coupled with the 5 dBm signal through a 90/10 coupler. The pump and signal waves were then launched into the lead silicate W-type fibre whose output was fed into an OSA to monitor the optical spectra. An idler wave was subsequently generated through the FWM interaction in the fibre with a frequency equal to $\omega_{idler}= 2\omega_{pump}$-$\omega_{signal}$. The FWM characterisation was carried out for two different pump power levels, with a maximum total input pump power of 20 dBm and 17 dBm respectively being successfully coupled into the lead silicate fibre in the two experiments. Furthermore, the signal wavelength was varied from 1540 nm to 1576 nm and the subsequent conversion efficiency values were calculated. The conversion efficiency (CE) is defined here as the difference in dB between the output idler power and the output signal power:

$$CE = \frac{P_{idler-out}}{P_{sig-out}} \tag{3.11}$$

This is different from its usual definition as the ratio between the output idler power and the *input* signal power. The definition adopted here is usually chosen for cases where the splice/coupling losses into the wavelength converter are high, so as to characterise the device only with respect to its performance as a nonlinear element.

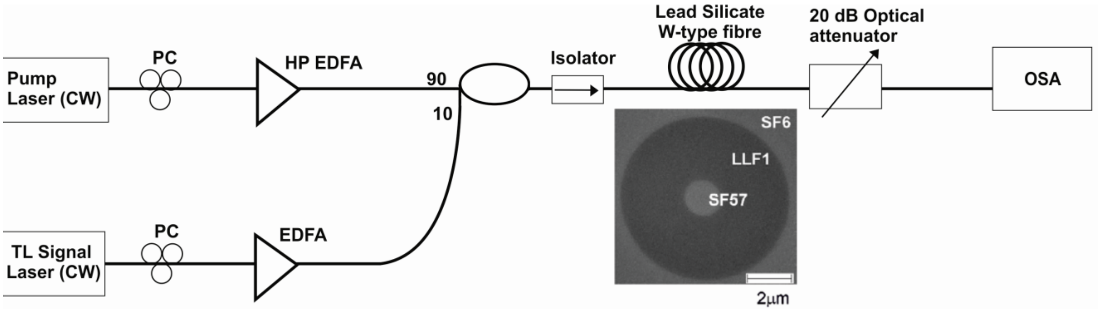

Figure 3.13: The experimental setup of the FWM in the lead silicate W-type fibre experiment. PC: Polarisation controller. HP EDFA: High power Erbium-doped fibre amplifier. OSA: Optical Spectrum Analyser.

The results of the FWM experiment along with simulation results of the conversion efficiency for various amounts of input pump power are shown in Figure 3.14a. The graph shows that for an input pump power of 20 dBm, a uniform conversion efficiency of approximately -21 dB across a wavelength range between 1540 nm to 1576 nm was achieved. A uniform conversion efficiency is also observed for a lower pump power of 17 dBm, as the figure illustrates. The theoretical curves representing the conversion efficiency for an increasing amount of input pump power show that a conversion efficiency approaching 0 dB across a wavelength range in excess of 100 nm can be achieved for an input pump power of 33 dBm (although the pump may need to be modulated to overcome SBS). Furthermore, in contrast to when operating in the normal dispersion regime where the bandwidth decreases with pump power [105], Figure 3.14a shows that operating in the anomalous dispersion regime results in an increase in both the efficiency and the FWM bandwidth with pump power.

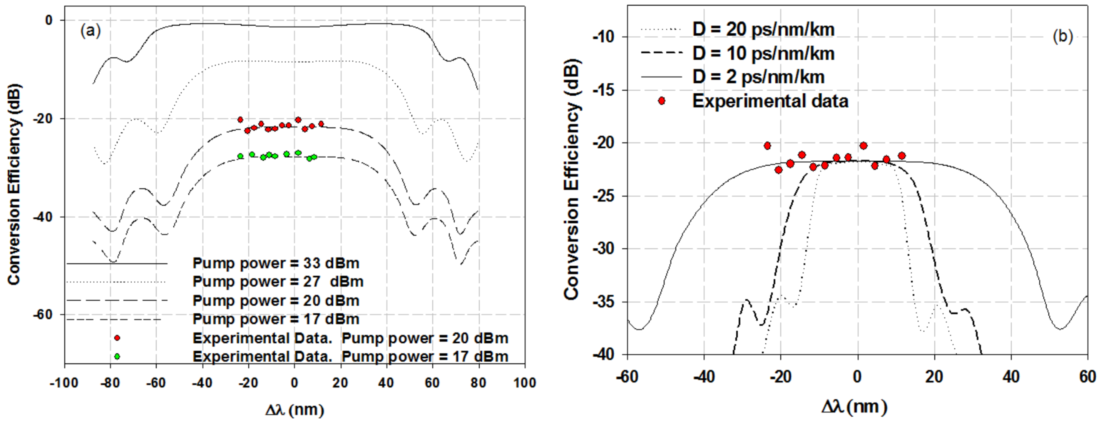

Figure 3.14: (a) Simulated and measured curves of the W-type fibre FWM conversion efficiency for various amounts of input pump power (b) Stimulated W-type fibre FWM conversion efficiency for various amounts of anomalous dispersion and a fixed dispersion slope of -0.017 ps/nm^2/km at 1563 nm . The experimental data obtained at 20 dBm input pump power is also shown.

To further highlight the good dispersion characteristics of the fibre, the effect of dispersion on the bandwidth of the conversion efficiency was numerically simulated and is shown in Figure 3.14b. The figure plots the FWM conversion efficiency in the W-fibre for various amounts of anomalous dispersion and a fixed dispersion slope of -0.017 ps/nm^2/km at 1563 nm and for a constant power (20 dBm of input pump power). As can be observed from the figure, the experimentally demonstrated broad conversion efficiency across 36 nm would not be achievable in fibres with dispersion of 10 ps/nm/km or 20 ps/nm/km at 1563 nm. The curves highlight that the full-width-half-maximum (FWHM) bandwidth reduces from 60 nm in the case of 2 ps/nm/km dispersion to just 20 nm in the case of 20 ps/nm/km. These results emphasise the importance of having a near-zero dispersion profile at the wavelengths of interest for applications requiring processing of wideband signals.

3.4 Conclusion

This chapter reported the theoretical and experimental work conducted on highly nonlinear lead silicate W-type fibres in the early stages of this PhD project.

The chapter opened with an introduction to lead silicate as a soft glass and discussed the advantages it possesses over silica and other optical soft glasses, which among others include a high nonlinear refractive index, a high SBS threshold and a ZDW that can be easily shifted towards the telecommunications wavelength.

The design process of the lead silicate fibres was explained in detail. This included a discussion on the process of engineering the dispersive properties of the fibre by studying the impact of its structural parameters on the waveguide and chromatic dispersion. The discussion was aided by numerical simulations solving the characteristic equation describing the mode propagation in optical fibres (following the model in [95]).

A fibre adopting a W-type index profile with a core diameter of 1.66 μm was fabricated using the rod-in-tube method. A 1.56 m sample of the fibre was spliced to SMF fibres and had its linear and nonlinear optical properties characterised at the telecommunications wavelengths. The characterisation measurements revealed that the fibre had a loss of 2.7 dB/m, a dispersion and dispersion slope of $\sim$2 ps/nm/km and -0.009 ps/nm^2/km respectively, a nonlinear coefficient of 820 /W/km and a SBS threshold of 30 dBm.

A FWM mixing experiment was carried out using this fibre sample, which demonstrated the benefits of the near-zero dispersion profile of the fibre at 1550 nm. A uniform FWM conversion efficiency of -21 dB across 36 nm was achieved for an input pump power of 20 dBm. Numerical analysis showed that this modest value of conversion efficiency can be increased to reach 0 dB by increasing the input pump power.

The lead silicate fibre sample that was used in this work represents the first generation of highly nonlinear lead silicate W-type fibre fabricated at the ORC. A second generation of fibres was fabricated with the aim to reduce the loss of the fibres towards the material loss figure of 1 dB/m. Chapter 4 will briefly report the optical characteristics of this new fibre generation along with its use for the demonstration of some all-optical signal processing applications.

Chapter 4

Phase Sensitive Amplification in Highly Nonlinear Lead Silicate W-type Fibres

4.1 Introduction

In the previous chapter, the optical characteristics of the lead silicate W-type fibre have highlighted the potential of this fibre technology for realising efficient and broadband nonlinear applications. This is made possible through two key traits: the high value of the fibre's effective nonlinearity coefficient and its low and flat dispersion profile. Such attributes lead to realising both strong net nonlinear effects in a very short length of fibre and achieving broadband nonlinear operation.

This chapter reports the work done towards exploiting these unique attributes in realising a broadband phase sensitive fibre optic parametric amplifier (PS-FOPA) in the lead silicate W-type fibre. As mentioned in Chapter 2, Section 2.2.2.2, parametric amplification can be attained through FWM by propagating a weak signal (probe) along with the higher power pump(s). This results in the amplification of the weak signal together with the generation of a new idler field. This form of fibre optic parametric amplifiers (FOPAs) is referred to as phase insensitive (PI) FOPAs. The presence of only the pump(s) and the signal at the input of an optical fibre make the direction of the power flow independent of the phase relation between the input fields. The signal in this case experiences gain regardless of its phase relative to that of the pump(s).

However, phase sensitivity can be achieved by a coherent interaction between the signal and any other participating field(s). Two different schemes exist, an interferometric scheme whereby the coherent interaction takes place between the signal and a pump residing at the same frequency [106, 107], and a FWM scheme whereby the coherent interaction occurs between the signal and an idler [108]. Both approaches result in a phase-dependent parametric gain of the signal, where power flow is a function of the relative phase between the participating input fields. The PS-FOPA configuration considered in this thesis is a non-interferometric (FWM-based) configuration and any reference to PS-FOPA hereon refers to this scheme.

Optical phase locking between the interacting waves can be achieved either through the use of an electro-optic modulator (EOM), generating multiple tones (sidebands) locked to the carrier [109], or through two FOPAs in cascade, producing a phase-locked idler wave in the first FOPA, and achieving phase sensitive amplification in the second [110]. Both schemes result in a fixed phase relationship between the participating input fields to the PSA.

Phase sensitive amplifiers (PSAs) have been known to offer additional advantages to those offered by their phase insensitive counterparts. The advantages include nearly noiseless amplification [111], reduction of phase and amplitude noise fluctuations [112] and elimination of modulation instability [113]. Furthermore, the advent of modulation formats which deploy the phase of the signal for data encoding such as differential phase shift keying (DPSK) and quaternary phase shift keying (QPSK), has led to an increased interest in applications utilising phase sensitive amplifiers. PSAs have been shown to efficiently regenerate DPSK [114] and QPSK [115] encoded signals, enabling the removal of phase jitter, a sub 3dB noise figure [116] and allowing multi-channel operation [117], all of which are attractive advantages in modern all-optical telecommunications systems.

The motivation behind realising a PSA in the W-type fibre stems from exploiting the low dispersion of the fibre in PSA-based processing applications of wideband signals. Moreover, the short length of the W-type fibre is also an added benefit, since it contributes to a more compact, stable and practical system, otherwise more difficult to realise with the typically longer silica fibres. PSA-based functions such as regeneration of phase shift keyed (PSK) signals can thus be realised in a broad wavelength range through the use of the lead silicate fibre.

This chapter begins by giving a brief background into phase sensitive amplifiers. It then proceeds to report the first PSA experiment conducted in the lead silicate W-type fibre, the parametric fluorescence (PF) experiment. The phase sensitive dynamic range (PSDR) of the fibre is also measured and the performance of the lead silicate fibre as a PSA is contrasted with another highly nonlinear soft glass fibre, namely a bismuth-oxide fibre.

In light of the results from these two experiments, a detailed numerical study is conducted to investigate how the performance of the lead silicate fibre can be improved. The study begins by contrasting the nonlinear performance of the first generation of lead silicate W-type fibres with a second generation which had reduced fibre losses. Furthermore, the study also investigates the effect of the fibre length on the nonlinear and dispersive performance and deduces the pump power requirement for achieving efficient phase regeneration.

Finally, the chapter presents a phase regeneration experiment conducted using the second generation of lead silicate W-type fibres. The experimental setup is discussed and the results of regenerating the phase of 40 Gb/s DPSK signals are presented.

4.2 Phase Sensitive Amplification - Background

The four coupled FWM differential equations (Equations 2.20- 2.23) describing the power flow of the pump, signal and idler fields indicate that FWM can be a phase sensitive process [118]. Indeed, solutions for this system of equations have been widely studied in literature [119, 120] and the signal gain of a non-degenerate FOPA can be expressed as [121]:

$$G_s = 1 + 2\sinh^2(\gamma P L_{eff}) + 2\sinh(\gamma P L_{eff})\cosh(\gamma P L_{eff})\sin(\theta) \tag{4.1}$$

where P is the pump power and γ and L_{eff} are the fibre's nonlinear coefficient and effective length respectively. θ is relative phase between the three input fields defined as [122, 123]:

$$\theta = \kappa + \phi_s(0) + \phi_i(0) - 2\phi_p(0) \tag{4.2}$$

Where $\phi_s(0)$, $\phi_i(0)$ and $\phi_p(0)$ refer to the initial phase (i.e at $z = 0$) of the signal, idler and pump respectively, and κ is the phase mismatch between the three optical fields.

Equation 4.1 for the signal gain, assumes a perfectly phase matched FOPA. i.e.:

$$\kappa = \Delta\beta = [\Delta\beta]_L + [\Delta\beta]_{NL} = 0 \tag{4.3}$$

The relative phase θ then becomes:

$$\theta = \phi_s(0) + \phi_i(0) - 2\phi_p(0) \tag{4.4}$$

Equation 4.1 indicates that if an idler is present at the input of a FOPA, the parametric gain of the signal becomes phase-dependent. Power flow in this case is a function of the relative phase between the three input fields defined in Equation 4.4, and can either flow from the pump to the signal and idler in the case of $\theta = \pi/2$, resulting in parametric

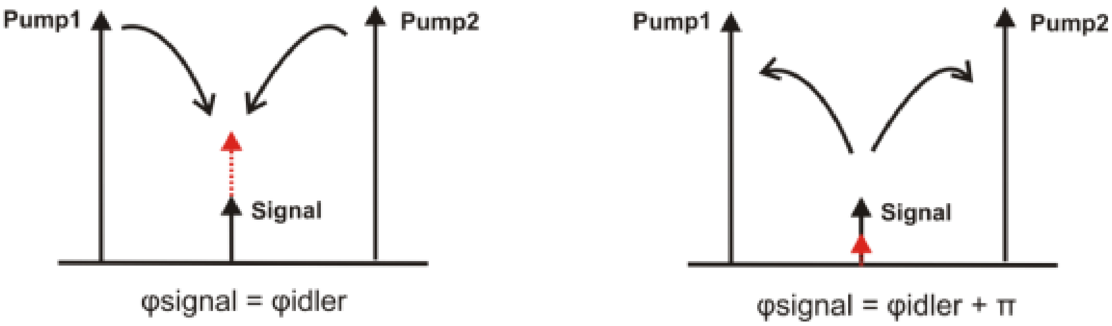

Figure 4.1: Illustration of power - phase relationship in a 2-pump degenerate PSA. Left: the power flows from the pumps to the signal resulting in parametric amplification. Right: the power flows from the signal to the pumps resulting in parametric attenuation.

amplification, or in the case of $\theta = -\pi/2$ from the signal and idler to the pump resulting in parametric attenuation (de-amplification)[122].

In the case of the absence of an idler field from the input of the FOPA, an idler will be generated with a phase ϕ_i:

$$\phi_i = 2\phi_p - \phi_s \tag{4.5}$$

Substituting Equation 4.5 into the relative phase relation (Equation 4.4) results in $\theta = 0$ and subsequently a signal gain G_s of:

$$G_s = 1 + 2\sinh^2(\gamma P L_{eff}) \tag{4.6}$$

Clearly Equation 4.6 shows that the signal gain in this case is phase-independent and the amplifier is a phase insensitive amplifier (PIA). Furthermore, the PI signal gain is 6 dB smaller than in the PS-FOPA phase-adjusted for maximum gain (i.e. with $\theta = \pi/2$) [121, 110].

Although the analysis outlined above corresponds to a single pump non-degenerate PSA, the same principles apply for the two-pump degenerate PSA scheme. Figure 4.1 illustrates the power transfer in this case, where the power can either flow from the two pumps to the signal resulting in parametric amplication (Figure 4.1 (left)), or from the signal to the pumps resulting in parametric attenuation (de-amplification) (Figure 4.1 (right)).

This gain-phase relationship of a PSA results in the amplification of the in-phase component of the signal and the attenuation of its quadrature component. Figure 4.2 depicts this effect, which manifests itself in the 'squeezing' of the signal phase and can thus be exploited in the reduction of the phase noise in phase-encoded signals. The extinction

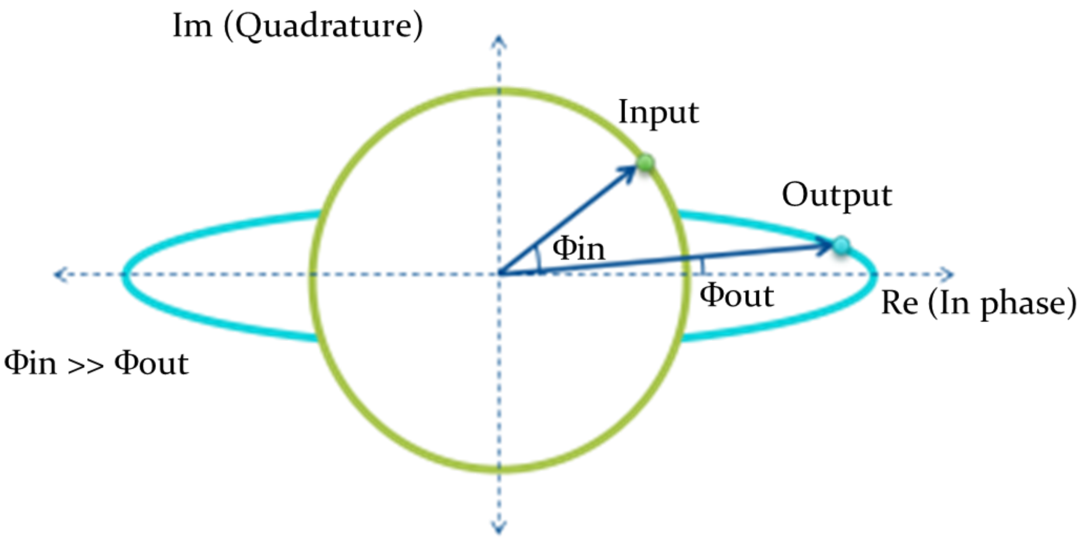

Figure 4.2: Impact of phase sensitive amplification on the phase of the signal.

ratio of maximal PSA amplification and maximal attenuation determines the amplifier's phase squeezing ability and is termed as the PSA swing or the phase sensitive dynamic range (PSDR). Nonlinear phase noise can impose severe performance limitations for systems utilising both the amplitude and phase of the optical carrier. PSA-based regenerators have been studied intensively in recent years and there have been numerous demonstrations of their effectiveness in removing both phase and amplitude noise from phase-encoded optical signals [124, 125, 126, 115].

4.3 Phase Sensitive Amplification Experiments

4.3.1 Parametric Fluorescence Experiment

In order to verify that PS operation could be achieved in the lead-silicate W-type fibre, a single-pump PS parametric fluorescence (PF) experiment was conducted. This experiment involves cascading two FOPAs. An amplified spontaneous emission (ASE) signal is launched into the first FOPA which acts as a phase insensitive amplifier (PIA). The parametrically amplified ASE from the PIA stage is then launched into the second FOPA, which provides phase sensitive amplification. The dispersive effects between the PIA and the PSA segments result in a wavelength-dependent phase modulation, thus enabling the observation of the gain-phase relationship of the PSA. The setup of this experiment is shown in Figure 4.3. The PIA consisted of a single CW laser pump operating at 1565 nm which was amplified before being launched to a 300-m long HNLF with a nonlinear coefficient of 11.6 /W/km, a zero dispersion wavelength (ZDW) of 1553 nm and a dispersion slope (DS) of 0.018 ps/nm^2/km. A strain gradient had been applied to

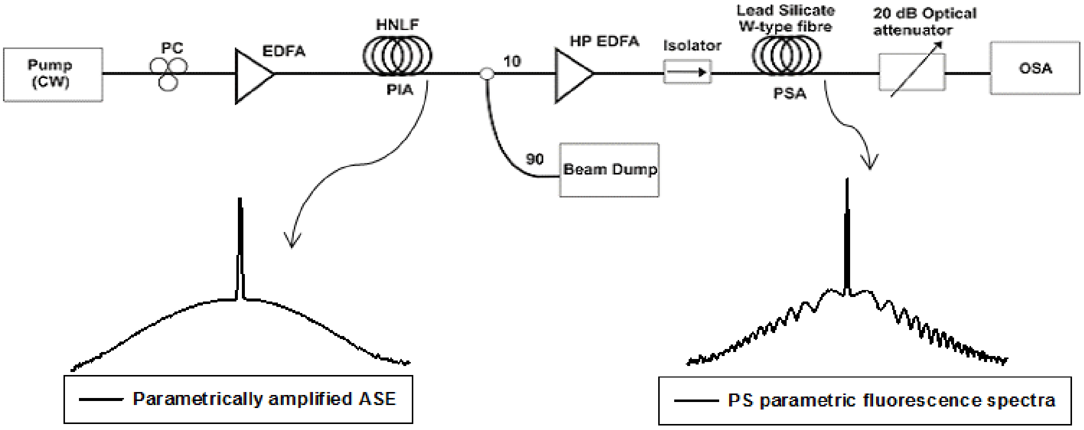

Figure 4.3: Experimental setup of the PS parametric fluorescence conducted in the W-fibre. Insets show spectra at the output of the PIA (left) and the PSA (right).

the HNLF to increase its SBS threshold to ∼26 dBm. The ASE of the amplifier experienced approximately 3 dB of parametric gain at the output of the HNLF, thus forming a ∼30 nm wide relative-phase stabilised signal. Both pump and ASE were amplified by another EDFA and were launched to the fibre under test.

Figure 4.4a shows the spectrum measured at the output of the PSA. The wavelength dependent phase mismatch resulting from the dispersive elements prior to the PSA gives rise to the characteristic gain peaks and attenuation troughs in the form of ripples, a clear sign of PS behaviour [127]. Owing to the low dispersion of the fibre across this whole wavelength range, the gain spectrum extends across the full 30 nm available bandwidth of the ASE. Furthermore, this result was benchmarked against a second sample of soft glass fibre of a similar length. This was a bismuth oxide fibre of a similar type to that

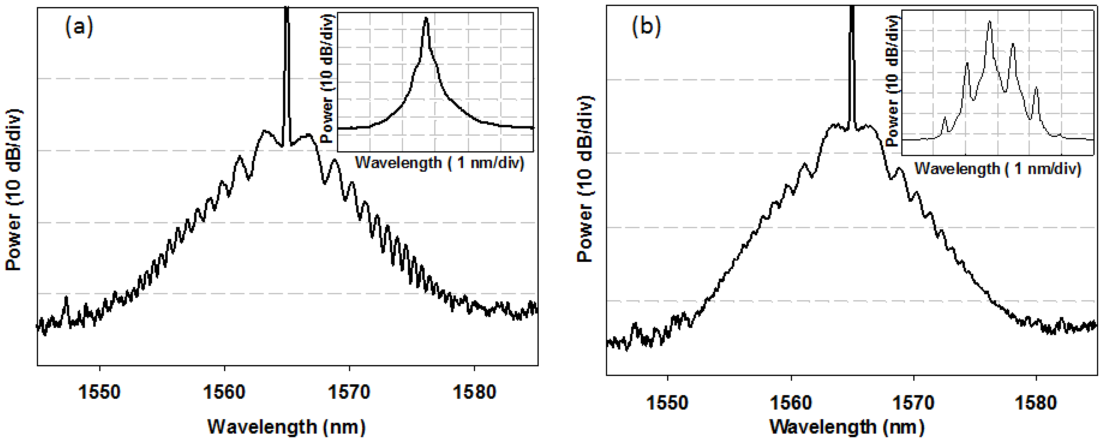

Figure 4.4: Spectral traces of PS parametric fluorescence in (a) the 1.56 m lead silicate fibre and (b) a 2 m long bismuth oxide fibre (resolution bandwidth (RB) = 0.06nm). Insets show zoomed-in traces of the output pump spectrum (P = 27.7 dBm) for the two cases (RB = 0.01nm).

previously used for an earlier PSA demonstration in [128]. The sample was 2 m long and had a loss of 0.9 dB/m, a nonlinear coefficient of 1100 /W/km, and a dispersion of -260 ps/nm/km at 1550 nm. This sample was spliced to silica pigtails at both ends and the splice losses were estimated to be about 3 dB per splice. Figure 4.4b shows the spectrum obtained at the output of this fibre. PS gain is also observed in this case, however its bandwidth is restricted to a much narrower spectral region, due to the higher dispersion of this fibre. Quantitatively, the 3-dB PSDR bandwidth, defined as the bandwidth over which the PSDR drops by 3 dB relative to its maximum value, could be measured directly from these spectral traces and was found to extend for 19 nm in the case of the lead silicate W-type fibre, while it was limited to only 7.4 nm in the case of the bismuth oxide fibre. In addition, the insets to the two graphs show spectral traces in the vicinity of the pump wavelengths for the same input power (approximately 28 dBm). The onset of SBS can already be clearly seen in the case of the bismuth fibre whereas there is no evidence of SBS in the lead-silicate fibre, where even higher pump powers could be used without evidence of SBS (note however, the small difference in length between the two samples).

4.3.2 Phase Sensitive Dynamic Range Measurement

A two-pump degenerate PSA was set up in order to measure the phase sensitive dynamic range achieved with the lead-silicate fibre (Figure 4.5). The scheme used in this

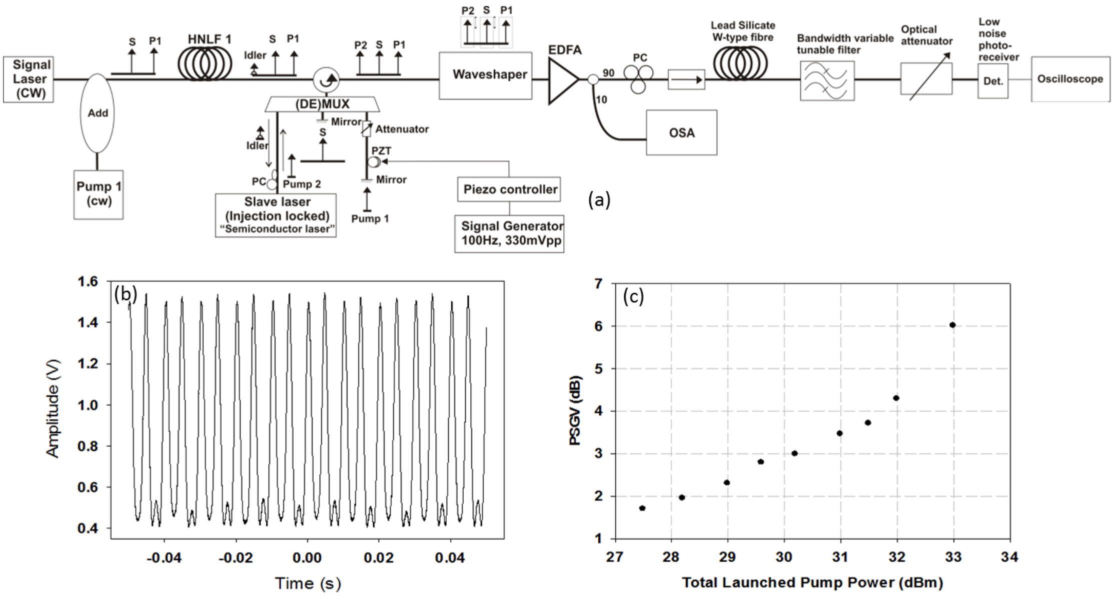

Figure 4.5: (a) The experimental setup of the PSDR characterisation experiment. PC: Polarisation controller. EDFA: Erbium-doped fibre amplifier. OSA: Optical spectrum Analyser. (b) An example trace of the voltage swing detected by the photo-receiver shown by the oscilloscope from which the PSDR is determined and (c) the measured PSDR (dB) as a function of increasing launched pump power (dBm).

experiment was based on a black-box PSA developed by R.Slavík et al. [129]. The first stage of the setup consisted of a PIA stage which was configured to ensure phase-locking between the two pumps and the signal and allow control of their relative powers. This was done by coupling one pump (pump 1) and the signal from two independent CW lasers into a HNLF, resulting in the generation of a new idler field. The weak idler was then used to injection-lock a slave semiconductor laser (pump 2), boosting the power level at this wavelength to that of the pump and the signal. The three optical fields were then fed into a programmable optical filter (Finisar Waveshaper), allowing careful adjustment of their power levels, to ensure that the powers of the two pumps were equalised throughout the experiment and the signal power remained fixed at a certain level (6 dBm). The pumps and the signal were then amplified through a high power EDFA, and their power levels were monitored on an optical spectrum analyser (OSA) connected to the output of a tap coupler. The amplified beams were fed through a polarisation controller and an isolator at the input of the lead silicate W-type fibre (PSA segment). The output of the PSA was subsequently filtered using a bandpass filter, rejecting the two pumps while keeping the signal. A piezo-electric transducer (PZT) driven by a 100 Hz signal generator was connected to pump 1 and periodically changed the phase of this field relative to pump 2 and the signal, thereby ultimately causing the PSA to swing between maximum gain and maximum attenuation. An oscilloscope was used at the output of the system to detect the effect of the PSA swing on the signal (Figure 4.5b). The PSDR was measured as the total input pump power into the fibre was varied from 22.2 dBm to 27.7 dBm. Figure 4.5c shows the measured PSDR of the lead silicate fibre as a function of the total launched pump power. A maximum PSDR of 6 dB was measured for an input pump power of 27.7 dBm (the maximum that could reliably be launched from the available amplifiers).

4.3.3 Optimisation Study – Enhancing the Nonlinear Performance of the W-type Fibre

While the wideband gain spectrum demonstrated in the first experiment has highlighted the benefits of the flat near-zero dispersion profile of the W-type fibre with respect to a PSA configuration, only a moderate PSDR value of 6 dB could be achieved with the available power.

The splice losses ultimately impose a limit on the maximum amount of power that can be launched into the fibre, thus limiting the performance of the fibre for several nonlinear applications. Generally, splice loss values in the range of 3.5-7 dB have been attained when attempting a splice between the small core lead silicate fibre and a SMF. With this limitation in mind, it is important to investigate ways to both reduce these values and also marginally overcome the performance cap placed by these losses through the use of longer/lower loss fibre samples since both the fibre length L and its propagation loss

Property	LSW1	LSW2
Nonlinear Coefficient	820 /W/Km	820 /W/km
Loss	2.7 dB/m	2.1 dB/m
Dispersion @ 1550 nm	2 ps/nm/km	-0.8 ps/nm/km
Effective Area	1.9 μm^2	1.9 μm^2
SBS Threshold	30 dBm	>30 dBm

Table 4.1: Optical properties of the first (LSW1) and second (LSW2) lead silicate W-type fibre generations.

α are incorporated in the γL_{eff} figure-of-merit (FOM) commonly used to benchmark the nonlinear performance of HNLFs [130]. Complex experiments such as phase/amplitude regeneration require careful experimental design, and it is usually of preference to use moderate amounts of power to minimise the risk to the various apparatus involved (through e.g. undesirable effects, such as fibre fuse). With this in mind, this section conducts a numerical study that attempts to highlight how a sample of optimum length and a lower propagation loss can enhance the nonlinear FOM without the need to prohibitively increase launch power levels to overcome splice losses.

A second generation of highly nonlinear lead silicate fibres was fabricated with the aim to reduce its loss. The characterisation of this new fibre generation was carried out by Dr. A. Camerlingo and the measurements revealed that a propagation loss value of 2.1 dB/m (improvement of 0.6 dB on the first generation of fibres) was achieved in the fabrication. The study that follows in this chapter, contrasts the performance of the two lead silicate W-type fibre generations of different propagation losses and also highlights the role that the sample length plays in enhancing the nonlinear FOM.

The two fibre generations are referred to in this study using the name codes that they

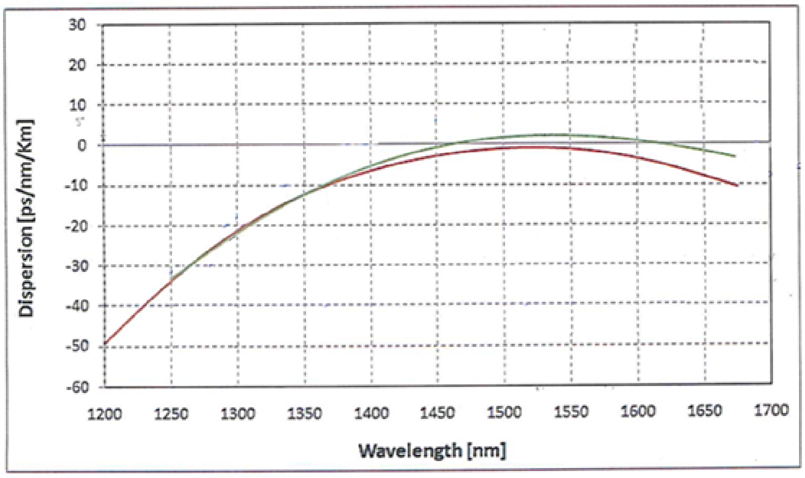

Figure 4.6: Measured chromatic dispersion curves of fibre LSW1 (green curve) and LSW2 (red curve) (courtesy of Dr. Giorgio Ponzo).

were given during the fabrication stage (LSWX). Fibre LSW1 represents the first generation of lead silicate fibres that had been used in the experiments of the previous sections and in Chapter 3, while fibre LSW2 represents the second generation with improved losses. Table 4.1 compares the optical properties of the two fibre samples used in the study, while Figure 4.6 compares their dispersion profiles. The second generation sample possesses very similar characteristics to that of the first generation with the main difference, beside the loss, being the dispersive characteristics. Indeed, the second generation of lead silicate fibres exhibits normal dispersion at 1550 nm, in contrast to the first generation which exhibits anomalous dispersion at the same wavelength.

The scope of the study includes the following:

- Comparison between the effective lengths of the two fibre generations
- FWM conversion efficiency vs. Fibre length
- FWM 3 dB bandwidth vs. Fibre length
- PSDR vs. Fibre length/pump power

4.3.3.1 Effective Length

The effective length of an optical fibre is given by (see Section 2.2.2.2):

$$L_{eff} = \frac{1 - \exp(-\alpha L)}{\alpha} \tag{4.7}$$

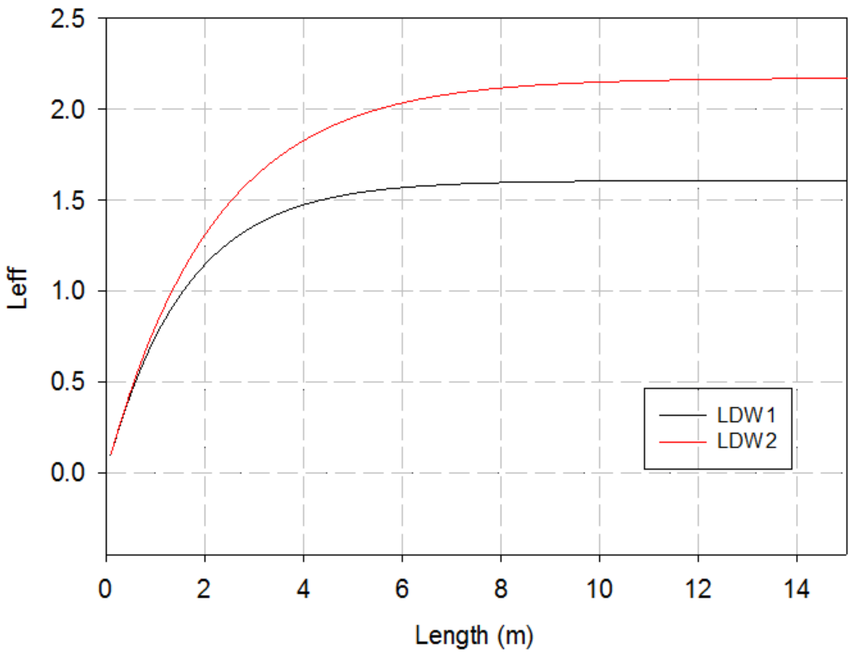

Figure 4.7: L_{eff} vs Length for the two lead silicate W-type fibre generations.

Where L and α refer to the fibre length and its propagation loss respectively. The two fibres under study have slightly different maximum effective lengths as can be seen in Figure 4.7. The lower loss of fibre LSW2 (2.1 dB/m) in comparison to that of LSW1 (2.7 dB/m) dictates that longer lengths of the former can be used before reaching the limit of $L_{eff-max} = 1/\alpha$. Indeed, approximately, 7 meters of LSW2 fibre can be used in contrast to only 5 meters to that of LSW1 before reaching the maximum effective length values of the two fibres. This results in approximately 30% improvement in the γL_{eff} FOM.

4.3.3.2 Four Wave Mixing Conversion Efficiency/Bandwidth

To further study the effect of the W-type fibre length on the nonlinear performance, a FWM numerical study was conducted. The FWM configuration used in the study was identical to that described in Figure 3.13, with a pump power value of 30 dBm and a signal power of 10 dBm. Plots of the FWM conversion efficiency vs. wavelength detuning for different fibre lengths are shown in Figure 4.8. The figures lay emphasis on

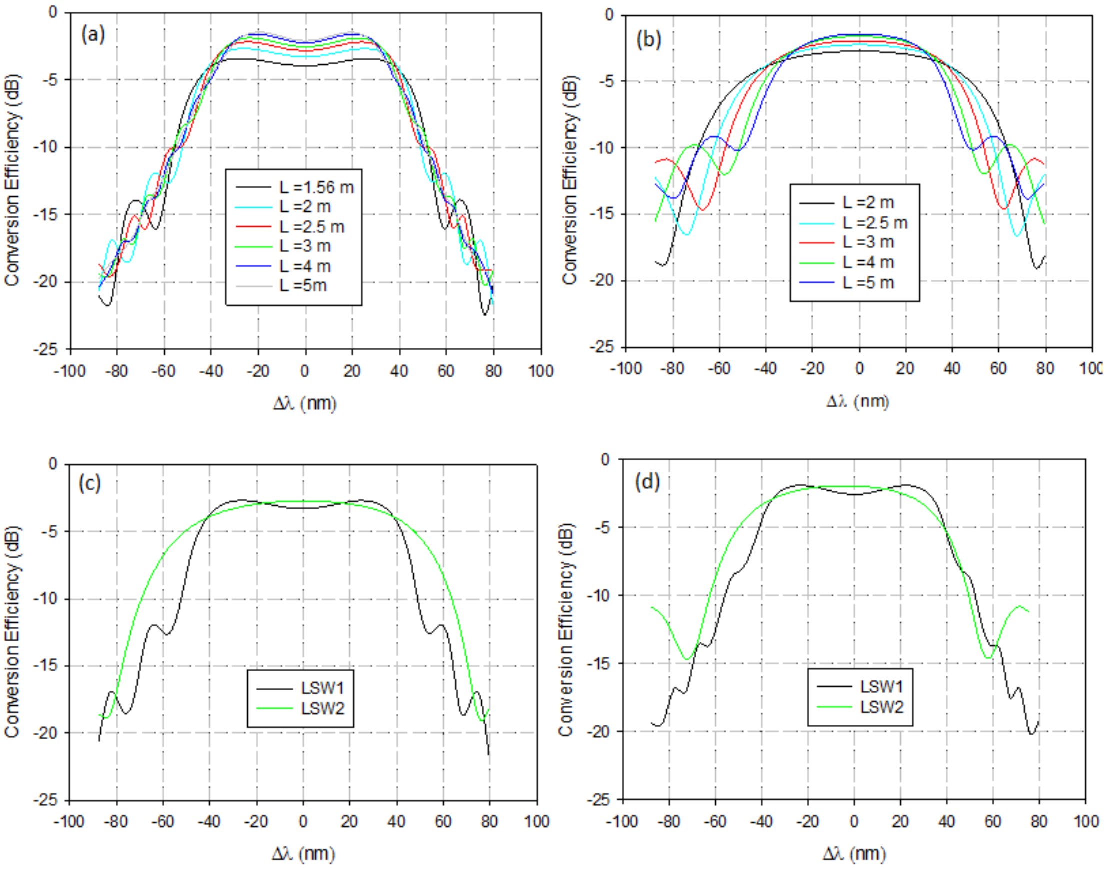

Figure 4.8: FWM conversion efficiency plots for different fibre lengths in two different lead silicate fibre generations (LSW1 (a) and LSW2 (b)). Comparison of FWM conversion efficiency for two different lead silicate fibre generations (LSW1 and LSW2) (c) sample length is 2 m, (d) sample length is 3 m.

how the FWM conversion efficiency and the 3-dB FWM bandwidth are affected by the length of the two W-type fibre generations (Figure 4.8a shows LSW1 while Figure 4.8b shows LSW2). While a more efficient FWM process can be achieved for longer lengths of fibre, the FWM 3-dB bandwidth of the fibres is adversely affected. The LSW2 samples have normal dispersion value at 1550 nm in contrast to the LSW1 family which exhibit anomalous dispersion at the same wavelength. The anomalous dispersion nature of the LSW1 fibre results in a 'dip' in the middle (close to the pump wavelength) of the FWM gain profile that is characteristic of anomalous fibres, and is often undesired in broadband applications. In contrast, the normal dispersion of the LSW2 family offers a smoother FWM gain profile, while its lower net dispersion values result in slightly broader 3-dB FWM bandwidth, as shown in Figure 4.8c and Figure 4.8d.

To help choose the optimum length of fibre for broadband nonlinear applications, Figures 4.9(a)-(d) plot the FWM conversion efficiency, a comparison between the idler/signal power levels and the FWM 3-dB bandwidth of the two W-type fibre families for different lengths of fibre. Note that the FWM conversion efficiency (Figure 4.9a) improvement attained when using a LDW2 sample of propagation loss of 2.1 dB/m as opposed to a LDW1 sample with 2.7 dB/m is too small to constitute a real advantage when comparing

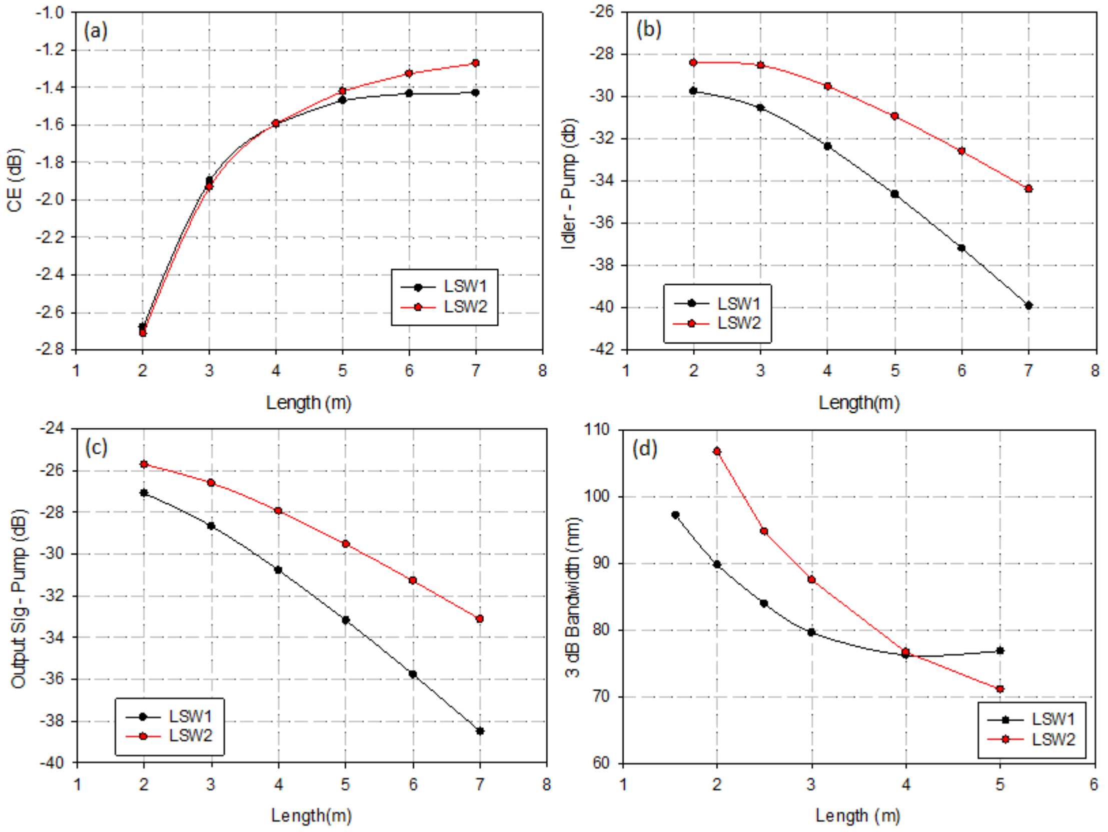

Figure 4.9: (a) Conversion efficiency vs fibre length (b) plot of difference between the idler and pump power levels vs fibre length (c) plot of difference between the output signal and pump power levels vs fibre length (d) FWM 3-dB bandwidth vs fibre length for the two fibre generations (LSW1 (black) and LSW2 (red))

two same length fibres. However, the lower loss of the LSW2 sample results in the generation of a stronger idler (Figure 4.9b) and a more significant output signal (Figure 4.9c). Furthermore, the lower dispersion of the LSW2 family gives rise to larger FWM 3-dB bandwidths for fibre lengths shorter than 4 meters (Figure 4.9d).

Since a trade-off between the FWM conversion efficiency and the FWM bandwidth need to be taken into account when choosing the sample length, it is deemed appropriate to opt for a 3 meter sample of fibre LSW2, since this represents a significant improvement in the nonlinear FOM when compared to the 1.56 m sample of fibre LSW1 that had been used experimentally, while also resulting in a broadband nonlinear performance.

4.3.3.3 Phase Sensitive Dynamic Range

The phase sensitive dynamic range (also called PSA swing [127]) of a phase sensitive amplifier is often used as a figure of merit for the amplifier's phase regenerative capability. It determines how the amplifier performs as a phase squeezing device and as a tool for removing phase noise from phase encoded signals.

To further understand the potential of this fibre technology, the PSDR of a LSW2 lead silicate fibre sample with parameters optimised for the application (i.e. 3 m long sample of 2.1 dB/m loss, as deduced above) was simulated numerically. The simulations were based on a 2-pump degenerate PSA and followed closely the experimental parameters presented in Section 4.3.2.

The results of this numerical study are shown in Figure 4.10a and Figure 4.10b (black curves). To put the 6 dB PSDR value experimentally obtained from using the 1.56 m LSW1 sample (Section 4.3.2) into perspective, Figure 4.10b shows a graph of the PSA phase transfer function for different values of PSDR. As the PSDR value increases from 0

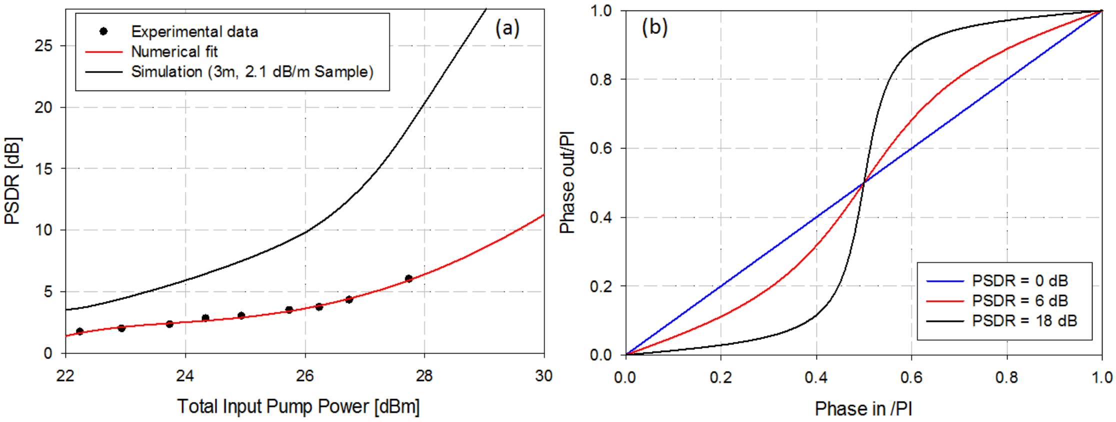

Figure 4.10: (a) Measured/simulated PSDR (dB) as a function of increasing input pump power (dBm) (b) A plot of PSA phase transfer function for different values of PSDR.

dB, the phase transfer function starts to depart from the linear to the nonlinear regime, and a moderate phase squeezing effect can be observed for a value of 6 dB PSDR (red curve).

The simulations show the margin of improvement in the PSDR of the amplifier achievable using the proposed fibre sample. Figure 4.10a shows that for identical input power levels to those used in the experiment, a value of approximately 18 dB PSDR for an input pump power of 27.7 dBm would be achievable using the proposed optimised sample. This value should still be below the SBS threshold for this sample, which is estimated (following a similar analysis to that presented in Chapter 3, Section 3.2.5.2) that it would tolerate at least 32 dBm of total power at the two pump wavelengths. Furthermore, this value of PSDR can be contrasted with the 6 dB value achieved experimentally (red curve) by comparing the plots of the phase transfer function in Figure 4.10b. Higher PSDR values push the transfer function towards the idealised staircase shaped function. Indeed for a value of 18 dB PSDR, one could already see the nearly digitised nature of the phase transfer function, where for almost all values of input phase, the output phase is restricted to values close to either 0 or π.

The conclusions from the numerical study presented in this section were fed back to the fibre fabrication team at the ORC in order to prepare a LSW2 sample with the required length (i.e. 3 m). However, only 1.7 m of lead silicate fibre had remained after fibre splicing to an SMF for the planned regeneration experiment, and an estimated splice loss of 6-6.5 dB was achieved. Due to the high splice losses of the LSW2 sample and its relatively short length, it was subject to similar power requirements to those associated with using the LSW1 sample which were deduced in Figure 4.10. The level of power required to achieve a PSDR $>$ 10 dB was deemed excessively high due to the high splice losses of the fibre.

The 1.7 m LSW2 sample was used in the phase regeneration experiment of 40 Gb/s DPSK signals, presented in the subsequent section. The high splice losses of the sample necessitated gating (modulating) the pumps and the signal of the regenerator so that the required peak power level can be achieved without increasing the average power to such prohibitive levels.

4.3.4 Phase Regeneration of 40 Gb/s DPSK Signals in a Highly Nonlinear Lead-Silicate W-type fibre

4.3.4.1 Introduction

Conducting a phase regeneration experiment of differential phase shift keying (DPSK) data signals in a short length of highly nonlinear lead silicate W-type fibre represents an important demonstration of what this novel soft glass fibre technology can achieve in the field of broadband all-optical signal processing. Furthermore, such an experiment also represents a great tool in further investigating the limitations of and exploring the main challenges associated with advancing this fibre technology further. Through this experiment, the practical advantages associated with some of the fibre's unique properties, such as its novel dispersion characteristics and short length have again been highlighted, while shortcomings such as the high splice losses of the fibre have also been underlined. For instance, one of the implications associated with having high splice losses, is the necessity of operating the regenerator in a burst mode to avoid the need for excessive CW pump power levels, as was concluded in the numerical study presented in Section 4.3.3.3.

The following subsection presents the phase regeneration of 40 Gb/s DPSK signals in a 1.7 m of second generation (LSW2) lead-silicate fibre. The experimental setup, based on a 2-pump degenerate PSA scheme, is discussed in detail. Furthermore, the performance of the system was assessed by comparing constellation diagrams of the data signal before and after regeneration for various levels of phase noise.

4.3.4.2 Experimental Setup and Results

The regeneration experiment was based on a degenerate two-pump phase sensitive amplifier (2P-PSA) configuration, the setup of which is shown in Figure 4.11. The data signal was a 40 Gb/s non-return-to-zero DPSK 2^{31}-1 pseudo-random bit sequence (PRBS) centered at a wavelength of 1555.64 nm. To emulate the effects of broadband phase-only noise, the phase noise generation setup of Figure 4.12 was used [131]. The signal was combined with narrowband (3-dB bandwidth of 1 nm) amplified spontaneous emission (ASE) with a Gaussian spectral profile centered at 1562 nm and launched into an HNLF. The ASE induced cross phase modulation (XPM) on the signal, thereby introducing broadband incoherent phase noise to it [131]. The inset of Figure 4.12 shows the XPM-induced spectral broadening of the signal with traces displayed before (black) and after (red) the HNLF. The magnitude of the phase perturbations was controlled by varying the corresponding power levels of the ASE noise. The distorted signal was then filtered and launched into the PSA regenerator, which was set up following a black-box configuration (for a detailed presentation, please refer to [124]). At the input of the regenerator, the signal was coupled with a continuous wave signal (Pump 1) operating at a wavelength of 1557.36 nm through an add/drop multiplexer. The data signal (acting as a pump here) and the CW signal were launched into a HNLF to generate a new phase-locked and modulation-free idler wave at 1553.9 nm. The HNLF used had a length of 300 m, a dispersion of - 0.01 ps/nm/km at 1550 nm, a nonlinear coefficient of 10.5 /W/km, and an insertion loss of 0.9 dB. The weak idler was then used to injection-lock a slave semiconductor laser (Pump 2) [129]. The three phase-locked optical fields were gated in time through a Mach-Zehnder modulator driven by 400 ns rectangular pulses

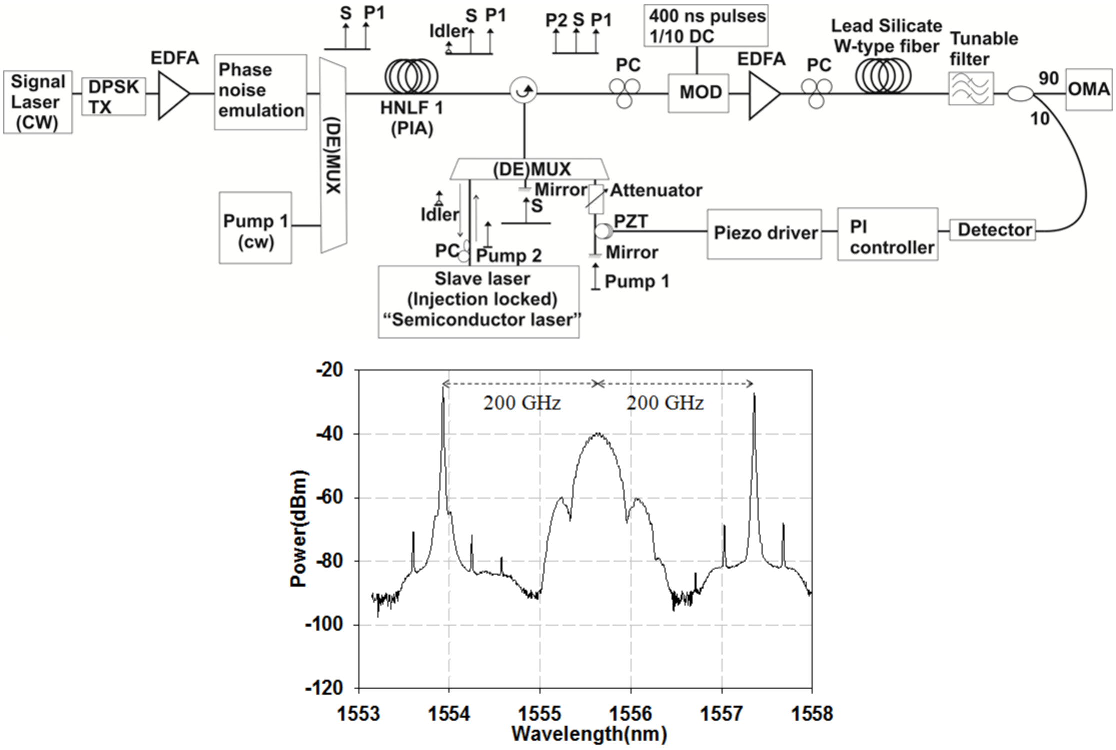

Figure 4.11: Top: Experimental setup of the 40Gb/s phase regenerator. Bottom: spectral trace at the input of the PSA. EDFA: Erbium Doped fibre Amplifier, MOD: modulator, PC: Polarisation controller.

with a duty cycle of 1:10. Time gating provided a means to increase the peak power of the pumps and signal by a factor of ten whilst retaining the same average power, so as to overcome the splice losses of the lead-silicate fibre that followed, without the need for excessive EDFA average power. This signal arrangement now formed the two pumps and signal required in a degenerate PS-FOPA (see inset to Figure 4.11). The three waves were amplified through a high power EDFA to a total power of approximately 31 dBm, before being fed through a polarisation controller and an isolator to the lead silicate

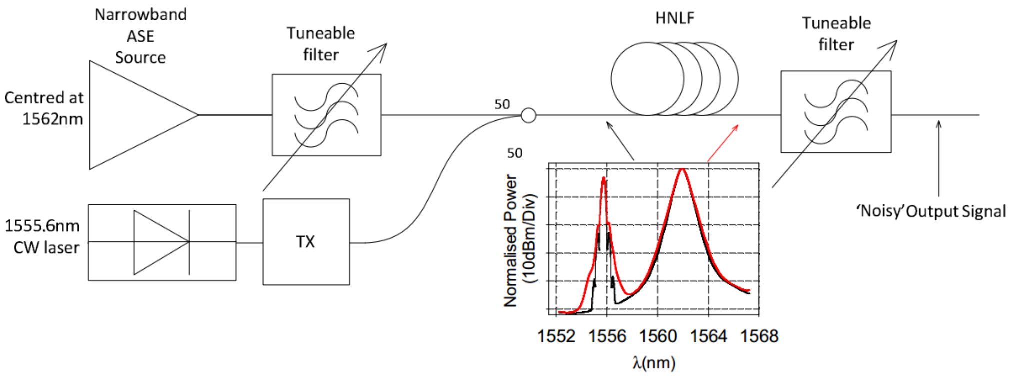

Figure 4.12: Experimental setup of the all-optical XPM-based phase noise emulator. Inset: Optical spectra of the DPSK signal and ASE pump at the input (black) and output (red) of the HNLF (courtasy of Mr. Liam Jones [131]).

W-type fibre where PS amplification was realised. The 1.7 m LSW2 sample which had a nonlinear coefficient of 820 /W/km, a propagation loss of 2.1 dB/m and a dispersion of -0.8 ps/nm/km at 1550 nm, was used as the PSA segment of the regenerator. At the output of the PSA, the signal was filtered to reject the two pumps. Part of the data signal was tapped-off to be used as the feedback in the phase locking portion of the setup and to compensate for any slow (sub-kilohertz) relative phase drifts between the three interacting waves. It consisted of an optical detector, a proportional integral controller and a piezo-electric transducer fibre stretcher located in the path of one of the pumps. The short length of the soft glass fibre contributed to a reduced acoustic pick-up relative to systems based on silica-based fibres (e.g. [124, 129]) and resulted in more stable locking of the feedback circuit. At the output of the regenerator, the data signal was characterised using an optical modulation analyser (OMA), consisting of an optical coherent detector and a real-time data acquisition system.

The relative power of the signal with respect to the pumps was adjusted to ensure optimal phase noise suppression with minimal amplitude degradation, which was achieved when the PSA operated in saturation. In this operating regime, a total phase-sensitive gain variation of approximately 4.5 dB was measured (this is to be contrasted to 14 dB which was measured when the PSA was not saturated). Higher order FWM products were observed at the output of the PSA owing to the low and flat dispersion characteristics of the W-type fibre (Figure 4.13).

Figure 4.14 presents constellation diagrams of the data signal before and after the regenerator for different noise levels. The signal was first assessed with no added noise, showing similar performance both before and after the regenerator (Figure 4.14a). With

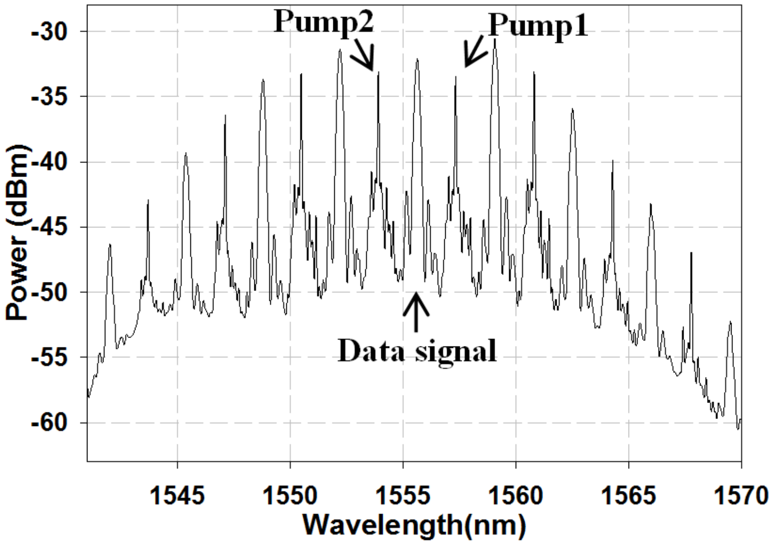

Figure 4.13: Spectral trace at the output of the PSA, showing the signal, the pumps and high-order FWM products.

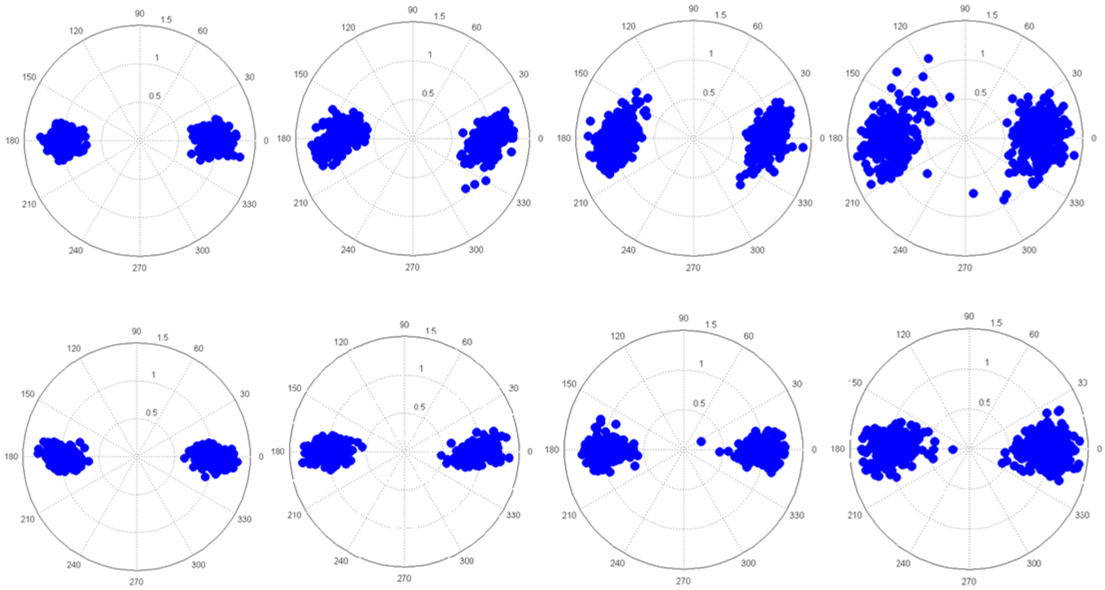

(a) (b) (c) (d)

Figure 4.14: (a)-(d) Constellation diagrams of the DPSK signal before (top) and after (bottom) regeneration for various noise levels. (a) represents the case of no added noise.

mainly phase noise added to the signal (Figure 4.14(b-d)), the constellation diagrams display a clear level of noise squeezing with negligible additional amplitude noise.

Furthermore, since Figure 4.14 only conveys the instantaneous regeneration capability of the PSA (i.e. during a single burst of the data signal), a set of accumulative constellation readings plotted as colour graded constellations were also taken and are displayed in Figure 4.15. The constellations represent the data gathered in 30 million consecutive bursts of data signals and thus convey a more representative measure of the regenerator

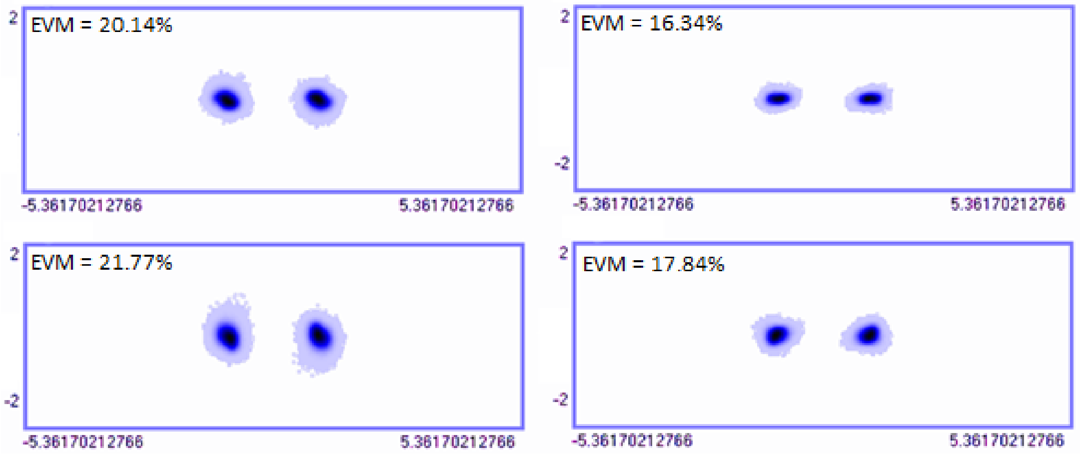

Figure 4.15: (colour graded DPSK constellation diagrams showing amplitude and phase changes before (left) and after (right) regeneration for two different noise levels. The constellations represent the data gathered in 30 million consecutive bursts of data signals.

long-term performance. Again, the figure shows a high degree of phase squeezing of the data signal for both noise levels.

To better quantify the level of improvement achieved in the signal quality, Figure 4.16 shows the root mean square (rms) error vector magnitude (EVM), the phase error and the rms magnitude error of the data signal before and after regeneration. Again the no-added-noise case (the leftmost data point in the graphs) shows almost no penalty due to the presence of the regenerator, and a universal improvement in the EVM of the data signal is observed for all the different noise levels examined. Figure 4.16b shows that the level of phase error is reduced by about a factor of 2 for all of the cases that we examined, confirming the regenerator capability for reducing phase noise. A slight (effectively negligible) deterioration in the magnitude error of the regenerated signals is observed in Figure 4.16c, mainly due to the phase-to-amplitude noise transformation occurring in the PSA.

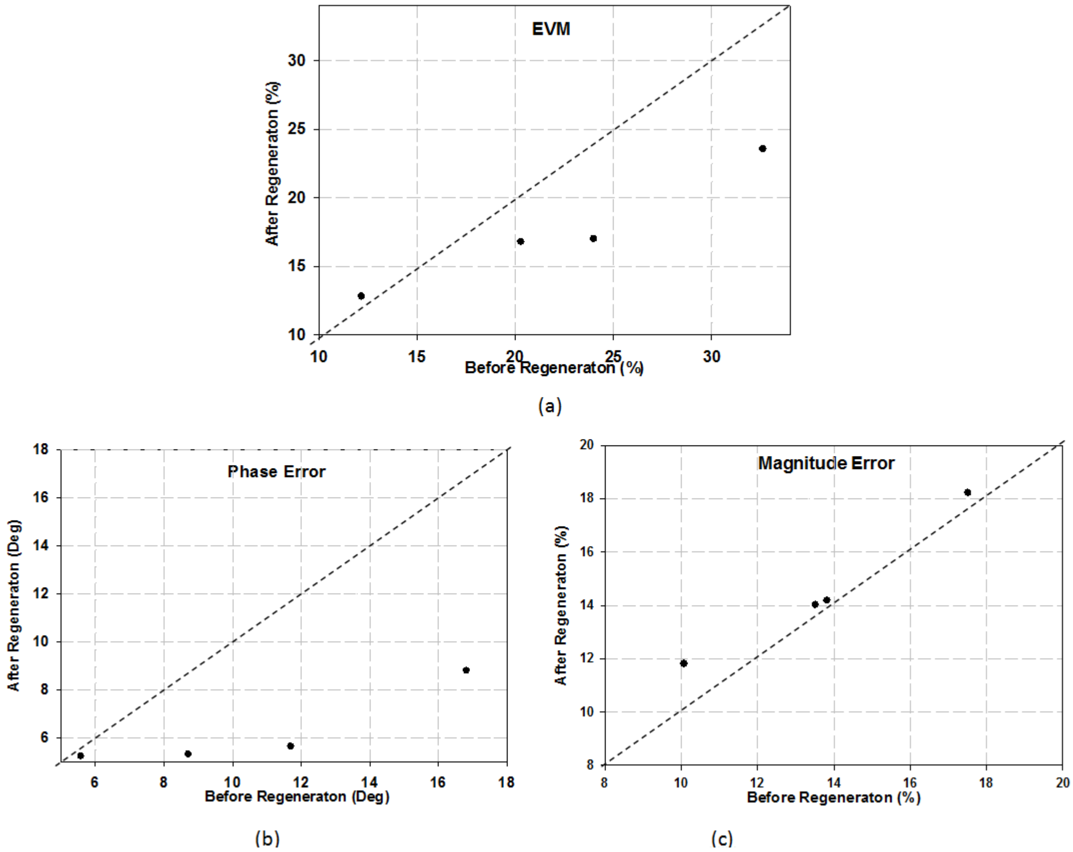

Figure 4.16: Plots of (a) EVM (b) phase and (c) magnitude error of the data signal before and after regeneration.

4.4 Conclusion

This chapter reported the phase sensitive amplification experiments conducted in highly nonlinear lead silicate fibres. The chapter opened by giving a brief background into the operation of phase sensitive fibre optic parametric amplifiers and then proceeded to discuss the PSA-based experiments.

The first experiment demonstrating PS amplification in a length of W-type lead silicate fibre was a parametric fluorescence experiment. The phase sensitive PF experiment demonstrated that PS gain can be observed over a broad bandwidth due to the relatively low dispersion of the fibre enabled by the W-index profile design. This was contrasted to the result achieved with a much higher dispersion bismuth oxide fibre of a similar length, which only showed strong PS gain within a limited bandwidth around the pump wavelength.

A two-pump degenerate PSA was employed to measure the PSDR that could be achieved with this fibre, which was measured to be 6 dB for a pump power of 27.7 dBm. There was no need to employ any active SBS suppression schemes in any of the experiments. Furthermore, to gain foresight into the promise of this fibre design, a numerical study was conducted to assess the performance gain achievable using a second generation of lead silicate fibre with better optimised physical characteristics for this application. The numerical study deduced that with the use of a fibre sample of optimum length (approximately 3 meters) and reduced propagation loss (2.1 dB/m), one can significantly enhance the nonlinear performance of the system without the need to increase pump power to excessive levels to achieve a good nonlinear FOM. Indeed, using a fibre with the aforementioned characteristics, it is believed that a PSDR value in excess of 18 dB should be readily achievable, indicating that such fibres could be employed to implement short-length devices for PSA-based processing applications of wideband signals.

The chapter then proceeded to reported the phase regeneration of 40 Gb/s data signals using saturated phase-sensitive amplifier based on a 1.7 m long of LSW2 fibre. The short fibre length drastically reduced the latency of the processing system relative to corresponding configurations based on germanium-doped HNLFs, and improved the system stability at the same time. Both the short and long term regeneration capability of the regenerator were assessed through the use of constellation diagrams and examination of the experimental data showed a significant level of phase noise reduction. Moreover, the low and flat dispersion profile of the fibre across the C-band highlights its potential for use in applications requiring wavelength multicasting.

The high splice losses have been underlined as a major limitation on the performance of this lead silicate fibre technology. The fabrication team at the ORC is working towards reducing the 5-6.5 dB splice loss figure reported in this chapter, and indeed further optimisation efforts have recently succeeded to reduce this figure [100]. Furthermore, tapering the input of the lead silicate fibre has been proposed as an alternative method to reduce the splice loss to bigger core SMF.

The lead silicate work presented in Chapter 3 and this chapter, investigated the platform's applicability for implementing all-optical signal processing applications at the telecommunication wavelengths. The rest of this thesis will focus on broadband technologies that enable the processing of optical signals both at the NIR and MIR. This was conducted within the framework of the CLARITY project which aims to implement an all-optical MIR to NIR wavelength converter based on tellurite fibres and silicon germanium waveguides. Chapter 5 investigates the optical characteristics of highly nonlinear tellurite fibres, while Chapter 6 and 7 focus on silicon germanium waveguides.

Chapter 5

Highly Nonlinear Tellurite Fibres

5.1 Introduction

The major limitations of Mid-IR photo-detection technology can be addressed by avoiding the direct detection of Mid-IR light and replacing it with the widely available ultra-sensitive Near-IR detectors through the use of an efficient MIR to NIR nonlinear converter. The broadband parametric amplification that FWM offers makes it the ideal nonlinear effect for MIR to NIR wavelength conversion. To implement such a conversion however, the third order nonlinear material on which the converter is based on will have to show optimum transmission and nonlinear behaviour in the 1-5 μm wavelength region.

Silica-based fibres possess exceptional chemical and physical characteristics in the visible and NIR wavelengths. However, the poor transmittance of silica at wavelengths beyond 2.5 μm makes conventional fibres unsuitable for MIR applications [132]. On the other hand, soft glasses such as fluoride, tellurite and chalcogenide show good transmission characteristics in both the NIR and MIR regime (Figure 5.1) and thus represent viable alternatives to silica-based technology. Tellurite glasses in particular, present themselves as good candidates for broadband applications since they possess a low glass transition temperature and are more thermally and chemically stable than fluoride glasses. Furthermore, they exhibit a nonlinear refractive index n_2 ranging between 20-50x10^{-20} m^2/W, i.e. about an order of magnitude higher than in fluoride and silica glasses, and a material ZDW that lies close to 2 μm, making it an easier task to design fibres with a ZDW close to 1.5 or 2 μm than in other infrared glasses such as chalcogenides, the ZDW of which lies beyond 5 μm [68, 93, 133]. Tellurite glasses also possess a damage threshold that is one order of magnitude higher than that of chalcogenides, in comparison with which they are also much less toxic. Due to these advantages, tellurite has been identified as the material of choice for the implementation of the MIR to NIR converter in optical fibres.

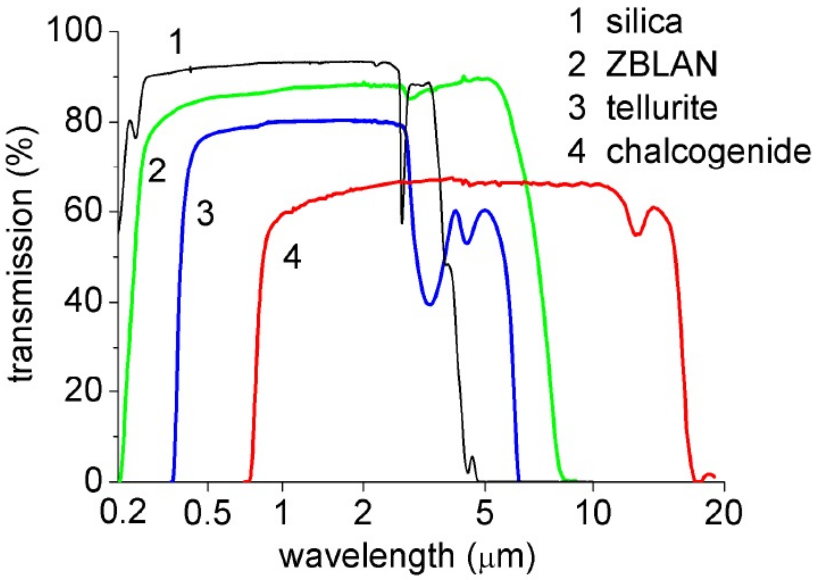

Figure 5.1: Bulk soft glasses losses between 0.2-20 μm (courtesy of Dr. Xian Feng).

The work reported in this chapter represents the early stages of fabricating low loss highly nonlinear tellurite fibres suitable for broadband MIR to NIR spectral translation. It reports the characterisation of the optical properties of the first generation of tellurite fibres at 1.55 and 2 μm. Close collaboration with the fabrication team was important as the characterisation data was fed back to the fabricators in order to fine-tune their fibre preparation procedure for subsequent fabrication attempts. This work was conducted within the EU project CLARITY.

The chapter starts by giving a brief account on the tellurite fibre design and fabrication. It then discusses the characterisation of the loss of the nonlinearity of the fibre at 1.55 and 2 μm. The measurement technique and the corresponding setup used to characterise the fibres nonlinearity are described and the experimental data of the nonlinear coefficient is compared with numerical simulations. Furthermore, demonstrations of wavelength conversion of CW signals at 1.55 and 2 μm are reported. The chapter closes with a numerical study highlighting the potential of using highly nonlinear tellurite fibres in broadband nonlinear spectral translation.

5.2 Fibre Design and Fabrication

The soft glass fibre fabrication team at the ORC, through the work of Dr. Xian Feng, was tasked with developing a preform dehydration method and subsequently fabricating low loss tellurite fibres across the 1-5 μm wavelength region. An account of the up-to-date progress of this task is reported here.

As can be seen from (Figure 5.1), tellurite glasses exhibit a drop in transmission values in the region of 3.5 μm. To compensate for this, it was proposed to dope the core glass with halides which are known to exhibit better transmission properties in the whole 0.2 and 7 μm wavelength region [134]. Furthermore, when using chlorine containing compounds such as lead chloride ($PbCl_2$) in the glass composition, the halogenation reaction that takes place ($OH^- + Cl^- = HCl \uparrow +O^{2-}$) helps to actively remove the OH groups from the glass, especially when using a dry atmosphere-filled glovebox. Therefore, the addition of such a compound together with proper dehydration of the glass was expected to eliminate the trough observed at 3.5 μm and improve the transmission of the glass across the whole region between 3 and 5 μm by approximately 20% [20].

The most promising glass composition has been identified as TeO_2PbCl_2 (TLX) thanks to its strong nonlinearity and good transmission properties up to 5 μm. However, a second glass variant was used (TeO_2-ZnO-BaO (TZB)) in the early fabrication attempts, which also exhibits low absorption in the MIR but lower nonlinear refractive index than TLX. The use of TZB provided a more straight-forward route towards the fabrication of small-core low loss fibres. All the experimental work reported in this chapter was conducted in a TZB fibre.

A simple step-index design was targeted for early fabrication attempts. Figure 5.2 shows an SEM image of the fibre which had a core diameter d of 4.2 μm and an outer diameter of 170 μm. The glass composition used was $70TeO_2$-20ZnO-10($BaO+BaCl_2$) and commercial chemicals with purities better than 99.999% were used as the raw materials for glass melting. The high-purity tellurite core-cladding preform was made using a built-in casting method and the NA of the fibre was estimated to be 0.25. The chemical batching, glass melting and preform casting were all processed inside an ultra-dry atmosphere filled glovebox with water level less than 0.2 ppm [20].

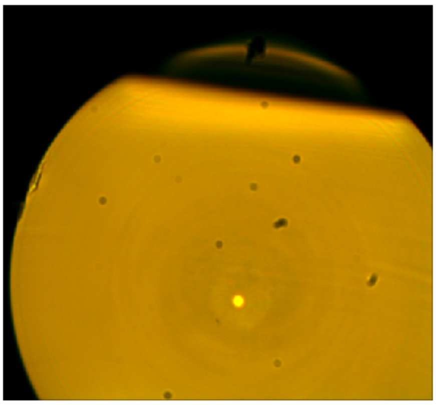

Figure 5.2: SEM image of the tellurite fibre (courtesy of Dr. Xian Feng).

5.3 Characterisation of Loss and Nonlinearity of Tellurite Fibre at 1.55 and 2 μm

5.3.1 Loss Characterisation

The loss of the dehydrated tellurite fiber was measured at two wavelength regions, namely 1.55 and 2 μm. The fiber loss was measured through cutback measurements, and was found to be 0.58 dB/m at 1.55 μm (Figure 5.3) and 2.8 dB/m at 2 μm.

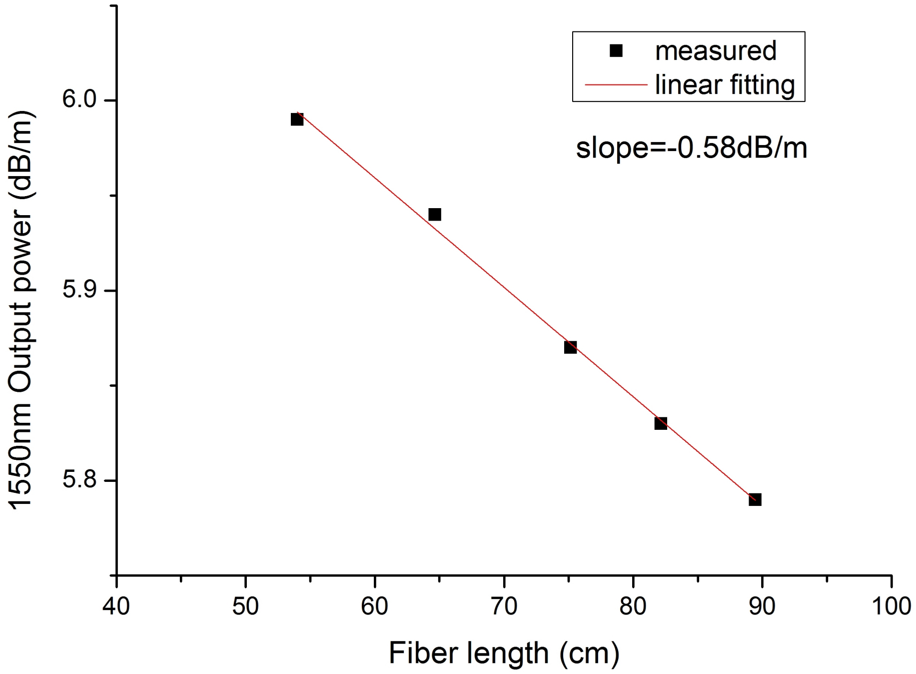

Figure 5.3: Loss measurement of TZB fiber at 1.55 μm using the cutback method. The measurement was conducted by Dr. X. Feng.

The measured loss figures at 1.55 and 2 μm are in line with the targeted values for the broadband nonlinear converter at those wavelengths. Furthermore, the effectiveness of the fibre preform fabrication process in reducing the water content and demonstrating low water absorption in the region of 3-5 μm has recently been reported [20].

5.3.2 Nonlinearity Characterisation

To measure the effective nonlinear coefficient of the fibre, a method based on the measurement of the nonlinear phase shift of a dual-frequency beat signal was utilised [135]. As explained in Chapter 2, a beat signal propagating down a fibre undergoes a nonlinear phase shift given by Equation 5.1:

$$\phi_{NL} = 2\gamma L_{eff} P \tag{5.1}$$

where γ , L_{eff} and P are the nonlinear coefficient, the effective length of the fibre under test and the power of the signal respectively. This nonlinear phase shift is related to the conversion efficiency (CE – defined as the ratio of the power of the converted idler to the output signal power) by Equation 5.2 [135]:

$$[CE_{linear}]^{-1} = \frac{J_0^2(\phi_{NL}/2) + J_1^2(\phi_{NL}/2)}{J_1^2(\phi_{NL}/2) + J_2^2(\phi_{NL}/2)} \tag{5.2}$$

where Ji is the i-th order Bessel function.

One can thus use the CE values recorded from a typical FWM experiment to extract the nonlinear phase shift (Equation 5.2) and subsequently calculate the value of the nonlinear coefficient γ (Equation 5.1). The impact of dispersive effects are assumed to be negligible.

Using this technique, the fibre was characterised in terms of its Kerr nonlinearity at two different wavelengths, 1.55 and 2 μm. At 1.55 μm, two amplified CW signals were coupled into a 2.4 m long fibre sample (Figure 5.4a). A lensed fibre was used to launch the 1.55 μm signals into the tellurite fibre with a coupling loss of 2 dB. The pump and the signal wavelengths were chosen to be sufficiently close to each other (within 0.2 nm) to avoid the impact of any dispersive effects. The polarisation was adjusted such that the nonlinear response was maximised when observed at the fibre output using an optical spectrum analyser (OSA)(Figure 5.4b). From the conversion efficiency

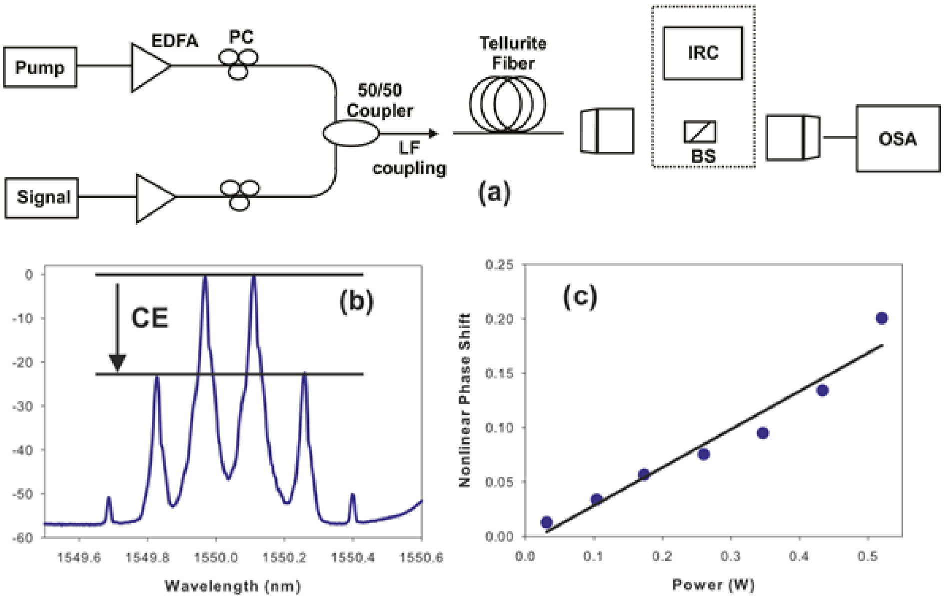

Figure 5.4: Experimental setup for the nonlinearity measurement. LF = Lensed fibre, BS= Beam Splitter, IRC = IR Camera. (b) Typical 1.55 μm spectrum where the conversion efficiency (CE) can be read (spectrum obtained for an input power of 485 mW) (c) plot of the nonlinear phase shift as a function of signal power.

values obtained, the nonlinear phase shift was calculated (Figure 5.4c) and from this the nonlinear coefficient γ was found to be 75 /W/km.

A similar characterisation procedure was followed at 2 μm. Figure 5.5 shows the experimental setup where the two CW lasers used in this case were a Cr-ZnS source operating at 2.006 μm, the output of which was lens-coupled into a single-mode fibre, and an amplified thulium-based fibre laser source with an output at 2.002 μm. The two signals were coupled together using a 2 μm 50:50 fibre coupler, and then free-space launched into a 4 m sample of the tellurite fibre through a combination of lenses (Figure 5.4a). This launch configuration resulted in a coupling loss of 5 dB. From these measurements the nonlinear coefficient at this wavelength was calculated to be 45 /W/km.

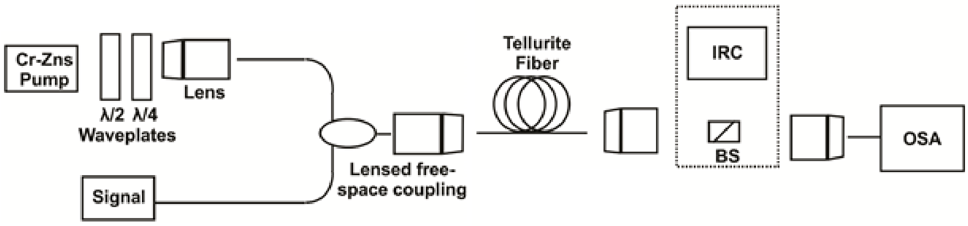

Figure 5.5: Experimental setup for the nonlinearity measurement at 2 μm.

The reasons behind the reduced value of the nonlinear coefficient γ at 2 μm as compared to 1.55 μm can be immediately appreciated by recalling its definition, i.e. $\gamma = (2\pi n_2)/(\lambda A_{eff})$, where λ is the wavelength and A_{eff} the effective mode area in the fibre. Both of these factors constrain the value of γ at longer wavelengths. The plot in Figure 5.6 illustrates this effect, whereas the insets to the figure depict simulations of the mode profile in the two wavelength regions, showing clearly the expansion in A_{eff} at longer wavelengths.

These simulations were carried out by the theory group in the National and Kapodistrian University of Athens (NKUA) which is one of the CLARITY project collaborators and had been tasked to perform all the numerical simulations in relevance to the project. The NKUA used a Mode-Solver and considered a simple step index fibre design as described by Figure 5.2. The effective mode area values at 1.55 and 2 μm were calculated to be 19.1 and 30 $\mu\mathrm{m}^2$ respectively. These large values of A_{eff} are responsible in the somewhat moderate γ values both at 1.55 and 2 μm.

A discrepancy between the experimental data and the numerical prediction of the value of gamma at 2 μm can be clearly seen. This is attributed to the uncertainty present in the experimental data where fewer data points were collected for this measurement due to the weak power of the idler generated. Furthermore, such low levels of idler power necessitated operating the OSA in high sensitivity mode where the lower scanning speed of the OSA could have attributed to misestimating the value of the CE due to the possible change in the launching conditions in the time between scanning the signal and the idler.

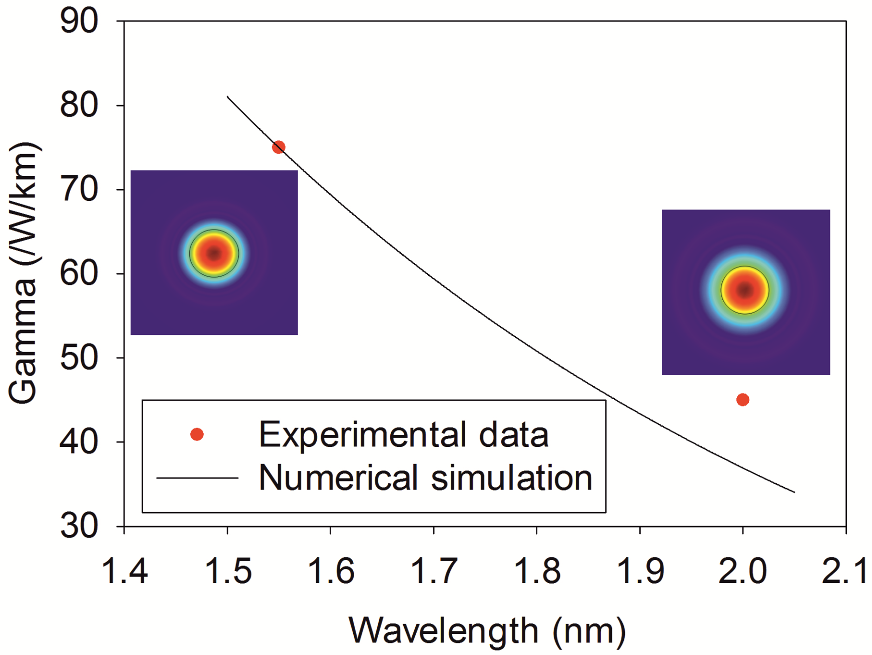

Figure 5.6: The nonlinear coefficient as a function of wavelength. Numerical simulations are provided by the NUKA

The simple step-index fibre design adopted here results in an A_{eff} value that is one order of magnitude larger than what is achievable using a microstructured fibre design [70]. This lower confinement results in the reduction of fibre nonlinearity by the same factor. However, it is important to note that the step index design was adopted since it provides the required dispersive characteristics for achieving the strict phase matching conditions of converting a MIR signal into the NIR (please refer to Section 5.5 for further details).

5.4 Wavelength Conversion Demonstrations at 1.55 and 2 μm

The combination of the low fibre attenuation and the relatively high nonlinearity coefficient at 1.55 μm allowed strong nonlinear effects to be observed in this short piece of fibre, even at modest power levels. An example of this is shown in Figure 5.7a, where the two tones used in the previous nonlinearity measurements were gated through a Mach-Zehnder modulator driven by 300 ns rectangular pulses with a duty cycle of 3:100. The modulated pump and signal were then amplified and coupled into the fibre, resulting in a total peak power of approximately 10 W at the fibre input. When the pump was placed very close to the signal wavelength ($\delta\lambda = 0.18nm$), a number of harmonics were generated through four-wave mixing (FWM) in the tellurite fibre as shown in Figure 5.7a, and a high conversion efficiency was observed, which approached 0 dB for the weaker of the two tones. Increasing the wavelength detuning to 5.5 nm (Figure 5.7b) reduces the conversion efficiency to -12 dB indicating the important role of dispersion on the FWM efficiency.

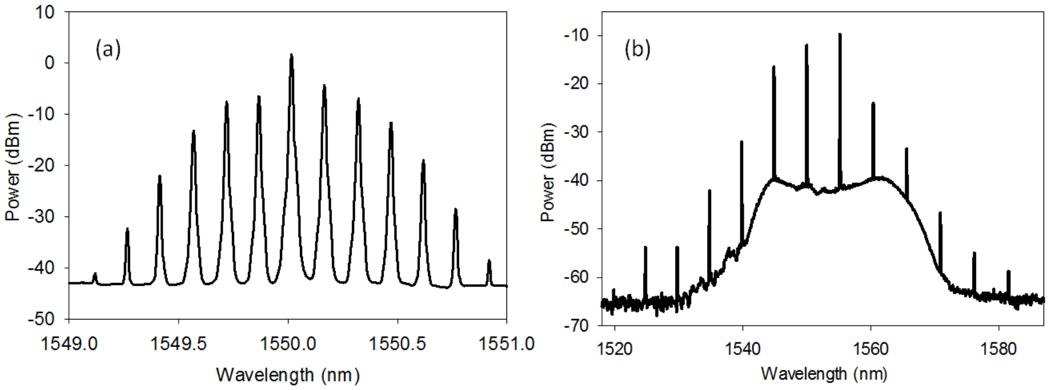

Figure 5.7: Spectrum after 2.4 m of TZB fibre with a gated pump and signal (a) with $\Delta\lambda$ of 0.18 nm (b) $\Delta\lambda$ of 5.5 nm between the pump and the signal

The full effect of the dispersive properties of the fibre on the FWM bandwidth was investigated at 1.55 μm. The conversion efficiency was measured as a function of the wavelength detuning between the fixed pump at 1.55 μm and the varying signal wavelength and is shown in Figure 5.8. Numerical approximations of the fibre dispersion which predict a ZDW at 2.69 μm and a dispersion and a dispersion slope of -100.92 ps/nm/km and 0.2 ps/nm^2/km respectively at 1.55 μm showed good agreement with the experimental data as indicated in the figure. Furthermore, the results show that the large normal chromatic dispersion of the fibre at 1.55 μm limits the 3-dB FWM bandwidth to approximately 5.8 nm (for the pump power used in this experiment). This

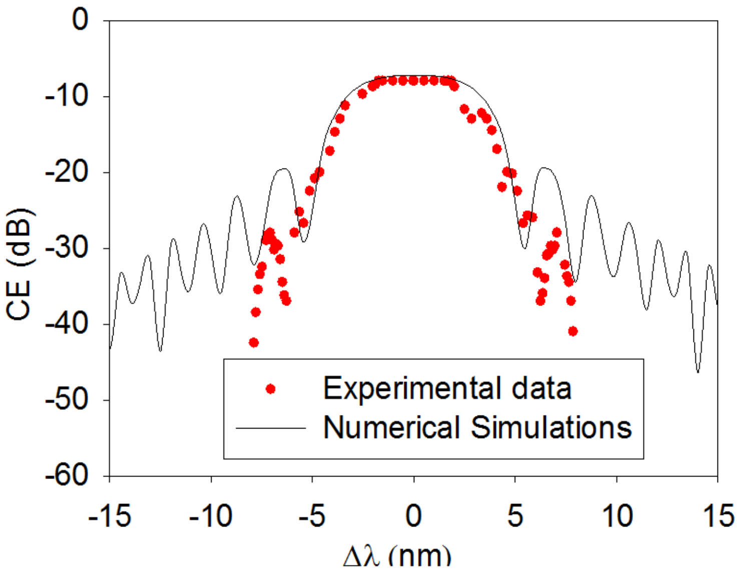

Figure 5.8: FWM conversion efficiency as a function of wavelength detuning at 1.55 μm.

was expected as the MIR to NIR nonlinear converter that the fibre aims to implement requires a ZDW that is far from the C-band and close to 2 μm wavelengths.

The combination of a lower nonlinearity, higher loss and lower coupling efficiency has resulted in somewhat less impressive performance at 2 μm . Figure 5.9a shows the spectrum obtained at the output of the fibre for 125 mW of power coupled into it, showing the nonlinear generation of an idler at 2.010 μm with a -42 dB conversion efficiency. Nevertheless, the calculations presented in Figure 5.9b illustrate that strong FWM conversion efficiency can still be obtained at these wavelengths at reasonable power levels. For instance, the FWM conversion efficiency can be increased by in excess of 10 dB to -28 dB if a 1 W pump is used.

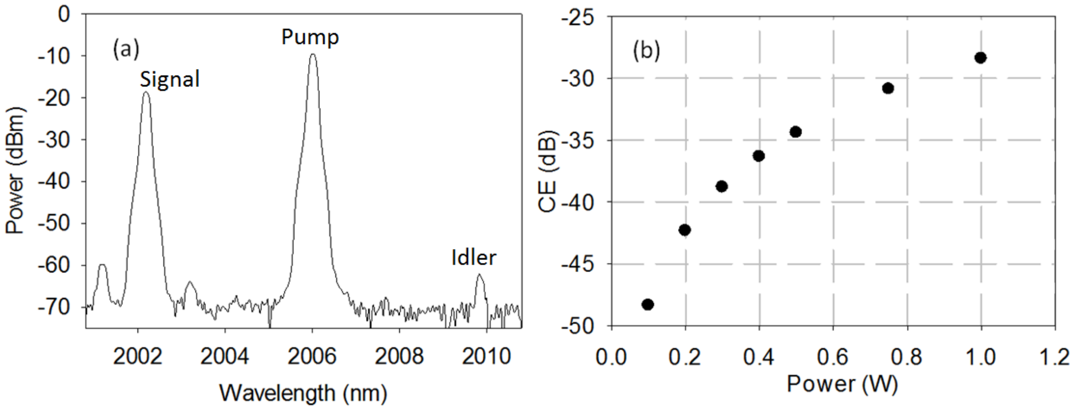

Figure 5.9: (a) Spectrum showing FWM taking place at 2 μm using CW signals. (b) plot of the calculated FWM conversion efficiency against input power.

5.5 Numerical Study: Tellurite Glass Fibre as a MIR to NIR Nonlinear Converter

As previously mentioned, TLX glass was chosen to fabricate a second generation of tellurite fibres to implement the broadband MIR to NIR nonlinear converter. This nonlinear wavelength conversion aims to translate a mid-IR signal seeded by a Quantum Cascade Laser (QCL) centred at 4.65 μm, to the near-IR region (1.3-1.7 μm) based on FWM process pumped by a tunable CW source covering the 2-2.5 μm wavelength region. In order to achieve such a broadband conversion, the fibre design needs to be carefully selected, so as to exhibit the proper dispersion characteristics required for achieving the phase matching conditions. Furthermore, efficient nonlinear conversion also requires the designed fibre to possess a large nonlinear parameter while still exhibiting single mode guidance at the pump wavelength. Finally, for the suggested simple step index design, fabrication requirements demand that the fibre numerical aperture (NA) be limited to a maximum value of 0.35 (corresponding to an index contrast of 0.03), since the stability of the fibre drawing is not guaranteed beyond this value.

This section will discuss the impact of the fibre design parameters, namely the core size and numerical aperture, on the fibre nonlinearity, mode properties and phase matching conditions.

5.5.1 Impact of Fibre Design Parameters on Mode Properties and Nonlinearity

Firstly, the impact of the fibre design on its modal properties was studied. Generally, in step index fibres, the V number (interpreted as normalised optical frequency) is used to determine the mode properties of a particular fibre design [2]:

$$V = \frac{\pi a}{\lambda}\sqrt{n_{co}^2 - n_{cl}^2} = \frac{2\pi a}{\lambda}NA \tag{5.3}$$

where a is the core diameter, λ is the wavelength, n_{co} is the refractive index of the core, n_{cl} is the refractive index of the cladding, and NA is the numerical aperture. For single mode operation, it is required that $V < 2.405$. Using this condition, Figure 5.10a maps the mode guidance properties of the fibre as a function of the core diameter and the NA, where the red portion of the plot indicates single mode guidance at wavelengths of 2 μm and beyond. The modal analysis presented here applies for any fibre with a step index design.

The impact of the core diameter and the NA on the fibre nonlinearity was also investigated. Recall that the nonlinear coefficient γ is given by:

$$\gamma = \frac{2\pi n_2}{\lambda A_{eff}} \tag{5.4}$$

where n_2, A_{eff} and λ are defined as before. From Equation 5.4 it can be seen that to study the impact of the fibre design on nonlinearity, the impact of a and NA on A_{eff} must be investigated first. For single mode fibres, the mode radius r and the effective area A_{eff} may be estimated from the core diameter a and the V number (which is related to a and NA through Equation 5.3 above) using Marcuse's equation [136]:

$$r = \frac{a}{2}(0.65 + \frac{1.619}{V^{3/2}} + \frac{2.879}{V^6}) \tag{5.5}$$

The effective area can thus be computed via:

$$A_{eff} = \pi r^2 \tag{5.6}$$

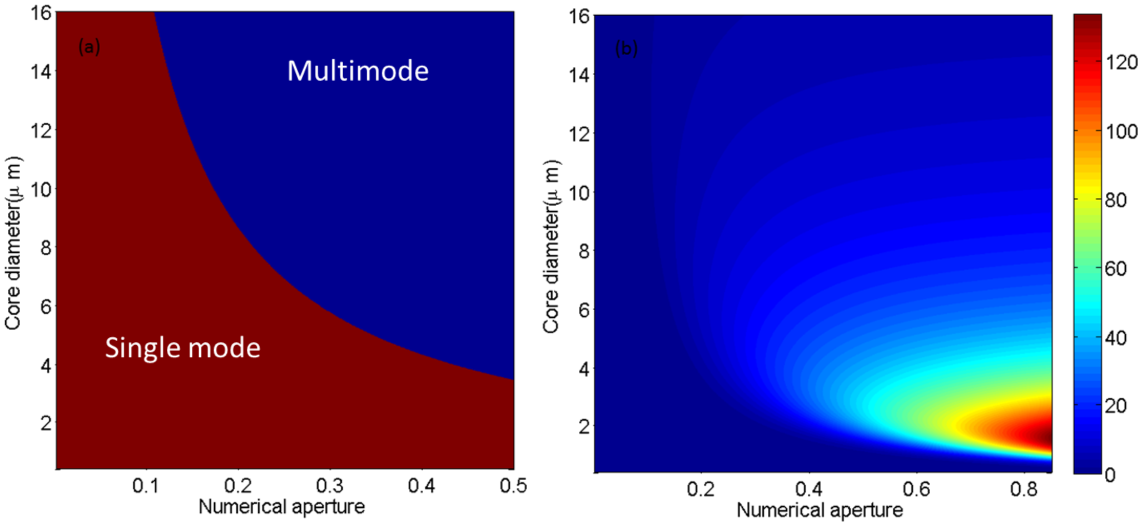

Figure 5.10: The impact of the fibre core diameter and NA on its (a) mode guidance properties (b) nonlinearity (in units of W/km).

By combining Equation 5.3, Equation 5.5 and Equation 5.6 into Equation 5.4, one can express the fibre nonlinearity coefficient γ as a function of the fibre design parameters a and NA. Figure 5.10b plots the nonlinearity coefficient for different core diameters and numerical apertures at 2.25 μm. As can be seen from the figure, for a fixed core size, a larger numerical aperture gives rise to a larger effective nonlinearity which is to be expected since a larger NA leads to a smaller effective mode area. It can thus be deduced from the two figures (Figure 5.10a and Figure 5.10b) that the fibre can satisfy both the fabrication constraints of an NA not exceeding 0.35 and achieving single mode guidance at the pump wavelengths provided that a core diameter no larger than 5.1 μm is used.

5.5.2 Impact of Fibre Design Parameters on Phase Matching Conditions

Achieving an efficient FWM process requires that the linear phase mismatch Δk_l between two pump photons $2\beta_p$, a signal photon β_s, and an idler photon β_i must balance the nonlinear phase mismatch Δk_{nl} that takes place due to the SPM and XPM effects during propagation:

$$\Delta k_l + \Delta k_{nl} = 0 \implies -\Delta k_l = \Delta k_{nl} \tag{5.7}$$

$$2\beta_p - \beta_s - \beta_i = 2\gamma P \tag{5.8}$$

where γ is the nonlinear coefficient and P is the peak pump power. For a large frequency detuning $(\Delta\omega)$ between the pump and the signal such as the case of converting a MIR signal to the NIR region, the linear phase mismatch Δk_l can be approximated using the second and forth order dispersion coefficients β_2 and β_4 respectively:

$$\Delta k_l = \beta_2(\Delta\omega)^2 + \frac{\beta_4(\Delta\omega)^4}{12} \tag{5.9}$$

The phase matching condition in Equation 5.8 can thus be expressed as:

$$2\gamma P = -\beta_2(\Delta\omega)^2 - \frac{\beta_4(\Delta\omega)^4}{12} \tag{5.10}$$

Contemplating Equation 5.10, one can see that the solution will depend on the signs of dispersion coefficients β_2 and β_4 [2]. Figure 5.11 plots the linear phase mismatch $-\Delta k_l$ against the frequency detuning $\Delta\omega$ for various sign combinations of β_2 and β_4. A solution to Equation 5.10 exists where the linear phase mismatch curve $-\Delta k_l$ intersects with the nonlinear phase mismatch line $2\gamma P$.

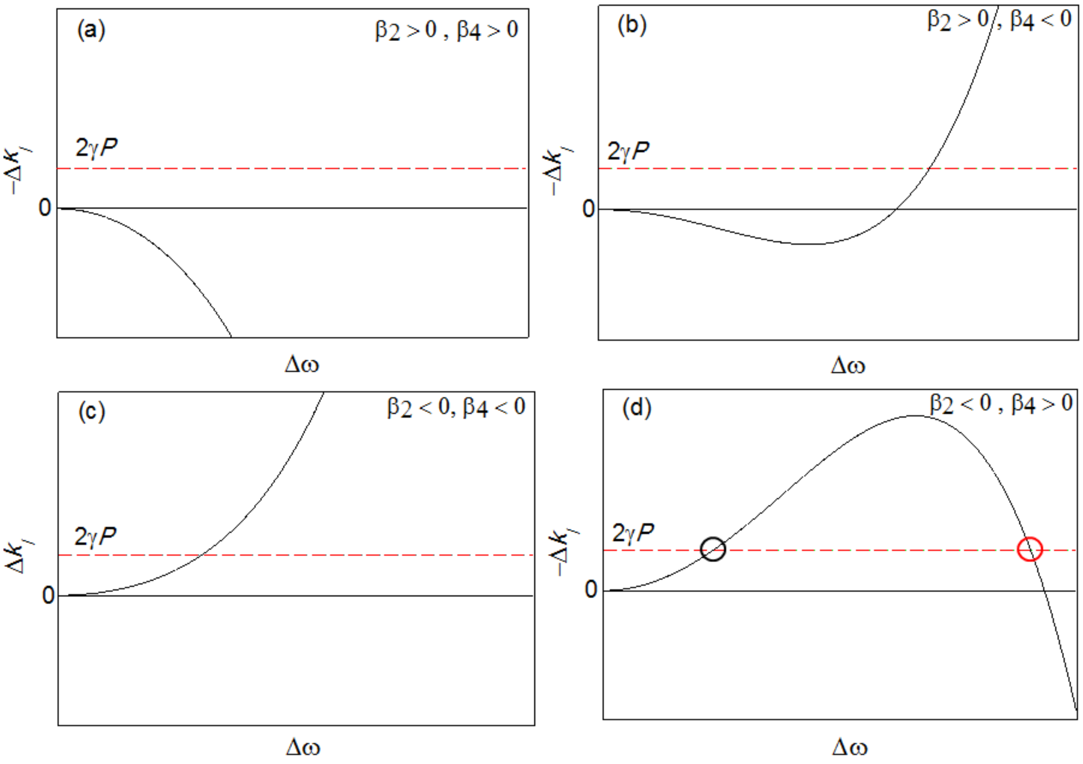

Figure 5.11: The linear phase mismatch as a function of frequency detuning for different signs of dispersion coefficients β_2 and β_4. The red dotted line represents the nonlinear phase mismatch.

Figure 5.11a shows that in the case where both dispersion coefficients are positive, no solutions to Equation 5.10 exist. Operating in this regime leads to a compromised FWM performance as no values of β_2 and β_4 can eliminate the FWM phase mismatch.

A positive β_2 and a negative β_4 lead to one solution to Equation 5.10 as depicted in Figure 5.11b. This phase matching condition has been used to demonstrate parametric amplification in fibre OPAs which are pumped in the normal dispersion regime [137].

Furthermore, a solution also exists for the case where both β_2 and β_4 are negative as illustrated in Figure 5.11c. Pumping in this anomalous dispersion regime leads to the generation of two spectral sidebands symmetrically positioned adjacent to the pump wavelength [138]. These amplification sidebands are a result of the gain provided by modulation instability (MI) that takes place due to the interplay between the dispersive and nonlinear effects during propagation.

Finally, Figure 5.11d depicts the graphical solutions to Equation 5.10 when $\beta_2 < 0$ and $\beta_4 > 0$. Interestingly, in this regime, the linear phase mismatch curve crosses the nonlinear mismatch line at two points, indicating the existence of two solutions to Equation 5.10 at two different values of pump-signal frequency detuning $\Delta\omega$. Pumping in this regime leads to the generation of broadband MI bands adjacent to the pump (corresponding to the first phase matching point denoted by the black circle) as well as discrete MI bands positioned further away from the pump (corresponding to the second phase matching point denoted by the red circle)[139].

While the second phase matching point in Figure 5.11d can be utilised to demonstrate a broadband spectral translation, significant power is lost in the MI bands adjacent to the pump, making the broadband conversion less efficient. This is in contrast to the second operating regime (Figure 5.11b) where only a single phase matching point further away from the pump is present. Therefore, in this study, where an ultra-efficient conversion of a MIR signal to a NIR idler is targeted, this regime (Figure 5.11b) was deemed as optimum. The design of the TLX fibre must thus exhibit these dispersive properties (i.e. $\beta_2 > 0$ and $\beta_4 < 0$) within the pump laser tunability range in order to achieve the efficient phase matching required.

The Sellmeier coefficients of the TLX glass were measured using data from spectroscopic ellipsometry (visible – 1.7 μm) and the prism method (2 – 4 μm)[140] (measurement conducted by Dr. Xian Feng). Figure 5.12a shows the fitted refractive index curve from 0.3 to 5 μm using the Sellmeier equation (Equation 3.8). For the TLX glass, the fitted six coefficients are $B_1 = 1.212$, $C_1 = 6.068\text{x}10^{-2}$, $B_2 = 2.157$, $C_2 = 7.068\text{x}10^{-4}$, $B_3 = 1.891\text{x}10^{-1}$ and $C_3 = 45.19$ respectively. The material dispersion curve of TLX was then calculated from the refractive index curve, as shown in Figure 5.12b. The ZDW of the bulk TLX glass is located at 2.30 μm.

The numerical model discussed in Chapter 3, Section 3.2 was used to estimate the chromatic dispersion of the fibre from its core diameter a and refractive index contrast Δn. Furthermore, another numerical model was developed to estimate the FWM phase matching curve from the fibre dispersion. The model was based on Biancalana and Skryabin's paper and is described in detail in [141].

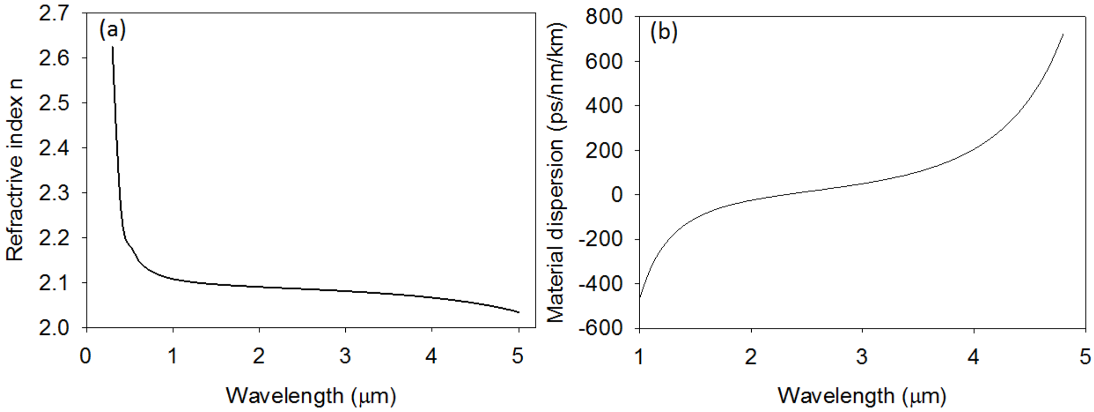

Figure 5.12: (a) Refractive index of TLX glass, plotted using the Sellmeier equation, (b) material dispersion of TLX glass.

Figure 5.13 shows the chromatic dispersion (top) and the phase matching curve (bottom) for a fibre with a of 2.5 (left), 3.25 (center) and 4 μm (right) for a fixed Δn value of 0.03. It can be seen that as the core diameter decreases, the pump wavelength required to achieve phased-matched conversion is shifted towards longer wavelengths. In fact, as the diameter decreases below 2.5 μm, no possible phase matching can be attained within the pump laser tuneability range of 2-2.5 μm.

Furthermore, the influence of the refractive index contrast was also analysed. Figure 5.14

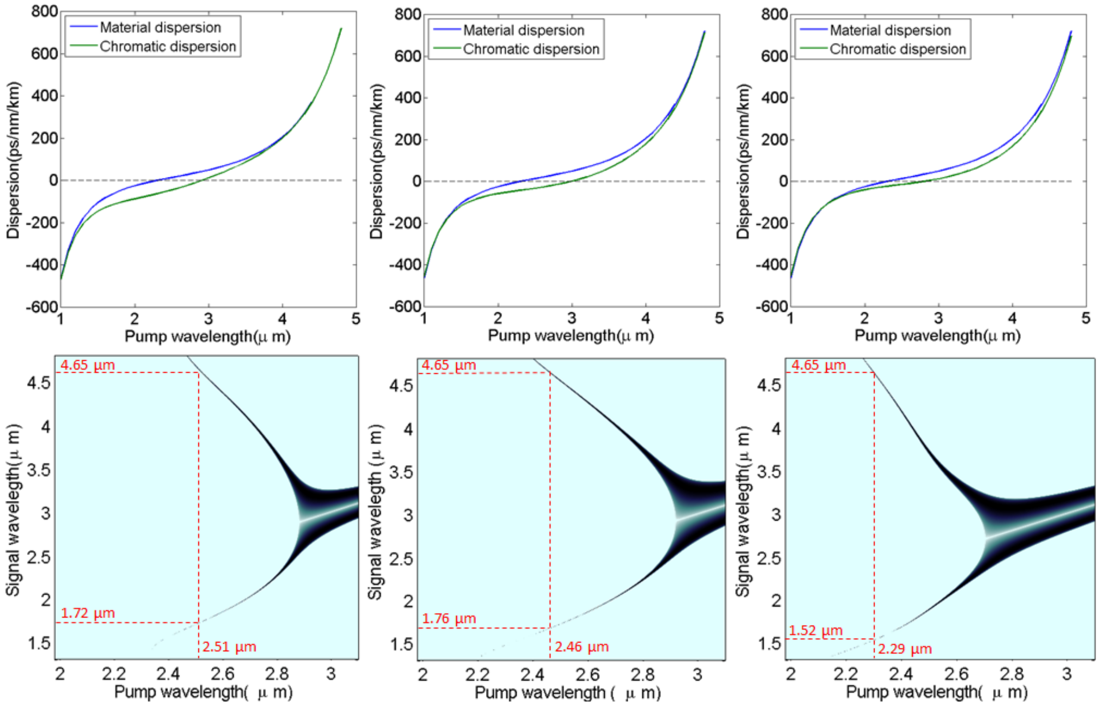

Figure 5.13: The influence of the core diameter on the dispersion curves (top) and the phase matching diagrams (bottom). Three core diameters of 2.5 μm (left), 3.25 μm (center) and 4 μm (right) and a fixed Δn= 0.03 are considered

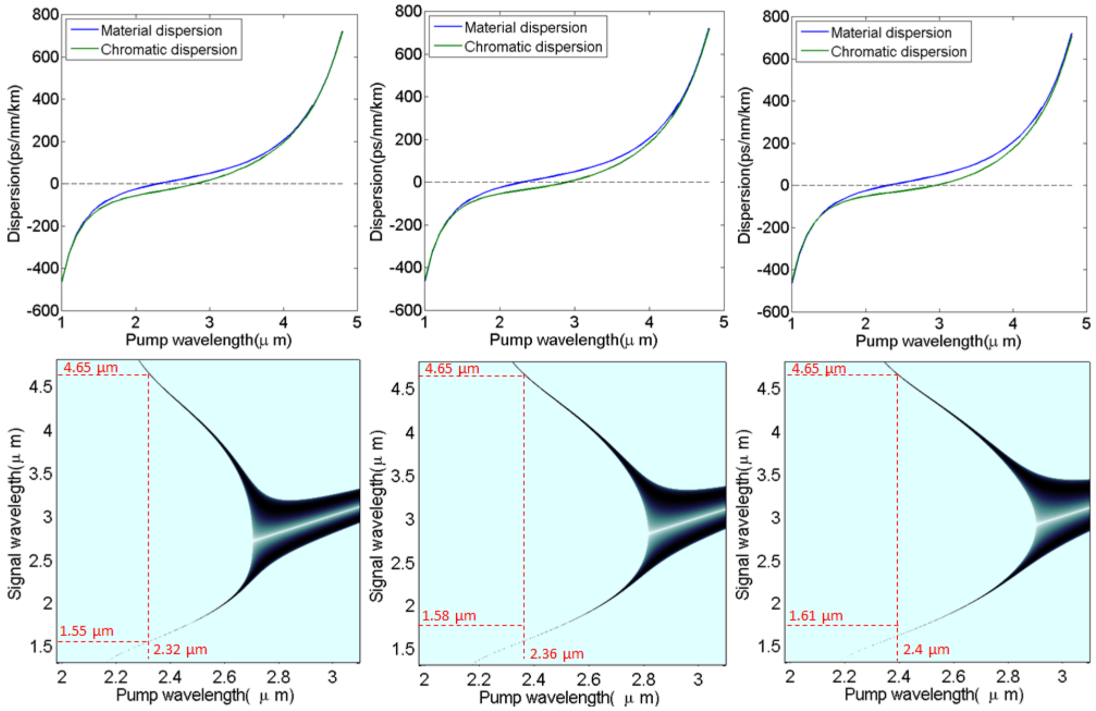

Figure 5.14: The influence of the core diameter on the dispersion curves (top) and the phase matching diagrams (bottom). Three Δn values of 0.02 (left), 0.025 (center) and 0.03 (right) and a fixed core diameter of 3.5 μm are considered

plots the chromatic dispersion (top) and the phase matching curve (bottom) for a fibre with a Δn of 0.02 (left), 0.025 (center) and 0.03 μm (right) for a fixed of core diameter of 3.5 μm. The figure demonstrates that an increase in the index contrasts leads to a shift in the required pump towards longer wavelengths. For instance, a 0.01 increase in Δn (from 0.02 to 0.03) leads to an increase in the required pump wavelength by 800 nm.

While theoretically five out of the six fibre designs presented in Figure 5.13 and Figure 5.14 are capable of achieving the required phase-matched nonlinear conversion, the design impact on nonlinearity (studied above) needs to be considered when choosing the optimum fibre parameters. Furthermore, while the IPG Photonics Cr^{2+}:ZnSe laser available for the conversion experiment is tunable from 1.98 μm to 2.5 μm, its output power is wavelength dependent and maximum power can be only attained within the 2.2-2.3 μm wavelength region. Taking all of this into account, it can be deduced that a fibre with a core diameter of 4 μm and Δn of 0.03 will satisfy the phase matching condition and achieve enhanced nonlinearity and single mode guidance at the wavelength region where the pump laser is most efficient.

This numerical study served as an important basis of understanding the influence of the fibre design parameters on its performance as a broadband wavelength converter. The results of the study were fed-back to the fibre fabricators at the ORC in order to prepare for subsequent fabrication attempts. Furthermore, the findings of these simulations were verified by the NKUA which conducted a more thorough numerical study that considered a number of parameters that were ignored here for the sake of simplicity. For instance, in addition to design considerations discussed above, the NKUA's detailed study into the fibre design also took into account the mode overlap between the 2 μm pump and the 4.65 μm signal fields, the fibre nonlinearity variation with wavelength in the region between 1-5 μm, polarisation effects and other nonlinear phenomena such as stimulated light scattering. When considering a pump power of 1 W, a fibre length of 1 m and fibre losses of 5 dB/m, their study has found that the fibre with the suggested design (a= 4 μm and Δn =0.03) would be able to convert the 4.65 μm MIR signal into the NIR with a -27 dB conversion efficiency.

5.6 Conclusions

This chapter presented tellurite glass fibres as a platform for broadband nonlinear applications. It highlighted the tellurite glasses' superior optical properties relative to other technological alternatives which makes them suitable for applications extending to the mid-IR. In particular, the high nonlinear coefficient, low transmission loss up to 5 μm and ease of design of their dispersion properties make them the ideal fibre material of choice for the implementation of broadband spectral nonlinear translators such as the MIR to NIR converter that CLARITY targets.

A method of reducing tellurite glass loss across the 3-5 μm wavelength window by adding halide compounds and preparing the preform in an ultra-dry atmosphere-filled glovebox was discussed and the TeO_2PbCl_2 (TLX) glass composition was identified by the fabrication team as the most promising composition thanks to its strong nonlinearity and low losses up to 5 μm.

A second glass variant was used (TeO_2-ZnO-BaO (TZB)) in the early fabrication attempts as it provided provided a more straight-forward route towards the fabrication of small-core low loss fibres. The loss of the dehydrated TZB fibre at 1.55 and 2 μm was characterised and was found to be 0.58 dB/m and 2.8 dB/m respectively. Furthermore, a method for measuring the fibre nonlinearity coefficient based on calculating the nonlinear phase shift of a dual-frequency beat signal was adopted and yielded γ values of 75 and 45 /W/km at 1.5 and 2 μm respectively.

Furthermore, the combination of low loss and high nonlinearity at 1.55 μm allowed the demonstration of efficient FWM in the TZB fibre with a conversion efficiency value approaching 0 dB for a total peak pump power of approximately 10 W. Although the FWM performance was far inferior at 2 μm, it is expected that by optimising the launching into the fibre, much higher conversion efficiency values can be obtained as numerical simulations show.

The chapter concluded with a numerical study into the potential of tellurite glass fibres in realising efficient MIR to NIR nonlinear conversion. The study discussed the influence of the fibre design parameters (core diameter d and index contrast Δn) on nonlinearity, mode properties and phase matching. The study established that a fibre with d of 4 μm and Δn of 0.03 would satisfy phase matching condition and achieve enhanced nonlinearity and single mode guidance at the pump laser wavelengths. Furthermore, a more comprehensive investigation carried out the NKUA, has concluded that the mode overlap between the MIR signal and the pump represents the major limiting factor in the conversion efficiency of the broadband converter. The study predicted a FWM conversion efficiency of -27 dB when a pump power of 1 W and a fibre length of 1 m were considered.

Chapter 6

Highly Nonlinear Silicon Germanium Waveguides

6.1 Introduction

As well as realising a MIR to NIR nonlinear wavelength converter based on soft glass fibre technology, it was also the aim to work towards a similar implementation, this time in a monolithically integratable chip-based platform. This work has also been conducted within the scope of the CLARITY project which aims to deliver a new class of MIR tools offering the potential for on chip integration of photonic functions, paving the way for lab on a chip systems at the MIR.

Of the various intergratable technologies currently available, silicon (Si) exhibits an excellent potential for monolithic integration and compatibility with CMOS technology. Furthermore, silicon photonics have attracted considerable attention as an emerging technology for all-optical signal processing in recent years, owing mainly to the attraction of silicon as a nonlinear material [25, 138, 142, 78, 143]. Silicon exhibits a large thermal conductivity, a high-optical-damage threshold, an enhanced transparency up to MIR wavelengths, immunity to two-photon absorption (TPA) effects in the MIR and most importantly perhaps a large Kerr nonlinear coefficient ($n_2 = 4.5 \text{ x } 10^{-18}$ m^2/W)[30]. These exceptional thermal and optical characteristics have allowed the demonstration of numerous optical nonlinear phenomena such as self-phase modulation [144, 145, 146], four wave mixing [147, 148] and associated parametric amplification [138], as well as stimulated Raman scattering [149] and its application for the implementation of Raman lasers [150, 151].

Although such great results are possible thanks to the good optical properties of silicon waveguides [76], a mix of silicon (Si) with other elements, and in particular germanium (Ge), can strongly enhance the nonlinear response [30]. The silicon germanium alloy

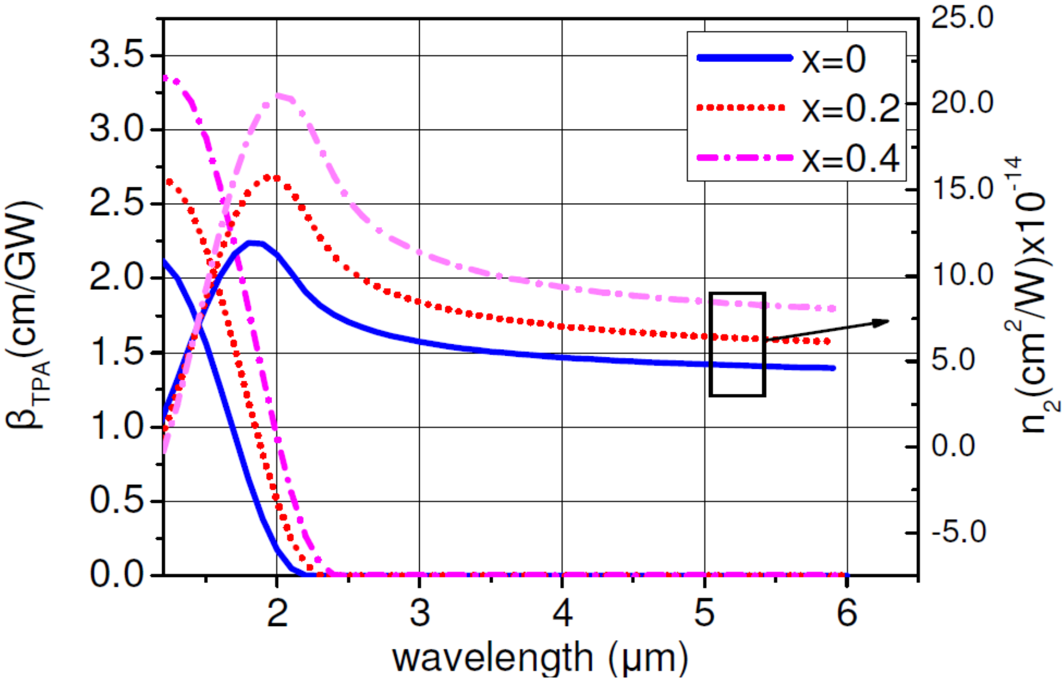

Figure 6.1: Nonlinear refractive index and TPA coefficient dependence on germanium concentration (x) (courtesy of Dr. Adonis Bogris).

($Si_{1-x}Ge_x$ - where x is the proportion of Ge in the alloy) has emerged as an attractive material for both micro- and opto-electronic devices thanks to the potential for bandgap and lattice parameter engineering that it offers [152]. For instance, SiGe modulators [153], light emitters [154] and photodetectors [155] have already been demonstrated. Very recently, SiGe alloys have also been identified as promising candidates for nonlinear applications in the midwave and longwave infrared, exhibiting stronger nonlinearities as compared to pure Si (Figure 6.1)[30]. Furthermore, the nonlinear properties of SiGe waveguides could also be interesting in the near-infrared and particularly at optical communication wavelengths. However, though germanium enhances the nonlinear response, this comes at the expense of an increase in the propagation loss due to the absorptive properties of Ge (Figure 6.1).

Due to the potential of the SiGe alloy outlined above and its maturity as a fabrication technology, SiGe waveguides have been identified as the platform of choice for implementing the monolithically integratable chip-based MIR to NIR nonlinear converter that CLARITY targets.

Two generations of SiGe waveguides were fabricated as part of the CLARITY project. The first generation of waveguides adopted a very simple constant germanium index profile and was used to study the linear and nonlinear optical properties of the SiGe alloy. The second generation of the waveguides, followed a more complex gradient germanium concentration profile, and was designed to allow broadband MIR to NIR spectral translation.

This chapter begins by briefly discussing the design and fabrication of the first generation SiGe waveguides. It then presents a detailed and systematic study of the linear and nonlinear properties of the waveguides at the telecommunications wavelengths. Waveguides of various widths and with a varying germanium concentration have been characterised in terms of loss, two-photon absorption, nonlinearity and dispersive properties. The experimental data is compared with numerical simulations performed by the NKUA. Finally, the overall performance of the different waveguides is compared and a trade-off analysis is performed.

6.2 Design and Fabrication of Silicon Germanium Waveguides

The first generation of SiGe waveguides followed a simple silicon on insulator (SOI) structure and adopted a constant germanium concentration profile. This was done in order to provide a simple route to study the effect of Ge concentration on the waveguide properties in the NIR and verify the accuracy of the NKUA's numerical model.

The waveguides were fabricated by CEA-Leti (a partner of the CLARITY project consortium). They consisted of epi-layers of SiGe grown on a Si substrate. First, 1.4 μm thick SiGe layers with different germanium concentrations were grown by reduced pressure chemical vapor deposition (RP-CVD) to control the Ge concentration in great precision and thus preserve uniformity. Standard photolithography and deep reactive ion etching techniques were used to form the strips. Finally, the waveguides were encapsulated with a 12 μm Si cladding layer epitaxially grown with the same RP-CVD technique. Epitaxial growth allows the realisation of low-loss fully crystalline structures while preserving IC processing compatibility.

Figure 6.2a shows a typical SEM cross-sectional image of the waveguide before and after (inset) encapsulation. The strip waveguides were 2.5 cm long (Figure 6.2b) with widths

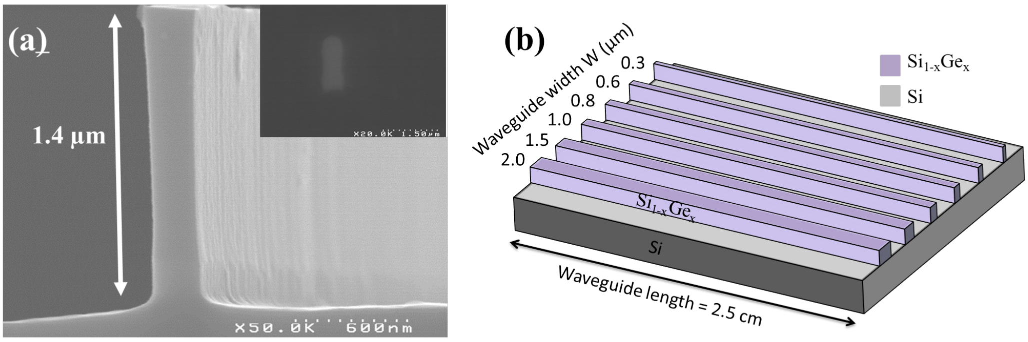

Figure 6.2: (a) Scanning Electron Microscopy (SEM) image of a SiGe waveguide, before and after (inset) encapsulation. (b) Sketch of SiGe waveguides before encapsulation.

W that varied from 0.3 μm to 2.0 μm, and Ge concentrations x that varied from 0.1 to 0.3.

6.3 Optical Properties of SiGe Waveguides at Telecommunications Wavelengths

In the following, the characterisation of linear and nonlinear optical properties of SiGe waveguides of varying germanium concentrations x (namely 10, 20 and 30% of Ge) and waveguide widths W (0.3, 0.6, 0.8, 1, 1.5 and 0.3 and 2.0 μm) is reported. The methodology of the experimental measurements is explained and the data is contrasted with numerical simulations conducted by the NKUA.

6.3.1 Loss Measurement

The most reliable method for measuring waveguide losses is called the Fabry-Perot resonance technique. The measurement relies on the observation of the periodic variation of the transmittance spectral fringes as the optical phase varies. Periodic transmission minima and maxima are formed when the end faces of a waveguide are parallel to each other. By measuring the transmitted power for different phase values, the waveguide attenuation can be estimated without requiring prior knowledge of the coupling efficiency. In practice, the phase difference can be tuned by changing the temperature of the waveguide or by varying the wavelength of the injected light. Since there is a temperature dependence in the coupling efficiency, wavelength tuning is usually deemed the best solution.

In the presence of loss, the transmission intensity from a Fabry-Perot cavity is given by [156]:

$$\frac{I_o}{I_i} = \frac{(1-R^2)G}{(1-GR)^2 + 4GR\sin^2(\delta/2)} \tag{6.1}$$

where R is the Fresnel reflectivity from the facet and $G = \exp(-\alpha L)$ is the total loss in the waveguide of length L and δ is the round-trip phase shift and can be expressed as follows:

$$\delta = \frac{4\pi n_{eff} L}{\lambda} \tag{6.2}$$

where n_{eff} is the mode effective index. Equation 6.2 shows that the effective index can be deduced from the spacing between the transmittance spectral fringes and in turn can be used to estimate the reflectivity using the Fresnel equation:

$$R = (\frac{n_{eff} - 1}{n_{eff} + 1})^2 \tag{6.3}$$

If a typical fringe is considered, such as the one depicted in Figure 6.3, the attenuation can be evaluated using two methods.

The first relies on the measurement of the extinction ratio between the maximum and minimum transmitted power P_{max} and P_{min} respectively. In this case, the loss can be calculated from Equation 6.1 and is given by [156]:

$$\alpha L = \ln(R \frac{1 + \sqrt{P_{min}/P_{max}}}{1 - \sqrt{P_{min}/P_{max}}}) \tag{6.4}$$

The other method relies on measuring the finesse. The finesse F defined as the ratio $(\delta\phi/\ \Delta\phi)$ between the inter-order phase difference $\delta\phi$ (difference between two fringes) and the bandwidth $\Delta\phi$ of the resonator at a transmitted power of 0.5 x $(P_{max} + P_{min})$. In this case, the loss can be written as follows [156]:

$$\alpha L = \ln(R \frac{\cos(\pi/F)}{1 - \sin(\pi/F)}) \tag{6.5}$$

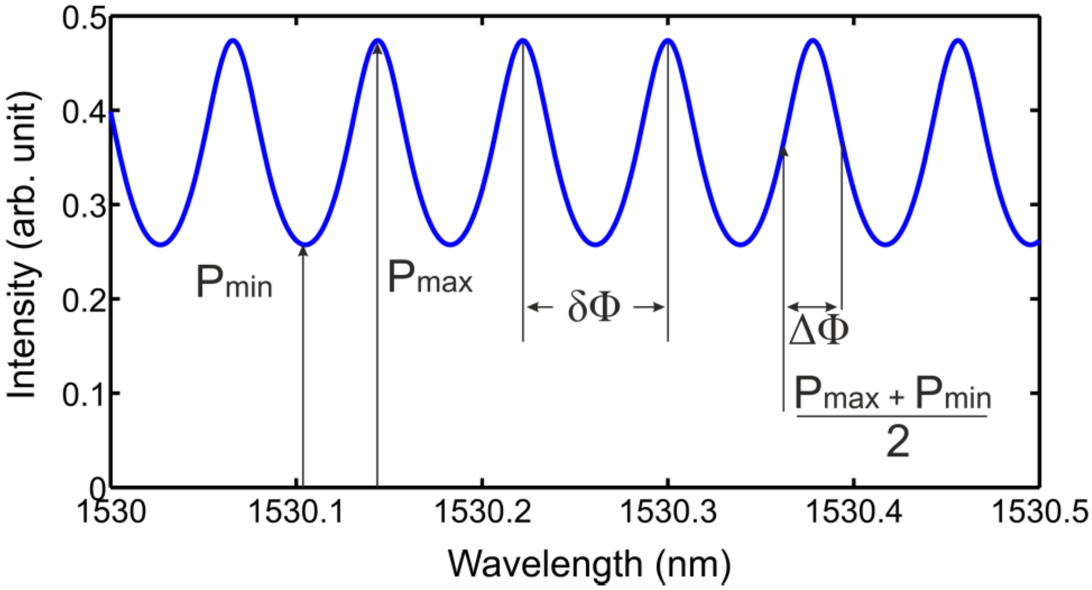

Figure 6.3: A typical fringe obtained in a Fabry-Perot cavity

The first method based on measuring the extinction ratio of the transmitted power was used. This is because it was deemed simpler to automate the process of detecting the periodic minima and maxima than the finesse. The experimental setup is shown in Figure 6.4a. As required by the method, the output of a CW tunable laser was coupled into the waveguide under test. The input polarisation was aligned to the axes

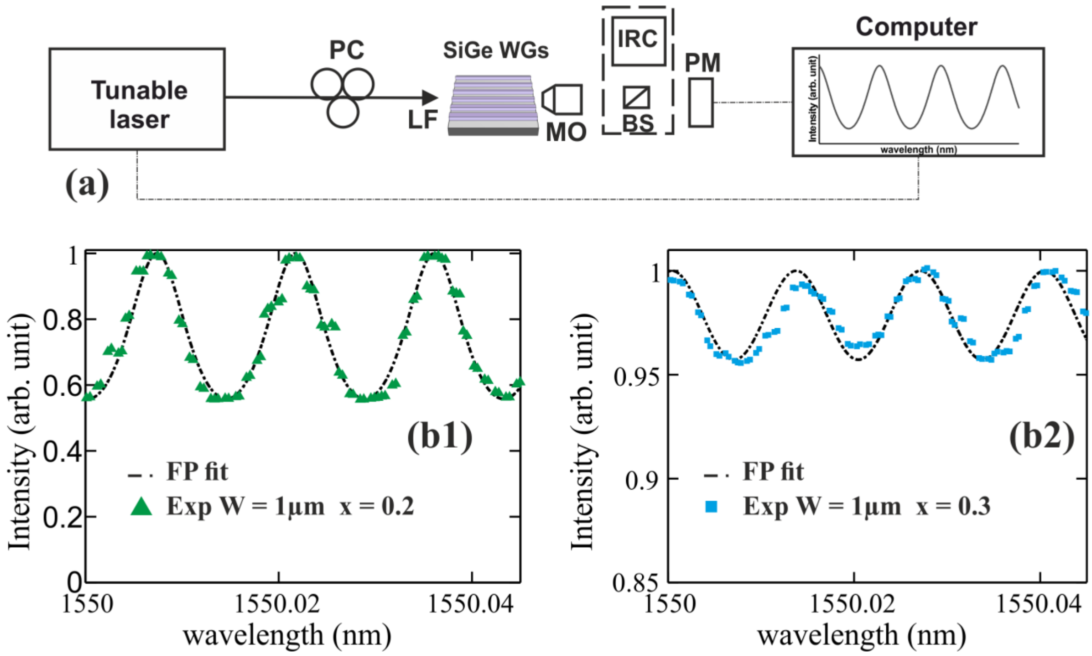

Figure 6.4: (a) Experimental setup for loss measurement. PC = polarisation controller, LF = Lensed Fibre, MO = Microscope Objective, BS = Beam Splitter, IRC = Infrared Camera, PM = Power Meter. (b) Spectral fringes and associated FP fit for a width of 1 μm at (b1) x = 0.2 and (b2) at x = 0.3

of the waveguide using a polarisation controller. Then, at the waveguide output, the light was collected by a microscope objective and directed to a power meter. A beam splitter was placed on the optical path to direct the light to an IR camera for guided mode observation and optimisation of the launching alignment. A computer-controlled routine was used to gradually sweep the laser wavelength and collect the power meter readings.

Figure 6.4b shows the measured power as a function of the wavelength for a width of 1 μm and for two different Ge concentrations. As expected for a FP cavity, typical fringes are observed, relating to interferences between the multiple reflections of light in the waveguide. Following fitting of the experimental measurements to Equation 6.4, the absorption parameter α was calculated to be 0.32 cm^{-1} (1.4 dB/cm) and 1.20 cm^{-1} (5.2 dB/cm) respectively for x = 0.2 (Figure 6.4b1) and x = 0.3 (Figure 6.4b2).

A systematic series of measurements of the losses for the whole set of the available waveguides was carried out. The results are reported in Table 6.1 as a function of the waveguide width and the Ge concentration. To understand the loss trend presented in Table 6.1, one must link the loss values with the waveguides' confinement factor and their effective mode area calculations (carried out by the NKUA group by means of a Finite Elements Method (FEM) solver). The effective mode area is defined by the ratio of an integral over the interaction area and an integral over the whole waveguide mode area and is given by [2]:

$$A_{eff} = \frac{[\iint |E|^2 \, dxdy]^2}{\iint |E|^4 \, dxdy} \tag{6.6}$$

where E governs the mode profile in the plane transverse to the propagation direction. The confinement factor represents the fraction of the mode energy density confined in the waveguide core and is estimated from [157]:

$$\tau_{xy} = \frac{\int_{W/2}^{-W/2} \int_{H/2}^{-H/2} |E(x,y)|^2 \, dxdy}{\iint\limits_{xy} |E(x,y)|^2 \, dxdy} \tag{6.7}$$

	x=0.1	x=0.2	x=0.3
0.3 μm	High loss (>5 dB/cm)	3.9	3.47
0.6 μm		2.38	4.56
0.8 μm		2.38	4.77
1.0 μm	4.75	1.40	5.21
1.5 μm	0.43	1.52	4.77
2.0 μm	0.65	2.60	4.34

Table 6.1: SiGe waveguides loss in dB/cm as a function of waveguide width and Ge concentration

When the effective mode area and the confinement factor calculations in Table 6.2 are compared with the experimental values of loss, a clear correlation is drawn. As the waveguide width decreases, losses increase due to poor confinement. Indeed, for small widths of 0.3 and 0.6 μm and x = 0.2, the confinement factor is around 0.2 and 0.55 respectively, indicating poor guiding which justifies the high loss figures reported. On the other hand, as the waveguide width increases, the confinement factor rapidly increases which results in a higher mode overlap with the lossier SiGe core. This can also be confirmed by noticing that for the same Ge concentration, the losses increase as the confinement factor increases. For instance, when larger widths of 1.5 and 2 μm and x = 0.2 are considered, the confinement factor is around 0.86 and 0.89 respectively, indicating that a higher mode overlap of the optical field with the SiGe core occurs for

Effective mode area (μm^2)												
	0.3 μm		0.6 μm		0.8 μm		1 μm		1.5 μm		2 μm	
	TE	TM	TE	TM	TE	TM	TE	TM	TE	TM	TE	TM
x=0.1	34.24	32.09	5.49	5.31	3.95	3.87	3.45	3.41	3.33	3.34	3.65	3.68
x=0.2	4.21	3.80	1.96	1.86	1.82	1.77	1.85	1.82	2.14	2.15	2.54	2.56
x=0.3	2.09	1.83	1.36	1.28	1.38	1.33	1.46	1.44	1.80	1.81	2.20	2.21
Confinement Factor												
x=0.1	0.065	0.069	0.297	0.306	0.448	0.456	0.559	0.563	0.712	0.711	0.778	0.775
x=0.2	0.199	0.22	0.558	0.57	0.692	0.7	0.772	0.78	0.863	0.86	0.897	0.894
x=0.3	0.317	0.361	0.681	0.706	0.792	0.804	0.852	0.857	0.915	0.914	0.936	0.934

Table 6.2: Numerical simulations of the effective mode area and confinement factor for all waveguides studied [39].

W = 2 μm than W = 1.5 μm. The net effect of this is to causes the optical filed to experience higher propagation losses in the case of W = 2 μm than W = 1.5 μm.

There thus are two competing phenomena: poor guiding occurring at small waveguide widths and high mode overlap with the lossy SiGe cores occurring at large waveguide widths. This means that there is an optimal value for low losses at each concentration, although this is not clearly shown in the x = 0.3 case probably due to uncertainty in the measurements estimated to be close to 10%.

Moreover, as expected, for a fixed waveguide width, the presence of germanium strongly increases the absorption loss. For instance, at a width of 1.5 μm, the losses evolve from 0.43 to 4.77 dB/cm when Ge concentration increases from 0.1 to 0.3. Note that low concentration (x = 0.1) leads to high loss when the width is too small ($\leq$ 1.0 μm) because of the poor confinement of light into the small-dimension waveguide. The poor confinement together with the high coupling losses is believed to have likely led to larger experimental errors in all measurements conducted for samples with concentration x = 0.1 as compared to higher Ge concentrations. Note finally, that the measured propagation losses were very similar for the TE and TM modes.

6.3.2 Nonlinearity Measurement

To measure the nonlinearity, the method (based on the measurement of the nonlinear phase shift of a dual-frequency beat signal) presented in Chapter 5, Section 5.3.2 was

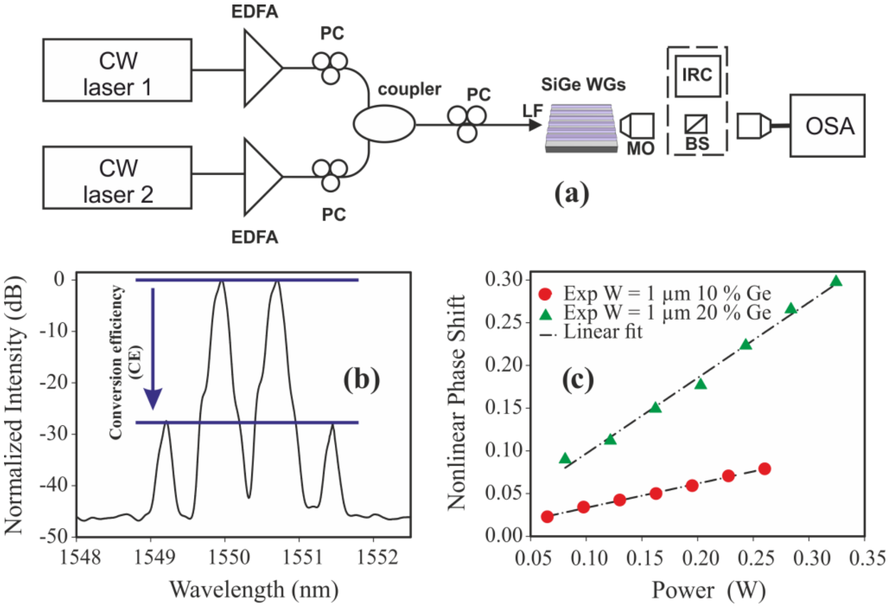

Figure 6.5: (a) Experimental setup for nonlinearity measurement. (b) Typical spectrum where the CE can be read (c) Typical plots of the nonlinear phase shift vs. the signal power for width of 1 μm and for x = 0.1 (red circles) and x = 0.2 (green triangles). The dotted-dashed lines correspond to linear fits.

adopted [135]. The experimental setup shown in Figure 6.5a was used for this measurement. Two CW signals were amplified and had their polarisation state adjusted through polarisation controllers. The signals were then combined through a 50/50 coupler and coupled into the waveguide under test using a lensed fibre. The two wavelengths were chosen to be sufficiently close to avoid the onset of dispersive effects [158]. The polarisation was adjusted such that the nonlinear response was maximised when analysed using an OSA at the output.

By recording the conversion efficiency through measurements on an OSA (Figure 6.5b) and using Equation 5.2, the nonlinear phase shift was plotted as a function of the average power for two different Ge concentrations of the 1 μm-width waveguide (Figure 6.5c). The nonlinear parameter γ was then obtained from the slope of the linear function (Equation 5.1) which fitted the experimental data.

All results are summarised in Figure 6.6. As expected from the literature [30], the nonlinearity increases with the Ge concentration. Smaller waveguide widths also result in higher values of γ, up to a value where the mode can no longer be confined in the waveguide, and then the trend is reversed. Typically, a maximum value is reached for widths between 0.8 μm and 1.0 μm. The results were also compared with simulations and are contrasted in Figure 6.6 showing good agreement.

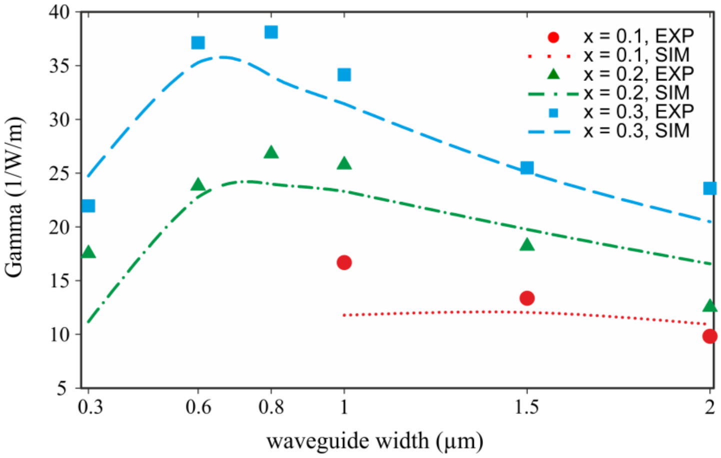

Figure 6.6: Nonlinear parameter γ as a function of the waveguide width for x = 0.1 (red circles), 0.2 (green triangles) and 0.3 (blue squares). The experimental results (symbols) are compared with numerical simulations in dotted (x = 0.1), dotted-dashed (x = 0.2) and dashed (x = 0.3) lines.

6.3.3 Two-Photon Absorption Measurement

As discussed in Chapter 2, Two-Photon Absorption (TPA) refers to a transition from the ground state of a system to a higher energy state through the absorption of two photons. This nonlinear absorption is a detrimental effect as it limits the maximum

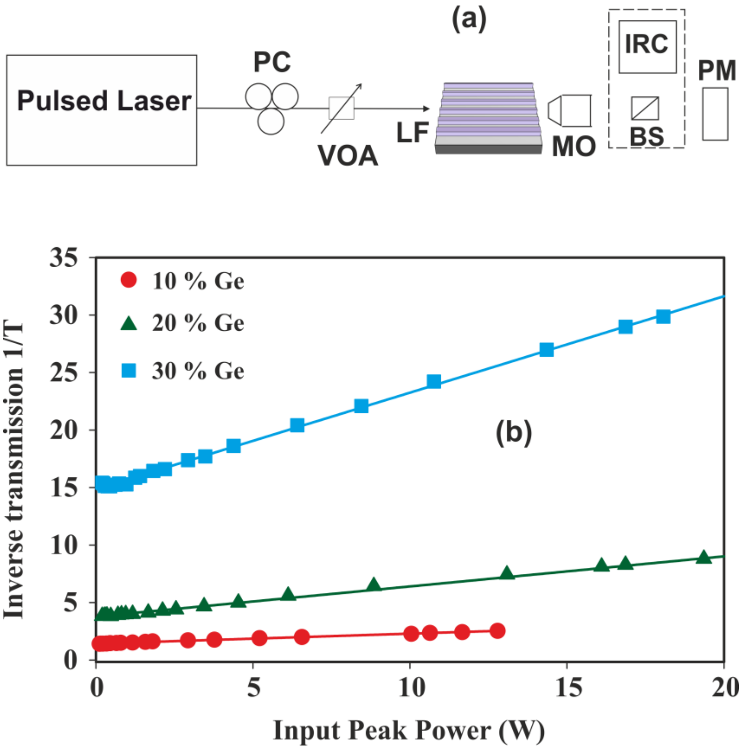

Figure 6.7: (a) Experimental setup for the TPA measurement. VOA = variable optical attenuator (b) Inverse transmission vs coupled input peak power for x = 0.1 (red circles), x= 0.2 (green triangles) and x = 0.3 (blue squares). The solid lines correspond to a linear fit.

transmitted power. The TPA coefficient, β_{TPA}, is related to the ratio of input power P_{in} to output power P_{out} as follows [159, 160]:

$$\frac{P_{in}}{P_{out}} = \frac{1}{T} = \exp(\alpha L)\frac{\beta_{TPA}}{A_{eff}} L_{eff} P_{in} + \exp(\alpha L) \tag{6.8}$$

Figure 6.7a shows the experimental setup for the TPA coefficient measurement. Figure 6.7b presents the inverse transmission corresponding to the ratio of input power to output power as a function of the input peak power for the three different concentrations in germanium and a fixed waveguide width of 2.0 μm. A pulsed source centered at 1550 nm producing 0.5 ps optical pulses with a 20-MHz repetition rate was used (Figure 6.8). A variable attenuator with an integrated power monitor controlled the input power into the waveguide. As expected from Equation 6.8, the TPA value can be extracted by applying a linear fit to this measurement, and making use of the previously measured values of loss and nonlinearity. Note that from the y-intersect one can recover the linear loss. The TPA values are reported in Table 6.3 and compared to the theoretical values which were calculated by the NKUA. A clear increase in the TPA is observed when the germanium concentration increases [30]. Furthermore, even though the trend predicted from both the experimental and theoretical values is similar, a discrepancy is observed. The main reason for this discrepancy is considered to be an overestimation of the theoretical value for the silicon TPA. In the theoretical model adopted by the NKUA, the TPA value of silicon was calculated following Garcia's model, which was fitted to the measurements of Bristow et al. reported in [161]. It is noted that even in the same reference, a comparison of the model with experimental results also suggests an overestimation of the TPA value.

Ge concentration	Experimental β_{TPA} (cm/GW)	Theoretical β_{TPA} (cm/GW)
x = 0.1	1.16	1.73
x = 0.2	1.24	2.15
x = 0.3	1.5	2.58

Table 6.3: TPA values in cm/GW for the SiGe waveguides with varying Ge concentration.

Furthermore, although there is a discrepancy between the measured and theoretically calculated TPA values, the numerically predicted n_2 values which NKUA estimated using the Kramers-Kronig nonlinear relation [30] are pretty close to the real ones as proven by the experimental characterisation of the FWM efficiency of the devices shown in Section 6.3.2. This can be understood since the power levels used in all of the characterisation experiments (apart from those presented in Figure 6.7) were too low for TPA to have any significant impact.

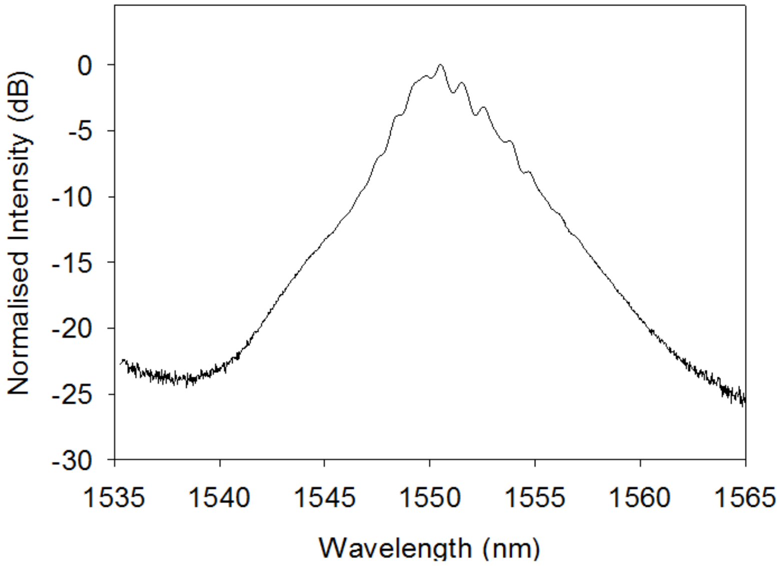

Figure 6.8: Spectral trace of the pulsed laser source used for the TPA measurement. The source produced 0.5 ps optical pulses with a 20-MHz repetition rate.

6.3.4 Dispersion and FWM Conversion Efficiency

Numerical calculations of the dispersive properties of the waveguides (as conducted by the NKUA) have suggested that the telecommunications C-band is far from the ZDW of the SiGe waveguides included in the study (Figure 6.9), and thus it is expected that the dispersion could drastically impact on the four-wave mixing bandwidth [162, 163]. In order to assess the impact of the dispersion and also to validate the NKUA's numerical simulations, the conversion efficiency as a function of wavelength was experimentally measured and contrasted with the NKUA's numerical predictions.

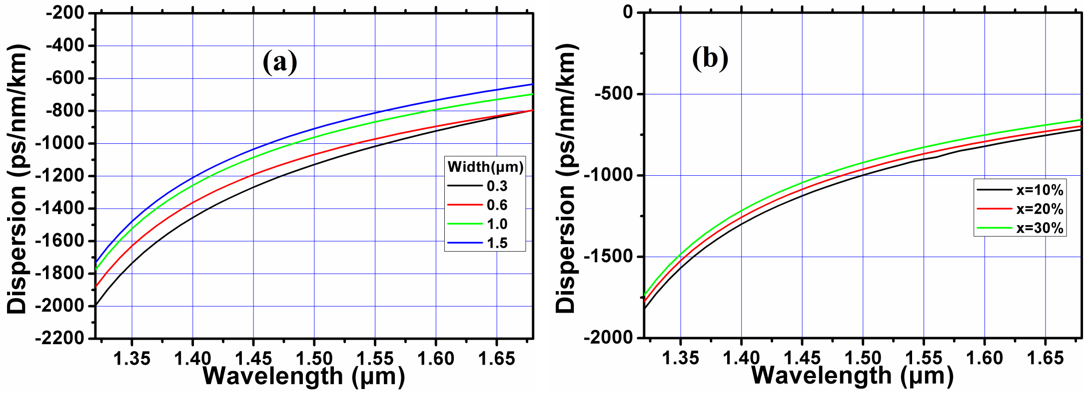

Figure 6.9: Dispersion curves for (a) Ge concentration x = 0.2 and different waveguide widths, (b) for width equal to 1 μm and different Ge concentrations (courtesy of Dr. Adonis Bogris).

6.3.4.1 Numerical Model

The numerical model that the NKUA developed involves the propagation of pump, signal and idler and is an expansion on the model presented in Chapter 2, Section 2.2.2.2, which did not account for two-photon absorption or free carrier effects. Since simulations from NKUA's model are used fairly extensively both in this section and in Chapter 7, a brief description of it is presented here.

The propagation of pump, signal and idler fields obey the following equations [164]:

$$\frac{\partial A_p}{\partial z} = \left\{ i(\beta_p + \beta_p^f) - \alpha_p/2 \right\} A_p + i(\gamma_p P_p + 2\gamma_{ps} P_s + 2\gamma_{pi} P_i) A_p + 2i\gamma_{pspi} A_s A_i A_p^* \quad (6.9)$$

$$\frac{\partial A_s}{\partial z} = \left\{ i(\beta_s + \beta_s^f) - \alpha_s/2 \right\} A_s + i(\gamma_s P_s + 2\gamma_{sp} P_p + 2\gamma_{si} P_i) A_s + i\gamma_{spip} A_i^* A_p^2 \quad (6.10)$$

$$\frac{\partial A_i}{\partial z} = \left\{ i(\beta_i + \beta_i^f) - \alpha_i/2 \right\} A_i + i(\gamma_i P_i + 2\gamma_{ip} P_p + 2\gamma_{is} P_s) A_i + i\gamma_{ipsp} A_s^* A_p^2 \quad (6.11)$$

where A_j, α_j, β_j are the field, the linear loss and propagation constants with j=p, s, i denoting the pump, signal and idler waves respectively. The nonlinear parameter γ_{ijkl} can be calculated provided that the Kerr coefficient n_2, two photon absorption β_{TPA}, effective mode area, modal refractive index and mode overlap factors are known for all possible combinations appearing in Equations 6.9, 6.10 and 6.11 [164]. The parameters

n_2 and β_{TPA} characterise the material. According to [30], Garcia's model, fitted to available experimental measurements, can be utilised to predict the n_2 and β_{TPA} evolution of Si, Ge and $Si_{1-x}Ge_x$ alloys for all the wavelengths of interest. Some of the aforementioned quantities must be calculated for the given structure through a waveguiding analysis. By means of a Finite Elements Method (FEM) solver, the effective refractive index, the effective mode area and the modal overlaps can be calculated.

The parameter β_j^f represents the free-carrier induced perturbations to the propagation constant described by the Drude model [78]. Finally, the Raman effect can be safely ignored due to its narrow bandwidth nature in silicon based waveguides [78].

6.3.4.2 Experimental Data

The experimental setup is similar to Figure 6.5a where "laser 1" is the pump having a fixed wavelength centered at 1.55 μm and "laser 2" is a tunable CW signal with low power compared to the pump. Figure 6.10 presents the wavelength dependence of the FWM conversion efficiency for the best performing waveguides for each Ge concentration. Furthermore, NKUA's simulations are in relatively good agreement with the experimental data, thus confirming the validity of the dispersion curves of Figure 6.9. The discrepancy between the experimental data and the simulations at large wavelength detuning in Figures 6.10(a) and (b), are attributed to the narrow nature of the CE troughs present at those wavelengths, which are difficult to resolve experimentally.

Moreover, for a total power of ~295 mW at the input of the waveguide, Figure 6.10 shows a 3dB bandwidth of ~19 nm (Figure 6.10a), ~21 nm (Figure 6.10b) and ~26 nm (Figure 6.10c) respectively for x = 0.1, x = 0.2 and x = 0.3. Furthermore, it was

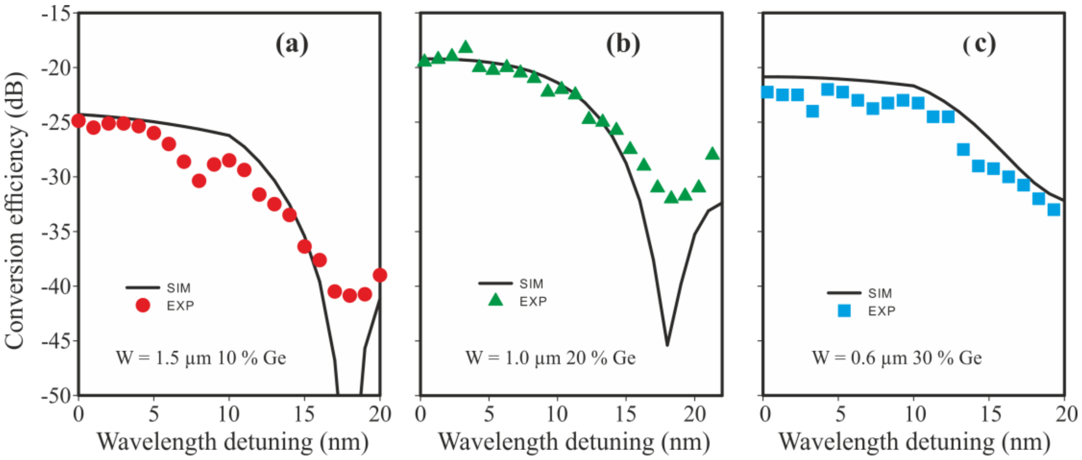

Figure 6.10: Conversion efficiency as a function of wavelength detuning from 1.55 μm for (a) W = 1.5 μm and x = 0.1 (red circles) (b) W = 1.0 μm and x = 0.2 (green triangles) and (c) W = 0.6 μm and x = 0.3 (blue squares). The solid lines correspond to numerical simulations. The input power was close to 295 mW.

observed that, for a given waveguide width, a higher germanium concentration results in a broader FWM bandwidth. This is because the addition of higher Ge concentrations results in bigger refractive index contrast between the core and cladding. This leads to stronger waveguide dispersion and lower overall chromatic dispersion of the waveguide at 1.55 μm (Figure 6.9), which results in lower FWM phase mismatch and broader FWM bandwidths.

6.3.5 Polarisation and FWM Conversion Efficiency

The effect of polarisation on the FWM performance of the waveguides was also studied. Figure 6.11 depicts the FWM conversion efficiency dependence on the state of polarisation for a waveguide of W = 1 μm and x = 0.2. The use of a polarisation controller and a polariser allowed the angle of polarisation of the two co-polarised incident beams to be swept from 0 to 180 degrees and the CE was subsequently measured. The polar plot displayed in Figure 6.11 shows a maximum of 1 dB variation in CE as the polarisation angle was swept from 0 to 180 degrees. This shows that the FWM performance of the waveguide is not strongly affected by the state of polarisation of the incident light

Furthermore, due to the fact that the losses are not significantly dependent on the polarisation and that the effective area is also very similar for TE and TM modes (Table 6.2), it is expected that a similar conclusion to that drawn from Figure 6.11 will hold for all waveguides.

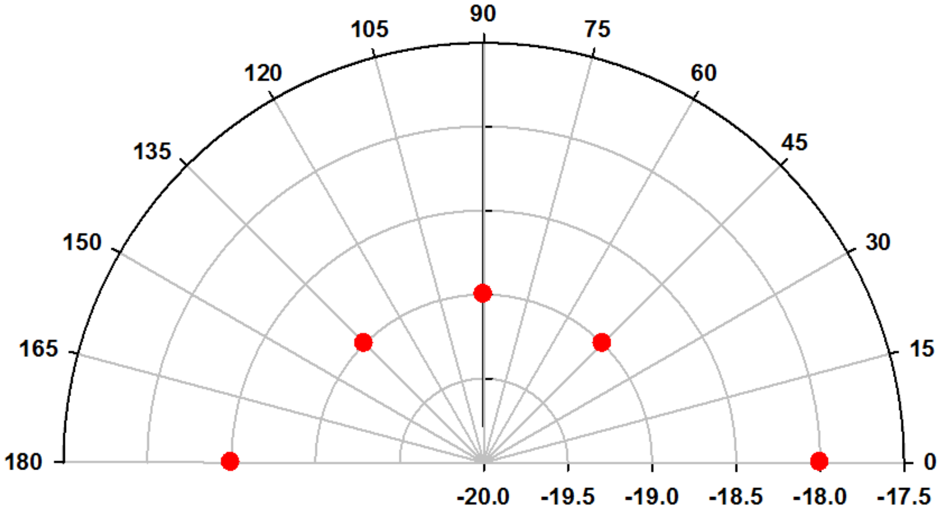

Figure 6.11: Polar plot of the conversion efficiency dependence on the angle of polarisation for a waveguide of W = 1 μm and x = 0.2

6.4 Discussion on Performance

Even though these SiGe waveguides were not specifically designed and optimised for nonlinear applications, the previous section has shown that their performance as broadband FWM-based devices operating in the C-band is noteworthy.

A common way to assess the performance of waveguides is the two-photon absorption figure of merit defined as $\mathrm{FOM}_{TPA} = \mathrm{n}_2/(\beta_{TPA}\lambda)$ [165]. For the SiGe waveguides considered in this study, this figure of merit takes values ranging from 0.55 to 0.48 as the Ge concentration increases from 10% to 30%. These values are close to the silicon FOM_{TPA} (typically 0.38 ± 0.17 [165]) indicating that SiGe has the potential to be a competitive waveguide technology. This TPA figure of merit is mainly used to assess whether TPA is a limiting factor when a material is considered for use in all-optical switching [166, 167]. However, for the amounts of coupled power considered in these experiments ($\leq$ 300 mW), the impact of TPA was not strongly significant (see Figure 6.7). Therefore, for a fairer assessment of the relative performance of the waveguides with respect to their linear loss and nonlinearity, one can use a simpler figure of merit, defined here as $\mathrm{FOM} = \gamma\ \mathrm{L}_{eff}$. Figure 6.12 is a plot of the FOM for each of the waveguides characterised. Clearly, the best performance is reached for x = 0.2 and a width of 1.0 μm.

Note that one could anticipate attaining much higher FOMs through adopting a more complex waveguide design. Indeed, as for silicon [138, 165], where higher FOM values where achieved by adopting a structure combining silicon waveguides with highly nonlinear organic cladding materials, both the waveguide nonlinearity and dispersion

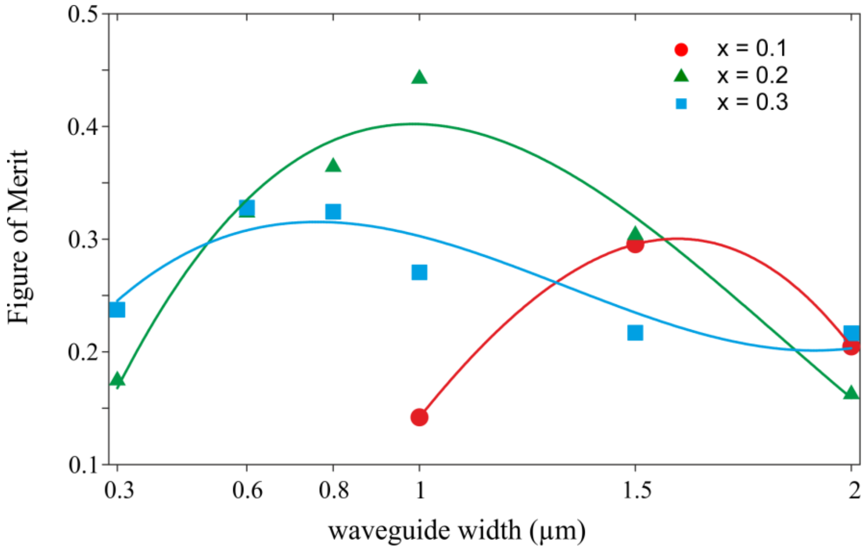

Figure 6.12: Figure of Merit as a function of the waveguide width for x = 0.1 (red circles), 0.2 (green triangles) and 0.3 (blue squares). The solid lines, corresponding to cubic polynomial fits, are only to guide the eye.

properties of SiGe waveguides at 1.55 μm can be significantly improved after appropriate engineering, thus making this waveguide technology a potential competitor to other state-of-art nonlinear waveguides with a new degree of freedom, namely, the germanium concentration profile.

For instance, broadband optical parametric amplification or highly efficient wavelength conversion can theoretically be attained by engineering the waveguide to exhibit anomalous chromatic dispersion at 1.55 μm. On this point, SiGe waveguides are once again similar to Si or other materials exhibiting a large refractive index. Indeed, one can engineer the cross section (width and also height) to apply large waveguide dispersion in order to shift the zero dispersion wavelength within the C-band. For the experiments reported in this chapter, the cross-sectional area of the waveguides were too large to reach the anomalous dispersion regime at 1.55 μm. However, with appropriate waveguide structural design and with the availability of an additional design degree of freedom embodied in the germanium concentration profile, it is expected that SiGe waveguides exhibiting a ZDW close to the telecommunications wavelengths can be realised.

In addition to dispersion engineering, SiGe waveguides can be made to exhibit higher FOM values than the ones reported here. Indeed, the loss figures are expected to be reduced by optimising the sidewall roughness of the waveguides during fabrication. Furthermore, the inclusion of low-index cladding material would significantly decrease the effective mode area and thus significantly boost the non-linear interactions. Also, numerical and experimental studies have concluded that the adoption of a graded germanium concentration profile (as will be explained in Chapter 7) gives rise to higher nonlinearities without excessively compromising the loss figures, thus leading to higher FOM values than in the case of the constant Ge concentration waveguides reported here.

6.5 Conclusion

This chapter reported the first comprehensive study of the linear and nonlinear properties of silicon germanium waveguides at the telecommunications wavelengths. The chapter began by highlighting the potential of the SiGe alloy as a platform for realising efficient nonlinear effects. In particular, SiGe technology was highlighted as an attractive solution for implementing a monolithically integratable chip-based MIR to NIR nonlinear converter that the CLARITY project targets.

The chapter then proceeded to discuss the design and the structure of the first generation of SiGe waveguides adopting a constant Ge concentration. The characterisation of these SiGe waveguides was then reported.

The loss, nonlinearity and two-photon absorption of SiGe waveguides of 10, 20 and 30% Ge concentration and of widths varying between 0.3 and 2 μm were characterised. The

	10% Ge	20% Ge	30% Ge
Range of losses (dB/cm)	0.6-5	1.5-4	3.5-5.2
Typical value (for a 2 μm width)	0.65	2.60	4.34

Table 6.4: Summary of waveguide loss measurements for varying levels of Germanium concentration

methodology of the measurement techniques was discussed and the experimental data were supported by numerical simulations provided by the NKUA.

The waveguide losses were found to be closely linked with the effective mode area and confinement factor. For instance, it was found that for small waveguide widths, the low confinement leads to poor guiding and high losses. Furthermore, for waveguides with larger widths, the increase in confinement factor results in a higher mode overlap with the lossier SiGe core. Table 6.4 presents a summary of the typical loss figures for the waveguides of varying Ge concentration.

The nonlinearity of the waveguides was found to increase with germanium concentration, as expected. The maximum value of nonlinear coefficient γ was found to occur for widths between 0.8 μm and 1.0 μm as these widths represent the optimum balance between the poor mode confinement that takes place at smaller widths and the larger effective mode areas that occur at bigger waveguide widths. Maximum γ values of 16, 26 and 37 /W/km were recorded for waveguides of 10, 20 and 30% Ge concentration respectively.

The nonlinear loss (TPA) of the waveguides was also measured and the TPA coefficient β_2 was found to increase with germanium concentration, with values of 1.16, 1.24 and 1.5 cm/GW for 10, 20 and 30% Ge concentration respectively. However, the TPA was too low to have any significant impact at the power levels considered in all of the characterisation measurements.

The effects of dispersion and polarisation on the nonlinear performance of the waveguides were also investigated. The FWM bandwidth was found to increase with Germanium concentration as higher Ge content leads to a reduced net chromatic dispersion at 1.55 μm. Furthermore, the FWM conversion efficiency was found to be largely independent of the state of polarisation, with a variation of just 1 dB for a 0 to 180 degrees variation in the angle of polarisation.

Finally, the chapter concluded by discussing the relative performance of the waveguides studied. A FOM based on γL_{eff} revealed that a waveguide of 1 μm width and 20% Ge concentration would provide the optimum performance as a nonlinear device, a conclusion which was in agreement with the experimental observations when FWM experiments were conducted in the various waveguides.

The study reported in this chapter represents the first of its kind on SiGe waveguides. It confirms SiGe waveguides as a promising candidate not just for the mid-infrared but also for all-optical processing at telecommunication wavelengths. While the performance of the SiGe waveguides reported here does not compare favourably to state-of-art silicon waveguides and nanowires, one should not overlook that these two technologies are currently at completely different stages of maturity. Furthermore, the findings of this study can inform the design of optimised nonlinear waveguides, allowing the manipulation of not just the waveguide dimensions but also the material composition.

Chapter 7

All-Optical FWM-Based Wavelength Conversion in SiGe Waveguides

7.1 Introduction

While the first generation of SiGe waveguides studied in Chapter 6 only represent an early fabrication attempt and are not specifically designed to optimally perform in the 1.55 μm wavelength region, the characterisation study has revealed high figures of merit indicating the suitability of the waveguides in realising highly efficient nonlinear effects, suitable for a wide range of all-optical processing applications. The concentration of germanium in the waveguides was shown to strongly affect the linear and nonlinear optical properties of the waveguides such as loss, two-photon absorption, nonlinearity and dispersion, thus adding another degree of freedom in the waveguide design.

This chapter aims to further investigate the potential of using SiGe waveguides as highly efficient all-optical processing devices. In doing so, it aims to demonstrate FWM-based wavelength conversion in the waveguides at 1.55 and 2 μm wavelengths.

Wavelength conversion based on FWM in $\chi^{(3)}$ media is becoming increasingly attractive for telecoms applications. The ultra-fast response time of $\chi^{(3)}$ nonlinearities makes FWM-based wavelength translation ideal in dense high speed wavelength division multiplexed (WDM) networks, where transparency to the bit rate and the modulation format are crucial requirements [12].

Furthermore, FWM-based wavelength conversion is not only limited to telecoms-based applications. In recent years research has focused on engineering devices, which, apart from exhibiting strong nonlinear characteristics, they also possess tightly controlled chromatic dispersion profiles, so that high FWM conversion efficiencies, high signal gains and broad operation bandwidths can be achieved. With such devices, the broadband phase-mathced spectral translation of MIR signals to NIR idlers that the CLARITY project targets, can be achieved.

The first part of this chapter reports wavelength conversion experiments of 40 Gbaud DPSK and QPSK signals at 1.55 μm using a 2.5 cm long silicon germanium waveguide. The waveguide used in these experiments has a 1 μm width and 20% germanium concentration ($Si_{0.8}Ge_{0.2}$), revealed by the characterisation study in Section 6.4 to possess the highest FOM of all (first generation) SiGe waveguides tested. The experimental setup is described and the wavelength conversion is characterised by conducting Bit-Error Ratio (BER) tests and contrasting constellation diagrams of the signal and the converted idler.

The second part of the chapter focuses on the nonlinear conversion from a MIR signal into a NIR idler using a 3 cm long graded index SiGe waveguide. The SiGe waveguide used in this set of experiments represents a second generation of waveguides which adopt a graded Ge concentration profile and which had been designed to show optimum broadband phase-matched FWM performance when pumped at wavelengths in the neighbourhood of 2.1 μm. The setup used is discussed and the experimental data of converting a signal centered at 2.65 μm to a 1.77 μm idler using a pump centered at 2.12 μm is presented. Furthermore, the data collected from CE versus wavelength detuning experiments are analysed and contrasted with numerical simulations from the NKUA.

7.2 FWM-based Wavelength Conversion of C-Band PSK Signals in a SiGe Waveguide

7.2.1 Device Description

The $Si_{0.8}Ge_{0.2}$ waveguide used for the conversion of telecommunications signals, was a strip waveguide embedded in Si and was fabricated by CEA-Leti. The waveguide had a width of 1 μm with a 2 μm taper at the entrance to facilitate more efficient coupling. The length of the taper was 0.5 mm and the total device length was 2.5 cm. The fabrication method consisted of realising a 1.4 μm thick SiGe layer directly on 200 mm Si substrates. The layer was epitaxially grown by reduced pressure chemical vapor deposition (RP-CVD) to control precisely the Ge percentage and uniformity. The strip was etched using inductively coupled plasma reactive ion etching (ICP RIE) technique and encapsulated by a 12 μm Si cladding layer with the same RP CVD technique. Figure 7.1 shows a typical scanning electron microscope (SEM) image of the waveguide cross-section before and after encapsulation.

The propagation loss of the waveguide, two-photon absorption and effective nonlinearity of the waveguide were measured at 1.55 μm to be 1.4 dB/cm, 1.25 cm/GW and 25.8 /W/m respectively, as reported in Chapter 6.

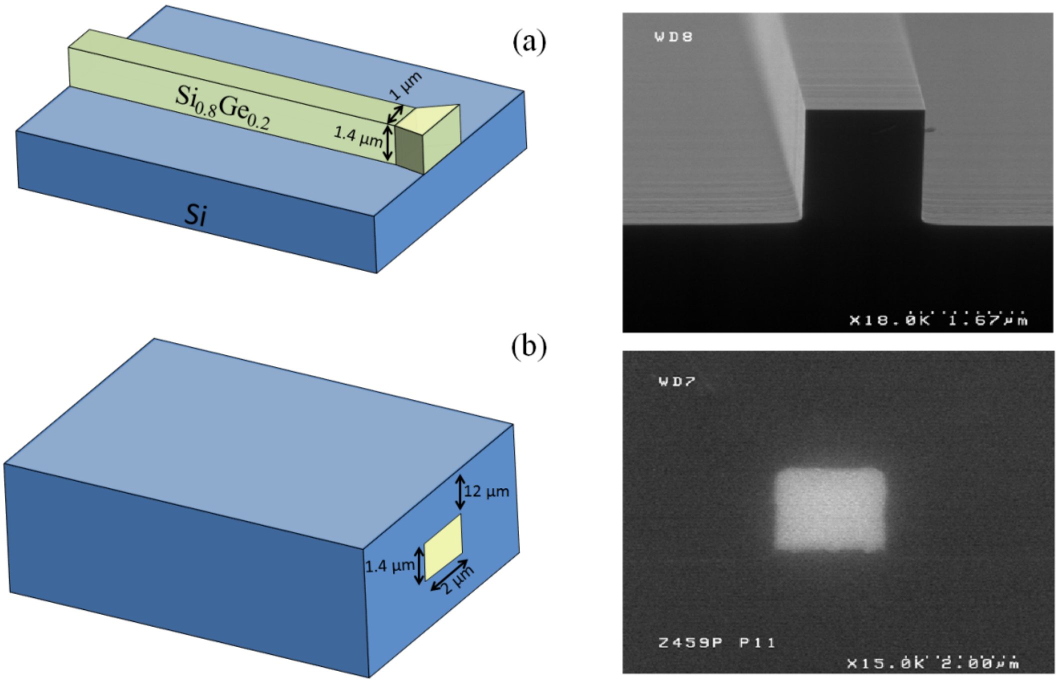

Figure 7.1: 1 μm wide SiGe strip waveguide before (a) and after (b) encapsulation in a 12 μm Si cladding layer. The total device length of 2.5 cm includes a 0.5 mm taper at its entrance.

From the waveguide analysis that NKUA conducted, it was concluded that the waveguide is predominantly quasi-TM for the aforementioned width, which can be also observed by noting that the effective mode areas for the two polarisation states are 1.82308 μm^2 for TM and 1.8508 μm^2 for TE respectively, indicating a marginally smaller A_{eff} and thus stronger nonlinear interactions for the TM mode. Figure 7.2 depicts the field profiles of the fundamental TE and TM modes at 1550 μm.

The calculation of the dispersion curve is a very useful tool for the evaluation of the bandwidth of the FWM process in the waveguide. NKUA's analysis showed that within

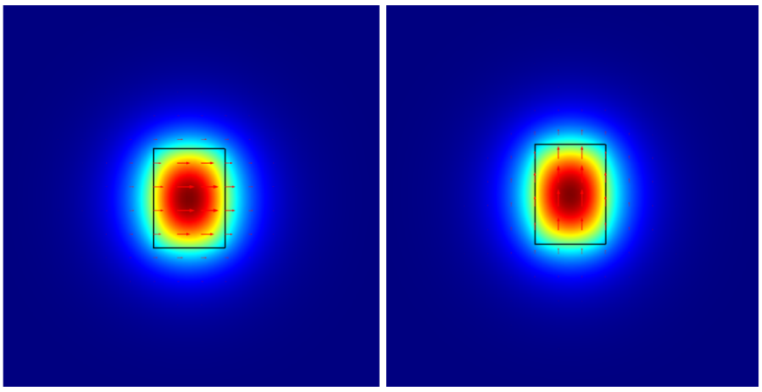

Figure 7.2: Field profiles of the TE (left, n_{eff}=3.5238) and TM (right, neff=3.52422) fundamental modes for waveguide width 1 μm height 1.4 μm (courtesy of Dr. Adonis Bogris)

the wavelength band under investigation, dispersion was always normal and quite far from any zero crossing.

The calculated dispersion curves for the two polarisation axes of the waveguide are shown alongside the effective mode area in Figure 7.3. As can be seen from the figure, the waveguide was predicted to exhibit -866 ps/nm/km dispersion for TE and -863 ps/nm/km for TM respectively at 1.55 μm. Furthermore, based on the numerical simulations of the effective area for the two polarisation states, the effective nonlinearity of the waveguide was estimated to be 22.95 and 23.3 /W/km for TE and TM respectively, indicating a close agreement with the experimental measurement reported in Chapter 6.

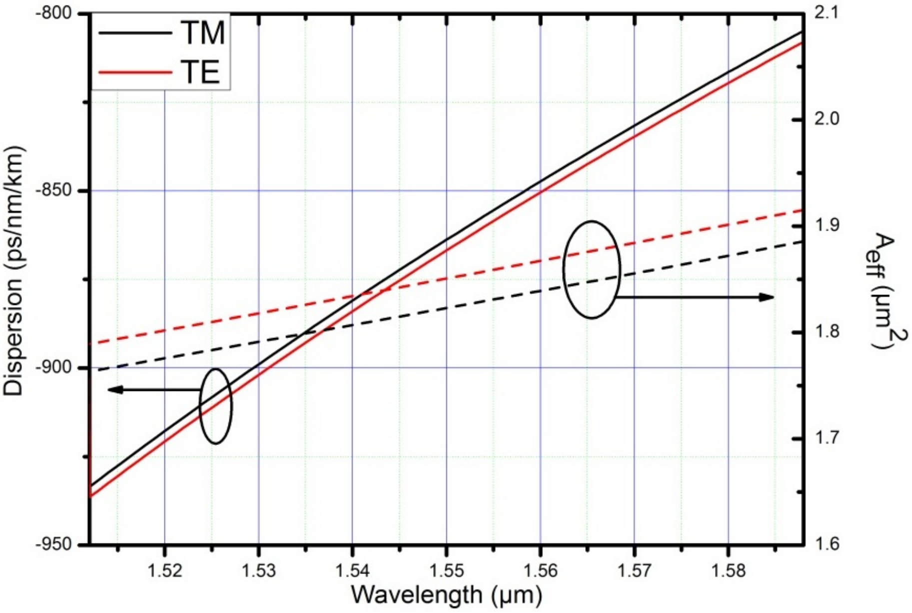

Figure 7.3: Dispersion curves and effective mode areas for the structure under investigation as a function of wavelength (courtesy of Dr. Adonis Bogris).

7.2.2 Experimental Setup and Results

The wavelength converter setup is shown in Figure 7.4. Light from a CW pump laser at 1557.36 nm was coupled through an 80/20 coupler with a 40 Gbaud non-return-to-zero (NRZ) DPSK (or QPSK) 2^{31}-1 pseudo-random bit sequence (PRBS) signal. The two signals were then amplified in an erbium doped fibre amplifier (EDFA) and their state of polarisation was aligned to the TE polarisation axis of the $\mathrm{Si}_{0.8}\mathrm{Ge}_{0.2}$ waveguide through a polarisation controller (PC). A commercial lensed fibre with a spot size of 2 μm was used to launch the signals into the waveguide, and a coupling loss of approximately 4.2 dB was measured, resulting in successfully coupling a total of 290 mW of pump power and 115 mW of signal power into the waveguide, which is well below the experimentally measured TPA threshold of 2.5 W.

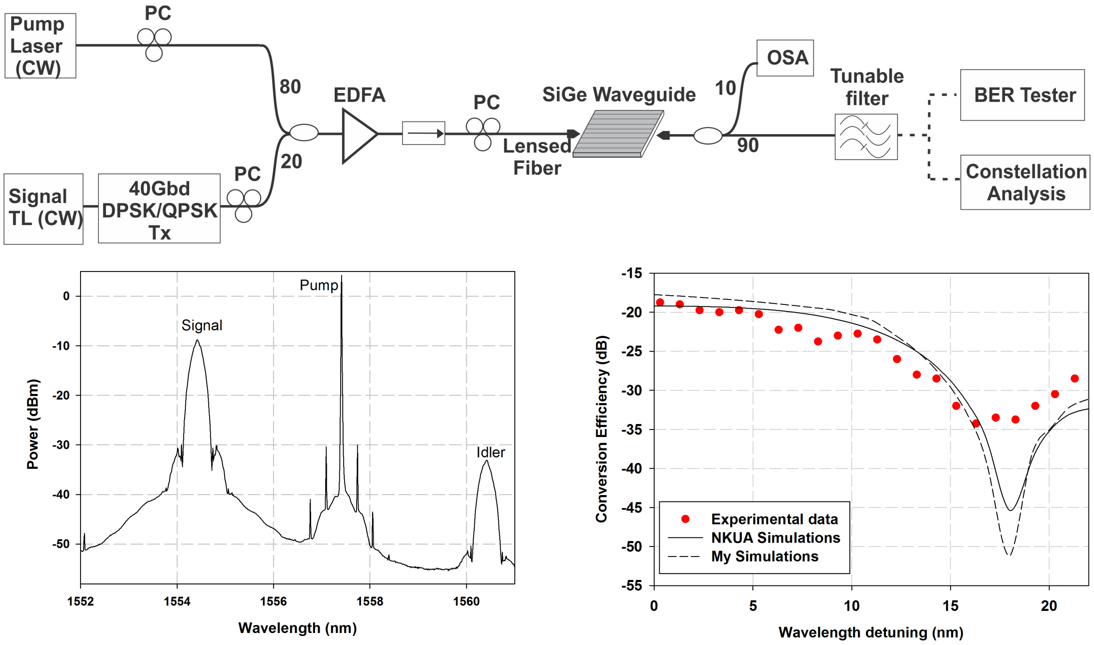

Figure 7.4: Experimental set-up used to characterise the wavelength converter. Bottom: spectral trace of FWM measured at the output of the waveguide (left); and numerical calculation (line) and experimental measurement (circles) of FWM conversion efficiency versus wavelength detuning (right).

At the output, the performance of the wavelength converter was assessed in terms of eye and constellation diagrams, as well as BER measurements. For this purpose, the converted signal (i.e. the FWM idler) was filtered using a 2 nm tunable bandpass filter and detected. For the BER measurements, the DPSK signal was demodulated using a 1-bit delay line interferometer (DLI) which was followed by an optically pre-amplified receiver, whereas for the QPSK signal, an optically pre-amplified coherent receiver and a real-time data acquisition system were used.

An optical spectral trace obtained at the output of the waveguide for a DPSK input signal with a 3 nm separation from the pump is shown at the bottom left of Figure 7.4. The figure shows a FWM conversion efficiency (CE) of ~-18 dB (defined as the ratio of the power of the converted idler to the output signal power). The OSNR of the converted signal was ~23 dB (Res=0.1nm). The FWM CE as a function of wavelength detuning between the pump and the data signal is also plotted (Figure 7.4 (bottom, right)). A 3 dB bandwidth of approximately 22 nm was measured. Furthermore, the experimental measurements show good agreement with both the results obtained from NKUA's numerical model (presenteed in Chapter 6 Section 6.3.4) and the those obtained using the more basic SSFT-based model described in Chapter 2, Section 2.2.2.2.

Figure 7.5a shows constellation diagrams of the original DPSK data signal (B2B) and the converted idler. The B2B measurement exhibited a root-mean-square (rms) error vector magnitude (EVM) of 6.2%, in contrast to the idler for which an rms EVM of 15.27% was measured. Furthermore, the eye diagrams shown in the inset of Figure 7.5b

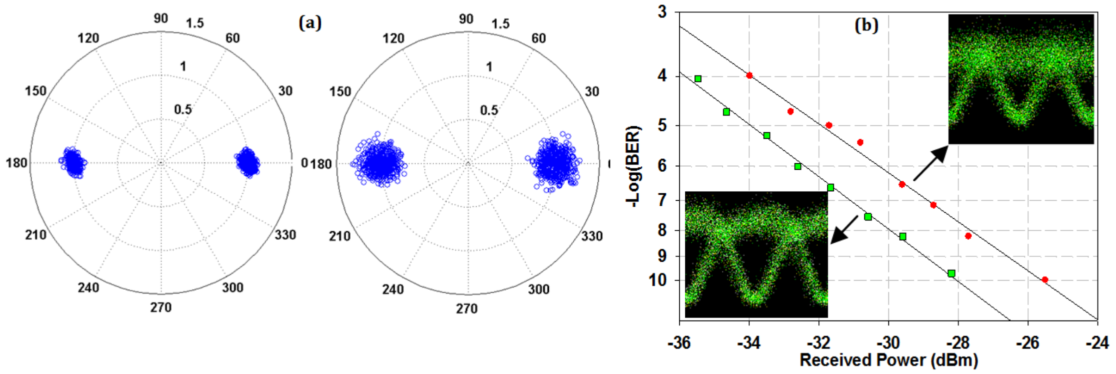

Figure 7.5: (a) Constellation diagrams for the original 40 Gbit/s DPSK signal (left) and idler (right) (b) BER curves and eye diagrams for the B2B (square) and the idler (circle).

show an open eye for the idler, albeit with some degradation in comparison to the B2B. BER measurements revealed an approximately 2.3 dB conversion penalty at a BER of 10^{-9} relative to the B2B.

Figure 7.6a shows the 40 Gbaud QPSK constellation diagrams for the B2B signal and the converted idler. An rms EVM of 9.7% was obtained for the B2B in contrast to 12.9% for the idler. Furthermore, the BER curves shown in Figure 7.6b show a 2 dB power penalty at BER = 10^{-3} as a result of the conversion. Since those BER measurements were taken using a real-time data acquisition system that samples discrete clusters of data at a time, no BER measurements lower than 10^{-6} were possible. This is because beyond this limit the system would need impractically long time to sample enough data bits and determine the BER result with sufficient accuracy.

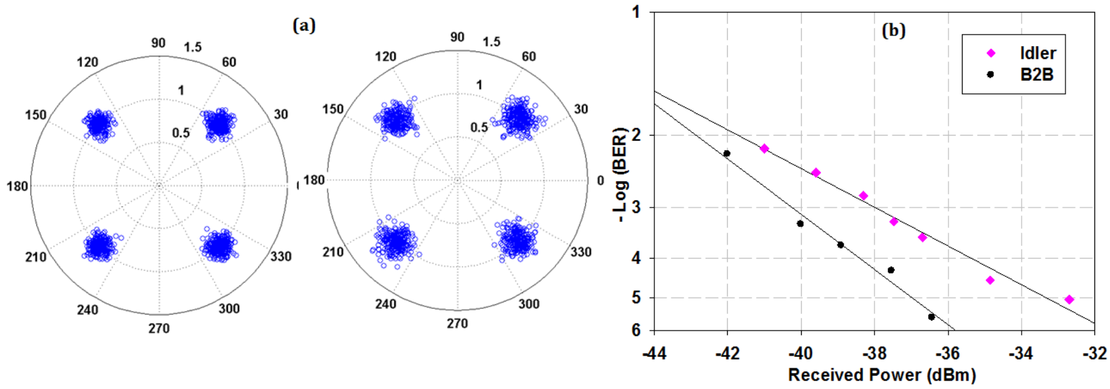

Figure 7.6: (a) Constellation diagrams for the 80 Gbit/s QPSK B2B signal (left) and idler (right) (b) BER curves for the B2B signal (circle) and the idler (diamond).

7.3 Wavelength Conversion of 2 μm Signals in Second Generation SiGe Waveguides

7.3.1 Introduction

This section reports the characterisation experiments carried out on the second generation of silicon-germanium waveguides. The characterisation experiments aimed to assess the performance of the waveguides as broadband wavelength converting elements when pumped in the vicinity of 2 μm. The experiments also aim to deduce the position of the zero dispersion wavelength of the waveguide in order to appreciate the accuracy of NKUA's numerical model in estimating the dispersion. In the experiments reported here, these particular waveguides are expected to exhibit a zero-dispersion wavelength in the vicinity of 2.0-2.1 μm. This would allow the use of a pump operating close to these wavelengths, together with a signal which would not extend too far in the mid-infrared.

These studies were of interest within the context of the CLARITY project, since a third, more optimised, waveguide generation will benefit from their outcome in the design process of the waveguides. Those final generation waveguides are predicted to perform better with respect to the overall objectives of CLARITY, owing to a more suitable dispersion profile (and a longer zero-dispersion wavelength) and better coupling, enabling the efficient conversion of a 4.65 μm MIR signal into the NIR when pumping at wavelengths longer than 2.4 μm.

7.3.2 Device Description

All the SiGe waveguides used in the previous experiments followed a simple silicon on insulator structure and a constant germanium concentration profile. Furthermore, these first generation waveguides, were not engineered to achieve broadband wavelength conversion but rather to allow a simple and direct route to investigating SiGe alloy's optical properties.

A second generation of SiGe waveguides was desgined by the NKUA to target broadband spectral translation when pumping in the 2-2.3 μm region. The design was based on extensive numerical modeling of the optical properties of various SiGe waveguide structures, and a SiGe waveguides on a silicon on insulator (SOI) substrate (Figure 7.7) was again selected. However, unlike the first generation of SiGe waveguides, the proposed design of the second generation adopted a gradient germanium concentration profile.

The proposed waveguide design favors TM polarisation to match that of the QCL sources available for use as the MIR seed signal. On top of the silicon dioxide (SiO_2) substrate a slab layer of thickness S is introduced as shown in the Figure 7.7. The SiGe section is offset by a silicon part of thickness δ. The waveguide width is denoted by W in the

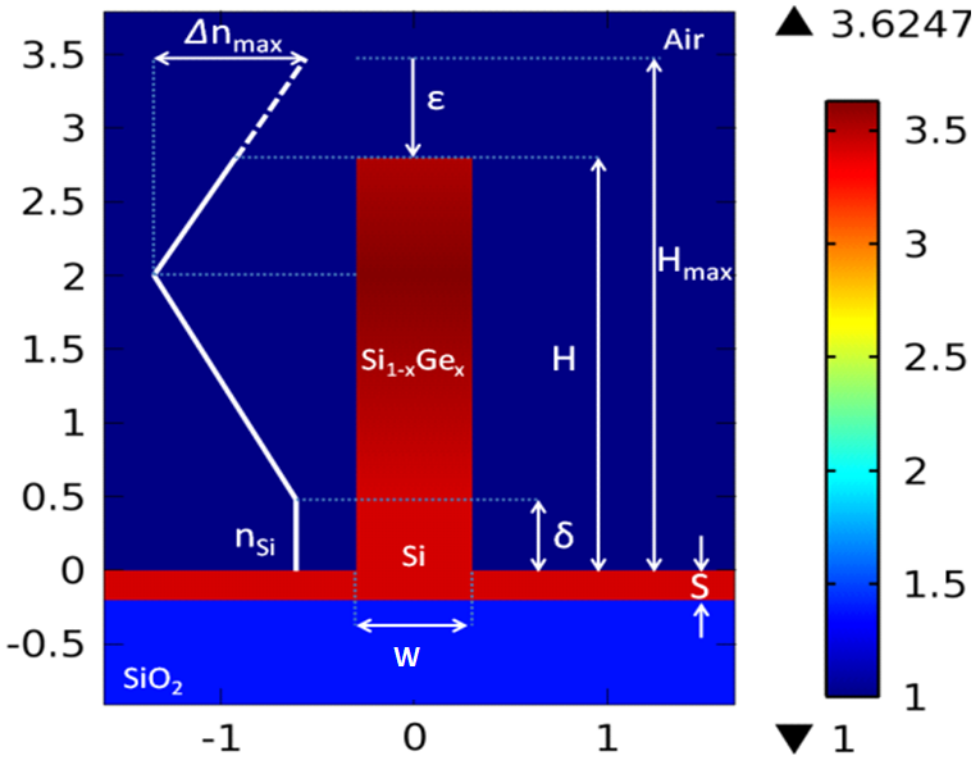

Figure 7.7: Generic structure of the SiGe based waveguide for MIR to NIR conversion (courtesy of Dr. Adonis Bogris)

figure, and H is total waveguide height after etching from the initial deposition (H_{max}) by ϵ. The index profile is a step-index in the horizontal x-direction and a double linearly graded one in the vertical y-direction. Furthermore, the index in the vertical direction varies from a minimum value of n$_{Si}$ (refractive index of silicon) at y=δ to a maximum of n_{Si}+Δ n_{max} at y=δ+H_{max}/2 and then reduce again to n_{Si} at y= H_{max} as depicted in Figure 7.7.

The height H (which also includes ϵ and δ since =δ+H_{max}-ϵ), the width W, the slab height S and the Ge concentration in the core $n_{Si} + \Delta n_{max}$ can all be tuned in order to properly engineer the waveguides dispersive properties to suit the MIR to NIR spectral translation that CLARITY targets. Calculations performed by the NKUA which in addition to studying the effect of these parameters on dispersion, also took into account the mode confinement in the waveguide, the mode overlap between the pump and the signal, and the fabrication capabilities of CEA-Leti (tasked with waveguides fabrication), have concluded that for an efficient MIR to NIR conversion, the structural parameters would take values within specific intervals given below:

- W (width): 400-600 nm
- H (height): 1.7-2.1 μm
- S (slab height): 200 nm

- δ (Silicon part height): 0-1 μm.
- maximum Ge concentration x: 40%

The device used in the broadband spectral conversion experiments reported in this chapter, is grown by reduced pressure chemical vapor deposition on silicon wafer and was also fabricated by CEA-Leti. The device presents a gradient Germanium profile obtained by varying the germane mass-flow during growth, the dichlorosilane mass-flow staying constant [168]. More precisely, in the SiGe layer the concentration of Ge is linearly increased from 0 % to 42 % and then decreased back to pure Si symmetrically as shown in Figure 7.7. The waveguide height is approximately 1.5 μm on a Si slab of 210 nm.

In order to optimise the launching efficiency, a 5 μm width taper has been added at the input of the 3 cm-long waveguide (see Figure 7.8). The waveguide has a nonlinearity of 35 /W/m at 2 μm and its losses are estimated to be close to 2 dB/cm.

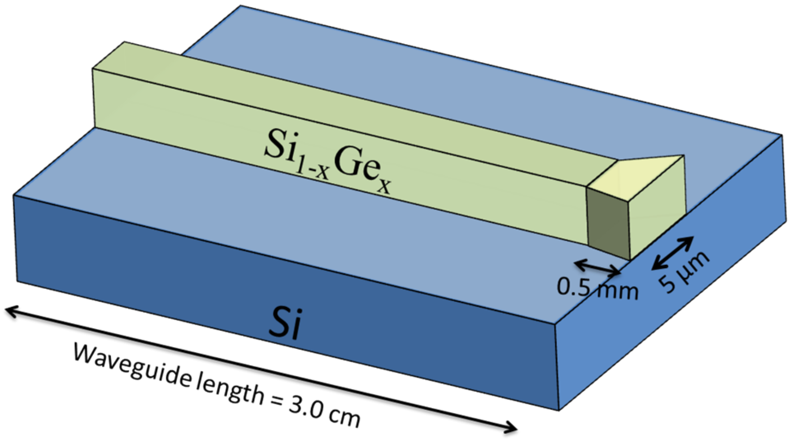

Figure 7.8: Sketch of the SiGe waveguide used in the MIR to NIR wavelength conversion experiments.

7.3.3 Experimental Procedure

This device has been specifically designed for wavelength conversion from MIR to NIR. The dispersion curve, calculated by the NUKA using a commercial mode solver is plotted in Figure 7.9a and presents a zero dispersion wavelength close to 2075 nm. As demonstrated before, the phase-matching condition for broadband degenerate four-wave mixing in a waveguide is given by:

$$\beta_2\omega^2 + \frac{\beta_4}{12}\omega^4 + 2\gamma P = 0 \tag{7.1}$$

where β_2 and β_4 are the second and fourth order dispersion respectively at the pump frequency, γ is the nonlinear parameter of the considered waveguide, P is the input power and ω is the frequency detuning between pump and signal.

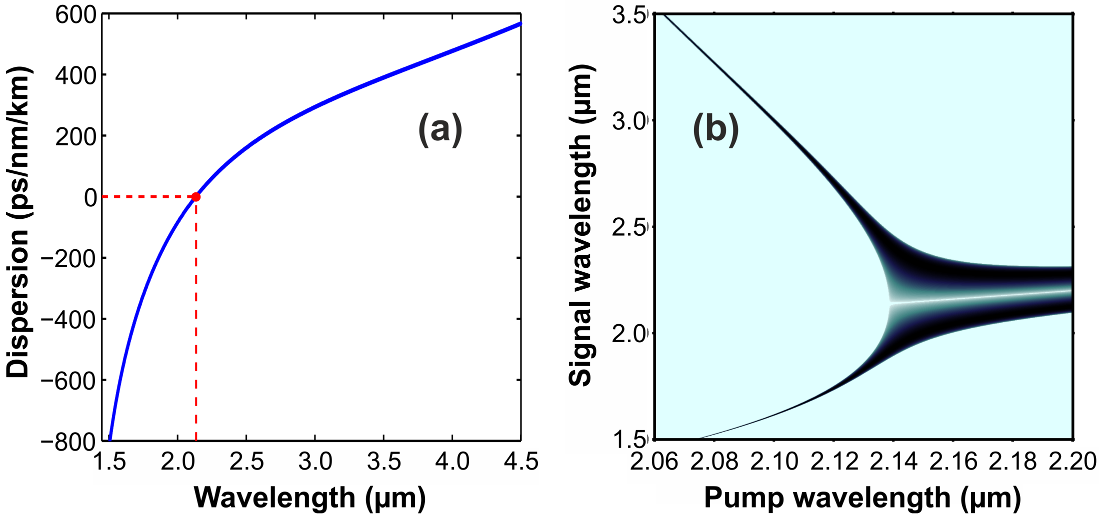

Figure 7.9: (a) Estimated dispersion curve. The red point corresponds to zero dispersion wavelength (b) Corresponding phase matching diagram.

The phase matching diagram associated with this dispersion was evaluated (using the same numerical model as in Chapter 5, Section 5.5.2) and is shown in Figure 7.9b. As has been mentioned in Chapter 5, four wave mixing is a similar process to modulation instability (MI) that is observed in anomalous dispersion regime exhibiting two gain bands in the spectrum. However, the gain bands originating from pumping in the normal dispersion regime are narrower and located further away from the pump [137, 169]. This means that experimentally, the conversion efficiency will be maximal for optimal wavelength defined as [169]:

$$\Omega_{opt} = \sqrt{\frac{2\sqrt{3(\beta_2^2 - 2\beta_4\gamma P)}}{\beta_4} - 6\frac{\beta_2}{\beta_4}} \tag{7.2}$$

It is clear from Equation 7.2 that the optimal wavelength depends strongly on both β_2 and β_4. Therefore, one can investigate the impact of the dispersion parameters (β_2 and β_4) on the FWM performance by varying the detuning between the pump and the signal and observing the impact on the conversion efficiency. The experimental data can then be contrasted with the numerical simulations of the dispersion and essential information about the real dispersive properties of the waveguide, in particular its zero-dispersion wavelength, can be extracted.

Following this methodology, two main experimental tests were adopted. The first is varying the pump wavelength with respect to the signal and assessing the corresponding

FWM conversion efficiency. The second is conducting the same assessment while varying the signal wavelength with respect to the pump.

7.3.4 Experimental Setup

The experimental setup is shown in Figure 7.10. The wavelength conversion experiments were carried out using two IPG single frequency broadly tunable CW lasers operating in the vicinity of 2 μm. The first, used as the pump, can be tuned from 2.0 to 2.5 μm whereas the second, used as the signal, can be tuned from 2.0 to 2.8 μm. A beam splitter adapted to the lasers' wavelength was used to couple together the signal and pump. Two waveplates were used to control the input polarisation into the waveguide. The light was coupled via a CaF_2 lens (transparent up to 8 μm) into a lensed fibre used to inject into the waveguide and collected at the output by a specific MIR objective lens. The output light was analysed on an optical spectrum analyser (OSA) limited to 2.4 μm.

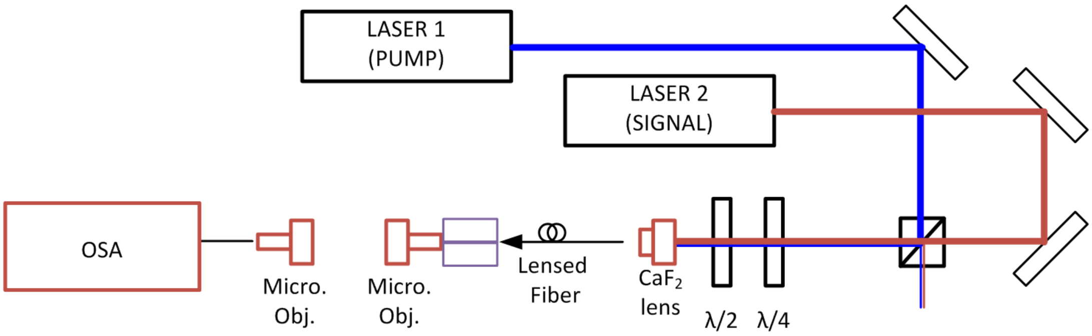

Figure 7.10: Experimental setup of the 2 μm broadband FWM experiment.

7.3.5 Typical Broadband FWM Spectra

The performance of the waveguide as a broadband nonlinear converter was assessed by placing the signal at a large wavelength detuning from the pump.

Figure 7.11 reports the spectra obtained when a pump centered at 2122 nm was used and the signal wavelength was varied. Figure 7.11a shows the converted idler for a signal centred close to the limit of the OSA (i.e. 2400 nm). Note that the conversion efficiency reading on the OSA, here -25 dB, does not represent the real value. This is because the output optics (such as the output micro-objective lenses and the fibre connecting to the OSA) have higher losses at longer wavelengths, thus resulting in bigger attenuation of the output signal than the shorter wavelength idler field. To deduce the correct value of the conversion efficiency, the loss of the output optics with respect to wavelength was characterised. This wavelength-dependent loss information was then used to compensate for the higher losses experienced by the signal than the idler, thus correcting the conversion efficiency values.

Figure 7.11b demonstrates an even broader conversion of a 2625 nm signal to a 1782 nm idler. Finally, Figure 7.11c presents one of the broadest wavelength conversions reported in literature when a signal at 2650 nm was converted to an idler at 1770 nm.

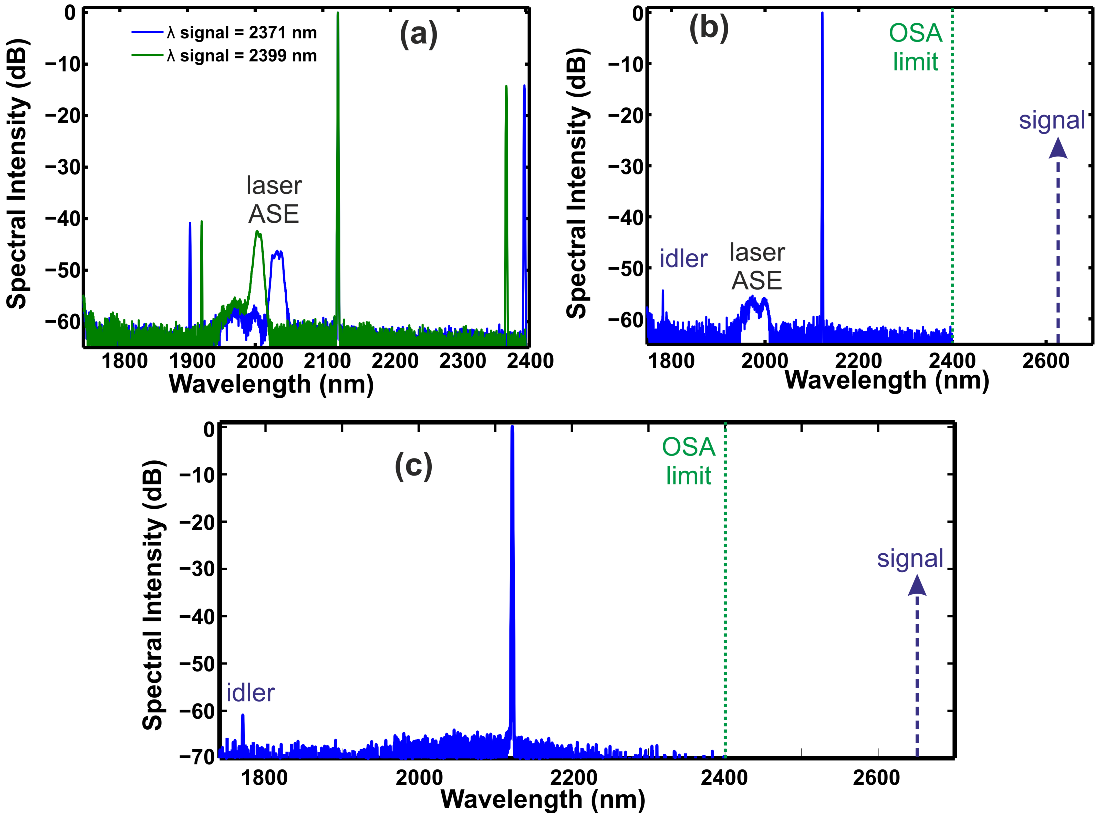

Figure 7.11: (a) Spectra for a signal at 2371 nm (green line) and at 2399 nm (blue line). (b) Spectra obtained for a signal centered at 2625 nm and (c) at 2650 nm. For all spectra, the pump wavelength is 2122 nm.

7.3.6 FWM Conversion Efficiency and ZDW Estimation

The conversion efficiency (CE), defined here as $P_{Signal(output)}/P_{idler(output)}$ was recorded for a wavelength sweep over the tunable range of the signal and pump lasers. The conversion efficiency values were deduced from the OSA up to 2.4 μm (OSA readings were corrected to account for the wavelength-dependent loss of the optics as explained above). For measurements beyond the OSA limit of 2.4 μm, the CE values were estimated through measuring the signal power at the output of the sample and then deducting the loss of the output optics at the signal wavelength.

7.3.6.1 Variation of the Pump Wavelength for a Fixed Signal Wavelength

The first test in investigating the dispersive properties of the waveguide was to observe the FWM CE when the signal was kept fixed and the pump wavelength was varied. Figure 7.12 shows the CE versus pump wavelength for three different signal wavelengths (a) 2290 nm (b) 2340 nm and (c) 2400 nm.

The experimental data are contrasted with the numerical simulations of the expected CE curve in each case. A pump power of approximately 75 mW and a signal power of 10 mW were used, and a loss of α= 2dB/cm and nonlinearity of γ=36 /W/m were considered in the simulations.

By contemplating the curves presented in Figure 7.12, a pattern can be recognised. When the experimental data (black circles) is compared to the numerical simulations of the CE curve based on a ZDW of 2075 nm (red line), the agreement is not satisfactory. The results however show a much better agreement if a 60 nm red shift in the ZDW (from 2075 nm to 2135nm) of the waveguide is considered (blue line). This was an early

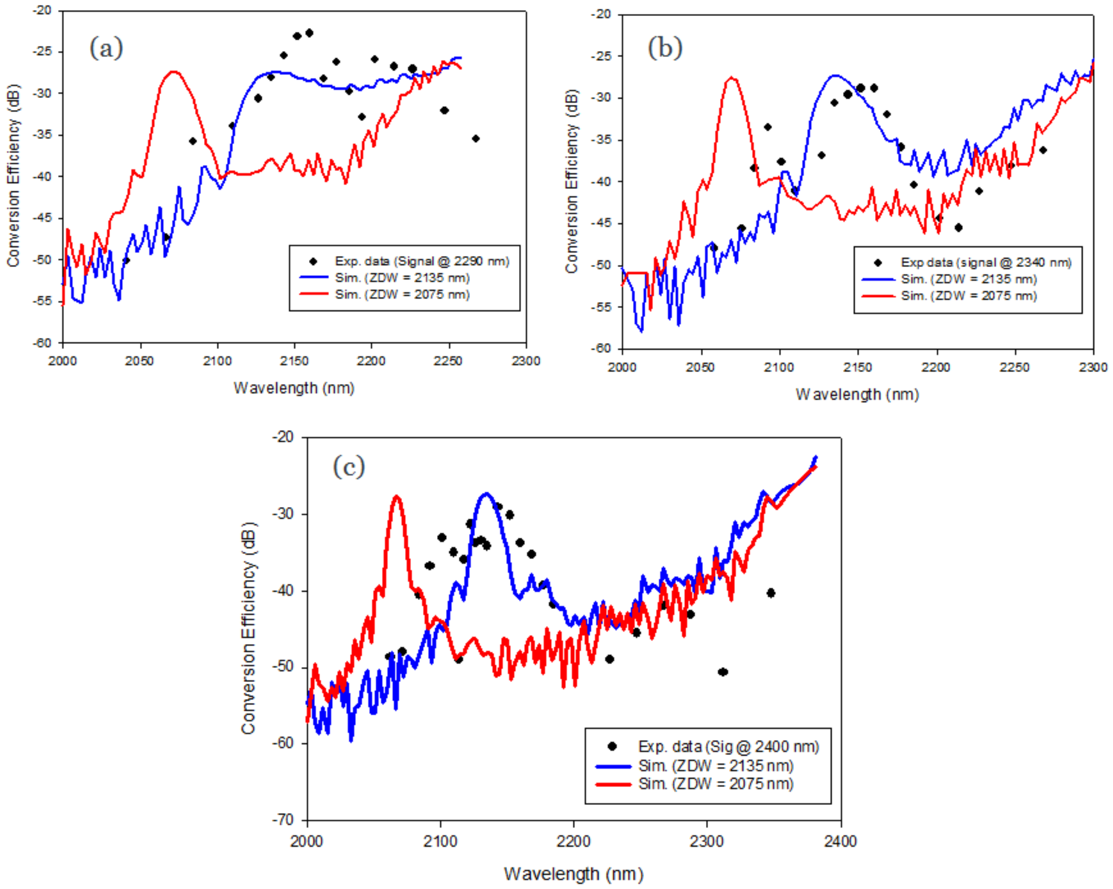

Figure 7.12: Conversion efficiency vs pump wavelength curves for three different signal wavelengths (a) 2290 nm (b) 2340 nm and (c) 2400 nm. The black circles represent the experimental data, and the red and the blue lines represent numerical simulations based on a ZDW of 2075 nm and 2135 nm respectively.

indication that the theoretical dispersion estimated by the NKUA could be inaccurate by 60 nm.

7.3.6.2 Variation of the Signal Wavelength for a Fixed Pump Wavelength

To put the 60 nm ZDW shift into prospective, Figure 7.13 depicts three plots: (a) the original dispersion contrasted with the one red-shifted by 60 nm (b) the phase matching curve of the original unshifted dispersion and (c) the phase matching curve corresponding to the 60 nm red-shifted dispersion curve.

The two phase matching curves (Figure 7.13 (b) and (c)) emphasise the importance of choosing the pump wavelength. For instance, selecting a pump wavelength of 2135 nm (as indicated by the dashed red line in Figure 7.13 (b) and (c)), would lead to operating in the anomalous dispersion regime if the unshifted dispersion is considered, and to operating in the normal regime if the shifted dispersion is considered. This would lead to a significant difference in the expected conversion efficiency vs signal wavelength curves. Thus, to verify the findings of the first test, the conversion efficiency evolution with the signal wavelength for a fixed pump was also assessed.

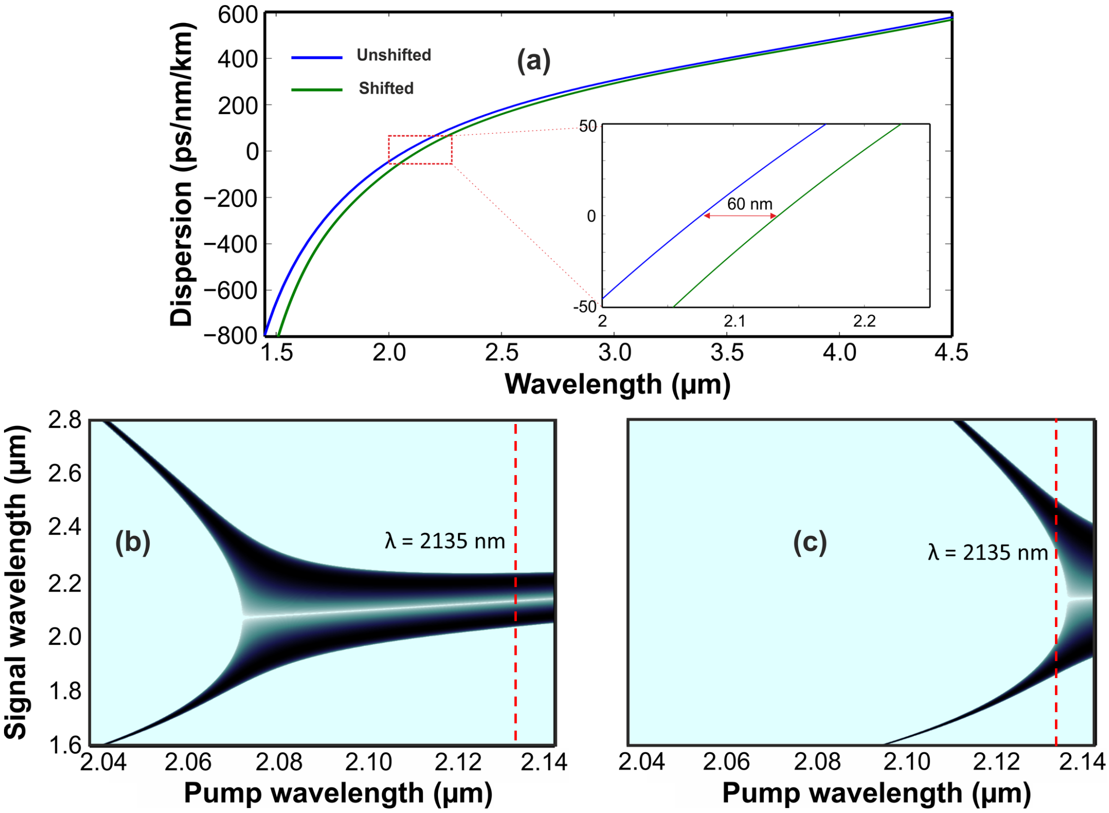

Figure 7.13: (a) Contrast of the the original unshifted dispersion curve (blue) with the shifted curve (green). Phase matching diagrams corresponding to the (b) original unshifted dispersion curve and (c) the shifted dispersion curve.

Figure 7.14 depicts the CE curves for four different pump wavelengths, 2047 nm (Figure 7.14a), 2160 nm (Figure 7.14b), 2065 nm (Figure 7.14c), and 2122 nm (Figure 7.14d). In all four figures the same pattern that was deduced from Figure 7.12 is repeated again. The experimental data shows a much better agreement with the numerical simulations for the case in which a 60 nm red shift in the ZDW is considered. In both Figures 7.12 and 7.14, the deviations from a perfect agreement between the experimental data and the simulations based on a shifted ZDW, can be considered to be within the measurements uncertainty. The source of such uncertainty is attributed to the change of launching conditions that takes place during the course of taking measurements. The complexity of the experimental setup meant that it was difficult to precisely keep the power levels constant at the various stages of the setup while taking such large amount of data points.

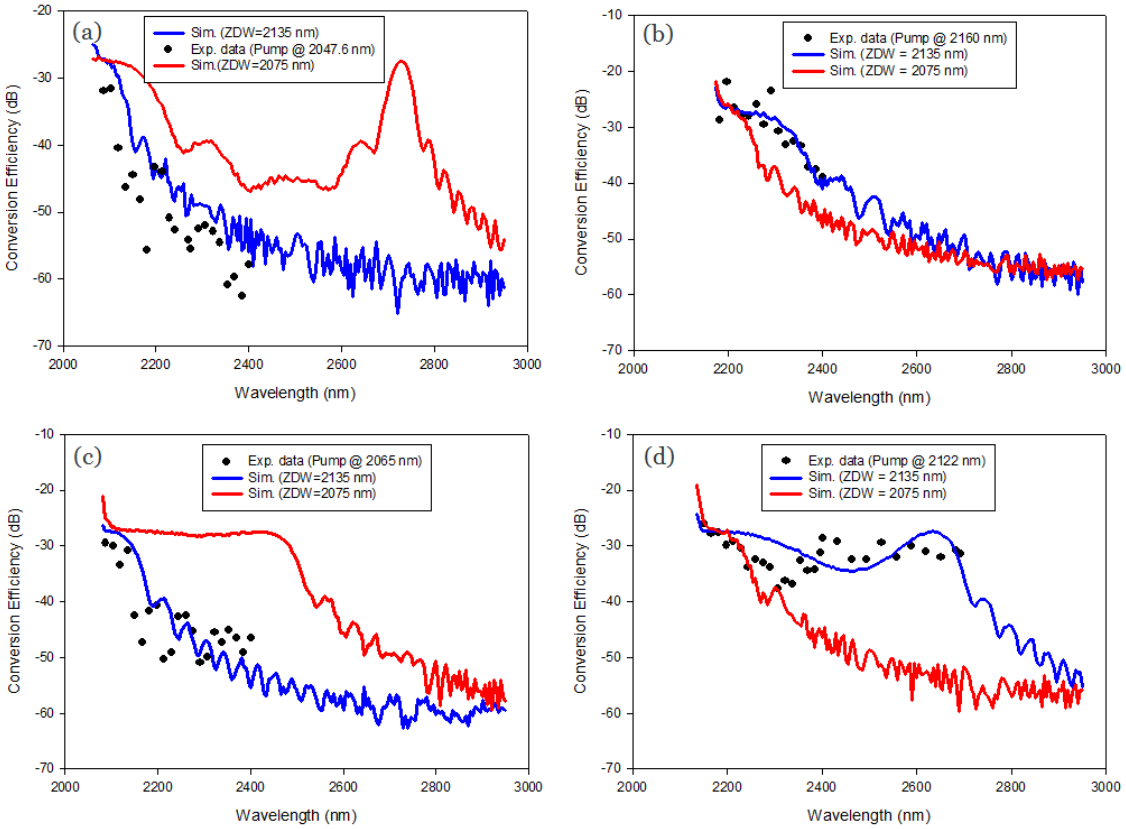

Figure 7.14: Conversion efficiency vs signal wavelength curves for three different pump wavelengths (a) 2047 nm, (b) 2160 nm, (c) 2065 nm and (d) 2122 nm. The black circles represent the experimental data, and the red and the blue lines represent numerical simulations based on a ZDW of 2075 nm and 2135 nm respectively.

This thus re-iterates that in NKUA's numerical model, the chromatic dispersion of the waveguide is mis-estimated. This represents an important conclusion since it impacts the design of the third (and final) generation of waveguides targeted for the broadband MIR to NIR spectral translation. For such conversion, the phase matched gain peaks are narrow and their position is very sensitive to the pump wavelength (and thus the

ZDW of the waveguide). These results were therefore fed back to the project partners and informed the design and fabrication of the next generation of waveguides. Since the experimental findings reported here played an important role in this corrective and optimisation process, a brief account of the conclusions of the project partners is given in the following subsection.

7.3.7 Feedback from the Experiments – Corrective Actions Tanken by the NKUA

The main reasons for the emergence of the 60 nm red shift of the measured ZDW with respect to the calculated one were considered to be:

- Non adequate description of the device geometry
- Non precise consideration of the refractive index dependence on the wavelength for silicon and SiGe devices

As far as the former reason is concerned, CEA-Leti has provided an SEM picture of the structure of the waveguide (Figure 7.15) used in the experiments in order to accurately account for the device geometry. The figure shows the cross section of the device where it is clear that there is a non-negligible sidewall leading to trapezoidal shape with a top width of 1 μm whereas the bottom width is about 1.289 μm. The use of the exact dimensions of the device in the mode solver by the NKUA provided a correction of the ZDW by 5 nm which was not adequate to explain the 60 nm declination reported from the experiments.

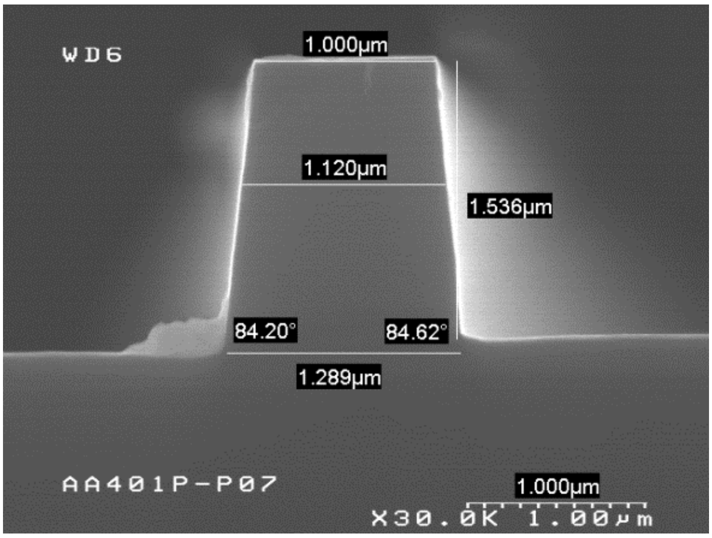

Figure 7.15: SEM picture of the studied device which exhibited the 60 nm discrepancy regarding the ZDW in comparison with the calculated values.

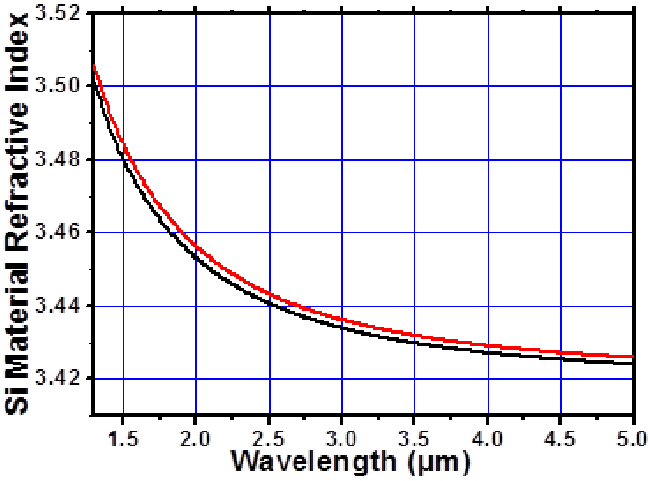

Figure 7.16: Si material refractive index as a function of the wavelength according to [170](black line), [171] (red line) (courtesy of Dr. Adonis Bogris).

The next step was to slightly modify the refractive index of Si and SiGe relying on the literature so as to better approximate the behavior of the devices. According to [170], the refractive index of silicon is given by the expression:

$$n_{Si}^2 = 11.6858 + 0.939816/\lambda^2 + 8.10461 \times 10^{-3} \times 1.1071^2/(\lambda^2 - 1.1071^2) \tag{7.3}$$

Furthermore, the refractive index for SiGe alloys is expressed as follows [170]:

$$n(Si_{1-x}Ge_x) = n(Si) + 0.37x + 0.22x^2 \tag{7.4}$$

Expressions 7.3 and 7.4 were originally utilised for the introduction of the material refractive index to the mode solver. In the literature, a different expression describing the wavelength dependence of the refractive index for SiGe alloys was also found [171]. The NKUA has found that adopting the definition in [171] rather than the one given by Equations 7.3 and 7.4 would lead to a difference in the refractive index of silicon depicted by Figure 7.16. The aforementioned difference changes the refractive index of the fundamental mode per wavelength resulting in a 20 nm red shift of the ZDW as depicted in Figure 7.17.

The 20 nm red shift due to the use of a different reference for the Si and SiGe properties together with the 5 nm red shift occurred when the geometry of the device was better approached reduce the discrepancy of 60 nm reported by the experiments to 35 nm. Although the NKUA has found that the CE experimental results show a better agreement when this 25 nm red shift in ZDW is considered, the assumption of a longer ZDW by 35 nm is still necessary so as to satisfactorily reproduce the experimental results. The identification of the cause for this ZDW difference is currently being investigated in more detail by the NKUA.

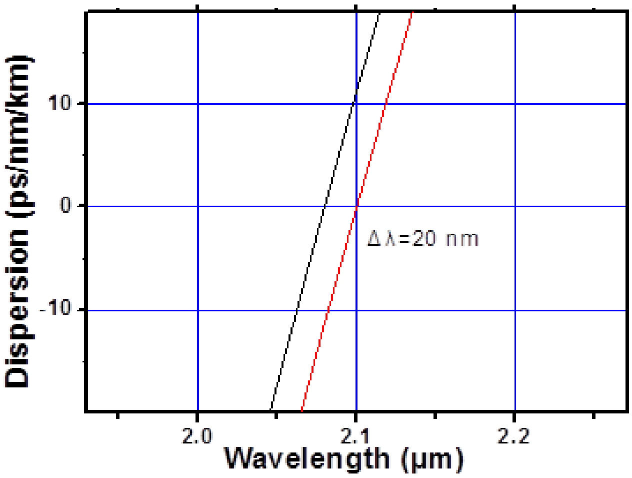

Figure 7.17: Dispersion of the waveguide structure predicted by the mode solver considering Si and SiGe properties based on [170] (black line) and [171] (red line). A 20 nm difference in the ZDW value is found between the two references (courtesy of Dr. Adonis Bogris).

7.4 Conclusion

This chapter reported the FWM experiments conducted in the first and second generations of silicon germanium waveguides.

The first generation of SiGe waveguides which adopted a constant germanium concentration profile and had its linear and nonlinear optical properties characterised in Chapter 6, was used to demonstrate FWM of 40 Gbps DPSK and 80 Gbps QPSK signals at 1550 nm. In particular, the 1 μm width waveguide with 20% Ge concentration which was singled out by the FOM study in Section 6.4 as the best waveguide, was used as the nonlinear wavelength converter.

Approximately 290 mW of pump power and 115 mW of signal power resulted in the generation of an idler with conversion efficiency of -18 dB and 23 dB OSNR. The quality of the conversion was assessed through BER tests and constellation diagrams. BER measurements on the DPSK idler showed an approximately 2.3 dB conversion penalty at a BER of 10^{-9} relative to the back-to-back signal. As for the QPSK case, a 2 dB power penalty was measured at BER = 10^{-3} as a result of the conversion. Furthermore, only minimal degradation was observed in the constellation diagrams and the EVM figures when comparing the idler to the B2B signal.

These results indicate that SiGe devices have the potential to be a competitive waveguide technology to silicon. However, one should not overlook that these two technologies are currently at completely different stages of maturity, and therefore the performance of the SiGe waveguide reported here does not compare favourably to state-of-art silicon waveguides. A number of factors which could enhance the nonlinear performance of the SiGe waveguide were considered. For instance, since the power into the waveguide was well below the TPA threshold, launching higher power levels is expected to significantly enhance the FWM efficiency. Filtering the EDFA-amplified pump and data signals prior to launching into the waveguide is also believed to improve the overall performance of the converter and reduce the conversion penalty even further. Furthermore, significant benefits in the FWM conversion efficiency can be obtained by using a longer device. Theoretical calculations show that by simply doubling the length of the waveguide to 5 cm, the FWM conversion efficiency would be improved by approximately 3.2 dB. Furthermore, as was the case in the characterisation study of Chapter 6, these results emphasise that through adopting a more complex waveguide design and/or germanium concentration profile, both the waveguide nonlinearity and dispersion properties at 1550 nm can be significantly improved, thus making this waveguide technology a potential competitor to other state-of-art nonlinear waveguides.

The second part of this chapter discussed the FWM experiments conducted in the second generation of SiGe waveguides at 2 μm. This waveguide generation adopted a gradient germanium concentration profile, the design and fabrication of which were discussed. Numerical simulations predicting the waveguide's chromatic dispersion were carried out by the NKUA prior to the experiments. A ZDW of 2075 nm was expected for the 1 μm width waveguide to be used in the experiments.

The experiments aimed to both demonstrate the ability of the waveguide in achieving broadband MIR to NIR wavelength conversion and examine the accuracy of NKUA's numerical model in predicting the dispersion of the waveguide. The latter goal was approached by experimentally estimating the zero-dispersion wavelength of the waveguide. The CE evolution as a function of pump and signal wavelength was studied and compared to NKUA's numerical predictions. The study has revealed that a 60 nm red shift in the theoretical ZDW of the waveguide, from 2075 to 2135 nm, is necessary to produce a good agreement with the experimental data. A brief account of the early corrective measures taken by the NKUA taken to allow for this ZDW shift was given.

The experiments have also demonstrated a conversion from a 2650 nm signal to a 1770 nm idler with - 32 dB conversion efficiency which is the one of the best results ever reported. It was not possible to demonstrate broader conversion because of the limitations (tunability) of the lasers used. However, these results show that MIR can be converted to NIR using this generation of graded index silicon germanium waveguides. Furthermore, for the waveguide used in these experiments, the phase matching curve shows that a signal close to 3.5 μm can be converted to the C-band of telecommunications wavelengths.

Chapter 8

Discussion and Conclusions

This thesis investigated all-optical signal processing applications in two different state of the art technologies: highly nonlinear soft glass fibres and silicon germanium waveguides.

Lead silicate and tellurite glasses were chosen as the glass host for fabricating highly nonlinear fibres. The first part of this thesis investigated the design methodology and the optical characteristics of a W-type lead silicate fibre. The characterisation work concluded that the first generation of the fabricated W-type fibre had a loss of 2.7 dB/m, a nonlinear coefficient γ of 820 /W/km and a dispersion and dispersion slope of 2 ps/nm/km and -0.009 ps/nm^2/km at 1550 nm respectively.

A number of all-optical signal processing applications were demonstrated in the fibre. Wavelength conversion of 1550 nm CW signals was demonstrated with -21 dB conversion efficiency and over 36 nm 3-dB bandwidth. Furthermore, numerical simulations have shown that a CE approaching 0 dB can be attained through the use of higher pump powers.

Phase sensitive amplification was also demonstrated in the W-type fibre. A parametric fluorescence experiment highlighted the merits of the low and flat dispersion profile of the fibre, as the phase sensitive gain spectrum extended across the full available bandwidth of the parametrically amplified ASE. Furthermore, a second generation of W-type lead silicate fibre, exhibiting lower losses of 2.1 dB/m, was used to regenerate the phase of 40 Gbit/s DPSK signals. The constellation diagrams of the demodulated data signal showed a high degree of phase noise squeezing for four different noise levels and the rms phase error of the 40 Gb/s data signals was reduced by a factor of 2.

The lead silicate W-type fibre has shown a strong potential in realising efficient nonlinear devices. Furthermore, the short length of fibre required to achieve high effective nonlinearity together with the novel dispersion properties of the fibre represent very attractive attributes in overcoming many of the practical limitations associated with silica-based HNLFs. For instance, J. Kakande's recent study on PSA-based phase and amplitude regenerators has shown that using long (hundreds of metres) spans of fibre makes ensuring uniform dispersion characteristics along the device length a very difficult task, which leads to a compromise in the efficiency and bandwidth characteristics of the regenerator [172]. The compactness that lead silicate fibre devices can offer leads to significantly superior uniformity along the entire length of the nonlinear fibre, a reduced acoustic and thermal pick-up and an overall more stable systems.

The performance of the lead silicate W-type fibre was hampered by the high splice losses to silica SMFs. The splice loss values reported in this work ranged between 5-6.5 dB which put significant limit on the amount of pump power that could be launched into the fibre. This represents the biggest challenge associated with this fibre technology, and although some progress has been made to reduce these loss figures [100], more radical approaches such as tapering the input of the lead silicate fibre to reduce the splice loss to the bigger core SMF, are expected to yield bigger improvements.

The second part of this thesis investigated all-optical signal processing applications in highly nonlinear tellurite fibres and silicon germanium waveguides and was closely aligned with the goals of the EU FP7 project CLARITY. Launched in 2011, CLARITY's main objective has been *to design and implement wide band, highly efficient mid-infrared to near-infrared converters relying on third order nonlinear effects in waveguides based on group IV materials and soft glass fibres.*

The work on highly nonlinear tellurite fibres reported in this thesis, represents the early stages of fabricating low loss highly nonlinear tellurite fibres suitable for broadband MIR to NIR nonlinear conversion.

The fabrication team at ORC has made significant advances towards reducing the loss of the tellurite fibres across the 3–5 μm wavelength window, by preparing the preform in an ultra-dry atmosphere-filled glovebox. The first generation the of dehydrated tellurite fibre, based on the TeO_2-ZnO-BaO (TZB) glass composition, was characterised in terms of loss and nonlinearity at 1.55 and 2 μm. The fibre loss was measured using the cutback method which yielded a loss of 0.58 and 2.8 dB/m at 1.55 and 2 μm respectively. The fibre nonlinearity was measured by calculating the phase shift that a dual-frequency beat signal experiences when travelling along the fibre. The measurement revealed that the nonlinear coefficient of the fibre is 75 and 45 /W/km at 1.5 and 2 μm respectively.

Following this characterisation, FWM-based wavelength conversion experiments at 1.55 and 2 μm were demonstrated in the TZB fibre. Highly efficient wavelength conversion was demonstrated in the fibre at 1.55 μm, with conversion efficiency values approaching 0 dB. However, the combination of higher losses and lower nonlinearity contributed to a much lower conversion efficiency of -42 dB at 2 μm for a pump power of 125 mW. Nevertheless, numerical simulations evaluated the scaling in the FWM conversion efficiency that can be attained in the tellurite fibre at 2 μm by using higher pump powers.

The work on tellurite fibres was carried out in close collaboration with the ORC soft glass fabrication team, and the characterisation data was fed back to the fabricators in order to further optimise their glass preparation process for subsequent fabrication attempts. Towards this goal, a numerical study of the tellurite fibre's potential as a mid- to near-IR spectral translator was conducted, and its results were also shared with the fabrication team. The numerical study relied on investigating the influence of the fibre design parameters, namely the core size and the refractive index contrast, on the fibre's nonlinearity, its mode properties and the FWM phase matching characteristics. The study established that a fibre with a core diameter of 4 μm and a core-cladding index difference of 0.03 would satisfy the phase matching conditions of MIR to NIR conversion and achieve enhanced nonlinearity and single mode guidance at the pump laser wavelengths.

These experimental and numerical demonstrations of the tellurite fibre's potential as a nonlinear medium have opened the prospect for using the fibre in a number of all-optical signal processing applications both at the NIR and MIR. In particular, the major advances towards reducing the loss of the fibres across the whole 1-5 μm wavelength window have made tellurite the glass of choice for realising fibre-based MIR to NIR wavelength convertors in preference to its closest competitor, chalcogenide. To that effect, tellurite fibres offer several advantages over chalcogenide such as the ease of dispersion engineering and a high damage threshold. However, realising efficient broadband MIR to NIR translation with conversion efficiency figures approaching 0 dB remains a difficult task using the simple step index tellurite fibre design suggested in this work. Such high values of conversion efficiency will require the use of more complex fibre structures such as a microstructure design, which would potentially enable much higher values of fibre nonlinearity and improved conversion efficiency figures.

To put the performance of the lead silicate and tellurite fibre technologies presented in this work into prospective, a figure of merit study comparing those fibres with other competing state of the art fibre technologies at 1.55 μm wavelength was conducted. Table 8.1 compares the parameters of the lead silicate and tellurite fibres with other HNLFs, namely the bismuth-oxide (Bi_2O_3) fibre which was used in Chapter 4, a highly nonlinear silica-based dispersion shifted fibre (DSF) [173] and a chalcogenide (As_2Se_3) fibre [174].

A number of FOMs are considered when comparing the different fibre technologies. The most basic figure of merit definition, FOM_{NL}, is a simple γ L_{eff} product. This FOM is often used in literature to differentiate between the nonlinear performance of the various fibre technologies when operating at relatively low pump powers (i.e. below the onset of parasitic nonlinear effects, such as stimulated Brillouin scattering and two photon absorption). The effective length calculations presented in Table 8.1 are based on a physical length L of 1-m for the lead silicate, tellurite, bismuth and chalcogenide fibres and 150-m for the dispersion shifted fibre. The shorter length of the soft glass fibres is

	Lead-Silicate	Tellurite	Bismuth	DSF	Chalcogenide
REF	Chapter 3, 4	Chapter 5	Chapter 4, [175]	[173]	[174]
Loss (dB/m)	2.1	0.58	0.9	0.001	1
γ (/W/km)	820	75	1100	21	1200
n_2 (m2/W)	3.84x10^{-19}	2.56x10^{-19}	8.17x10^{-19}	3.20x10^{-20}	9.00x10^{-16}
GVD (ps/nm/km)	-0.8	-100.92	-260	0.03	-504
L_{eff} (m)	0.793	0.936	0.903	147.439	0.893
Brillouin g_B (m/W)	4.00x10^{-11}	1.70x10^{-10}	6.44x10^{-11}	7.19x10^{-12}	6.00x10^{-9}
TPA (m/W)	Negligible	Negligible	Negligible	Negligible	2.50x10^{-12}
$\mathrm{FOM}_{NL} = \gamma\ L_{eff}$ (/W)	0.65	0.07	0.99	3.096	1.07
$\mathrm{FOM}_{SBS} = P_{SBS}\ \gamma\ L_{eff}$	0.82	0.13	1.08	0.38	12.77
$\mathrm{FOM}_{TPA} = n_2/(\lambda\ \beta)$	∞	∞	∞	∞	232.26
$\mathrm{FOM}_D = \lvert D/\gamma \rvert$ (W.ps /nm)	0.00097	1.345	0.236	0.00143	0.42

Table 8.1: Optical properties for five HNLFs and their figures of merit at 1550nm. The values coloured in red correspond to the technology with the best FOM.

justified due to the higher values of both the loss and nonlinearity in comparison to silica at 1.55 μm. This leads to shorter soft glass fibre devices with high effective nonlinearity that can only be matched using a few hundreds of metres of a silica-based device.

When taking this figure of merit into account, the dispersion shifted fibre emerges as the fibre with the best FOM. The ultra-low loss of silica allows the use of long effective fibre lengths ($L \approx L_{eff}$), compensating for the inferior nonlinearity values of silica compared to soft glasses.

The higher values of γ of the bismuth-oxide and chalcogenide fibres together with their lower loss in comparison with the lead silicate fibres result in slightly higher nonlinear figures of merit. However, it should be noted that the fibre loss of the lead silicate fibre reported here (2.1 dB/m) is expected to be further reduced to approach that of the material loss of 1 dB/m at 1550 nm. Such loss reduction would enhance the nonlinear FOM of the lead silicate fibre and bring it closer to the values of the bismuth and chalcogenide fibres.

The FOM based on the $\gamma\ L_{eff}$ product would not be a correct measure for evaluating a fibre's nonlinear performance when pump power loss induced by SBS and/or TPA becomes significant. In [130], J. Lee defined a FOM that incorporates the Kerr nonlinearity of optical fibre and the SBS-associated pump power limit. This FOM, labelled FOM_{SBS} in the table , is defined as:

$$FOM_{SBS} = P_{SBS}\gamma L_{eff} \tag{8.1}$$

Where P_{SBS} is the SBS threshold power which determines the upper limit of the input pump power available within the fibre. The definition of P_{SBS} given in Equation 2.30 and that of γ in Equation 2.14 can be substituted in Equation 8.1 to give:

$$FOM_{SBS} = (42\pi n_2)/(\lambda g_B) \tag{8.2}$$

Where n_2 is the nonlinear refractive index of the material and g_B is the Brillouin gain coefficient.

When FOM_{SBS} is taken into consideration, Table 8.1 shows that the gap between the bismuth and the lead silicate fibre FOMs is reduced (0.82 for the lead silicate and 1.08 for the bismuth). The ultra-high value of nonlinear coefficient of chalcogenide results in a high FOM in this case while the opposite is true for the silica DSF.

However, the conclusion derived from FOM_{SBS} calculations should be read with caution. Although the FOM_{SBS} for the chalcogenide fibre suggests that high pump powers can be launched without stimulating Brillouin scattering, chalcogenide fibres have a low power damage threshold that is usually 1-2 order of magnitude less than other soft glass fibres [176], thus preventing high pump powers to be launched into the fibre. Furthermore, while TPA effects are negligible in the other glasses considered here, the same cannot be stated for chalcogenide. When the commonly used FOM incorporating TPA ($\mathrm{FOM}_{TPA} = \mathrm{n}_2/(\lambda\ \beta)$) is considered, the TPA value of $2.50\mathrm{x}10^{-12}$ m/W for the $\mathrm{As_2Se_3}$ glass fibre considered here results in $\mathrm{FOM}_{TPA} = 232.26$, in contrast to the very large FOMs obtained for the other fibres in Table 8.1 due to their negligible values of TPA. The TPA of the chalcogenide fibre can be put into prospective by comparing it to that of a semiconductor such as silicon, of which the TPA coefficient is 3 orders of magnitude larger than chalcogenide at 1.55 μm. Chalcogenide is thus considered to possess a moderate TPA value at 1.55 μm in contrast to the high value of silicon and the low/negligible values of silica and the other soft glass fibres considered in Table 8.1.

Table 8.1 also presents another figure of merit, FOM_D, which is defined as the ratio between the group velocity dispersion D and the nonlinear coefficient γ [177]. FOM_D represents the magnitude of the dispersive effects against that of the nonlinear effects of the fibre and should be small enough that broadband nonlinear processes such as FWM satisfy the phase matching conditions to grow efficiently [177]. It is important to emphasise that the dispersion considered in Table 8.1 is measured at 1.55 μm and as such the FOM_D used here is devised as an indication of platform's suitability for telecoms applications and would not extend to other wavelengths.

The table shows that the lead silicate fibre exhibits the best FOM among all the fibre considered, followed by the silica DSF. Furthermore, the lead silicate fibre shows over 2 orders of magnitude improvement in the FOM over the bismuth fibre. This superiority was clearly observed experimentally in the parametric fluorescence experiment of Chapter 4. In that experiment, the phase sensitive parametric gain extended across the full bandwidth of the ASE in the case of the lead silicate W-type fibre, while the bandwidth was restricted to a much narrower spectral region in the case of the bismuth fibre, due to the higher dispersion of the fibre.

In all the FOMs studied in Table 8.1, the tellurite fibre has had the worst FOM among the fibres considered. However, this is not surprising since the step index design adopted for the fibre results in a much lower nonlinear coefficient than what is achievable using a microstructured fibre design as in the case of the lead silicate and the bismuth fibre. As mentioned in Chapter 5, there have been demonstrations of highly nonlinear tellurite fibres adopting a holey structure and achieving γ of 675 /W/km, loss of 0.18 dB/m and a dispersion of -10 ps/nm/km at 1550 nm [70]. When the optical characteristics of such fibre are considered, one obtains a $\text{FOM}_{NL} = 0.66$, $\text{FOM}_{SBS} = 0.3$ and $\text{FOM}_{D} = 0.0148$, which represent 2-90 times improvement in the FOMs from the tellurite fibre reported in Table 8.1.

It is important to remember that the tellurite fibre reported in this thesis was not designed with telecoms applications in mind. Rather, the step index design was adopted since it provides the required dispersion characteristics needed to achieve the strict FWM phase matching conditions of MIR to NIR conversion.

The above observations lead to an important conclusion. The choice of the best fibre technology to implement a certain nonlinear effect will strongly depend on the application. From the discussion above, the main points that one needs to consider when comparing the various technologies can be summarised as follows:

- Pump power limitations associated with the technology
- Suitability of the material for dispersion engineering at the wavelength of interest
- Transmission loss across the region of operation
- Device compactness
- Physical attributes of the medium, e.g. fragility, toxicity, etc.

The choice of the optimum fibre platform could vary depending on which of the five points above are relevant to the application.

The final part of this thesis reported the work conducted in silicon germanium waveguides. The enhanced nonlinear response of silicon germanium relative to pure silicon, in addition to the potential of SiGe alloy for band gap and lattice parameter engineering and its compatibility with CMOS technology, has made SiGe waveguides promising candidates for implementing a range of nonlinear applications in the midwave and longwave infrared. In particular, the technology offers an attractive solution for implementing a monolithically integratable chip-based MIR to NIR nonlinear converter that the CLARITY project aims to deliver.

The first generation of SiGe waveguides reported in this work, adopted a simple SOI design and a constant germanium concentration. The first detailed study of the linear and nonlinear characteristics of silicon germanium waveguides at the telecommunications wavelength was reported.

The loss, nonlinearity and two-photon absorption of SiGe waveguides of 10, 20 and 30% Ge concentration and of widths varying between 0.3 and 2 μm were characterised, revealing a strong impact of the proportion of germanium on the optical properties of the waveguides. For instance, a higher concentration of germanium was found to increase the linear loss and TPA of the waveguides, while giving rise to an enhanced nonlinearity. Furthermore, Ge concentration was also found to impact the dispersive properties of the waveguides. This strong dependence on germanium concentration gives rise to a valuable additional design degree of freedom, where both the waveguides' nonlinear performance and their dispersive properties can be appropriately engineered to suit a host of nonlinear applications at the NIR and MIR wavelengths.

A figure-of-merit study was conducted to deduce the SiGe waveguide with the optimum nonlinear performance of all the waveguides characterised. The FOM study, based on γL_{eff} metric, revealed that a waveguide of 1 μm width and 20% Ge concentration would exhibit the optimum performance as a nonlinear device, a conclusion that was supported by experimental observations of FWM performance in the various waveguides.

The 1 μm width waveguide with 20% Ge concentration was used to demonstrate FWM-based wavelength conversion of 40 Gbaud DPSK and QPSK signals. An idler with a conversion efficiency of -18 dB and 23 dB OSNR was generated using an estimated 290 mW of pump power. BER measurements revealed an approximately 2.3 dB conversion penalty at a BER of 10^{-9} relative to the back-to-back signal for the DPSK case and a 2 dB power penalty at BER = 10^{-3} for the QPSK case. Although SiGe waveguide technology is still at a very early stage of development, these results further proved that SiGe devices have the potential to realise efficient nonlinear applications and be a competitive waveguide technology to silicon.

A second generation of SiGe waveguides adopting a graded germanium concentration profile was used to demonstrate broadband FWM-based wavelength conversion at 2 μm. The experiments have demonstrated a conversion of a 2650 nm CW signal to a 1770 nm idler with - 32 dB conversion efficiency which is the one of the best results ever reported in the literature. The FWM experiments have also highlighted a discrepancy between the numerically expected ZDW of the waveguide and that estimated experimentally. The study has revealed that a 60 nm red shift in the theoretical ZDW of the waveguide, from 2075 to 2135 nm, is necessary to produce a good agreement with the experimental data. These conclusions were fed back to the theoretical team at the NKUA to study the origin of such shift and fine-tune their numerical model before the fabrication of further waveguide iterations.

The 2 μm FWM experiments show that MIR can be converted to NIR using this generation of graded index silicon germanium waveguides. Furthermore, while the tunability of the lasers available for the experiments hindered the demonstration of broader FWM bandwidths, for the waveguide used in these experiments, numerical simulations of the phase matching curve shows that a signal close to 3.5 μm can be converted to the C-band of telecommunications wavelengths.

A similar FOM study to that presented above was conducted to compare the merits of the various state of the art waveguide technologies. Table 8.2 contrasts the optical characteristics of the 1 μm width $Si_{0.8}Ge_{0.2}$ waveguide with a silicon nanowire waveguide [178], a chalcogenide (As_2S_3) rib waveguide [179] and an amorphous silicon (a-Si) waveguide [180]. The figures of merit FOM_{NL}, FOM_{TPA} and FOM_D used for comparison are defined as above.

	$Si_{0.8}Ge_{0.2}$ WG	Silicon nanowire	Chalcogenide WG	a-Si WG
REF	Chapter 6, 7	[178]	[179]	[180]
Loss (dB/cm)	1.4	4	0.05	4
γ (/W/m)	25.8	150	1.7	332
n_2 (m^2/W)	1.16x10^{-17}	6.00x10^{-18}	2.9x10^{-18}	1.75x10^{-17}
GVD (ps/nm/km)	-866	21	-342	-6500
L_{eff} (cm)	0.85	0.65	0.99	0.6535
TPA (m/W)	1.25x10^{-11}	5.00x10^{-12}	6.20x10^{-15}	2.3x10^{-12}
$FOM_{NL} = \gamma L_{eff}$ (/W)	0.22	0.98	0.017	2.17
$FOM_{TPA} = n_2/(\lambda\ \beta)$	0.60	0.77	301.77	4.91
$FOM_D = \lvert D/\gamma \rvert$ (W.ps /nm)	0.0335	0.00014	201.18	0.0196

Table 8.2: Optical properties for four nonlinear waveguides and their figures of merit at 1550nm. The values coloured in red correspond to the technology with the best FOM.

Table 8.2 suggests that based on the simple FOM definition of γL_{eff} , the a-Si waveguide exhibits the highest FOM thanks to its large nonlinear coefficient and small effective mode area (A_{eff} = 0.21 μm^2). Furthermore, the stronger confinement of the silicon nanowire [178] results in a higher FOM than that of the SiGe waveguide.

When TPA is considered, the FOM shows a clear advantage for the chalcogenide (As_2S_3) waveguide over the other platforms. This is because chalcogenide exhibits a TPA coefficient which is between 2-3 orders of magnitude smaller than the other waveguides considered here. The FOM_{TPA} of silicon and silicon germanium are similar and, as discussed in Chapter 6, higher FOM_{TPA} values of SiGe waveguides could be attained through using a graded germanium concentration profile.

The TPA-based analysis presented here is strongly dependent on wavelength. This is due to the variation of both the TPA coefficient β and nonlinear refractive index n_2 with wavelength. For instance, in Chapter 6, Figure 6.1 highlighted that the TPA of both silicon and silicon germanium starts to diminish beyond 2 μm. Furthermore, higher concentration of germanium is found to shift the position of the peak value of the nonlinear index n_2 towards longer wavelengths, where 40% of germanium results in a peak value of n_2 at around 2 μm. Using SiGe waveguides at 2 μm would thus result in a clear advantage in the FOM over silicon. The same behaviour for a-Si is observed, where the TPA becomes insignificant at wavelengths longer than 2 μm [181]. As for chalcogenide, the value of the TPA coefficient starts to decrease beyond 0.7 μm, reaching negligible values at wavelengths longer than 1.62 μm [182] .

Table 8.2 also contrasts the performance of the various waveguide platforms using the dispersion-based figure of merit FOM_D at 1.55 μm. In this case, the dispersion engineered silicon nanowire exhibits the best FOM. Note that while the chalcogenide (As_2S_3) rib waveguide presented in Table 8.2 exhibits a large GVD at 1550 nm, there have been demonstrations of dispersion-engineered chalcogenide waveguides exhibiting a ZDW close to 1550 nm [183]. However, since the material ZDW of chalcogenide lies close to 5 μm, precise engineering of the dispersion and shifting the ZDW to much shorter wavelengths are more challenging tasks than is the case for silicon and silicon germanium. The necessity to include large waveguide dispersion in the case of chalcogenide, often leads to structures with very small effective areas leading to problems with coupling and power handling. Those were among the reasons of preferring a silicon based platform over a chalcogenide one for the CLARITY project.

The CMOS-compatible amorphous silicon waveguide technology has been demonstrated to have a high nonlinear coefficient [184] and low TPA thanks to its wider band-gap relative to silicon [185]. However, the optical properties of a-Si waveguides vary greatly depending on the composition, atomic arrangement and the fabrication conditions [180]. Furthermore, there have also been reports of material degradation within minutes of light exposure [186]. Nevertheless, progress has been made towards solving these problems, and there have been numerous demonstrations of efficient nonlinear effects both at the telecoms and the MIR wavelengths using a-Si waveguides [180, 181].

In summary, similar considerations to those presented in the fibre study above, hold for waveguides. In addition to those, CMOS-compatibility could also be highly desired for some applications. Furthermore, mode overlap with the device core and polarisation insensitivity could also be factors when considering a particular fibre or waveguide design. For instance, one particular key advantage of the SiGe technology that influenced the choice of waveguide platform in CLARITY is that the $Si_{1-x}Ge_x$ compound offers continuous variation of the refractive index versus molar fraction. Subsequently, the choice of SiGe allows matching the core/cladding index gap to that of the QCL laser available as the MIR source. These traits, along with the strong potential that the technology has shown at both the C-Band and the MIR wavelengths, have highlighted the SiGe platform versatility and its promise for realising a wide range of efficient all-optical signal processing applications.

Chapter 9

Future Work

The experimental and theoretical work presented in previous chapters has highlighted both the merits and the challenges associated with the lead silicate and tellurite fibres and silicon germanium waveguides. This chapter presents an account of the future work that needs to be conducted in those all-optical signal processing technologies. It suggests directions for tackling the challenges associated with each technology and recommends further experimental work.

Highly Nonlinear Lead Silicate Fibres

The highly nonlinear lead silicate W-type fibres have shown strong potential for applications in the NIR. The suitability to precisely tailor the dispersive properties of the fibres together with the large values of γ enabled by the W-type design are extremely attractive attributes for realising efficient phase-matched nonlinear processes, such as phase sensitive amplification. Furthermore, the short length of these fibre devices avoids the detrimental effects of ZDW variation along the fibre length and enables the realisation of compact and stable systems.

A major practical limitation associated with this fibre technology is the high splice losses. The 5-6.5 dB splice losses reported in this thesis meant that it was often necessary to use excessively high average pump powers or modulate the pump in order to mitigate this limiting factor. However, such solutions are undesired in practical systems where the use of low average power CW pumps is a necessity. Consequently, in order to enhance the performance of the lead silicate fibres and make them a viable and competitive technology, a significant reduction in splice losses must be achieved.

The first step towards this goal is to understand the origin of these high losses. A study must be conducted in order to ascertain the level of contribution of the various loss mechanisms involved such as mode mismatch, Fresnel reflection and physical defects. Such a study will help to estimate the minimum value of splice loss achievable and conclude whether this technology can be competitive.

The loss originated due to the modal mismatch between the lead silicate fibre and the SMF can be theoretically alleviated through the adoption of a taper. This option must be explored to assess the level of improvement that it can provide. Furthermore, an understanding of the degree of the physical damage that the fibre endures during the splicing process will help determine whether such damage constitutes a limit on the minimum loss achievable. Overall, a reduction of the splice losses to 0.5-1 dB would significantly increase the potential of this fibre technology and address the practical constraints associated with power efficiency [100].

Another factor that can lead to an improvement in the performance of processing systems based on lead silicate fibres is a reduction in the fibre propagation losses. While some progress has already been attained towards this goal, the record loss figure of 2.1 dB/m achieved for the second generation of lead silicate fibres is still considered to be moderate. A further reduction of the loss figure towards the material loss of the bulk Schott SF57 glass of 0.3 dB/m [187] is expected to be achievable. Indeed, the fabrication team at the ORC has already drawn other MOFs made from the same lead silicate glass with loss figures of approximately 1 dB/m [22, 23]. Such an improvement would yield an increase in the γ L_{eff} figure of merit by approximately 22%.

Experimentally, the benefits of the novel dispersion profile of the W-type fibre could be better demonstrated by implementing a 1-pump non-degenerate PSA in the fibre. This is because, in contrast to the 2-pump degenerate scheme reported in this thesis which is inherently single channel, a 1-pump non-degenerate PSA is WDM-compatible. Implementing a PSA using this scheme would thus illustrate the practicality of this fibre technology by demonstrating the wideband parametric gain enabled by the low and flattened dispersion profile of the lead silicate W-type fibre and required by WDM systems .

It was not possible to carry out BER tests in my experiments, since the regenerator operated in

Another important experimental assessment would be the characterisation of the performance of a PSA-based phase and amplitude regenerator based on this fibre using BER tests. It was not possible to carry out BER tests in the regeneration experiment reported in Chapter 4, since the regenerator operated in burst mode which made synchronising the data signals with the optical modulation analyser (OMA) an extremely challenging task. However, once the splice losses are reduced, CW pumps could be used which would alleviate the synchronicity problem. BER tests can then be used to appreciate the long term performance of the lead silicate fibre as a phase regenerator and benchmark it against competing technologies. In particular, the benefits of having a compact system enabled by the short length of the lead silicate fibre are expected to reflect in a more stable system and a superior BER performance.

Highly Nonlinear Tellurite Fibres

The work on highly nonlinear tellurite fibres has demonstrated the potential of this technology for applications both at the NIR and MIR. The fabricated tellurite fibres have shown low losses across the 1-5 μm wavelength region, thus confirming the effectiveness of the preform preparation procedure developed at the ORC in reducing the OH-induced absorption of the glass. Furthermore, the simple step index fibre design provided an effective route in precisely engineering the dispersive properties of the fibre for applications requiring broadband FWM-based MIR to NIR wavelength conversion. However, the moderate values of γ of the fibre together with the poor modal mismatch between the 2 μm pump and the MIR signal are predicted to negatively impact the FWM process and result in low values of conversion efficiency.

An important future direction would thus be to investigate alternative fibre designs to the simple step index structure reported in this thesis. Adopting a more complex fibre design structure such as a holey or a wagon wheel (WW) structure [188], is predicted to give rise to higher values of fibre nonlinearity and improved FWM conversion efficiency figures. However, such designs are also expected to have some drawbacks. The surface roughness of such structure is expected to give rise to higher fibre losses in the NIR. Furthermore, the power coupling efficiency is also expected to drop relative to the simple step index structure. A full detailed study into the trade-offs of several fibre designs needs to be conducted to conclude the design with the best nonlinear performance. The study should also take into account the impact of structural deviations between the design and the fabrication on the dispersive properties of the fibre. Fibre designs with wavelength-scale core and cladding features are likely to result in strong dependence of the ZDW position on small variation in structural dimensions.

Once an optimum design is concluded, a detailed characterisation study of loss and nonlinearity should be conducted. The loss measurement should cover the entire 1-5 μm region while precise knowledge of the value of γ across the 1-2 μm region would also be important.

Silicon Germanium Waveguides

The work conducted on SiGe waveguides has shown the strong potential of this newly emerging platform for all-optical signal applications at the NIR and MIR. The wavelength conversion experiment conducted at telecommunication wavelengths has demonstrated that an impressive performance can be achieved even for devices that had not been specifically engineered for this purpose. Furthermore, using these devices for applications at the MIR wavelengths where TPA effects are negligible and the nonlinearity is optimum, has resulted in record performance and demonstrated the versatility of the SiGe devices as an all-optical signal processing platform. This has paved the way for potentially realising lab-on-a-chip systems where sensing, nonlinear signal processing and signal detection can be all realised in CMOS-compatible SiGe-based devices.

In terms of the possible future work for this waveguide technology, a recommended direction would be to investigate the full potential of these waveguides at the NIR wavelengths. To achieve such a goal, the gained understanding of the impact of germanium on the optical properties of the SiGe alloy can be exploited to design a new generation of SiGe waveguides showing optimum dispersive and nonlinear characteristics at the NIR. Adopting a waveguide design with a high index contrast and smaller width and height dimensions is expected to shift the ZDW to the telecommunication wavelengths and result in much higher values of nonlinear coefficient γ. Such a design is expected to yield an order of magnitude increase in the value of the nonlinear coefficient making SiGe waveguide technology a strong competitor to other state-of-art nonlinear photonic chips.

An important demonstration of the optimised SiGe waveguides's potential for telecommunications applications would be to implement a PSA-based phase and amplitude regenerator in the waveguides. The ultra-high value of γ is expected to give rise to high PSDR figures. This would enable operating the regenerator deep in the saturation regime where squeezing of both the phase and amplitude can be achieved. This together with the system stability enabled by the short device length is expected to reflect in impressive BER performance.

Another recommendation would be to continue the work started at 2 μm wavelengths. While the experiments reported in this thesis were limited by the tunability of the laser sources available, numerical simulations of the FWM phase matching curve of the SiGe waveguide used indicate that the waveguide can achieve conversion of a 3.5 μm signal to the C-band of the electromagnetic spectrum. As such, the use of an OPO as the seed signal would be a further important demonstration of the SiGe platform's suitability in achieving efficient broadband MIR to NIR wavelength conversion. Furthermore, such an experiment would also be a valuable tool in confirming the early findings of a shift in the ZDW of the waveguide used. Further conversion efficiency vs wavelength experiments would help verify whether the estimations of the ZDW shift are consistent with the early findings and would inform the design of future waveguide generations.

The CLARITY project targets the production of a final generation of SiGe waveguides designed to demonstrate broadband wavelength translation of the 4.65 μm wavelength window to NIR wavelength. This is an extremely challenging task since the experimental observation of such broadband conversion relies on the accurate prediction of the position of the phase matched FWM gain peaks. As such, a variation as small as 1 nm in the estimation of the ZDW position can lead to mis-estimating the position of those peaks and thus the failure to observe the nonlinear conversion. An accurate understanding of the origin of the ZDW shift must then be gained in order to accurately model the chromatic dispersion profile of the final generation of SiGe waveguides. Even when the origin of the ZDW discrepancy is fully understood and accounted for in future models, the accuracy of the new model should be checked against the experimental estimations of the ZDW. This can be done by conducting similar 2 μm wavelength conversion experiments in the final generation of SiGe waveguides to those reported in the Chapter 7, before proceeding with the broader wavelength conversion that CLARITY aims to deliver.

List of Publications

Journal Papers

1. **M. A. Ettabib**, L. Jones, J. Kakande, R. Slavik, F. Parmigiani, X. Feng, F. Poletti, G. M. Ponzo, J. Shi, M. N. Petrovich, W. H. Loh, P. Petropoulos, and D. J. Richardson, "Phase sensitive amplification in a highly nonlinear lead-silicate fiber," Opt. Express, vol. 20, no. 2, pp. 1629–1634, 2012.
2. **M. A. Ettabib**, F. Parmigiani, X. Feng, L. Jones, J. Kakande, R. Slavik, F. Poletti, G. M. Ponzo, J. Shi, M. N. Petrovich, W. H. Loh, P. Petropoulos, and D. J. Richardson, "Phase regeneration of DPSK signals in a highly nonlinear lead-silicate W-type fiber," Opt. Express, vol. 20, no. 24, pp. 27419–27424, 2012.
3. **M. A. Ettabib**, K. Hammani, F. Parmigiani, L. Jones, A. Kapsalis, A. Bogris, D. Syvridis, M. Brun, P. Labeye, S. Nicolletti, and P. Petropoulos, "FWM-based wavelength conversion of 40 Gbaud PSK signals in a silicon germanium waveguide," Opt. Express, vol. 21, no. 14, pp. 16683–16689, 2013.
4. K. Hammani, **M. A. Ettabib**, A. Bogris, A. Kapsalis, D. Syvridis, M. Brun, P. Labeye, S. Nicoletti, D. Richardson, and P. Petropoulos, "Optical properties of silicon germanium waveguides at telecommunication wavelengths," Opt. Express, vol. 21, no. 14, pp. 16690–16701, 2013.

Conference Submissions

1. **M. A. Ettabib**, L. Jones, J. Kakande, R. Slavik, F. Parmigiani, X. Feng, F. Poletti, G. Ponzo, J. Shi, M. Petrovich, P. Petropoulos, W. Loh, and D. Richardson, "Phase sensitive amplification in a highly nonlinear lead-silicate fibre," in Optical Communication (ECOC), 2011 37th European Conference and Exhibition on, 2011, pp. 1–3.
2. **M. A. Ettabib**, F. Parmigiani, X. Feng, L. Jones, J. Kakande, R. Slavik, F. Poletti, G. M. Ponzo, J. Shi, M. N. Petrovich, P. Petropoulos, W. H. Loh, and D. J. Richardson, "All-optical phase regeneration in a highly nonlinear lead-silicate fiber," in Advanced Photonics Congress. Optical Society of America, 2012, p.JM5A.11.

3. **M. A. Ettabib**, K. Hammani, F. Parmigiani, L. Jones, A. Kapsalis, A. Bogris, D. Syvridis, M. Brun, P. Labeye, S. Nicoletti, and P. Petropoulos, "FWM-based wavelength conversion in a silicon germanium waveguide," in Optical Fiber Communication Conference/National Fiber Optic Engineers Conference 2013. Optical Society of America, 2013, p. OTh1C.4.

4. K. Hammani, **M. A. Ettabib**, A. Bogris, A. Kapsalis, D. Syvridis, M. Brun, P. Labeye, S. Nicoletti, D. J. Richardson, and P. Petropoulos, "Linear and nonlinear properties of sige waveguides at telecommunication wavelengths," in Optical Fiber Communication Conference/National Fiber Optic Engineers Conference 2013. Optical Society of America, 2013, p. JTh2A.34.

5. L. Jones, F. Parmigiani, V. Rancano, **M. A. Ettabib**, P. Petropoulos, and D. Richardson, "Transmission Performance of Phase-Preserving Amplitude Regenerator based on Optical Injection Locking," in Optical Fiber Communication Conference/National Fiber Optic Engineers Conference 2013. Optical Society of America, 2013, p. OW4C.4.

6. **M. A. Ettabib**, K. Hammani, X. Feng, M. Belal, J. Shi, A. Bogris, A. Kapsalis, D. Syvridis, D. Richardson, and P. Petropoulos, "Highly nonlinear tellurite glass fiber for broadband applications," in Optical Fiber Communication Conference and Exposition (OFC/NFOEC), 2014 and the National Fiber Optic Engineers Conference, 2014, p. Tu2K.3.

References

[1] P. A. Franken, A. E. Hill, C. W. Peters, and G. Weinreich, "Generation of optical harmonics," *Phys. Rev. Lett.*, vol. 7, pp. 118–119, 1961.

[2] G. P. Agrawal, *Nonlinear Fiber Optics*, 3rd ed. Academic Press, 2006.

[3] F. Träger, *Springer Handbook of Lasers and Optics.* Springer, 2007.

[4] J. Toulouse, "Optical nonlinearities in fibers: review, recent examples, and systems applications," *J. Lightwave Technol.*, vol. 23, no. 11, pp. 3625–3641, 2005.

[5] R. Song, J. Hou, S. Chen, W. Yang, and Q. Lu, "High power supercontinuum generation in a nonlinear ytterbium-doped fiber amplifier," *Opt. Lett.*, vol. 37, no. 9, pp. 1529–1531, 2012.

[6] V. V. Alexander, O. P. Kulkarni, M. Kumar, C. Xia, M. N. Islam, F. L. T. Jr., M. J. Welsh, K. Ke, M. J. Freeman, M. Neelakandan, and A. Chan, "Modulation instability initiated high power all-fiber supercontinuum lasers and their applications," *Opt. Fiber Technol.*, vol. 18, no. 5, pp. 349 – 374, 2012.

[7] L. Rasmussen, M. Lawaetz, J. Serup, L. Bjoern, B. Vennits, A. Blemings, and B. Eklof, "Randomized clinical trial comparing endovenous laser ablation, radiofrequency ablation, foam sclerotherapy, and surgical stripping for great saphenous varicose veins with 3-year follow-up," *J. Vasc. Surg. Venous. Lymphat. Disord.*, vol. 1, no. 4, pp. 349 – 356, 2013.

[8] O. P. Kulkarni, "Single mode optical fiber based devices and systems for mid-infrared light generation," Ph.D. dissertation, University of Michigan, Ann Arbor, 2011.

[9] V. V. Alexander, "Fiber based infrared lasers and their applications in medicine, spectroscopy and metrology," Ph.D. dissertation, University of Michigan, Ann Arbor, 2013.

[10] D. J. Richardson, "Filling the light pipe," *Science*, vol. 330, no. 6002, pp. 327–328, 2010.

[11] H. Ishikawa, *Ultrafast All-Optical Signal Processing Devices.* Wiley, 2008.

[12] J. Hansryd, P. Andrekson, M. Westlund, J. Li, and P. Hedekvist, “Fiber-based optical parametric amplifiers and their applications,” *IEEE J. Sel. Top. Quant. Electron.*, vol. 8, no. 3, pp. 506–520, 2002.

[13] Z. Li, A. M. Heidt, J. M. O. Daniel, Y. Jung, S. U. Alam, and D. J. Richardson, “Thulium-doped fiber amplifier for optical communications at 2 μm,” *Opt. Express*, vol. 21, no. 8, pp. 9289–9297, 2013.

[14] A. Schliesser, N. Picque, and T. W. Hansch, “Mid-infrared frequency combs,” *Nature Photon.*, vol. 6, pp. 440–449, 2012.

[15] J. K. Ranka, R. S. Windeler, and A. J. Stentz, “Visible continuum generation in air-silica microstructure optical fibers with anomalous dispersion at 800 nm,” *Opt. Lett.*, vol. 25, no. 1, pp. 25–27, 2000.

[16] D. K. Serkland and P. Kumar, “Tunable fiber-optic parametric oscillator,” *Opt. Lett.*, vol. 24, no. 2, pp. 92–94, 1999.

[17] T. W. Neely, L. Nugent-Glandorf, F. Adler, and S. A. Diddams, “Broadband mid-infrared frequency upconversion and spectroscopy with an aperiodically poled $LiNbO_3$ waveguide,” *Opt. Lett.*, vol. 37, no. 20, pp. 4332–4334, 2012.

[18] B. Kuyken, X. Liu, J. Osgood, R.M., Y. Vlasov, G. Roelkens, R. Baets, and W. M. J. Green, “Frequency conversion of mid-infrared optical signals into the telecom band using nonlinear silicon nanophotonic wires,” in *Optical Fiber Communication Conference and Exposition (OFC/NFOEC), 2011 and the National Fiber Optic Engineers Conference*, 2011, pp. 1–3.

[19] D. Nikogosyan, *Properties of Optical and Laser-Related Materials: A Handbook*. Wiley, 1997.

[20] X. Feng, J. Shi, M. Segura, N. M. White, P. Kannan, W. H. Loh, L. Calvez, X. Zhang, and L. Brilland, “Halo-tellurite glass fiber with low oh content for 2-5 μm mid-infrared nonlinear applications,” *Opt. Express*, vol. 21, no. 16, pp. 18 949–18 954, 2013.

[21] K. M. Kiang, K. Frampton, T. Monro, R. Moore, J. Tucknott, D. Hewak, D. Richardson, and H. N. Rutt, “Extruded singlemode non-silica glass holey optical fibres,” *Electron. Lett.*, vol. 38, no. 12, pp. 546–547, 2002.

[22] A. Camerlingo, X. Feng, F. Poletti, G. M. Ponzo, F. Parmigiani, P. Horak, M. N. Petrovich, P. Petropoulos, W. H. Loh, and D. J. Richardson, “Near-zero dispersion, highly nonlinear lead-silicate w-type fiber for applications at 1.55μm,” *Opt. Express*, vol. 18, no. 15, pp. 15 747–15 756, 2010.

[23] X. Feng, F. Poletti, A. Camerlingo, F. Parmigiani, P. Petropoulos, P. Horak, G. M. Ponzo, M. Petrovich, J. Shi, W. H. Loh, and D. J. Richardson, “Dispersion controlled highly nonlinear fibers for all-optical processing at telecoms wavelengths,” *Opt. Fiber Technol.*, vol. 16, no. 6, pp. 378 – 391, 2010.

[24] N. Kapany and R. Simms, “Recent developments in infrared fiber optics,” *Infrared Phys.*, vol. 5, no. 2, pp. 69 – 80, 1965.

[25] J. Leuthold, C. Koos, and W. Freude, “Nonlinear silicon photonics,” *Nature Photon.*, vol. 4, pp. 535–544, 2010.

[26] C. Koos, L. Jacome, C. Poulton, J. Leuthold, and W. Freude, “Nonlinear silicon-on-insulator waveguides for all-optical signal processing,” *Opt. Express*, vol. 15, no. 10, pp. 5976–5990, 2007.

[27] V. Ta’eed, M. R. E. Lamont, M. Pelusi, M. A. F. Roelens, D. Moss, S. Madden, D.-Y. Choi, B. Luther-Davies, and B. J. Eggleton, “Chalcogenide glass photonic chips for all-optical signal processing,” in *Optical Fiber Communication and Optoelectronics Conference, 2007 Asia*, 2007, pp. 558–560.

[28] V. Ta’eed and B. Eggleton, “Ultrafast all-optical signal processing using chalcogenide glass based photonic chips,” in *Transparent Optical Networks, 2007. ICTON ’07. 9th International Conference on*, vol. 1, 2007, pp. 228–231.

[29] B. J. Eggleton, B. Luther-Davies, and K. Richardson, “Chalcogenide photonics,” *Nature Photon.*, vol. 3, pp. 141–148, 2011.

[30] N. Hon, R. Soref, and B. Jalali, “The third-order nonlinear optical coefficients of si, ge, and si1-xgex in the midwave and longwave infrared,” *J. Appl. Phys.*, vol. 110, no. 1, pp. 011 301–011 301–8, 2011.

[31] A. Camerlingo, F. Parmigiani, X. Feng, F. Poletti, P. Horak, W. Loh, D. Richardson, and P. Petropoulos, “Multichannel wavelength conversion of 40-gb/s nonreturn-to-zero dpsk signals in a lead silicate fiber,” *IEEE Photon. Technol. Lett.*, vol. 22, no. 15, pp. 1153–1155, 2010.

[32] A. Camerlingo, F. Parmigiani, R. Slavic, X. Feng, F. Poletti, P. Horak, W. Loh, P. Petropoulos, and D. Richardson, “Generation of ultra-high repetition rate pulses in a highly nonlinear dispersion-tailored compound glass fibre,” in *Photonics Society Summer Topical Meeting Series, 2010 IEEE*, 2010, pp. 184–185.

[33] M. Ettabib, L. Jones, J. Kakande, R. Slavik, F. Parmigiani, X. Feng, F. Poletti, G. Ponzo, J. Shi, M. Petrovich, P. Petropoulos, W. Loh, and D. Richardson, “Phase sensitive amplification in a highly nonlinear lead-silicate fibre,” in *Optical Communication (ECOC), 2011 37th European Conference and Exhibition on*, 2011, pp. 1–3.

[34] M. A. Ettabib, L. Jones, J. Kakande, R. Slavík, F. Parmigiani, X. Feng, F. Poletti, G. M. Ponzo, J. Shi, M. N. Petrovich, W. H. Loh, P. Petropoulos, and D. J. Richardson, “Phase sensitive amplification in a highly nonlinear lead-silicate fiber,” *Opt. Express*, vol. 20, no. 2, pp. 1629–1634, 2012.

[35] M. A. Ettabib, F. Parmigiani, X. Feng, L. Jones, J. Kakande, R. Slavík, F. Poletti, G. M. Ponzo, J. Shi, M. N. Petrovich, P. Petropoulos, W. H. Loh, and D. J. Richardson, “All-optical phase regeneration in a highly nonlinear lead-silicate fiber,” in *Advanced Photonics Congress.* Optical Society of America, 2012, p. JM5A.11.

[36] M. A. Ettabib, F. Parmigiani, X. Feng, L. Jones, J. Kakande, R. Slavík, F. Poletti, G. M. Ponzo, J. Shi, M. N. Petrovich, W. H. Loh, P. Petropoulos, and D. J. Richardson, “Phase regeneration of dpsk signals in a highly nonlinear lead-silicate w-type fiber,” *Opt. Express*, vol. 20, no. 24, pp. 27 419–27 424, 2012.

[37] M. Ettabib, K. Hammani, X. Feng, M. Belal, J. Shi, A. Bogris, A. Kapsalis, D. Syvridis, D. Richardson, and P. Petropoulos, “Highly nonlinear tellurite glass fiber for broadband applications,” in *Optical Fiber Communication Conference and Exposition (OFC/NFOEC), 2014 and the National Fiber Optic Engineers Conference*, 2014, p. Tu2K.3.

[38] K. Hammani, M. A. Ettabib, A. Bogris, A. Kapsalis, D. Syvridis, M. Brun, P. Labeye, S. Nicoletti, D. J. Richardson, and P. Petropoulos, “Linear and nonlinear properties of sige waveguides at telecommunication wavelengths,” in *Optical Fiber Communication Conference/National Fiber Optic Engineers Conference 2013.* Optical Society of America, 2013, p. JTh2A.34.

[39] K. Hammani, M. A. Ettabib, A. Bogris, A. Kapsalis, D. Syvridis, M. Brun, P. Labeye, S. Nicoletti, D. Richardson, and P. Petropoulos, “Optical properties of silicon germanium waveguides at telecommunication wavelengths,” *Opt. Express*, vol. 21, no. 14, pp. 16 690–16 701, 2013.

[40] M. A. Ettabib, K. Hammani, F. Parmigiani, L. Jones, A. Kapsalis, A. Bogris, D. Syvridis, M. Brun, P. Labeye, S. Nicoletti, and P. Petropoulos, “Fwm-based wavelength conversion in a silicon germanium waveguide,” in *Optical Fiber Communication Conference/National Fiber Optic Engineers Conference 2013.* Optical Society of America, 2013, p. OTh1C.4.

[41] M. A. Ettabib, K. Hammani, F. Parmigiani, L. Jones, A. Kapsalis, A. Bogris, D. Syvridis, M. Brun, P. Labeye, S. Nicolletti, and P. Petropoulos, “Fwm-based wavelength conversion of 40 gbaud psk signals in a silicon germanium waveguide,” *Opt. Express*, vol. 21, no. 14, pp. 16 683–16 689, 2013.

[42] A. Ghatak and K. Thyagarajan, *An Introduction to Fiber Optics.* Cambridge University Press, 1998.

[43] M. Bass and O. S. of America, *Handbook of optics*, ser. Handbook of Optics. McGraw-Hill, 2001, no. v. 1-2.

[44] E. W. V. Stryland, M. A. Woodall, H. Vanherzeele, and M. J. Soileau, "Energy band-gap dependence of two-photon absorption," *Opt. Lett.*, vol. 10, no. 10, pp. 490–492, 1985.

[45] L. Vivien and L. Pavesi, *Handbook of Silicon Photonics*, ser. Series in Optics and Optoelectronics. Taylor & Francis, 2013.

[46] S. Krishnamurthy, Z. G. Yu, L. P. Gonzalez, and S. Guha, "Temperature- and wavelength-dependent two-photon and free-carrier absorption in gaas, inp, gainas, and inasp," *J. Appl. Phys.*, vol. 109, no. 3, pp. 033 102–033 102–9, 2011.

[47] R. Boyd, *Nonlinear Optics.* Elsevier Science, 2003.

[48] S. Afshar, W. Q. Zhang, H. Ebendorff-Heidepriem, and T. M. Monro, "Small core optical waveguides are more nonlinear than expected: experimental confirmation," *Opt. Lett.*, vol. 34, no. 22, pp. 3577–3579, 2009.

[49] B. E. Olsson and D. Blumenthal, "All-optical demultiplexing using fiber cross-phase modulation (xpm) and optical filtering," *IEEE Photon. Technol. Lett.*, vol. 13, no. 8, pp. 875–877, 2001.

[50] X. Tang, S. H. Chung, A. Karar, J. Cartledge, A. Shen, and G.-H. Duan, "Spectral filtering characteristics of a quantum-dash fabry-perot laser and its implications on 40 gb/s xpm based optical retiming performance," *J. Lightwave Technol.*, vol. 29, no. 1, pp. 31–36, 2011.

[51] R. Tang, P. S. Devgan, V. S. Grigoryan, P. Kumar, and M. Vasilyev, "In-line phase-sensitive amplification of multi-channel cw signals based on frequency non-degenerate four-wave-mixing in fiber," *Opt. Express*, vol. 16, no. 12, pp. 9046–9053, 2008.

[52] M. Marhic, *Fiber Optical Parametric Amplifiers, Oscillators and Related Devices.* Cambridge University Press, 2008.

[53] T. Torounidis and P. Andrekson, "Broadband single-pumped fiber-optic parametric amplifiers," *IEEE Photon. Technol. Lett.*, vol. 19, no. 9, pp. 650–652, 2007.

[54] G. Agrawal, *Fiber-Optic Communication Systems*, ser. Wiley Series in Microwave and Optical Engineering. Wiley, 2012.

[55] G. P. Agrawal, "Nonlinear fiber optics: its history and recent progress (invited)," *J. Opt. Soc. Am. B*, vol. 28, no. 12, pp. A1–A10, 2011.

[56] C. S. Bres, A. O. J. Wiberg, B. P. P. Kuo, N. Alic, and S. Radic, "Wavelength multicasting of 320-gb/s channel in self-seeded parametric amplifier," *IEEE Photon. Technol. Lett.*, vol. 21, no. 14, pp. 1002–1004, 2009.

[57] P. Hedekvist, M. Karlsson, and P. Andrekson, "Fiber four-wave mixing demultiplexing with inherent parametric amplification," *J. Lightwave Technol.*, vol. 15, no. 11, pp. 2051–2058, 1997.

[58] S. Ono, R. Okabe, F. Futami, and S. Watanabe, "Novel demultiplexer for ultra high speed pulses using a perfect phase-matched parametric amplifier," in *Optical Fiber Communication Conference, 2006 and the 2006 National Fiber Optic Engineers Conference. OFC 2006*, 2006, pp. 3 pp.–.

[59] A. Ruffin, "Stimulated brillouin scattering: an overview of measurements, system impairments, and applications," in *Optical Fiber Measurements, 2004. Technical Digest: Symposium on*, Sept 2004, pp. 23–28.

[60] M. Ferreira, *Nonlinear Effects in Optical Fibers*, ser. Wiley-OSA Series on Optical Communication. Wiley, 2011.

[61] A. Snyder and J. Love, *Optical Waveguide Theory*, ser. Science paperbacks. Springer, 1983.

[62] A. Ghatak and K. Thyagarajan, *An Introduction to Fiber Optics.* Cambridge University Press, 1998.

[63] M. Marhic, *Fiber Optical Parametric Amplifiers, Oscillators and Related Devices.* Cambridge University Press, 2008.

[64] M. Hirano, T. Nakanishi, T. Okuno, and M. Onishi, "Silica-based highly nonlinear fibers and their application," *IEEE J. Sel. Top. Quant. Electron.*, vol. 15, no. 1, pp. 103–113, 2009.

[65] M. Onishi, T. Okuno, T. Kashiwada, S. Ishikawa, N. Akaska, and M. Nishimura, "Highly nonlinear dispersion shifted fiber and its application to broadband wavelength converter," in *Integrated Optics and Optical Fibre Communications, 11th International Conference on, and 23rd European Conference on Optical Communications (Conf. Publ. No.: 448)*, vol. 2, 1997, pp. 115–118 vol.2.

[66] K.-W. Chung and S. Yin, "A highly nonlinear dispersion-shifted fiber with 9.3 μm^2 effective area and low loss for all fiber wavelength converter," *Microw. Opt. Techn. Let.*, vol. 40, no. 2, pp. 153–156, 2004.

[67] M. Hirano, T. Nakanishi, T. Okuno, and M. Onishi, "Broadband wavelength conversion over 193-nm by hnl-dsf improving higher-order dispersion performance," in *Optical Communication, 2005. ECOC 2005. 31st European Conference on*, vol. 6, 2005, pp. 43–44 vol.6.

[68] J. Wang, E. Vogel, and E. Snitzer, “Tellurite glass: a new candidate for fiber devices,” *Opt. Mater.*, vol. 3, no. 3, pp. 187 – 203, 1994.

[69] X. Feng, A. K. Mairaj, D. W. Hewak, and T. M. Monro, “Nonsilica glasses for holey fibers,” *J. Lightwave Technol.*, vol. 23, no. 6, p. 2046, 2005.

[70] A. Mori, K. Shikano, K. Enbutsu, K. Oikawa, K. Naganuma, M. Kato, and S. Aozasa, “1.5 μm band zero-dispersion shifted tellurite photonic crystal fiber with a nonlinear coefficient γ of 675w1km1,” in *Optical Communication (ECOC), 29th European Conference and Exhibition on*, 2004, p. paper Th3.3.6.

[71] A. Zakery and S. Elliott, *Optical Nonlinearities in Chalcogenide Glasses and Their Applications*, ser. Springer Series in Optical Sciences. Springer, 2007.

[72] H. Ebendorff-Heidepriem, K. Furusawa, D. J. Richardson, and T. M. Monro, “Fundamentals and applications of silica and nonsilica holey fibers,” *Proc. SPIE*, vol. 5350, pp. 35–49, 2004.

[73] H. Ebendorff-Heidepriem, P. Petropoulos, S. Asimakis, V. Finazzi, R. Moore, K. Frampton, F. Koizumi, D. Richardson, and T. Monro, “Bismuth glass holey fibers with high nonlinearity,” *Opt. Express*, vol. 12, no. 21, pp. 5082–5087, 2004.

[74] G. Brambilla, F. Xu, P. Horak, Y. Jung, F. Koizumi, N. P. Sessions, E. Koukharenko, X. Feng, G. S. Murugan, J. S. Wilkinson, and D. J. Richardson, “Optical fiber nanowires and microwires: fabrication and applications,” *Adv. Opt. Photon.*, vol. 1, no. 1, pp. 107–161, 2009.

[75] E. C. Mägi, L. B. Fu, H. C. Nguyen, M. R. Lamont, D. I. Yeom, and B. J. Eggleton, “Enhanced kerr nonlinearity in sub-wavelength diameter as2se3 chalcogenide fiber tapers,” *Opt. Express*, vol. 15, no. 16, pp. 10 324–10 329, 2007.

[76] H. K. Tsang and Y. Liu, “Nonlinear optical properties of silicon waveguides,” *Semicond. Sci. Technol.*, vol. 23, no. 6, p. 064007, 2008.

[77] L. J., K. C., and F. W., “Nonlinear silicon photonics,” *Nature Photon.*, vol. 4, no. 8, pp. 535–544, 2010.

[78] Q. Lin, O. J. Painter, and G. P. Agrawal, “Nonlinear optical phenomena in silicon waveguides: modeling and applications,” *Opt. Express*, vol. 15, no. 25, pp. 16 604–16 644, 2007.

[79] T. Vallaitis, S. Bogatscher, L. Alloatti, P. Dumon, R. Baets, M. L. Scimeca, I. Biaggio, F. Diederich, C. Koos, W. Freude, and J. Leuthold, “Optical properties of highly nonlinear silicon-organic hybrid (soh) waveguide geometries,” *Opt. Express*, vol. 17, no. 20, pp. 17 357–17 368, 2009.

[80] J. A. Moon and D. T. Schaafsma, "Chalcogenide fibers: An overview of selected applications," *Fiber Integrated Opt.*, vol. 19, no. 3, pp. 201–210, 2000.

[81] L. Gruner-Nielsen, S. Herstrm, S. Dasgupta, D. Richardson, D. Jakobsen, C. Lundstrom, P. Andrekson, M. E. V. Pedersen, and B. Palsdottir, "Silica-based highly nonlinear fibers with a high sbs threshold," in *Winter Topicals (WTM), 2011 IEEE*, 2011, pp. 171–172.

[82] J. Kakande, R. Slavík, F. Parmigiani, A. Bogris, D. Syvridis, L. Grüner-Nielsen, R. Phelan, P. Petropoulos, and D. J. Richardson, "Multilevel quantization of optical phase in a novel coherent parametric mixer architecture," *Nature Photon.*, vol. 5, no. 12, pp. 748–752, 2011.

[83] J. Nicholson, "Supercontinuum generation in germanium-doped fibers and comparison with microstructured fibers," in *Holey Fibers and Photonic Crystals/Polarization Mode Dispersion/Photonics Time/Frequency Measurement and Control, 2003 Digest of the LEOS Summer Topical Meetings*, 2003, pp. TuA4.1/56–TuA4.1/57.

[84] Y. Aoki, K. Tajima, and I. Mito, "Input power limits of single-mode optical fibers due to stimulated brillouin scattering in optical communication systems," *J. Lightwave Technol.*, vol. 6, no. 5, pp. 710–719, 1988.

[85] L. Gruner-Nielsen, S. Dasgupta, M. Mermelstein, D. Jakobsen, S. Herstrom, M. E. V. Pedersen, E. Lim, S. Alam, F. Parmigiani, D. J. Richardson, and B. Palsdottir, "A silica based highly nonlinear fibre with improved threshold for stimulated brillouin scattering," in *Optical Communication (ECOC), 2010 36th European Conference and Exhibition on*, 2010, pp. 1–3.

[86] X. Feng, T. Monro, V. Finazzi, R. Moore, K. Frampton, P. Petropoulos, and D. Richardson, "Extruded singlemode, high-nonlinearity, tellurite glass holey fibre," *Electron. Lett.*, vol. 41, no. 15, pp. 835–837, 2005.

[87] S. Fujino, H. Ijiri, F. Shimizu, and K. Morinaga, "Measurement of viscosity of multi-component glasses in the wide range for fibre drawing," *J. Jpn. Instrum. Met.*, vol. 62, p. 106110, 1998.

[88] A. Camerlingo, F. Parmigiani, X. Feng, F. Poletti, P. Horak, W. H. Loh, P. Petropoulos, and D. J. Richardson, "Multichannel wavelength conversion of 40gbit/s nrz dpsk signals in a highly nonlinear dispersion flattened lead silicate fibre," in *Advanced Photonics & Renewable Energy.* Optical Society of America, 2010, p. NThA3.

[89] A. Camerlingo, F. Parmigiani, X. Feng, F. Poletti, W. Loh, D. Richardson, and P. Petropoulos, "160-to-40gibt/s time demultiplexing in a low dispersion lead-silicate w-index profile fiber," in *Optical Fiber Communication Conference and*

Exposition (OFC/NFOEC), 2011 and the National Fiber Optic Engineers Conference, 2011, pp. 1–3.

[90] X. Feng, G. M. Ponzo, F. Poletti, A. Camerlingo, F. Parmigiani, M. Petrovich, P. Petropoulos, N. White, W. Loh, and D. Richardson, “A single-mode, high index-contrast, lead silicate glass fibre with high nonlinearity, broadband near-zero dispersion at telecommunication wavelengths,” in *Optical Communication (ECOC), 2010 36th European Conference and Exhibition on*, 2010, pp. 1–3.

[91] I. H. Malitson, “Interspecimen comparison of the refractive index of fused silica,” *J. Opt. Soc. Am.*, vol. 55, no. 10, pp. 1205–1208, 1965.

[92] T. Miyashita and T. Manabe, “Infrared optical fibers,” *IEEE Trans. Microw. Theory Tech.*, vol. 30, no. 10, pp. 1420–1438, 1982.

[93] G. Ghosh, “Sellmeier coefficients and chromatic dispersions for some tellurite glasses,” *J. Am. Ceram. Soc.*, vol. 78, no. 3, pp. 2828–2830, 1995.

[94] W. Dumbaugh and J. Lapp, “Heavy-metal oxide glasses,” *J. Am. Ceram. Soc.*, vol. 75, no. 9, pp. 2315–2326, 1992.

[95] F. Poletti, X. Feng, G. M. Ponzo, M. N. Petrovich, W. H. Loh, and D. J. Richardson, “All-solid highly nonlinear singlemode fibers with a tailored dispersion profile,” *Opt. Express*, vol. 19, no. 1, pp. 66–80, 2011.

[96] A. Snyder and J. Love, *Optical Waveguide Theory*, ser. Science paperbacks. Springer, 1983.

[97] D. Marcuse, “Light transmission optics (second edition),” *J. Opt. Soc. Am.*, vol. 73, no. 5, p. 720, 1983.

[98] Schott optical glass catalogue – version 1.8e, 2009. [Online]. Available: http://www.schott.com/advanced_optics/english/download/schott_optical_glass_catalogue_v18e_2009_en.pdf

[99] T. MIYA, K. Okamoto, Y. Ohmori, and Y. Sasaki, “Fabrication of low dispersion single-mode fibers over a wide spectral range,” *IEEE J. Quant. Electron.*, vol. 17, no. 6, pp. 858–861, 1981.

[100] X. Feng, J. Shi, G. M. Ponzo, F. Poletti, M. N. Petrovich, N. White, P. Petropoulos, M. Ibsen, W. H. Loh, and D. Richardson, “Fusion-spliced highly nonlinear soft-glass w-type index profiled fibre with ultra-flattened, low dispersion profile in 1.55μm telecommunication window,” in *37th European Conference and Exposition on Optical Communications.* Optical Society of America, 2011, p. We.10.P1.05.

[101] J. Jasapara, R. Bise, T. Her, and J. Nicholson, “Effect of mode cut-off on dispersion in photonic bandgap fibers,” in *Optical Fiber Communications Conference, 2003. OFC 2003*, March 2003, pp. 492–493 vol.2.

[102] R. Hui and M. O'Sullivan, *Fiber Optic Measurement Techniques.* Elsevier Science, 2009.

[103] M. Smith and D. Roland, "Understanding differences between otdr and cutback attenuation measurements in multimode graded index fiber," in *Lasers and Electro-Optics Society Annual Meeting, 1996. LEOS 96., IEEE*, vol. 1, 1996, pp. 168–169 vol.1.

[104] A. Yeniay, J. Delavaux, and J. Toulouse, "Spontaneous and stimulated brillouin scattering gain spectra in optical fibers," *J. Lightwave Technol.*, vol. 20, no. 8, pp. 1425–1432, 2002.

[105] S. Asimakis, P. Petropoulos, F. Poletti, J. Y. Y. Leong, R. C. Moore, K. E. Frampton, X. Feng, W. H. Loh, and D. J. Richardson, "Towards efficient and broadband four-wave-mixing using short-length dispersion tailored lead silicate holey fibers," *Opt. Express*, vol. 15, no. 2, pp. 596–601, 2007.

[106] M. Marhic, C. Hsia, and J.-M. Jeong, "Optical amplification in a nonlinear fibre interferometer," *Electron. Lett.*, vol. 27, no. 3, pp. 210–211, 1991.

[107] W. Imajuku, A. Takada, and Y. Yamabayashi, "Low-noise amplification under the 3 db noise figure in high-gain phase-sensitive fibre amplifier," *Electron. Lett.*, vol. 35, no. 22, pp. 1954–1955, 1999.

[108] R. Tang, P. Devgan, V. Grigoryan, and P. Kumar, "Inline frequency-non-degenerate phase-sensitive fibre parametric amplifier for fibre-optic communication," *Electron. Lett.*, vol. 41, no. 19, pp. 1072–1074, 2005.

[109] O.-K. Lim, V. Grigoryan, M. Shin, and P. Kumar, "Ultra-low-noise inline fiber-optic phase-sensitive amplifier for analog optical signals," in *Optical Fiber communication/National Fiber Optic Engineers Conference, 2008. OFC/NFOEC 2008. Conference on*, 2008, pp. 1–3.

[110] C. Lundstrom, J. Kakande, P. Andrekson, Z. Tong, M. Karlsson, P. Petropoulos, F. Parmigiani, and D. Richardson, "Experimental comparison of gain and saturation characteristics of a parametric amplifier in phase-sensitive and phase-insensitive mode," in *Optical Communication, 2009. ECOC '09. 35th European Conference on*, 2009, pp. 1–2.

[111] A. Bogris, D. Syvridis, and C. Efstathiou, "Noise properties of degenerate dual pump phase sensitive amplifiers," *J. Lightwave Technol.*, vol. 28, no. 8, pp. 1209–1217, 2010.

[112] H. P. Yuen, "Reduction of quantum fluctuation and suppression of the gordon–haus effect with phase-sensitive linear amplifiers," *Opt. Lett.*, vol. 17, no. 1, pp. 73–75, 1992.

[113] W. Imajuku and A. Takada, "Reduction of fiber-nonlinearity-enhanced amplifier noise by means of phase-sensitive amplifiers," *Opt. Lett.*, vol. 22, no. 1, pp. 31–33, 1997.

[114] K. Croussore and G. Li, "Phase and amplitude regeneration of differential phase-shift keyed signals using phase-sensitive amplification," *IEEE J. Sel. Top. Quant. Electron.*, vol. 14, no. 3, pp. 648–658, 2008.

[115] J. Kakande, A. Bogris, R. Slavik, F. Parmigiani, D. Syvridis, P. Petropoulos, and D. Richardson, "First demonstration of all-optical qpsk signal regeneration in a novel multi-format phase sensitive amplifier," in *Optical Communication (ECOC), 2010 36th European Conference and Exhibition on*, 2010, pp. 1–3.

[116] Z. Tong, C. Lundstrm, P. A. Andrekson, C. J. McKinstrie, M. Karlsson, D. J. Blessing, E. Tipsuwannakul, B. J. Puttnam, H. Toda, and L. Grner-Nielsen, "Towards ultrasensitive optical links enabled by low-noise phase-sensitive amplifiers," *Nature Photon.*, no. 7, p. 430436, 2011.

[117] R. Tang, M. Shin, P. Devgan, V. Grigoryan, M. Vasilyev, and P. Kumar, "Toward in-line phase-sensitive fiber-parametric amplification of multichannel signals," in *Lasers and Electro-Optics, 2006 and 2006 Quantum Electronics and Laser Science Conference. CLEO/QELS 2006. Conference on*, 2006, pp. 1–2.

[118] C. McKinstrie and S. Radic, "Phase-sensitive amplification in a fiber," *Opt. Express*, vol. 12, no. 20, pp. 4973–4979, 2004.

[119] J. A. Armstrong, N. Bloembergen, J. Ducuing, and P. S. Pershan, "Interactions between light waves in a nonlinear dielectric," *Phys. Rev.*, vol. 127, pp. 1918–1939, 1962.

[120] Y. Chen and A. W. Snyder, "Four-photon parametric mixing in optical fibers: effect of pump depletion," *Opt. Lett.*, vol. 14, no. 1, pp. 87–89, 1989.

[121] P. Andrekson, "Phase-sensitive fiber-optic parametric amplifiers and their applications," in *IEEE Photonics Society, 2010 23rd Annual Meeting of the*, 2010, pp. 455–456.

[122] R. Tang, J. Lasri, P. S. Devgan, V. Grigoryan, P. Kumar, and M. Vasilyev, "Gain characteristics of a frequency nondegenerate phase-sensitive fiber-optic parametric amplifier with phase self-stabilized input," *Opt. Express*, vol. 13, no. 26, pp. 10 483–10 493, 2005.

[123] M. Marhic, *Fiber Optical Parametric Amplifiers, Oscillators and Related Devices.* Cambridge University Press, 2008.

[124] R. Slavik, A. Bogris, F. Parmigiani, J. Kakande, M. Westlund, M. Skold, L. Gruner-Nielsen, R. Phelan, D. Syvridis, P. Petropoulos, and D. Richardson,

"Coherent all-optical phase and amplitude regenerator of binary phase-encoded signals," *IEEE J. Sel. Top. Quant. Electron.*, vol. 18, no. 2, pp. 859–869, 2012.

[125] K. Croussore, I. Kim, C. Kim, Y. Han, and G. Li, "Phase-and-amplitude regeneration of differential phase-shift keyed signals using a phase-sensitive amplifier," *Opt. Express*, vol. 14, no. 6, pp. 2085–2094, 2006.

[126] D. Levandovsky, M. Vasilyev, and P. Kumar, "Amplitude squeezing of light by means of a phase-sensitive fiber parametric amplifier," *Opt. Lett.*, vol. 24, no. 14, pp. 984–986, 1999.

[127] J. Kakande, C. Lundström, P. A. Andrekson, Z. Tong, M. Karlsson, P. Petropoulos, F. Parmigiani, and D. J. Richardson, "Detailed characterization of a fiber-optic parametric amplifier in phase-sensitive and phase-insensitive operation," *Opt. Express*, vol. 18, no. 5, pp. 4130–4137, 2010.

[128] K. Croussore and G. Li, "Phase regeneration of nrz-dpsk signals based on symmetric-pump phase-sensitive amplification," *IEEE Photon. Technol. Lett.*, vol. 19, no. 11, pp. 864–866, 2007.

[129] R. Slavík, F. Parmigiani, J. Kakande, C. Lundström, M. Sjödin, P. A. Andrekson, R. Weerasuriya, S. Sygletos, A. D. Ellis, L. Grüner-Nielsen, D. Jakobsen, S. Herstrøm, J. O'Gorman, A. Bogris, D. Syvridis, S. Dasgupta, P. Petropoulos, and D. J. Richardson, "All-optical phase and amplitude regenerator for next-generation telecommunications systems," *Nature Photon.*, vol. 4, no. 10, pp. 690–695, 2010.

[130] J. H. Lee, T. Tanemura, K. Kikuchi, T. Nagashima, T. Hasegawa, S. Ohara, and N. Sugimoto, "Experimental comparison of a kerr nonlinearity figure of merit including the stimulated brillouin scattering threshold for state-of-the-art nonlinear optical fibers," *Opt. Lett.*, vol. 30, no. 13, pp. 1698–1700, 2005.

[131] L. Jones, F. Parmigiani, J. Kakande, P. Petropoulos, and D. J. Richardson, "All-optical broadband phase noise emulation," in *Advanced Photonics Congress.* Optical Society of America, 2012, p. JM5A.19.

[132] O. Humbach, H. Fabian, U. Grzesik, U. Haken, and W. Heitmann, "Analysis of oh absorption bands in synthetic silica," *J. Non-Cryst. Solids*, vol. 203, no. 0, pp. 19 – 26, 1996.

[133] X. Feng, J. C. Flanagan, K. E. Frampton, P. Petropoulos, N. M. White, J. H. Price, W. H. Loh, H. N. Rutt, and D. J. Richardson, "Developing single-mode tellurite glass holey fiber for infrared nonlinear applications," *Adv. Sci. Tech.*, vol. 55, pp. 108–117, 2008.

[134] R. M. Almeida and L. F. Santos, "Structure and properties of long-wavelength-transmitting halide glasses," *J. Am. Ceram. Soc.*, vol. 72, no. 11, pp. 2065–2070, 1989.

[135] A. Boskovic, L. Gruner-Nielsen, O. A. Levring, S. V. Chernikov, and J. R. Taylor, "Direct continuous-wave measurement of n_2 in various types of telecommunication fiber at 1.55 μm," *Opt. Lett.*, vol. 21, no. 24, pp. 1966–1968, 1996.

[136] D. Marcuse, "Loss analysis of single-mode fiber splices," *Bell Syst. Tech. J.*, vol. 56, no. 5, pp. 703–718, 1977.

[137] J. D. Harvey, R. Leonhardt, S. Coen, G. K. L. Wong, J. Knight, W. J. Wadsworth, and P. S. Russell, "Scalar modulation instability in the normal dispersion regime by use of a photonic crystal fiber," *Opt. Lett.*, vol. 28, no. 22, pp. 2225–2227, 2003.

[138] M. A. Foster, A. C. Turner, J. E. Sharping, B. S. Schmidt, M. Lipson, and A. L. Gaeta, "Broad-band optical parametric gain on a silicon photonic chip," *Nature Photon.*, vol. 441, pp. 960–963, 2006.

[139] X. Liu, B. Kuyken, G. Roelkens, R. Baets, R. M. Osgood, and W. M. J. Green, "Bridging the mid-infrared-to-telecom gap with silicon nanophotonic spectral translation," *Nature Photon.*, vol. 6, pp. 667–671, 2012.

[140] H. Tompkins and W. McGahan, *Spectroscopic Ellipsometry and Reflectometry: A User's Guide.* Wiley, 1999.

[141] F. Biancalana and D. V. Skryabin, "Vector modulational instabilities in ultra-small core optical fibres," *J. Opt. A-Pure Appl. Op.*, vol. 6, no. 4, p. 301, 2004.

[142] C. Koos, L. Jacome, C. Poulton, J. Leuthold, and W. Freude, "Nonlinear silicon-on-insulator waveguides for all-optical signal processing," *Opt. Express*, vol. 15, no. 10, pp. 5976–5990, 2007.

[143] L. Oxenlowe, M. Galili, M. Pu, H. Ji, H. Hu, K. Yvind, J. Hvam, H. C. H. Mulvad, E. Palushani, J. Areal, A. Clausen, and P. Jeppesen, "Ultra-fast optical signal processing in nonlinear silicon waveguides," in *Group IV Photonics (GFP), 2011 8th IEEE International Conference on*, 2011, pp. 335–337.

[144] E. Dulkeith, Y. A. Vlasov, X. Chen, N. C. Panoiu, and J. Richard M. Osgood, "Self-phase-modulation in submicron silicon-on-insulator photonic wires," *Opt. Express*, vol. 14, no. 12, pp. 5524–5534, 2006.

[145] H. K. Tsang, C. S. Wong, T. K. Liang, I. E. Day, S. W. Roberts, A. Harpin, J. Drake, and M. Asghari, "Optical dispersion, two-photon absorption and self-phase modulation in silicon waveguides at 1.5m wavelength," *Appl. Phys. Lett.*, vol. 80, no. 3, pp. 416–418, 2002.

[146] O. Boyraz, T. Indukuri, and B. Jalali, "Self-phase-modulation induced spectral broadening in silicon waveguides," *Opt. Express*, vol. 12, no. 5, pp. 829–834, 2004.

[147] H. Fukuda, K. Yamada, T. Shoji, M. Takahashi, T. Tsuchizawa, T. Watanabe, J. ichi Takahashi, and S. ichi Itabashi, "Four-wave mixing in silicon wire waveguides," *Opt. Express*, vol. 13, no. 12, pp. 4629–4637, 2005.

[148] B. Lee, A. Biberman, A. Turner-Foster, M. Foster, M. Lipson, A. Gaeta, and K. Bergman, "Demonstration of broadband wavelength conversion at 40 gb/s in silicon waveguides," *IEEE Photon. Technol. Lett.*, vol. 21, no. 3, pp. 182–184, 2009.

[149] R. Claps, D. Dimitropoulos, Y. Han, and B. Jalali, "Observation of raman emission in silicon waveguides at 1.54 μm," *Opt. Express*, vol. 10, no. 22, pp. 1305–1313, 2002.

[150] O. Boyraz and B. Jalali, "Demonstration of a silicon raman laser," *Opt. Express*, vol. 12, no. 21, pp. 5269–5273, 2004.

[151] H. S. Rong, A. S. Liu, R. Jones, O. Cohen, D. Hak, R. Nicolaescu, A. Fang, and M. Paniccia, "An all-silicon raman laser," *Nature Photon.*, vol. 433, pp. 292–294, 2005.

[152] D. J. Paul, "Si/sige heterostructures: from material and physics to devices and circuits," *Semicond. Sci. Technol.*, vol. 19, no. 10, p. R75, 2004.

[153] P. Chaisakul, D. Marris-Morini, M.-S. Rouifed, G. Isella, D. Chrastina, J. Frigerio, X. L. Roux, S. Edmond, J.-R. Coudevylle, and L. Vivien, "23 ghz ge/sige multiple quantum well electro-absorption modulator," *Opt. Express*, vol. 20, no. 3, pp. 3219–3224, 2012.

[154] L. Tsybeskov and D. Lockwood, "Silicon-germanium nanostructures for light emitters and on-chip optical interconnects," *Proc. IEEE*, vol. 97, no. 7, pp. 1284–1303, 2009.

[155] P. Chaisakul, D. Marris-Morini, G. Isella, D. Chrastina, M.-S. Rouifed, X. Le Roux, S. Edmond, E. Cassan, J.-R. Coudevylle, and L. Vivien, "10-gb/s ge/sige multiple quantum-well waveguide photodetector," *IEEE Photon. Technol. Lett.*, vol. 23, no. 20, pp. 1430–1432, 2011.

[156] G. Tittelbach, B. Richter, and W. Karthe, "Comparison of three transmission methods for integrated optical waveguide propagation loss measurement," *PURE APPL. OPT.*, vol. 2, no. 6, p. 683, 1993.

[157] L. Coldren, S. Corzine, and M. Mashanovitch, *Diode Lasers and Photonic Integrated Circuits*, ser. Wiley Series in Microwave and Optical Engineering. Wiley, 2012.

[158] A. Lamminp, T. Niemi, E. Ikonen, P. Marttila, and H. Ludvigsen, "Effects of dispersion on nonlinearity measurement of optical fibers," *Opt. Fiber Technol.*, vol. 11, no. 3, pp. 278 – 285, 2005.

[159] H. Tsang, R. Penty, I. White, R. S. Grant, W. Sibbett, J. B. D. Soole, H. LeBlanc, N. C. Andreadakis, R. Bhat, and M. Koza, "Two-photon absorption and self-phase modulation in ingaasp/inp multi-quantum-well waveguides," *J. Appl. Phys.*, vol. 70, no. 7, pp. 3992–3994, 1991.

[160] T.-K. Liang and H.-K. Tsang, "Nonlinear absorption and raman scattering in silicon-on-insulator optical waveguides," *IEEE J. Sel. Top. Quant. Electron.*, vol. 10, no. 5, pp. 1149–1153, 2004.

[161] A. Bristow, N. Rotenberg, and H. van Driel, "Two-photon absorption and kerr coefficients of silicon for 850-2200 nm," *Appl. Phys. Lett.*, vol. 90, no. 19, pp. 191 104–191 104–3, 2007.

[162] B. Batagelj, "Conversion efficiency of fiber wavelength converter based on degenerate fwm," in *Transparent Optical Networks, 2000 2^{nd} International Conference on*, 2000, pp. 179–182.

[163] N. Shibata, R. Braun, and R. Waarts, "Phase-mismatch dependence of efficiency of wave generation through four-wave mixing in a single-mode optical fiber," *IEEE J. Quant. Electron.*, vol. 23, no. 7, pp. 1205–1210, 1987.

[164] Q. Lin, T. J. Johnson, R. Perahia, C. P. Michael, and O. J. Painter, "A proposal for highly tunable optical parametric oscillation in siliconmicro-resonators," *Opt. Express*, vol. 16, no. 14, pp. 10 596–10 610, 2008.

[165] T. Vallaitis, S. Bogatscher, L. Alloatti, P. Dumon, R. Baets, M. L. Scimeca, I. Biaggio, F. Diederich, C. Koos, W. Freude, and J. Leuthold, "Optical properties of highly nonlinear silicon-organic hybrid (soh) waveguide geometries," *Opt. Express*, vol. 17, no. 20, pp. 17 357–17 368, 2009.

[166] K. W. DeLong, K. B. Rochford, and G. I. Stegeman, "Effect of two–photon absorption on all-optical guided-wave devices," *Appl. Phys. Lett.*, vol. 55, no. 18, pp. 1823–1825, 1989.

[167] V. Mizrahi, M. A. Saifi, M. J. Andrejco, K. W. DeLong, and G. I. Stegeman, "Two-photon absorption as a limitation to all-optical switching," *Opt. Lett.*, vol. 14, no. 20, pp. 1140–1142, 1989.

[168] P. Barritault, M. Brun, P. Labeye, O. Lartigue, J.-M. Hartmann, and S. Nicoletti, "Mlines characterization of the refractive index profile of sige gradient waveguides at 2.15 μm," *Opt. Express*, vol. 21, no. 9, pp. 11 506–11 515, 2013.

[169] S. Pitois and G. Millot, "Experimental observation of a new modulational instability spectral window induced by fourth-order dispersion in a normally dispersive single-mode optical fiber," *Opt. Commun.*, vol. 226, pp. 415–422, 2003.

[170] E. Palik, *Handbook of Optical Constants of Solids*, ser. Academic Press handbook series. Academic Press, 1991, no. v. 2.

[171] J. Humlivcek, A. Roseler, T. Zettler, M. G. Kekoua, and E. V. Khoutsishvili, "Infrared refractive index of germanium-silicon alloy crystals," *Appl. Opt.*, vol. 31, pp. 90–94, 1992.

[172] J. K. Kakande, "Phase sensitive parametric amplifiers and their applications," Ph.D. dissertation, University of Southampton, 2013.

[173] T. Okuno, M. Hirano, T. Kato, M. Shigematsu, and M. Onishi, "Highly nonlinear and perfectly dispersion-flattened fibres for efficient optical signal processing applications," *Electron. Lett.*, vol. 39, pp. 972–974(2), 2003.

[174] M. Asobe, T. Kanamori, K. Naganuma, H. Itoh, and T. Kaino, "Third–order nonlinear spectroscopy in as2s3 chalcogenide glass fibers," *J. Appl. Phys.*, vol. 77, no. 11, pp. 5518–5523, 1995.

[175] J. H. Lee, T. Nagashima, T. Hasegawa, S. Ohara, N. Sugimoto, and K. Kikuchi, "Bismuth-oxide-based nonlinear fiber with a high sbs threshold and its application to four-wave-mixing wavelength conversion using a pure continuous-wave pump," *J. Lightwave Technol.*, vol. 24, no. 1, p. 22, 2006.

[176] A. Glass, A. Guenther, and U. S. N. B. of Standards, *Laser induced damage in optical materials, 1977: proceedings of a symposium, October 4-6, 1977, NBS Boulder, Colorado*, ser. ASTM special technical publication. The Supt. of Docs., U.S. Govt. Print. Off., 1978.

[177] T. Inoue, T. Yagi, and S. Namiki, "Highly nonlinear fiber devices for optical networks," in *Lasers and Electro-Optics Society, 2005. LEOS 2005. The 18th Annual Meeting of the IEEE*, 2005, pp. 157–158.

[178] M. A. Foster, A. C. Turner, M. Lipson, and A. L. Gaeta, "Nonlinear optics in photonic nanowires," *Opt. Express*, vol. 16, no. 2, pp. 1300–1320, 2008.

[179] S. J. Madden, D.-Y. Choi, D. A. Bulla, A. V. Rode, B. Luther-Davies, V. G. Ta'eed, M. D. Pelusi, and B. J. Eggleton, "Long, low loss etched As_2S_3 chalcogenide waveguides for all-optical signal regeneration," *Opt. Express*, vol. 15, no. 22, pp. 14 414–14 421, 2007.

[180] J. Matres, G. C. Ballesteros, P. Gautier, J.-M. Fédéli, J. Martí, and C. J. Oton, "High nonlinear figure-of-merit amorphous silicon waveguides," *Opt. Express*, vol. 21, no. 4, pp. 3932–3940, 2013.

[181] L. Shen, N. Healy, P. Mehta, T. D. Day, J. R. Sparks, J. V. Badding, and A. C. Peacock, "Nonlinear transmission properties of hydrogenated amorphous silicon

core fibers towards the mid-infrared regime," *Opt. Express*, vol. 21, no. 11, pp. 13 075–13 083, 2013.

[182] A. Tuniz, G. Brawley, D. J. Moss, and B. J. Eggleton, "Two-photon absorption effects on raman gain in single mode as2se3 chalcogenide glass fiber," *Opt. Express*, vol. 16, no. 22, pp. 18 524–18 534, 2008.

[183] M. R. Lamont, B. Luther-Davies, D.-Y. Choi, S. Madden, and B. J. Eggleton, "Supercontinuum generation in dispersion engineered highly nonlinear($\gamma = 10$ /w/m) as2s3 chalcogenide planar waveguide," *Opt. Express*, vol. 16, no. 19, pp. 14 938–14 944, 2008.

[184] K. Narayanan and S. F. Preble, "Optical nonlinearities in hydrogenated-amorphous silicon waveguides," *Opt. Express*, vol. 18, no. 9, pp. 8998–9005, 2010.

[185] S. K. OLeary, S. R. Johnson, and P. K. Lim, "The relationship between the distribution of electronic states and the optical absorption spectrum of an amorphous semiconductor: An empirical analysis," *J. Appl. Phys.*, vol. 82, no. 7, pp. 3334–3340, 1997.

[186] B. Kuyken, H. Ji, S. Clemmen, S. K. Selvaraja, H. Hu, M. Pu, M. Galili, P. Jeppesen, G. Morthier, S. Massar, L. Oxenløwe, G. Roelkens, and R. Baets, "Nonlinear properties of and nonlinear processing in hydrogenated amorphous silicon waveguides," *Opt. Express*, vol. 19, no. 26, pp. B146–B153, 2011.

[187] S. Jiang, *Advances in Glass and Optical Materials: Proceedings of the 107th Annual Meeting of The American Ceramic Society, Baltimore, Maryland, USA 2005, Ceramic Transactions*, ser. Ceramic Transactions Series. Wiley, 2012.

[188] T. Delmonte, M. A. Watson, E. J. O'Driscoll, X. Feng, T. M. Monro, V. Finazzi, P. Petropoulos, J. H. Price, J. C. Baggett, W. Loh, D. J. Richardson, and D. P. Hand, "Generation of mid-ir continuum using tellurite microstructured fiber," in *Conference on Lasers and Electro-Optics/Quantum Electronics and Laser Science Conference and Photonic Applications Systems Technologies.* Optical Society of America, 2006, p. CTuA4.